Meshless Investigation for Nonlocal Elasticity: Static and Dynamic

by

Xuejiao Huang

Thesis

Submitted to the Queen Mary University of London

for the degree of

Doctor of Philosophy

School of Engineering and Material Science

Queen Mary University of London

August 2016

Declarations

I, Xuejiao Huang, confirm that the research included within this thesis is my own work or that where it has been carried out in collaboration with, or supported by others, that this is duly acknowledged below and my contribution indicated. Previously published material is also acknowledged below.

I attest that I have exercised reasonable care to ensure that the work is original, and does not to the best of my knowledge break any UK law, infringe any third party's copyright or other Intellectual Property Right, or contain any confidential material.

I accept that the College has the right to use plagiarism detection software to check the electronic version of the thesis.

I confirm that this thesis has not been previously submitted for the award of a degree by this or any other university.

The copyright of this thesis rests with the author and no quotation from it or information derived from it may be published without the prior written consent of the author.

Signature: Xuejiao Huang

Date: 25/07/2016

Details of collaboration and publications: please refer to section "8.4 List of Publications".

Acknowledgments

Above all, I would like to express my sincere gratitude to my supervisor Dr. Pihua Wen for his guidance and full support throughout my Ph.D. study I have spent at Queen Mary University of London (QMUL). I understand that he has placed numerous trust on me, and I hope that I have achieved his high expectations. I cannot remember exactly how many times during my four-year study that he could not find the interval to take a rest and discuss yet another problem that I encountered with my research. His help always pulls me back on the right track. I have also benefited a lot from his serious attitude, extraordinary motivation and professional work, which will have an essential impact on my future career.

I would also like to thank the Department of Engineering and Material Science for providing financial support via the China Scholarship Council (CSC) throughout my time at QMUL.

My warm gratitude also goes to a number of colleagues, Dr. Fang Su, Miss Yang Wang, Dr. Tomas Lukas, Miss Tianyi Tao, Mr. Xiang Shen, Mr. Chao Shi and Mrs Mouna Chetehouna for their valuable help and suggestions during my Ph.D. study. Further thanks go to all academics who have given me a little bit of their time for guidance and support, Prof. M.H. Ferry Aliabadi, Dr. Fangxin Zou, Mr. Yanhong Chen, thank you. All staffs who have spent time replying my emails and offered valuable help are appreciated. My apologies to anyone who I have not mentioned.

A special thanks, however, is reserved for Prof. Ping Cao in Central South University (CSU), who encouraged me to pursue my Ph.D. abroad. The sweet memories I share with Miss Linqi Huang, Miss Jin Jin, Dr. Xiang Fan, Dr. Chengzhi Pu

in CSU are always motivating me.

My deepest love goes to my family. Many thanks to my parents for always being there in my tough times, and for educating and encouraging me all these years with ever-lasting support.

Finally, I would like to say thank you to all of the wonderful people I have met at QMUL over the past four years, in particular, my husband, Mr. Xiang Li. His love and support have been invaluable.

Abstract

The numerical treatment of nonlocal problems, which taking into account material microstructures, by means of meshless approaches is promising due to its efficiency in addressing integropartial differential equations. This thesis focuses on the investigation of meshless methods to nonlocal elasticity.

Firstly, mathematical constructions of meshless shape functions are introduced and their properties are discussed. Shape functions based upon different radial basis function (RBF) approximations are implemented and solutions are compared. Interpolation errors of different meshless shape functions are examined.

Secondly, the Point Collocation Method (PCM), which is a strong-form meshless method, and the Local Integral Equation Method (LIEM) that bases on the weak-form, are presented. RBF approximations are employed both in PCM and LIEM. The influences of support domains, different kinds of RBFs and free parameters are studied in PCM. While in LIEM, analytical forms of integrals, which is new in meshless method, is addressed. And, the number of straight lines that enclose the local integral domain as well as the integral radius are analyzed. Several examples are conducted to demonstrate the accuracy of PCM and LIEM. Besides, comparisons are made with Abaqus solutions.

Then, PCM and LIEM are applied to nonlocal elastostatics based on the Eringen's model. Formulations of both methods are reported in the nonlocal frame. Numerical examples are presented and comparisons between solutions obtained from both methods are made, validating the accuracy and effectiveness of meshless methods for solving static nonlocal problems. Simultaneously, the influence of

characteristic length and portion factors are investigated.

Finally, LIEM is employed to solve nonlocal elastodynamic problems. The Laplace transform method and the time-domain technique are implemented in LIEM respectively as the time marching schemes. Numerical solutions of both approaches are compared, showing reasonable agreements. The influence of characteristic length and portion factors are investigated in nonlocal dynamic cases as well.

Contents

List of Tables

List of Figures

List of Abbreviations

1D	One-dimensional
2D	Two-dimensional
FEM	Finite Element Method
XFEM	Extended Finite Element Method
PIM	Point Interpolation Method
RBFs	Radial Basis Functions
RPIM	Radial Point Interpolation Method
PCM	Point Collocation Method
LIEM	Local Integral Equation Method
SPH	Smooth Particle Hydrodynamics
NSF	Normalized Smoothing Function
DEM	Diffuse Element Method
MLS	Moving Least-Square
EFG	Element-Free Galerkin method
RKPM	Reproducing Kernel Particle Method
PUFEM	Partition of Unity Finite Element Method
GFEM	Generalized Finite Difference Method
FPM	Finite Point Method
MLPG	Meshless Local Petrov-Galerkin method
LBIE	Local Boundary Integral Equation method
LPIM	Local Point Interpolation Method
LRPIM	Local Radial Point Interpolation Method

BPIM	Boundary Point Interpolation Method
BRPIM	Boundary Radial Point Interpolation Method
MWS	Meshless Weak-Strong form methods
BEM	Boundary Element Method
BNM	Boundary Node Method
HBIE	Hybrid Boundary Integral Equation method
HBPIM	Hybrid Boundary Point Interpolation Method
HBRPIM	Hybrid Boundary Radial Point Interpolation Method
EXP	Gaussian RBF
MQ	Multiquadrics RBF
TPS	Thin Plate Spline RBF
NL-PCM	PCM for Nonlocal Elastostatics
NL-LIEM	LIEM for Nonlocal Elastostatics

List of Nomenclature

$\boldsymbol{P_n}$	Polynomial basis functions
$\boldsymbol{K}$	Number of nodes in the support domain
$\boldsymbol{b_n}$	Unknown coefficients corresponding to polynomial basis
$\boldsymbol{U}$	Nodal values
$\boldsymbol{\Phi}$	Shape functions
$\boldsymbol{R_m}$	Radial basis functions
$\boldsymbol{a_m}$	Unknown coefficients corresponding to radial basis
$\boldsymbol{\Omega}$	Problem domain
$\boldsymbol{\sigma_{ij}}$	Normal stress components
$\boldsymbol{\tau_{ij}}$	Shear stress components
$\boldsymbol{\varepsilon_{ij}}$	Strain components
$\boldsymbol{f_i}$	Body force components
$\boldsymbol{u_i}$	Displacement components
$\boldsymbol{E}$	Young's modulus
$\boldsymbol{\mu}$	Poisson's ratio
$\boldsymbol{M}$	Number of nodes in the problem domain
$\boldsymbol{M_D}$	Number of nodes on the displacement boundary
$\boldsymbol{M_T}$	Number of nodes on the traction boundary
$\boldsymbol{u_i^0}$	Prescribed displacement
$\boldsymbol{t_i^0}$	Prescribed traction
$\boldsymbol{\Gamma}$	Problem boundary
$\boldsymbol{\Omega_s}$	Local integral domain

$\boldsymbol{\Gamma_s}$	Local integral boundary
$\boldsymbol{u_i^*}$	Test function
$\boldsymbol{n}$	Unit outward normal
$\boldsymbol{\Gamma_D}$	Displacement boundary
$\boldsymbol{\Gamma_T}$	Traction boundary
$\boldsymbol{L_s}$	Interior local boundary
$\boldsymbol{\Delta}$	Distance between field nodes
$\boldsymbol{L}$	Number of straight lines
$\boldsymbol{D}$	Radius of local integral domains
$\boldsymbol{V}$	Domain volume
$\boldsymbol{l}$	Characteristic length
$\mathbf{x}$	Collocation points
$\mathbf{x}'$	Domain integration points
$\bar{\boldsymbol{\sigma}}$	Local (classical) stress
$\boldsymbol{\alpha}(\lvert\mathbf{x}\text{-}\,\mathbf{x}'\rvert/\boldsymbol{l})$	Nonlocal kernel
$\boldsymbol{\xi_1}$	Portion factor related to local phase
$\boldsymbol{\xi_2}$	Portion factor related to nonlocal phase
$\boldsymbol{\Delta V_q}$	Sub integral domains
$\mathbf{x}'_p$	Integral points in ΔV_q
$\boldsymbol{\Delta_l}$	Length of the l^{th} straight line
$\boldsymbol{\rho}$	Mass density
$\boldsymbol{\ddot{u}_i}$	Acceleration
$\boldsymbol{\dot{u}_i}$	Velocity
$\boldsymbol{p}$	Laplace parameter
$\widehat{\boldsymbol{f}}(\boldsymbol{p})$	Laplace transform of a function $f(t)$
$\widehat{\bar{\boldsymbol{\sigma}}}$	Local (classical) stress in Laplace domain
$\widehat{\boldsymbol{u}}_i$	Displacement components in Laplace domain
$\widehat{\boldsymbol{u}}_i^0$	Prescribed displacement in Laplace domain
$\widehat{\boldsymbol{t}}_i^0$	Prescribed traction in Laplace domain

η	Free parameter in the inverse Laplace transform procedure
γ	Free parameter in the Newmark method
β	Free parameter in the Newmark method
Δt	Time step
c_1	Longitudinal wave speed
b	Specified length
u_i/b	Normalized displacements
σ_{ij}/b	Normalized stresses
$c_1 t/b$	Normalized time

CHAPTER 1

Introduction

1.1 Background and Motivation

Composites are being increasingly indispensable in comprehensive applications of modern technology and arouse much compelling attention among scientific communities because of their superior properties, e.g., chemical resistance, substantial weight savings whereas significant improvements in strength over similar metal parts, and, moreover, the ability to deform and recover to their original shape without major damage. Besides, their unique thermal properties and low electronic conductivity make them employed as a more satisfactory and cost effective solution for various branches of engineering.

Vast research investigations have been devoted to the mechanical behaviour of composites, which is of crucial importance in potential applications of composite technology to large variety of problems. However, experimental efforts with composite materials are both prohibitively expensive and formidably difficult, since the internal structure of composites, characterized by sophisticated microstructures, can never be precisely described over the entire range of size scales. Consequently, great endeavours concerning to develop appropriate models for composites are car-

ried out in different approaches. In general, there are two classical methods to model composite materials. The atomic or molecular modelling, based especially on the atomic lattice theory, is the first one that should be referred to. In spite of its applicability at micro scales, it is restricted to deal with limited numbers of atoms and molecules. Otherwise, the foregoing models give rise to the same disadvantages with experimental studies, namely, computationally costly and complicated. The other alternative way is the continuum mechanics, e.g., the elasticity theory. Due to its less lavish in computational expenditure and simpler in formula aspect, continuum mechanics approach has been adopted to explore physical and mechanical properties of composites such as wave propagation, bucking and free vibration at microscopic levels.

Most continuum theories rely on the fundamental assumption of material homogeneity at any arbitrary size scales, which means the equilibrium equations can be validated over each of infinitesimal volumes in the finite body as far as it is concerned. And the standard constitutive models in classical theories describe stresses at a material point of interest depending solely on the strain at that point only. However, it is known to all that the physical nature of a material is represented by a large numbers of essential constituents such as atoms or molecules gathered together. The lattice distance between individual atoms or molecules cannot afford to be ignored when it becomes obviously comparable to external scales and the discrete microstructure in composites can no longer be treated as homogeneous continuum at small size. In other words, material behaviours are size independent in classical continuum theories and thus accurate prediction of mechanical properties of composites cannot archive if the prominent size effect has not been taken into account. Therefore, nonlocal theories framed in the realm of continuum theories have been initiated for which allowing the consideration of size effects in the study of microstructures in composites.

Another motivation of nonlocal theories grounds on the fact that classical continuum theories give rise to physically unrealistic results in the existence of sharp geometrical singularities. A typical case is the singular stress predicted at the crack front in the context of continuum fracture mechanics, which has become a topic of major concern in the research community. This inability reveals the intrinsic shortcoming of classical elasticity, that is, the lack of accommodating the internal characteristic length of a material in the analysis.

Nonlocal theories provide a possible solution to deal with the embarrassment embedded in classical continuum approaches by regarding the material microstructure and accounting for the internal characteristic length. Solutions for nonlocal problems are nevertheless generally difficult to solve analytically and/or numerically since the constitutive relations for which are of integropartial differential equations and even the simplest one-dimensional problems are extraordinary complex mathematically in analytical solutions. Consequently, to treat these problems numerically may be the only solution that is effective as well as practicable.

Recently, the idea of 'Meshless' or 'Meshfree' , aimed at getting rid of at least part of meshes or elements by constructing the interpolation or approximation entirely in terms of nodes, turned to intrigue the interests of the academic and research community. Although in some of the meshless methods, background grids are still required, they reduce the time and cost spent on the mesh generation to a great extent and moving discontinuities can usually be treated without burdened remeshing and hence eliminating the loss of accuracy. For these reasons, meshless methods are possible to deal with large classes of problems which are very awkward with mesh-based methods. On the aforementioned grounds and motivations, mesh reduction techniques are employed to solve nonlocal elasticity mechanical problems in the presented thesis.

This introductory chapter is structured as follows. In the next section, an overview

of the development of nonlocal elasticity theories will be given. And then a brief review of meshless methods will be presented. Finally, the scope of this thesis will close this chapter.

1.2 Nonlocal Elasticity Theories

Early investigation of nonlocal elasticity theories can be traced back nearly fifty years ago when the description of range effects as well as the cohesive forces were concerned in elastic materials [1]. Almost simultaneously, an approach based on the crystal lattice theory considering elastic media with microstructures was proposed and applied to the description of interactions between crystal defects and dislocations [2]. And, moreover, Krumhansl [3] derived a continuum method on the basis of atomic lattice theory. Later, Edelen and Eringen [4, 5] characterized the theories of nonlocal elasticity by imposing a nonlocal character to fields such as mass, body forces or internal energy.

Improvements have been made by the work of Polizzotto [6, 7] who took the nonlocality residuals into account by means of thermodynamics and solved the nonhomogeneous nonlocal elasticity problems. Contributions based on the energy residuals in thermodynamic principles are from various aspects emerged, including nonlocal damage [8], heat conduction [9], gradient plasticity [10], wave propagation [11], electronic analysis [12], fracture [13], and, nonlocal properties of currently prevalent materials such as nanostructures, functionally graded materials and smart materials [14–16].

A leap has been provided in extending nonlocal elasticity theories to practical problems since the simplified nonlocal elasticity theories were promising for linear homogeneous isotropic media by the work of Eringen and co-workers [17, 18] in which only the stress and strain relations are regarded as nonlocality and character-

ized by an attenuation function. Recently, low-residual approximate solutions for one- and two-dimensional nonlocal elasticity are obtained based on the Eringen's model and can be used as benchmarks for nonlocal elastic problems [19].

Stress singularities predicted at a sharp crack front is a typical awkward issue in continuum fracture mechanics needed to be resolved since the classical theories have no association with material internal characteristic length as pointed out by Eringen [20] and consequently limiting their applications only to macrostructures. Nonlocal elasticity theories provide the feasibility to defeat the inherent shortcoming of classical elasticity theories at the existence of a shape crack tip and relevant literatures are extensively traceable. For instance, crack problems in functionally graded materials and piezoelectric materials were investigated [21, 22], Stamoulis [23] studied the crack growth influenced by size effects under bending, Allegri [24] derived stresses at the crack-tip in orthotropic bodies, Mousavi [25] modeled cracks by continuous distributed straight dislocations and obtained no singularities at the crack tip.

Recently, various industries express a keen interest in composite materials and reopen the discussion of size effects. Nonlocal elasticity theories, based on continuum approaches, are widely employed to adequately descript the physical nature of material microstructures, and to capture the material behaviour taking place at microstructure, or, even, at atomic or molecular scales. A list of references related to the hottest composites are also extensive, starting with the work of Peddieson [26] who showed the potentiality of nonlocal theories to nanomaterial. Wang et al [27] analyzed the elastic buckling of nanotubes taking size effects into account by use of the nonlocal elasticity theory. Pradhan et al [28] obtained analytical solutions for vibration of nanoplates. Murmur et al [29] investigated the vibration response a double-nanoplate-system assumed to be bonded by an enclosing elastic medium under biaxial compression. More recent vibration investigations of nanoplates can

be found in [30, 31], which concerned the free vibration and the nonlinear vibration of piezoelectric nanoplates. Besides, bending, buckling and free vibration of nanobeams were investigated, see [32, 33]. Static and stability study of functionally graded nanobeams and their nonlinear free vibration was recently presented in [34, 35]. Moreover, an overview of the application of nonlocal elastic models to simulate carbon nanotubes and graphene can be seen in [36]. Their progresses on carbon nanotubes and graphene are far to be exhaustive and just to refer some latest ones [37, 38].

The aforementioned advances are mainly focusing on the constitutive relations of nonlocal elastic models, another parallel contribution to nonlocal elasticity theories is related to boundary value problems. Investigations related to questions such as the conditions for the existence of fundamental solutions as well as the existence and uniqueness of solutions were addressed by Rogula [39] and Altan [40, 41], respectively. To this concern, related variational principles were developed by Polizzotto [6].

Although a comprehensive review of nonlocal models and theories applied in plasticity and damage can be found in [42], we mainly focus on nonlocal elasticity theories in the presented thesis and a historical overview of which can be found in [43].

1.3 Meshless Methods

There is no denying that the Finite Element Method (FEM) proposed in the 1950s is one of the milestones in the fields of both academic and industries. It has been successfully applied to most engineering branches including not only linear problems but also nonlinear cases because in which complicated structures can be resolved flexibly in terms of information provided by elements or meshes. The availability

of well-developed commercial FEM packages is another stimulating factor that lead to its prevalent for solving practical issues related to solids and structures.

Although FEM is thoroughly developed, it is not without limitations. For instance, the accuracy of solutions cannot guarantee when distorted or low quality meshes are created, and that is the price to pay in mesh-reliant methods. In addition, FEM struggle inevitably against problems with discontinuities that deviate from original element edges. Hence, the most feasible strategy to deal with moving discontinuities is to remesh in each step hereby insuring element edges remain align with the discontinuities. Unfortunately, such remeshing is evidently time consuming as well as high price in human interaction since the projection of field variables between meshes is required in successive stages and then subsequently resulting in a degradation of accuracy in FEM solutions. In order to describe the discontinuities in the realm of mesh-based approach, an alternative way aimed at easy re-constructing the mesh, named extended finite element method (XFEM), was proposed by Belytschko et al [44]. Some recent progresses of XFEM are cited to reflect that it still be an active topic in the research community [45, 46].

Specifically, in simulations of problems involved in extremely large deformations such as metal extrusion and molding, high-speed impact and coupled fluid-solid, considerable loss of accuracy in FEM solutions arise from the element distortions. And, for crack propagation cases with complex and arbitrary paths, additional computation cannot be avoided duo to the remeshing. Moreover, FEM is based on continuum theories, it is hard to model the failure process of a material consisted of a large number of small particles. Serious errors occur when non-linear or path-dependent problems are analyzed.

Taking advantages of predefined elements or meshes information in FEM formulations is the fundamental reason for the above-mentioned drawbacks. The most immediate idea to overcome the disadvantages is to get rid of the elements and

meshes in the numerical analysis. Therefore, the concepts of meshless or meshfree methods came into being. Briefly speaking, a meshless or meshfree method depends on the interpolation or approximation over a set of randomly distributed nodes in the problem domain rather than a predefined mesh, and hence it has a promising applications to various aspects.

The numerical treatment of nonlocal elastic problems, characterized by a stress and strain relationship of convolutive type, by means of meshless methods was developed due to its efficiency in dealing with integropartial differential equations. More than ten years ago, a meshless method was applied to solve dynamic crack problems nonlocally [47]. Sladek [48] proposed the nonlocal boundary integral formulation for softening damage. More lately, meshless collocation techniques on the basis of RBFs was employed to address nonlocal problems of Timoshenko nanobeams related to bending, bucking and free vibration [49] and to solve a nonlocal boundary value problem [50]. Among others, the potentialities of meshless methods within nonlocal solid mechanical problems were presented by the work of Wen and Huang [51–53].

An intensive discussion of historical developments and basic solution procedures of meshless methods will be given in Chapter 2.

1.4 Scope of the Present Thesis

Remaining chapters of this thesis are outlined as follows:

Chapter 2 begins with an overview of meshless methods. Different kinds of mesh reduction methods are reviewed. Then, the general solution procedures of meshfree methods as well as their future developments are introduced.

Chapter 3 presents the interpolation and/or approximation scheme for meshless methods. Shape function constructions especially by means of Point Interpola-

tion Method (PIM), Radial Basis Functions (RBFs) and Radial Point Interpolation Method (RPIM) are systemically discussed. RPIM shape functions based on different RBFs approximations are implemented in 1D and 2D domain. And interpolation errors of meshless shape functions based on different RBFs are examined.

Chapter 4 introduces the meshless Point Collocation Method (PCM) for 1D and 2D isotropic solids. Several numerical examples are carried out by both the PCM code and ABAQUS simulations. The influence of different types of RBFs, support domains as well as free parameters are examined. Comparisons between results are conducted, showing great agreement when appropriate approximation schemes and parameters are selected.

Chapter 5 presents the formulations of meshless Local Integral Equation Method (LIEM) for the 2D isotropic medium in great details. Analytical solutions for domain integrals are derived by taking advantage of the unit test function and the Multiquadric (MQ) RBF. Besides, the convergence of LIEM is investigated. Numerical solutions of three examples are compared with ABAQUS and PCM results, which indicate the accuracy of LIEM.

Chapter 6 discusses the application of PCM and LIEM to nonlocal elastostatics based on the Eringen's model. Formulations of both methods are presented in the nonlocal frame and then employed to solve nonlocal elastic problems numerically. Comparisons between solutions derived from both methods confirm the accuracy and effectiveness of meshless methods in dealing with nonlocal elastostatic problems. Simultaneously, free parameters in Eringen's model are examined as well.

Chapter 7 derives the formulation of LIEM for nonlocal elastodynamics. Nonlocal time-dependent problems are resolved by LIEM in the Laplace transform domain and in the time-domain, respectively. The Durbin's inversion method is employed in the Laplace transform method, while the Newmark method is chosen as the time marching scheme in the time-domain technique. Two examples are car-

ried out and the influence of free parameters are studied. Additionally, numerical solutions form both methods are compared, showing reasonable agreement.

Chapter 8 summarizes this thesis and suggests the future work as well as possible improvements. The author's publications during the doctoral research are also listed.

CHAPTER 2

An Overview of Meshless Methods

2.1 Introduction

A multitude of meshless methods have been developed over the last three decades. It is noteworthy that they are in fact originated from the mesh-free idea in spite of significant varieties of names between many individual methods. Meshless strong-form methods that base on some collocation techniques and usually discretize at field nodes are truly meshfree methods since no numerical integration is involved and no mesh is needed for field variable approximations. However, other meshless methods, such as those based upon the Galerkin weak-form, an auxiliary background grid is needed for numerical integrations. Therefore, they are basically not truly meshfree methods.

This chapter is aimed at presenting an overview of the historical developments of meshless methods, followed by their general solution procedures. And some remarks and future developments close this chapter.

2.2 Historical Developments

2.2.1 Smooth Particle Hydrodynamics (SPH)

The advent of meshless methods is traceable to more than thirty years ago with the developing of finite difference methods for arbitrary irregular meshes [54]. However, due to the prevalence of FEM, the research interest focused on it was rare. In 1977, Lucy [55] and Gingold [56] proposed a Lagrangian method on the basis of kernel estimated method, which was firstly employed for modelling astrophysical phenomena without boundaries including exploding stars and dust clouds etc.. This method is the well-known Smooth Particle Hydrodynamics (SPH), which regards the fluid as a group of moving particles and the governing differential equations were rewritten as the kernel estimates integrals.

In despite of the roaring success of SPH, the publications were very modest compared with other methods in those times and were mainly presented in the papers of Monaghan and co-workers [57]. There were hardly any applications of SPH to other kinds of problems until the 90's. It consequently revealed some inherent shortcomings of SPH including tensile instability, lack of interpolation consistency in field variable approximations, and difficulty in enforcing displacement boundary conditions [58]. Over the last decades, there have been substantial improvements and modifications in SPH. Johnson [59] developed a normalized smoothing function (NSF) algorithm that improve the accuracy of SPH impact computations. Dyka [60] figured out the origin of the tensile instability and proposed a stabilized scheme. Vignjevic [61] described a specific treatment of zero-energy modes.

The applications of SPH include a wide range of aspects, such as the simulation of stars collisions [62], incompressible flows [63], gravity currents [64], heat transfer [65] and so on. Besides, SPH has shown its capacity to simulate high velocity

impact problems. Randles and Libersky [66] have made great efforts to apply SPH to impact problems. Liu and co-workers have applied SPH to underwater explosions [67].

2.2.2 Diffuse Element Method (DEM)

Another scheme to construct meshfree approximations, which emerged ten years later after SPH was initially introduced, is the moving least-square (MLS) approximations proposed by Lancaster and Salkauskas [68]. Then, Nayroles et al firstly applied MLS in the Galerkin technique in 1992 to formulate the Diffuse Element Method (DEM) [69], which bases on the thought that replacing the interpolation within a FEM element by the MLS local interpolation [70]. Many academicians indicated that it was only after the DEM that the idea of 'meshless' or 'meshfree' began to intrigue the interests of the academic and research community.

2.2.3 Element-Free Galerkin Method (EFG)

Belytschko and colleagues announced another extraordinary idea in 1994 related to Element-Free Galerkin Method (EFG) [71] that can be regarded as an extension of Nayroless DEM. This class of methods introduces a series of refinements and improvements over DEM formulations. Firstly, it properly determines the approximation derivatives because Belytschko have stated that neglecting some derivatives detracts significantly from the accuracy of the DEM. In addition, Belytschko have shown that DEM fails to pass the patch test on the account of the fact that the MLS trial function does not yield an interpolation and the essential boundary conditions cannot directly satisfy. Therefore, implementation of essential boundary conditions was achieved by the employment of Lagrange Multipliers in the EFG. Moreover, Chung [72] proposed local and global error estimates for EFG. Belytschko et al

[73, 74] conducted a deep exploration on the numerical integration and the approximation scheme. The EFG method was found to be more consistent, accurate and stable than the DEM, although the 'improvements' result in substantially more expensive than SPH.

The prevalence of EFG among other meshless methods pushes forward its application extending to a variety of problems. Belytschko [75] have used EFG to simulate the fracture and crack propagation. Krysl [76] applied EFG in the analysis of arbitrary Kirchhoff shells. Hengen [77] combined the EFG and FEM and hence maximized their own strengths. Du [78] applied EFG in 2D shallow water flows in rivers. Cordes [79] used EFG to solve solid mechanics problems containing material discontinuities. Zhang [80] proposed a meshless model for the mechanics analysis of jointed rock structures based on the EFG method.

2.2.4 Reproducing Kernel Particle Method (RKPM)

In 1995, Liu [81] proposed the Reproducing Kernel Particle Method (RKPM), which was motivated by the theory of wavelets as well as the attributions of the EFG method. RKPM is another path to overcome the lack of consistency in SPH and successful applications have been found in the multiscale technique [82], acoustics analysis [83], structural dynamics [81], fluid dynamics [84], stress concentration [85], large deformation analysis [86], metal forming process analysis [87], shear-deformation beams and plates [88], micro-electromechanical system [89], etc..

2.2.5 H-p Cloud

In the same year, Duarte and Oden [90] proposed a new methodology called H-p Cloud. It used MLS interpolations to build a partition of unity and its convergence was proved by Liu et al [91]. Then, it is employed as a low-cost procedure to

construct trial and test functions for Galerkin approximations. Mendonca [92] used H-p Cloud method to solve Timoshenko beam problems, while Garcia [93] applied it on the Mindlin's thick plate model.

2.2.6 Partition of Unity

Another two steps deserve to be mentioned in the advance of meshfress methods are the proposed of the Partition of Unity Finite Element Method (PUFEM) and Generalized Finite Difference Method (GFEM) [94, 95]. Both of them can deal with randomly distributed nodes. Furthermore, the PUFEM has played an crucial role that closely resembles MLS and partitions of unity, as can be seen from the article by Babuska and Melenk [96].

2.2.7 Finite Point Method (FPM)

The Finite Point Method was developed by Onate [97] in 1996, which was formulated on the basis of a weighted least-square interpolation of nodal values and node collocation for evaluating the approximation integrals. Fluid problems were originally addressed by the proposed method [98] and then other problems associated with elastic mechanics were concerned [99]. Recently, Ortega [100] improved the adaptive features of FPM and guaranteed its accuracy and cost effectiveness when it is employed to solve practical fluid problems. In addition, Aluru [101] proposed the so-called Point Collocation Method (PCM) that has been applied to analyse piezoelectric devices [102] on reproducing kernel approximations basis. And the importance of positivity conditions has been pointed out for the purpose of establishing a robust PCM [103].

2.2.8 Meshless Local Petrov-Galerkin (MLPG)

A significant achievement in the evolution of meshless methods should be attributed to Atluri and Zhu [104] who introduced the Meshless Local Petrov-Galerkin (MLPG) in 1998, which presented another route to implement the meshfree idea on the basis of local weak form that get rid of the auxiliary grids thoroughly. Besides, the employment of Petrov-Galerkin method greatly simplify the integration appeared in the local weak form. Therefore, MLPG can be performed easily in a truly meshless sense.The proposed method was constructed within the MLS framework until other approximation approaches were used to formulate MLPG. Plenty of MLPG schemes was derived benefiting from the fact that test functions can be selected arbitrarily in the Petrov-Galerkin method [105].

MLPG has been applied to many areas including elastostatic and elastodynamic problems of solids [106, 107], high order partial differential equations for thin beams [108] and thick beams (shear deformable beams) [109], plate structures [110], vibration analysis for solids [111], linear fracture problems [112], fluid mechanics problems [113], crack propagation [114], high-speed impact [115], etc.. A special instance of MLPG, called the Local Boundary Integral Equation method (LBIE), has demonstrated its talent in both linear and non-linear boundary value problems [116].

2.2.9 Radial Basis Functions (RBFs)

Radial Basis Functions (RBFs) was initially presented as the multiquadrics by Kansa in 1991 for the sake of resolving partial differential equations and fluid dynamic issues by taking advantages of collocation methods [117]. Although collocation methods are relatively easy and straight-forward, they usually fail to derive a sparse stiffness matrix when a global support domain is employed, that may lead to sub-

stantially rise in computational time and cost supposing that there were vast of collocation points located within the problem domain. On the other hand, compactly supported RBFs have been applied to solve partial differential equations as well. However, the accuracy is not inspiring compared with solutions from global supported RBFs even though the stiffness matrix is not dense anymore. Additionally, the mix of governing equations and boundary conditions in RBFs absolutely lead to a set of asymmetric system equations. As a consequence, the RBF Hermite-Collocation method [118] was proposed as a tool to prevent the annoying asymmetry.

RBF approximation technique has drawn the attention of academics and researchers since the beginning of Kansa's attempt. However, its applications to practical problems are hardly be seen in the literature and plenty of investigations have been carried out mathematically. Some applications deserve to be mentioned are concerned in the transport phenomena [119] and heat conduction [120].

2.2.10 Point Interpolation Method (PIM)

Liu and co-workers [121] introduced the Point Interpolation Method (PIM) in 2001 as an alternative method to construct the meshless approximation based on the interpolation technique. Therefore, shape functions in PIM is characterized by the Kronecker delta function property, demonstrating one of the major differences between the interpolation technique and the MLS approximation.

Two kinds of PIM formulations have been developed using the polynomial basis [122] and the RBFs [123]. However, problems arise when applying the polynomial PIM for the reason that the interpolation matrix is sensitive to the selection of polynomial basis. In other words, inappropriate selections may give rise to a badly conditioned matrix, or even worse, suffer from singularities. By contrast, the Ra-

dial Point Interpolation Method (RPIM) is more stable and robust for managing arbitrarily distributed nodes and hence extensively employed to different branches of engineering. e.g., two- and three-dimensional solid mechanics [122], piezoelectric material [124], material nonlinear problems in civil engineering [125] and so on.

One more trouble relies on the fact that the approximation function could be discontinuous since no weighted function is employed in PIM. Great efforts have been devoted saving it from this trouble. For instance, the Local Radial Point Interpolation Methods (LRPIM) was put forward by using multiquadric RBFs as the approximation scheme and has been explored in details in [126].

Besides, PIM and RPIM shape functions have been extended to the boundary integration equations of partial differential equations and formulated the Boundary Point Interpolation Method (BPIM) and the Boundary Radial Point Interpolation Method (BRPIM) respectively [127]. Boundary conditions of the proposed methods can be enforced easily benefiting from the Kronecker delta function property of their shape functions and consequently resulting in high efficiency.

2.2.11 Meshless Weak-Strong (MWS) Form Methods

In spite of the high accuracy of meshless methods based on Galerkin methods, it needs a background grids to carry out numerical integrals. Moreover, they are computationally more expensive than FEM. On the contrary, collocation methods are usually unstable and less accurate even though they are computationally efficient. Therefore, great interest has been triggered to look for a more ideal method that discarding a portion or even all of the background grids and ensuring the stability as well as the accuracy of a specific method. Zhang [128, 129] have proposed the least-squares collocation meshless method and weighted least-square meshless method

as an attempt to reach the aforementioned goal. Besides, Liu and Gu [130] developed a series of meshless methods based on the combination of Galerkin methods and collocation techniques, named Meshfree Weak-Strong (MWS) form methods, aiming at applying both of the strong-form and weak-form formulations simultaneously in a particular problem in order to derive the discretized system equations. Nodes located on or close to the domain boundaries with derivative boundary conditions are treated by the weak-form, whereas collocation points are all treated by the strong-form. Advantages of both methods are gathered in the MWS method so improvements of solutions and the saving of computational resources can be seen obviously.

2.2.12 Others

Although several widespread meshless methods are reviewed in the previous sections, it is noteworthy that there are plenty of other meshless method in the literature. Mukherjee [131] presented a meshless method based on the Boundary Element Method (BEM) named the Boundary Node Method (BNM), for which the application can be seen in [132] and numerical solutions are well presented. However, it is time consuming since the the number of system equations double resulting from the enforcement of boundary conditions in BNM. The Finite Spheres, which is in fact a special MLPG method, was introduce in 2000 [133]. Its approximation scheme is implemented by use of the partition of unity and hence no concerns are needed about the boundary conditions. In addition, a group of hybrid-based meshless methods have also arised such as the Hybrid Boundary Integral Equation method(HBIE) [134], Hybrid Boundary Point Interpolation Method (HBPIM) and the Hybrid Boundary Radial Point Interpolation Method (HBRPIM) [135]. The most prominent characteristic of these hybrid-based methods is they usually result

in a symmetric system matrix and it is an advantage for them to couple with other developed meshless methods that have the same symmetric property.

2.3 General Solution Procedures

The most significant differences between meshless methods and FEM is the construction of shape functions. Predefined elements and meshes are introduced so that shape functions can be constructed using elements or meshes information in FEM. Whereas in meshless methods, only field nodes located within the support domain are selected to construct shape functions for specific points of interest. General solution procedures of meshless methods are outlined in this section as follows.

Step 1: Creation of field nodes

The problem domain is shown in Figure 2.1 (a). A set of randomly distributed field nodes is firstly generated in the problem domain and on its boundary, see Figure 2.1 (b). The density of field nodes which usually associate with field variables depends on the required accuracy.

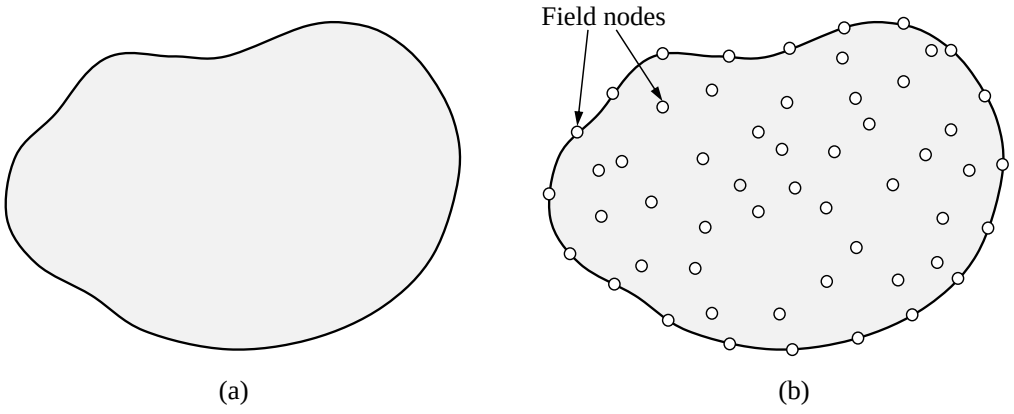

Figure 2.1: *(a) Problem domain; (b) Field nodes distribute in the problem domain and on the boundary.*

Step 2: Construction of shape functions

Shape functions of a point of interest **x** within a problem domain in meshless methods can be constructed by means of interpolating or approximating the field variable such as the displacement u over its support domain using information of field nodes, i.e.,

$$u(\mathbf{x}) = \sum_{i=1}^{n} \phi_i(\mathbf{x}) u_i = \Phi(\mathbf{x}) \mathbf{U}_\mathrm{s} \tag{2.1}$$

in which n is the total number of nodes located in the support domain of point **x**, ϕ_i is the shape function of the i^{th} node within its support domain, u_i is the nodal value at the i^{th} point, $\mathbf{U}_\mathrm{s}$ is the vector that collects all nodal values in the problem domain.

A support domain of a point **x** that includes all field nodes in the problem domain is called global support domain. However, local support domain is the one that widely used in meshless methods, which means only some specific nodes are taken advantage of to approximate or interpolate the function value at **x**, and shape functions outside the local support domain will be regarded as zero. Local support domains are usually circular or rectangular as shown in Figure 2.2, they can however have different geometrical shapes and dimensions corresponding to different points.

Step 3: Formation of discretized global system equations

Discrete equations can be formulated in terms of nodal values using their shape functions and weak-form or strong-form formulations. And then these discretized equations are assembled into the global system equations for the entire problem domain.

Step 4: Solving global system equations

Solutions for the field variable are obtained for all points in the problem domain and can be subsequently utilized to achieve other purposes. Flow chart of meshless methods can be seen in Figure 2.3.

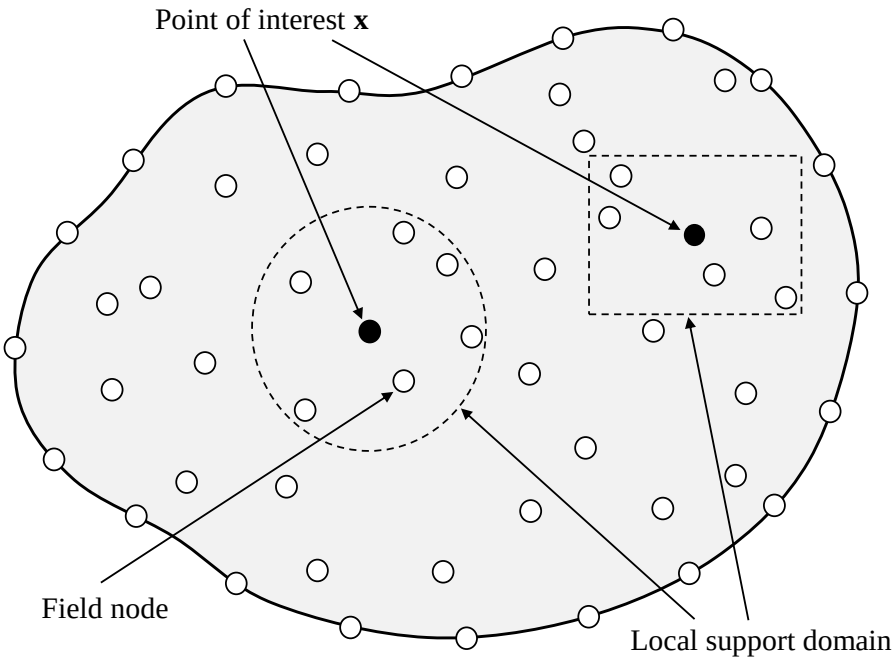

Figure 2.2: *Local support domains.*

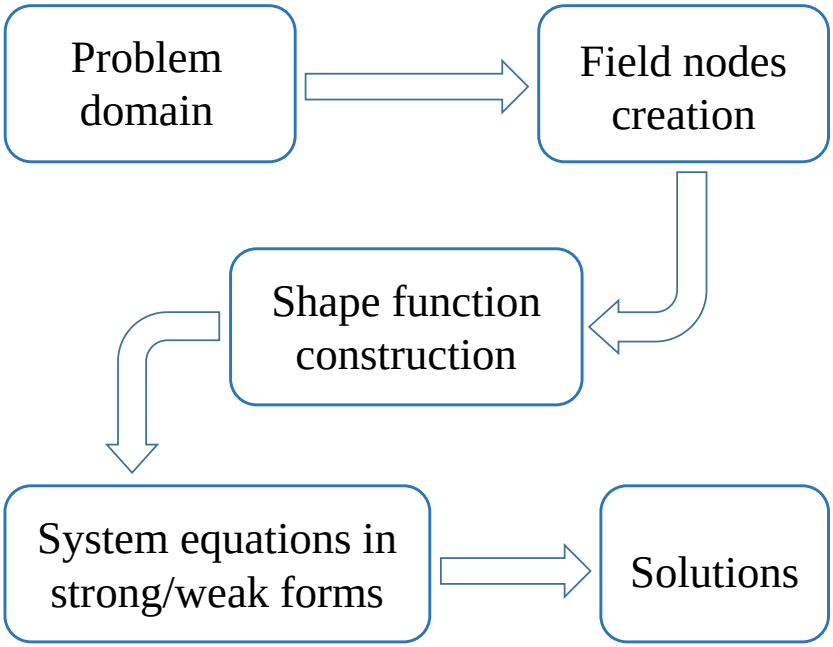

Figure 2.3: *Flow chart of Meshless methods.*

2.4 Summary and Future development

Some overview papers, related to the developments of meshless methods [58, 136] and its applications to electromagnetics [137], computational fluid dynamics [138], laminated and functionally graded plates and shells [139], structure and fracture mechanics [140], heat transfer and fluid flow [141], material forming[142], should be referred to. Additionally, Some main meshless methods are summed up in Table 2.1 on the basis of the discussions in this chapter.

It is until recently that meshless methods are commercially available. Nevertheless, no rigorous demonstration has been performed mathematically on these methods compared with the fully developed FEM. And the computational efficiency has become another issue of major concern since the preferred weak-formed meshless methods are stable and accurate but time-consuming. Moreover, the applications of meshless methods to practical problems have not yet achieved striking improvements. Therefore, more efforts are needed in order to make fully used of meshless methods.

Table 2.1: *Main types of meshless methods*

Meshless/Meshfree methods	**Approximation / interpolation scheme**	**Discretization scheme**
Smoothed Particle Hydrodynamics (SPH) [56]	Kernel estimate	Collocation method
Diffuse Element Method (DEM) [69]	Moving least-square	Collocation method
Element-Free Galerkin method (EFG) [71]	Moving least-square	Galerkin weak form
Reproducing Kernel Particle Method (RPKM) [81]	Reproducing kernel estimate	Galerkin weak form
H-p clouds [90]	Moving least-square interpolation	Galerkin weak form
Partition of Unity Method (PUM) [94]	Partition of unity	Galerkin weak form
Finite Point Method (FPM) [97]	Moving least-square	Collocation method
Point Collocation Method (PCM) [101]	Reproducing kernel estimate	Collocation method
Local Petrov-Galerkin method (MLPG) [104]	Moving least-square	Petrov-Galerkin weak form
Local Boundary Integral Equation method (LBIE) [116]	Moving least-square	Petrov-Galerkin weak form
Radial Basis Functions meshless method (RBF) [117]	Radial basis functions	Collocation method
Point Interpolation Method (PIM) [121]	Point interpolation	Galerkin weak form
Meshfree Weak-Strong form methods (MWS) [130]	Moving least-square + point interpolation	Galerkin weak form + collocation method

CHAPTER 3

Meshless Shape Function Construction

3.1 Introduction

The primary issue needed to be fulfilled is to construct shape functions in order to interpolate or approximate unknown field variables before solving a problem governed by a set of partial differential equations numerically. Meshless shape functions usually approximate unknown field variables such as displacement components at points of interest by use of a group of field nodes located randomly in the support domain. Lots of well-developed and efficient interpolation and approximation techniques are available in the history of meshless methods. Among others, the Moving Least Square (MLS) approximation as well as the Point Interpolation Method (PIM) have been widely used. In this chapter, mathematical constructions of meshless shape functions based mainly upon point interpolation approaches are presented. Also, their consistency, continuity and other distinct properties are discussed. Then, shape functions are implemented and the influences of parameters are investigated in details. Finally, interpolation errors of meshless shape functions

based on different RBFs are examined.

3.2 Polynomial Point Interpolation Methods

One of the most widely used meshless shape function construction methods deserves to be mentioned is the Point Interpolation Method (PIM), which results in different forms by means of different basis functions employed to carry out the interpolation schemes. Polynomials have been used as the basis functions in a variety of numerical approaches [121].

Consider a problem domain Ω represented by a group of arbitrarily distributed nodes. The unknown field variable u at a point of interest $\mathbf{x}$ can be interpolated over its support domain and expressed as

$$u(\mathbf{x}) = \sum_{n=1}^{N} P_n(\mathbf{x}) b_n = \{\ p_1(\mathbf{x}) \quad p_2(\mathbf{x}) \quad \cdots \quad p_N(\mathbf{x})\ \} \begin{Bmatrix} b_1 \\ b_2 \\ \vdots \\ b_N \end{Bmatrix} = \mathbf{p}^{\mathrm{T}}\mathbf{b} \tag{3.1}$$

in which $n = 1, 2, \ldots, N$ is the number of monomials in the polynomial basis function $\{\mathbf{p}\}_{n=1}^{N}$ with degree $\leq T-1$ and $p_n(\mathbf{x})$ is the prescribed monomial, $\{\mathbf{b}\}_{n=1}^{N}$ are the unknown coefficients to be determined.

In a two-dimensional problem domain, the complete quadratic basis functions are in the form of

$$\mathbf{p}^{\mathrm{T}} = \{\ 1 \quad x \quad y \quad x^2 \quad xy \quad y^2\ \} \tag{3.2}$$

Therefore, the approximation of function u over a set of nodes i.e. $\mathbf{x}_k = (x_k, y_k), k =$

$1, 2, \ldots, K$ within its support domain yields K algebraic equations as follows:

$$\begin{cases} b_1 + b_2 x_1 + b_3 y_1 + b_4 x_1^2 + b_5 x_1 y_1 + b_6 y_1^2 = u_1 \\ b_1 + b_2 x_2 + b_3 y_2 + b_4 x_2^2 + b_5 x_2 y_2 + b_6 y_2^2 = u_2 \\ \vdots \\ b_1 + b_2 x_K + b_3 y_K + b_4 x_K^2 + b_5 x_K y_K + b_6 y_K^2 = u_K \end{cases} \tag{3.3}$$

which can be rewritten in the form of

$$\begin{bmatrix} 1 & x_1 & y_1 & x_1^2 & x_1 y_1 & y_1^2 \\ 1 & x_2 & y_2 & x_2^2 & x_2 y_2 & y_2^2 \\ \vdots & \vdots & \vdots & \vdots & \vdots & \vdots \\ 1 & x_K & y_K & x_K^2 & x_K y_K & y_K^2 \end{bmatrix} \begin{Bmatrix} b_1 \\ b_2 \\ b_3 \\ b_4 \\ b_5 \\ b_6 \end{Bmatrix} = \begin{Bmatrix} u_1 \\ u_2 \\ \vdots \\ u_K \end{Bmatrix} \tag{3.4}$$

(3.3) and (3.4) demonstrate that the total number of nodes K included in the support domain always equals the total number of monomials N in the basis function in PIM, namely, $K = N$. Consequently, the general matrix form of the PIM approximation scheme for two-dimensional problems can be expressed by enforcing $u(\mathbf{x})$ in (3.1) equals nodal values at K nodes within the support domain, as

$$\underbrace{\begin{bmatrix} 1 & x_1 & y_1 & \cdots & p_N(\mathbf{x}_1) \\ 1 & x_2 & y_2 & \cdots & p_N(\mathbf{x}_2) \\ \vdots & \vdots & \vdots & \ddots & \vdots \\ 1 & x_K & y_K & \cdots & p_N(\mathbf{x}_K) \end{bmatrix}}_{\mathbf{P}_0} \underbrace{\begin{Bmatrix} b_1 \\ b_2 \\ \vdots \\ b_N \end{Bmatrix}}_{\mathbf{b}} = \underbrace{\begin{Bmatrix} u_1 \\ u_2 \\ \vdots \\ u_K \end{Bmatrix}}_{\mathbf{U}_\mathrm{P}} \tag{3.5}$$

The matrix form of (3.5) can be written as

$$\mathbf{P}_0\mathbf{b} = \mathbf{U}_\mathrm{P} \tag{3.6}$$

where $\mathbf{b}$ denotes the vector of unknowns, and $\mathbf{U}_\mathrm{P}$ is the vector that collects all nodal values. Therefore, unknown coefficients $\mathbf{b}$ can be determined by

$$\mathbf{b} = \mathbf{P}_0^{-1}\mathbf{U}_\mathrm{P} \tag{3.7}$$

It is notable that $\mathbf{b}$ is dependent only on the coordinates of field nodes used in $\mathbf{P}_0$ and nodal values in the corresponding support domains, which means that $\mathbf{b}$ remains constants unless the nodal coordinates or values used in the interpolation differed.

Substituting (3.7) into (3.1), we obtain

$$u(\mathbf{x}) = \mathbf{p}^\mathrm{T}(\mathbf{x})\mathbf{P}_0^{-1}\mathbf{U}_\mathrm{P} = \mathbf{\Phi}^\mathrm{T}(\mathbf{x})\mathbf{U}_\mathrm{P} = \sum_{k=1}^{K}\phi_k u_k \tag{3.8}$$

where $\mathbf{\Phi}$ represents the vector of shape functions and is defined by

$$\mathbf{\Phi}^\mathrm{T}(\mathbf{x}) = \mathbf{p}^\mathrm{T}(\mathbf{x})\mathbf{P}_0^{-1} = \begin{Bmatrix}\phi_1(\mathbf{x}) & \phi_2(\mathbf{x}) & \cdots & \phi_k(\mathbf{x})\end{Bmatrix} \tag{3.9}$$

The i^{th} derivatives of shape functions can be derived easily as well in the following forms:

$$\mathbf{\Phi}^{(i)}(\mathbf{x}) = \frac{\partial^i \mathbf{p}^\mathrm{T}(\mathbf{x})}{\partial \mathbf{x}^i}\mathbf{P}_0^{-1} = \begin{Bmatrix}\phi_1^{(i)}(\mathbf{x}) & \phi_2^{(i)}(\mathbf{x}) & \cdots & \phi_k^{(i)}(\mathbf{x})\end{Bmatrix}^\mathrm{T} \tag{3.10}$$

Some of the properties with respect to polynomial PIM shape functions are listed below.

■ **Consistency**

Establishing polynomial PIM shape functions of high order consistency can be realized without difficulties by raising the highest complete order of the monomial used in the polynomial basis functions. In other words, a complete polynomial basis of order m guarantees the C^m consistency, which is one of the characteristics of polynomial PIM shape functions.

■ **Continuity**

Continuity over the entire problem domain cannot be guaranteed when the polynomial PIM shape functions are locally supported. This is due to the fact that weighted functions are not employed and the matrix $\mathbf{P}_0$ changes suddenly as new nodes enter or exit the local support domains. However, the discontinuity does not arise regarding to the strong-forms and the local weak-forms.

■ **Kronecker delta function property**

Polynomial PIM shape functions satisfy the Kronecker delta function property and are characterized as

$$\Phi_i(\mathbf{x} = \mathbf{x}_j) = \begin{cases} 1 & i = j \quad i, j = 1, 2, \ldots, K \\ 0 & i \neq j \quad i, j = 1, 2, \ldots, K \end{cases} \tag{3.11}$$

since the interpolation lead to $u(x_i) = u_i$ at each node within the support domain.

■ **Linear independence**

Linear independence property is required in the polynomial basis functions for ensuring the existence of $\mathbf{P}_0^{-1}$ in (3.8). Inappropriate selection of polynomial basis

may lead to bad condition or even singularity of matrix $\mathbf{P}_0$.

3.3 Radial Basis Functions (RBFs)

Radial Basis Functions (RBFs) have been regarded as a practical solution in data interpolation for nodes or grids scattered irregularly. More importantly, singularities of polynomial PIM shape functions can be prevented by the employment of RBFs instead of polynomial basis functions.

A continuous function $u(\mathbf{x})$ can be interpolated over a set of nodes $\mathbf{x}_k = (x_k, y_k), k = 1, 2, \ldots, K$ as

$$u(\mathbf{x}) = \sum_{m=1}^{M} R_m(|\mathbf{x} - \mathbf{x}_m|)a_m = \mathbf{R}^{\mathrm{T}}\mathbf{a} \tag{3.12}$$

where $R_m(\cdot)$ is the RBF and $m = 1, 2, \ldots, M$ denotes the number of RBFs, a_m are unknown coefficients to be found, $|\mathbf{x} - \mathbf{x}_m|$ denotes the distance that usually taken to be Euclidean between $\mathbf{x}$ and $\mathbf{x}_m$. It can be seen obviously that $R_m(|\mathbf{x} - \mathbf{x}_m|)$ depends only on $|\mathbf{x} - \mathbf{x}_m|$ which can be written as

$$|\mathbf{x} - \mathbf{x}_m| = \sqrt{(x - x_m)^2 + (y - y_m)^2} \tag{3.13}$$

Therefore, the exact interpolation of function $u(\mathbf{x})$ yields M linear equations for every node, as

$$\begin{cases} a_1 R_1(|\mathbf{x}_1 - \mathbf{x}_1|) + a_2 R_2(|\mathbf{x}_1 - \mathbf{x}_2|) + \cdots + a_M R_M(|\mathbf{x}_1 - \mathbf{x}_M|) = u_1 \\ a_1 R_1(|\mathbf{x}_2 - \mathbf{x}_1|) + a_2 R_2(|\mathbf{x}_2 - \mathbf{x}_2|) + \cdots + a_M R_M(|\mathbf{x}_2 - \mathbf{x}_M|) = u_2 \\ \vdots \\ a_1 R_1(|\mathbf{x}_M - \mathbf{x}_1|) + a_2 R_2(|\mathbf{x}_M - \mathbf{x}_2|) + \cdots + a_M R_M(|\mathbf{x}_M - \mathbf{x}_M|) = u_M \end{cases} \tag{3.14}$$

which can be written in the form of

$$\underbrace{\begin{bmatrix} R_1(|\mathbf{x}_1 - \mathbf{x}_1|) & R_2(|\mathbf{x}_1 - \mathbf{x}_2|) & \cdots & R_M(|\mathbf{x}_1 - \mathbf{x}_M|) \\ R_1(|\mathbf{x}_2 - \mathbf{x}_1|) & R_2(|\mathbf{x}_2 - \mathbf{x}_2|) & \cdots & R_M(|\mathbf{x}_2 - \mathbf{x}_M|) \\ \vdots & \vdots & \ddots & \vdots \\ R_1(|\mathbf{x}_M - \mathbf{x}_1|) & R_2(|\mathbf{x}_M - \mathbf{x}_2|) & \cdots & R_M(|\mathbf{x}_M - \mathbf{x}_M|) \end{bmatrix}}_{\mathbf{R}_0} \underbrace{\begin{Bmatrix} a_1 \\ a_2 \\ \vdots \\ a_M \end{Bmatrix}}_{\mathbf{a}} = \underbrace{\begin{Bmatrix} u_1 \\ u_2 \\ \vdots \\ u_M \end{Bmatrix}}_{\mathbf{U}} \tag{3.15}$$

The matrix form of (3.15) can be written as

$$\mathbf{R}_0 \mathbf{a} = \mathbf{U} \tag{3.16}$$

Provided that the inverse of $\mathbf{R}_0$ exists, the unknown coefficient $\mathbf{a}$ can be derived by any standard matrix inversion techniques as

$$\mathbf{a} = \mathbf{R}_0^{-1} \mathbf{U} \tag{3.17}$$

A wide range of studies have been carried out theoretically and empirically with the purpose of seeking a class of RBFs producing the matrix $\mathbf{R}_0$ without singularities for any group of nodes, which results in plenty of positive definite RBFs that

always ensure their determinant $|R_0| \neq 0$. Some of the most commonly used RBFs are listed in Table 3.1.

Table 3.1: *Commonly used RBFs*

RBFs	Expression	Shape Parameters
Gaussian (EXP)	$R_m(r) = \exp(-r^2/2c_0^2)$	$c_0 > 0$
Multiquadrics (MQ)	$R_m(r) = (r^2 + c_0^2)^{1/2}$	$c_0 > 0$
Inverse multiquadrics	$R_m(r) = (r^2 + c_0^2)^{-1/2}$	$c_0 > 0$
Thin Plate Spline (TPS)	$R_m(r) = r^2 \ln(r)$	N/A
Cubic	$R_m(r) = r^3$	N/A
Linear	$R_m(r) = r$	N/A

Note: $r = |\mathbf{x} - \mathbf{x}_m|$ is a free parameter that associates with the distance between field nodes in the problem domain.

3.4 Radial Point Interpolation Method (RPIM)

The above-mentioned RBFs fail to pass the patch test on the account of the fact that the interpolation scheme in RBFs cannot achieve even the first order consistency. However, it can be addressed without too much trouble by simply adding some polynomial terms and then the polynomial consistency can be ensured. Besides, studies have found that polynomial augmentations in RBFs not only improve the interpolation stability and accuracy, but also reduce the sensitivity of free parameters. Therefore, Wang et al [123] proposed the Radial Point Interpolation Method (RPIM) in the framework of meshfree methods. Its approximation scheme can be written as

$$u(\mathbf{x}) = \sum_{m=1}^{M} R_m(|\mathbf{x} - \mathbf{x}_m|)a_m + \sum_{n=1}^{N} P_n(\mathbf{x})b_n = \mathbf{R}^{\mathrm{T}}\mathbf{a} + \mathbf{p}^{\mathrm{T}}\mathbf{b} \tag{3.18}$$

The matrix form that represents a set of linear equations obtained by enforcing the approximation function goes through nodal values as in the standard PIM can be expressed as

$$\mathbf{R}_0\mathbf{a} + \mathbf{P}_0\mathbf{b} = \mathbf{U} \tag{3.19}$$

in which $\mathbf{U}$ denotes the vector that collects nodal values and

$$\mathbf{U} = \begin{Bmatrix} u_1 & u_2 & \cdots & u_M \end{Bmatrix}^{\mathrm{T}} \tag{3.20}$$

However, there are more unknowns than the total number of equations in (3.19), so a further set of constraint conditions should be introduce to ensure a unique solution as

$$\sum_{m=1}^{M} p_n(\mathbf{x}_m)a_m = \mathbf{P}_0^{\mathrm{T}}\mathbf{a} = 0 \qquad n = 1, 2, \cdots, N \tag{3.21}$$

where

$$\mathbf{P}_0^{\mathrm{T}} = \begin{bmatrix} p_1(\mathbf{x}_1) & p_1(\mathbf{x}_2) & \cdots & p_1(\mathbf{x}_M) \\ p_2(\mathbf{x}_1) & p_2(\mathbf{x}_2) & \cdots & p_2(\mathbf{x}_M) \\ \vdots & \vdots & \ddots & \vdots \\ p_N(\mathbf{x}_1) & p_N(\mathbf{x}_2) & \cdots & p_N(\mathbf{x}_M) \end{bmatrix} \tag{3.22}$$

Considering (3.19) and (3.21) yields an augmented matrix

$$\widetilde{\mathbf{U}} = \begin{bmatrix} \mathbf{U} \\ 0 \end{bmatrix} = \underbrace{\begin{bmatrix} \mathbf{R}_0 & \mathbf{P}_0 \\ \mathbf{P}_0^{\mathrm{T}} & 0 \end{bmatrix}}_{\mathbf{A}} \underbrace{\begin{Bmatrix} \mathbf{a} \\ \mathbf{b} \end{Bmatrix}}_{\mathbf{a}_0} = \mathbf{A}\mathbf{a}_0 \tag{3.23}$$

in which

$$\widetilde{\mathbf{U}} = \{u_1 \quad u_2 \quad \cdots \quad u_M \quad 0 \quad 0 \cdots \quad 0\}^{\mathrm{T}} \tag{3.24}$$

$$\mathbf{a}_0 = \{a_1 \quad a_2 \quad \cdots \quad a_M \quad b_1 \quad b_2 \cdots \quad b_N\}^{\mathrm{T}} \tag{3.25}$$

Form (3.23), coefficient $\mathbf{a}_0$ can be obtained by

$$\mathbf{a}_0 = \begin{Bmatrix} \mathbf{a} \\ \mathbf{b} \end{Bmatrix} = \mathbf{A}^{-1}\widetilde{\mathbf{U}} \tag{3.26}$$

Substitute (3.26) into (3.18) yields the form of

$$\begin{aligned} u(\mathbf{x}) = \{ \ \mathbf{R}^{\mathrm{T}}(\mathbf{x}) \quad \mathbf{p}^{\mathrm{T}}(\mathbf{x}) \ \} \begin{Bmatrix} \mathbf{a} \\ \mathbf{b} \end{Bmatrix} &= \{ \ \mathbf{R}^{\mathrm{T}}(\mathbf{x}) \quad \mathbf{p}^{\mathrm{T}}(\mathbf{x}) \ \}\mathbf{A}^{-1}\widetilde{\mathbf{U}} \\ &= \widetilde{\mathbf{\Phi}}^{\mathrm{T}}(\mathbf{x})\widetilde{\mathbf{U}} \end{aligned} \tag{3.27}$$

in which $\widetilde{\mathbf{\Phi}}^{\mathrm{T}}(\mathbf{x})$ is the RPIM shape functions and can be expressed as

$$\begin{aligned} \widetilde{\mathbf{\Phi}}^{\mathrm{T}}(\mathbf{x}) &= \{ \ \mathbf{R}^{\mathrm{T}}(\mathbf{x}) \quad \mathbf{p}^{\mathrm{T}}(\mathbf{x}) \ \}\mathbf{A}^{-1} \\ &= \{ \ \phi_1(\mathbf{x}) \quad \phi_2(\mathbf{x}) \quad \cdots \quad \phi_M(\mathbf{x}) \quad \phi_{M+1}(\mathbf{x}) \quad \cdots \quad \phi_{M+N}(\mathbf{x}) \ \} \end{aligned} \tag{3.28}$$

Therefore, RPIM shape functions regarding to nodal values are derived as

$$\mathbf{\Phi}^{\mathrm{T}}(\mathbf{x}) = \{ \ \phi_1(\mathbf{x}) \quad \phi_2(\mathbf{x}) \quad \cdots \quad \phi_M(\mathbf{x}) \ \} \tag{3.29}$$

and (3.27) can be overwrite as

$$u(\mathbf{x}) = \mathbf{\Phi}^{\mathrm{T}}(\mathbf{x})\mathbf{U} = \sum_{m=1}^{M} \phi_m u_m \tag{3.30}$$

Additionally, derivatives of $u(\mathbf{x})$ can be easily derived as

$$u_{,i}(\mathbf{x}) = \mathbf{\Phi}_{,i}^{\mathrm{T}}(\mathbf{x})\mathbf{U} \tag{3.31}$$

where the comma denotes a partial differentiation in terms of the variable x or y represented by i.

Some of the properties of RPIM shape functions are listed below.

■ **Consistency**

The consistency over the entire problem domain cannot be ensured when new nodes enter in or exit from the local support domains.

■ **Continuity**

High continuity of RBFs results in high continuity of RPIM shape functions.

■ **Kronecker delta function property**

RPIM shape functions satisfy the Kronecker delta function property since the exact interpolation technique is employed.

3.5 Implementation

In this section, RPIM shape functions will be implemented by use of both the global and local support domains. Two examples are presented to investigate the properties of RPIM shape functions and comparisons between results obtained from different RBFs, i.e., the Gaussian (EXP) and the Multiquadrics (MQ) in Table 3.1, are made. Additionally, the influence of free parameters in RBFs is analyzed as well.

3.5.1 Support Domains and Free Parameters

The most commonly used support domains in RPIM shape functions are of circle and rectangular shapes. Since the circle ones are simple in construction and implementation, they are employed in this section and in the following sections. Circle support domains with the radius r_0 are usually centred at a point of interest $\mathbf{x}$ and the number of field nodes within the circle is determined to be $K = 12$ in this chapter. However, all of the field nodes in the problem domain Ω are selected to carry out the interpolation or approximation scheme if the global support domain is utilized.

Both of the EXP-RBF and MQ-RBF in Table 3.1 involve the free parameter c_0, which at the following examples is taken as a constant as $c_0 = 2\Delta_{min}$, where Δ_{min} is the smallest distances between field nodes in the problem domain. However, the influence of c_0 on the RPIM shape functions are examined later.

3.5.2 1D RPIM Shape Functions with Global Support Domain

Firstly, a one-dimensional example is carried out to investigate the globally supported RPIM shape functions, which means all of the nodes located in the problem domain are involved in the interpolation scheme. As shown in Figure 3.1, a set of field nodes (9 in total) are regularly and evenly distributed in a 1D domain

$x_k \in [0, 1]$, and their coordinates are $x_k = (k-1)/8$.

Two kinds of RBFs, i.e., MQ-RBF and EXP-RBF, are employed. Besides, RPIM-MQ and RPIM-EXP are referred to in the following to represent RPIM shape functions using MQ-RBF and EXP-RBF, respectively.

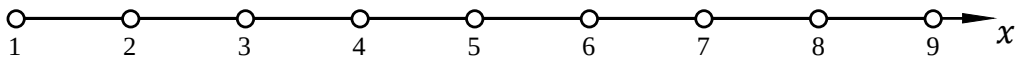

Figure 3.1: *Field nodes used in 1D RPIM shape functions with global support domain.*

RPIM-MQ and RPIM-EXP shape functions and their first order derivatives are plotted in Figure 3.2 and Figure 3.3 with respect to different polynomial basis such as linear polynomials $\mathbf{p}^{\mathrm{T}} = \{\ 1 \quad x\ \}$ and quadratic polynomials $\mathbf{p}^{\mathrm{T}} = \{\ 1 \quad x \quad x^2\ \}$ used in shape function constructions. From Figure 3.3 one can see that the influence of polynomial terms is quit tiny. But it has been found that they do help to improve the consistency as well as the stability of the interpolation scheme. More importantly, all of the shape functions obtained in Figure 3.2 satisfy the Kronecker delta function property.

Output data of RPIM-MQ shape functions and their derivatives for node 5 calculated at point $x = 0.5$ and point $x = 0.74$ are listed in Table 3.2 and Table 3.3, respectively. Data in Table 3.2 numerically confirms that RPIM shape function possesses the Kronecker delta function property. Whereas Table 3.3 reflects another important property of RPIM shape functions, namely, the partitions of unity.

Another two output samples related to RPIM-EXP shape functions are also presented, see Table 3.4 and Table 3.5, which lead to similar conclusions drawn in the study of RPIM-MQ shape functions.

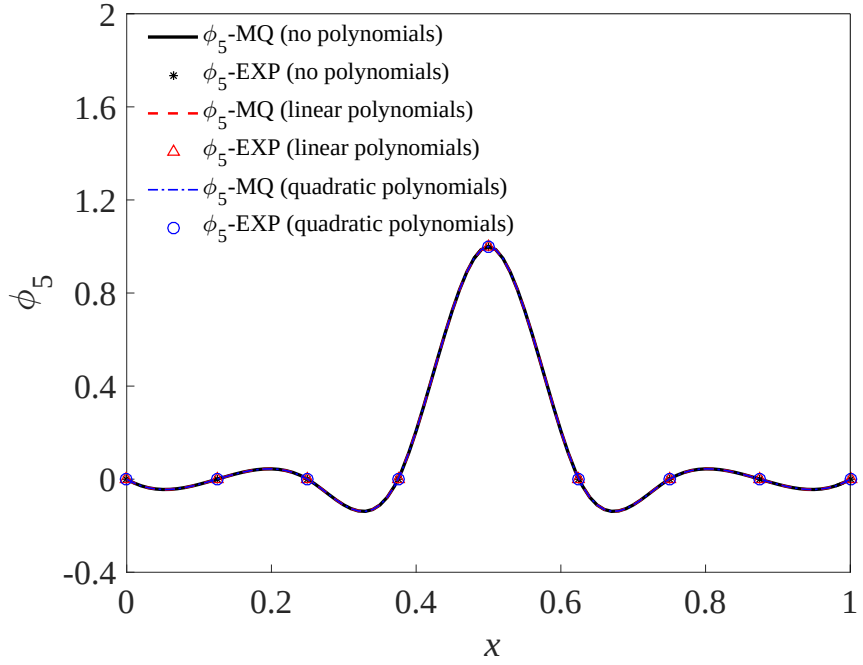

Figure 3.2: *RPIM-MQ and RPIM-EXP shape functions for node 5 at point* $x = 0.5$ *with different number of polynomials.*

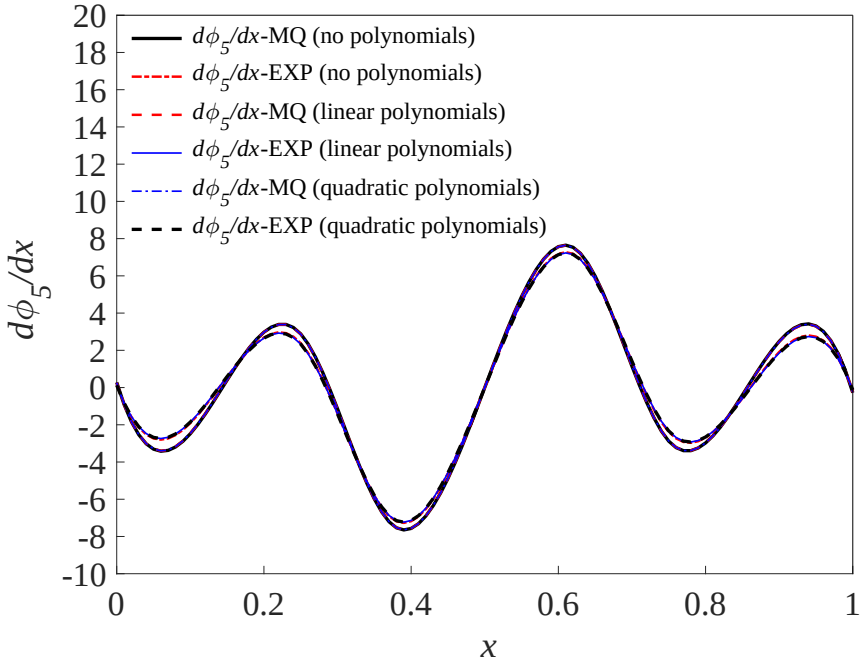

Figure 3.3: 1^{st} *derivatives of RPIM-MQ and RPIM-EXP shape functions for node 5 at point* $x = 0.5$ *with different number of polynomials.*

Table 3.2: *Numerical data of RPIM-MQ shape functions for node 5 calculated at node* $x = 0.5$ *by use of the global support domain (with quadratic polynomials)*

Node	x_k	ϕ_5	$\frac{d\phi_5}{dx}$	$\frac{d^2\phi_5}{dx^2}$
1	0.0	0.00000	0.25973	-2.32088
2	0.125	0.00000	-1.12850	11.39770
3	0.25	0.00000	2.86999	-33.65880
4	0.375	0.00000	-7.39344	133.19000
5	0.5	1.00000	0.00000	-217.21600
6	0.625	0.00000	7.39344	133.19000
7	0.75	0.00000	-2.86999	-33.65880
8	0.875	0.00000	1.12850	11.39770
9	1.0	0.00000	-0.25973	-2.32088

Table 3.3: *Numerical data of RPIM-MQ shape functions for node 5 calculated at node* $x = 0.74$ *by use of the global support domain (with quadratic polynomials)*

Node	x_k	ϕ_5	$\frac{d\phi_5}{dx}$	$\frac{d^2\phi_5}{dx^2}$
1	0.0	-0.00130	0.13168	0.82402
2	0.125	0.00430	-0.43104	-0.76230
3	0.25	-0.00890	0.90438	-1.03568
4	0.375	0.01770	-1.80184	3.88474
5	0.5	-0.03540	3.64290	-14.46230
6	0.625	0.08670	-9.24295	106.30300
7	0.75	0.97960	3.04884	-198.51200
8	0.875	-0.05210	4.60628	121.49800
9	1.0	0.00940	-0.85825	-17.73780
		$\sum \phi = 1.00000$		

Table 3.4: *Numerical data of RPIM-EXP shape functions for node 5 calculated at node* $x = 0.5$ *by use of the global support domain (with quadratic polynomials)*

Node	x_k	ϕ_5	$\frac{d\phi_5}{dx}$	$\frac{d^2\phi_5}{dx^2}$
1	0.0	0.00000	0.12323	-0.48433
2	0.125	0.00000	-0.70778	3.77222
3	0.25	0.00000	2.33308	-18.72240
4	0.375	0.00000	-7.03573	112.68900
5	0.5	1.00000	0.00000	-194.50900
6	0.625	0.00000	7.03573	112.68900
7	0.75	0.00000	-2.33308	-18.72240
8	0.875	0.00000	0.70778	3.77222
9	1.0	0.00000	-0.12323	-0.48433

Table 3.5: *Numerical data of RPIM-EXP shape functions for node 5 calculated at node* $x = 0.74$ *by use of the global support domain (with quadratic polynomials)*

Node	x_k	ϕ_5	$\frac{d\phi_5}{dx}$	$\frac{d^2\phi_5}{dx^2}$
1	0.0	-0.00140	0.13079	1.68462
2	0.125	0.00700	-0.66908	-8.05821
3	0.25	-0.01920	1.83889	20.26500
4	0.375	0.03890	-3.74450	-35.46800
5	0.5	-0.06730	6.57607	42.01890
6	0.625	0.12380	-12.65580	41.82910
7	0.75	0.94630	6.12120	-140.84400
8	0.875	-0.03190	2.74718	86.80420
9	1.0	0.00380	-0.34472	-8.23218
		$\sum \phi = 1.00000$		

3.5.3 1D RPIM Shape Functions with Local Support Domain

Properties of RPIM shape functions with local support domains are examined by another 1D example as shown in Figure 3.4. The total number of field nodes is taken as 21 in a domain $x_k \in [0, 1]$, and their coordinates are $x_k = (k-1)/20$.

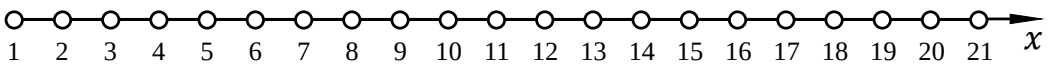

Figure 3.4: *Field nodes used in 1D RPIM shape functions with local support domains.*

MQ-RBF and EXP-RBF are augmented by quadratic polynomials to form RPIM shape functions. Output data for node 11 in Figure 3.4 evaluated at point $x = 0.5$ and point $x = 0.24$ are obtained by RPIM-MQ and RPIM-EXP, and presented in Table 3.6 to Table 3.9.

It can been seen in Table 3.6 and Table 3.8 that only a part of nodes in the problem domain are selected to construct RPIM-MQ shape functions. They, however, obtain results possessing the Kronecker delta function property within the local support domain. For example, at point $x = 0.5$ in Table 3.6 where node 11 is located, it is clearly shown that

$$\phi_i(\mathbf{x}) = \begin{cases} 1 & i = 11 (\mathbf{x} = \mathbf{x}_i) \\ 0 & i \neq 11 (\mathbf{x} \neq \mathbf{x}_i) \end{cases} \tag{3.32}$$

The observation of Table 3.7 and Table 3.9 have found that even RPIM shape functions are locally supported, they satisfy the partitions of unity within each local support domain, which means $\sum_{k=1}^{K} \phi_k(\mathbf{x}) = 1.0$ can be achieved in all local support domains. However, the summation of shape functions in Table 3.9 is not equal to but approximate 1.0 because of inevitable numerical errors in the calculation of complicated RBFs.

Table 3.6: *Numerical data of RPIM-MQ shape functions for node 11 calculated at $x = 0.5$ by use of local support domains (with quadratic polynomials)*

Node	x_k	ϕ_{11}	$\frac{d\phi_{11}}{dx}$	$\frac{d^2\phi_{11}}{dx^2}$
5	0.2	0.00000	0.18336	-4.20902
6	0.25	0.00000	-0.77520	19.03910
7	0.3	0.00000	1.86029	-47.20410
8	0.35	0.00000	-3.80301	100.09800
9	0.4	0.00000	7.73407	-228.71500
10	0.45	0.00000	-18.72450	844.79000
11	0.5	1.00000	0.00000	-1367.60000
12	0.55	0.00000	18.72450	844.79000
13	0.6	0.00000	-7.73407	-228.71500
14	0.65	0.00000	3.80301	100.09800
15	0.7	0.00000	-1.86029	-47.20410
16	0.75	0.00000	0.77520	19.03910
17	0.8	0.00000	-0.18336	-4.20902

Table 3.7: *Numerical data of RPIM-MQ shape functions for node 11 calculated at* $x = 0.24$ *by use of local support domains (with quadratic polynomials)*

Node	x_k	ϕ_{11}	$\frac{d\phi_{11}}{dx}$	$\frac{d^2\phi_{11}}{dx^2}$
1	0	0.00350	-0.35030	-5.74308
2	0.05	-0.01540	1.52937	24.01660
3	0.1	0.03790	-3.78724	-54.09260
4	0.15	-0.08260	8.43049	76.95430
5	0.2	0.22320	-25.36320	459.50400
6	0.25	0.93360	13.04500	-1196.72000
7	0.3	-0.14230	9.51451	957.50100
8	0.35	0.06300	-4.55779	-387.94200
9	0.4	-0.03190	2.34444	191.61100
10	0.45	0.01650	-1.21997	-98.14990
11	0.5	-0.00820	0.61248	48.55100
12	0.55	0.00360	-0.27128	-20.34120
13	0.6	-0.00090	0.07356	4.84687
		$\sum \phi = 1.00000$		

Table 3.8: *Numerical data of RPIM-EXP shape functions for node 11 calculated at $x = 0.5$ by use of local support domains (with quadratic polynomials)*

Node	x_k	ϕ_{11}	$\frac{d\phi_{11}}{dx}$	$\frac{d^2\phi_{11}}{dx^2}$
5	0.2	0.00000	0.08297	-0.58831
6	0.25	0.00000	-0.46798	3.98696
7	0.3	0.00000	1.46369	-15.36820
8	0.35	0.00000	-3.51383	48.28720
9	0.4	0.00000	7.62784	-154.75700
10	0.45	0.00000	-18.72680	751.84100
11	0.5	1.00000	0.00000	-1266.80000
12	0.55	0.00000	18.72680	751.84100
13	0.6	0.00000	-7.62784	-154.75700
14	0.65	0.00000	3.51383	48.28720
15	0.7	0.00000	-1.46369	-15.36820
16	0.75	0.00000	0.46798	3.98696
17	0.8	0.00000	-0.08297	-0.58831

Table 3.9: *Numerical data of RPIM-EXP shape functions for node 11 calculated at* $x = 0.24$ *by use of local support domains (with quadratic polynomials)*

Node	x_k	ϕ_{11}	$\frac{d\phi_{11}}{dx}$	$\frac{d^2\phi_{11}}{dx^2}$
1	0	0.00110	-0.10145	-2.71359
2	0.05	-0.00640	0.60991	14.75290
3	0.1	0.02170	-2.10789	-41.84010
4	0.15	-0.06070	6.12152	65.52850
5	0.2	0.19690	-22.57520	472.50500
6	0.25	0.96250	10.01870	-1217.39000
7	0.3	-0.17060	12.42520	987.22600
8	0.35	0.08670	-6.96972	-419.19700
9	0.4	-0.04840	4.02260	213.95600
10	0.45	0.02540	-2.14779	-106.54300
11	0.5	-0.01140	0.97170	46.05100
12	0.55	0.00380	-0.32838	-15.03270
13	0.6	-0.00070	0.06085	2.69946
		$\sum \phi = 0.99990$		

3.5.4 2D RPIM Shape Functions with Global Support Domain

Secondly, RPIM shape functions are investigated in a two-dimensional (2D) example using the global support domain. It can be seen in Figure 3.5 that a 2D problem domain $x_k \in [0,1], y_k \in [0,1]$ is represented by 5×5 points of regularly distributed field nodes, and their coordinates are $x_k = (k-1)/4, y_k = (k-1)/4$.

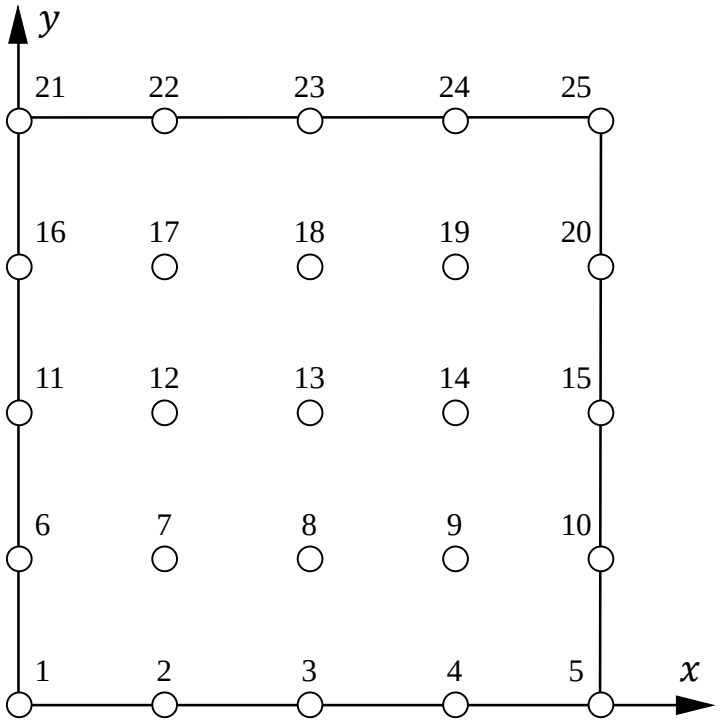

Figure 3.5: *Field nodes used to construct 2D RPIM shape functions.*

RPIM-MQ and RPIM-EXP shape functions are constructed with quadratic polynomials $\mathbf{p}^{\mathrm{T}} = \{\ 1 \quad x \quad y \quad x^2 \quad xy \quad y^2\ \}$. Figure 3.6 to Figure 3.8 plot the distribution of RPIM shape functions, their first order and second derivatives, in which Figure 3.6 again proves the Kronecker delta function property that being embedded in the RPIM shape functions. However, differences arise in the first order derivatives shown in Figure 3.7, and it differs more greatly in Figure 3.8 concerning their second order derivatives.

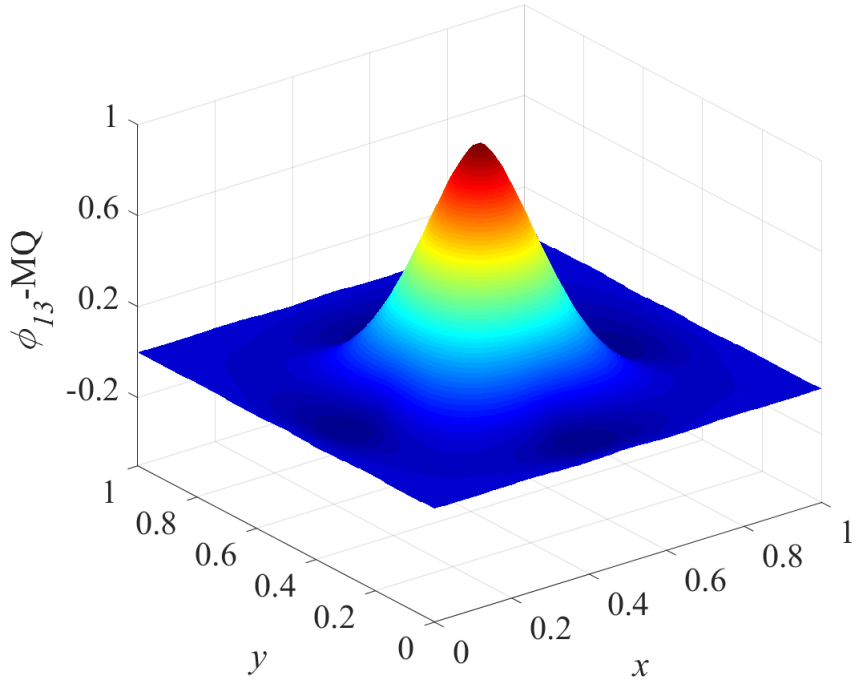

(a)

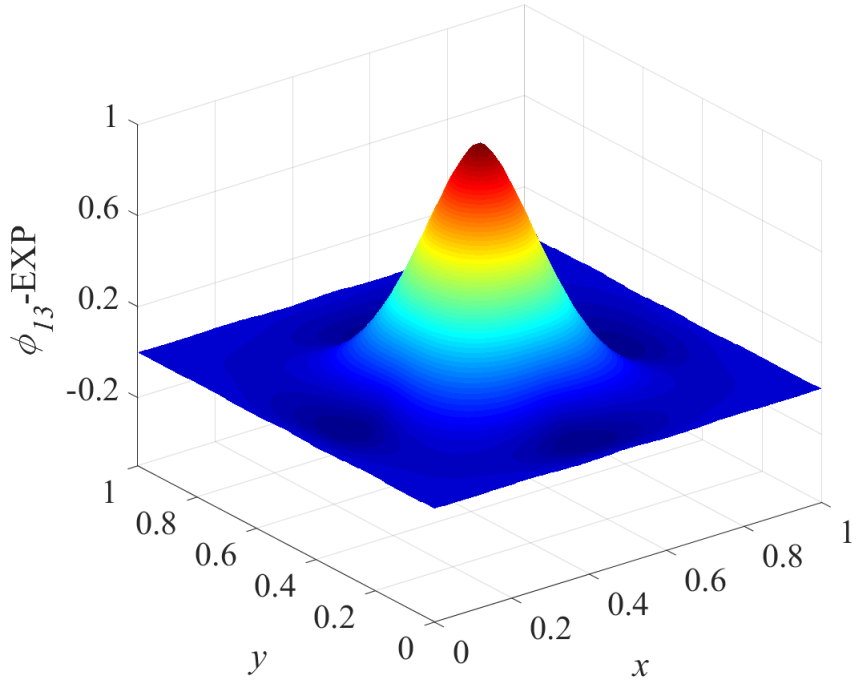

(b)

Figure 3.6: *(a) RPIM-MQ shape functions for node 13 at* $\boldsymbol{x} = (0.5, 0.5)$ *; (b) RPIM-EXP shape functions for node 13 at* $\boldsymbol{x} = (0.5, 0.5)$.

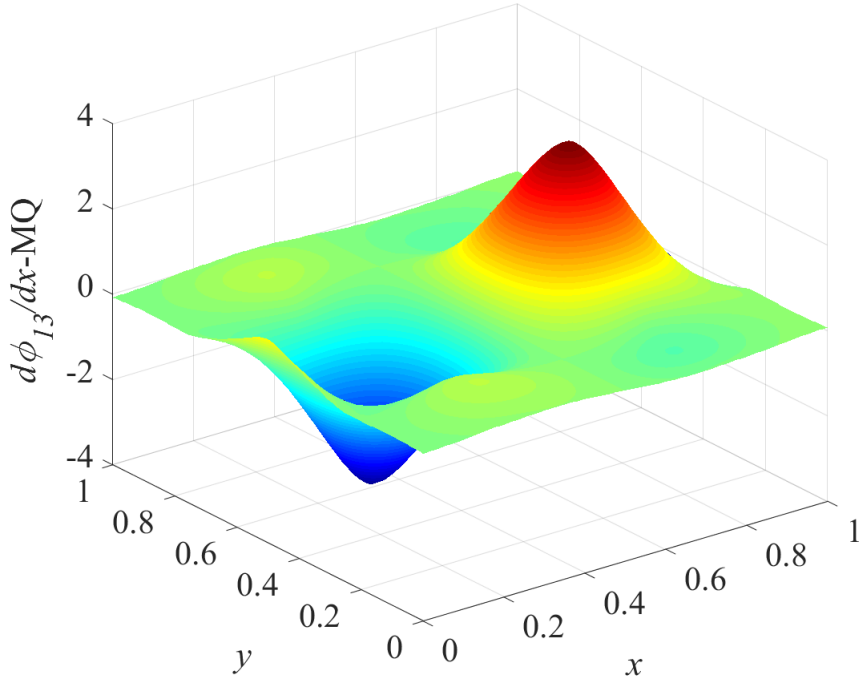

(a)

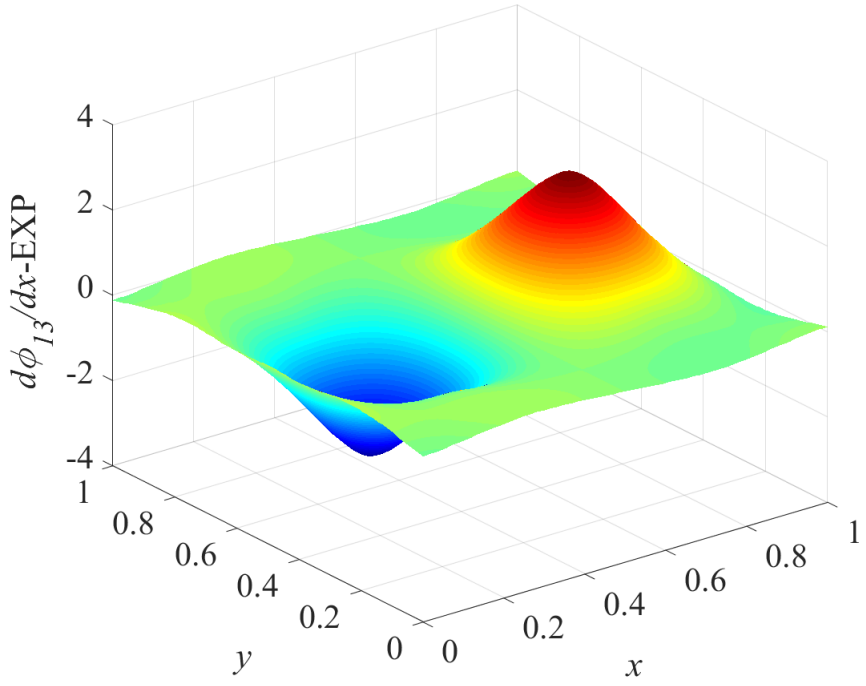

(b)

Figure 3.7: *(a)* 1^{st} *derivative of RPIM-MQ shape functions for node 13 at* $\boldsymbol{x} = (0.5, 0.5)$ *;* *(b)* 1^{st} *derivative of RPIM-EXP shape functions for node 13 at* $\boldsymbol{x} = (0.5, 0.5)$.

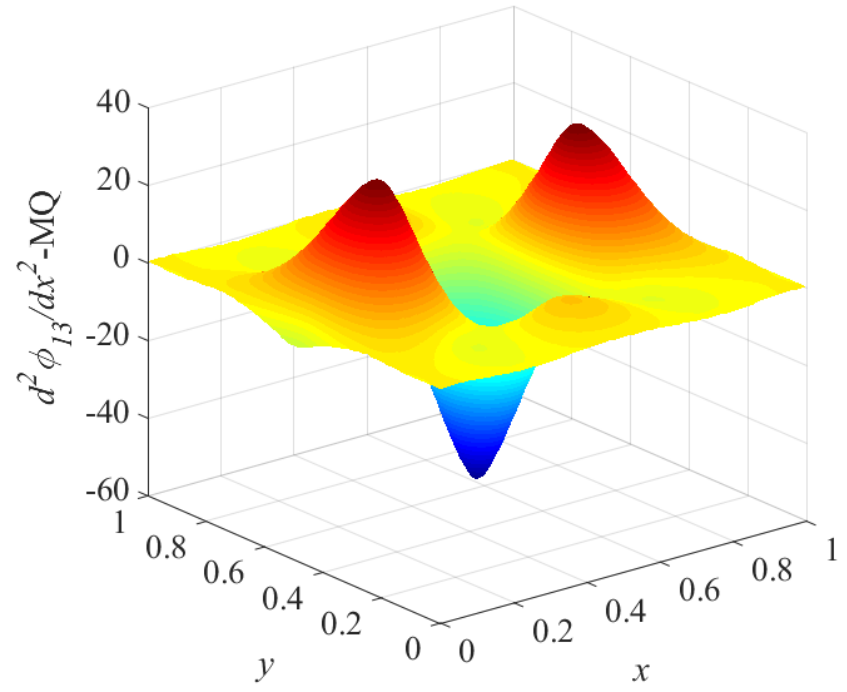

(a)

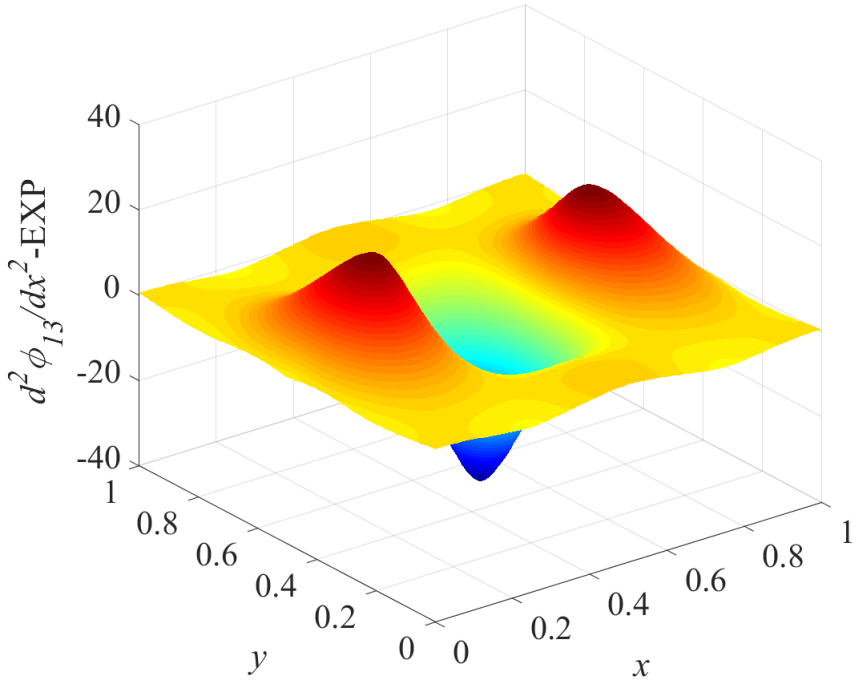

(b)

Figure 3.8: *(a)* 2^{nd} *derivative of RPIM-MQ shape functions for node 13 at* $\boldsymbol{x} = (0.5, 0.5)$ *;* *(b)* 2^{nd} *derivative of RPIM-EXP shape functions for node 13 at* $\boldsymbol{x} = (0.5, 0.5)$.

Specifically, the distribution of RPIM shape functions and their derivatives for node 13 along the middle line of the problem domain, namely, $y = 0.5$, are shown in Figure 3.9 to Figure 3.11. Gaps between RPIM-MQ and RPIM-EXP increase when the derivative order varies from 1 to 2. Consequently, numerical solutions based on derivative information of RPIM shape functions may lead to results with considerable differences when different kinds of RBFs are employed.

RPIM-MQ and RPIM-EXP output data for node 13 in Figure 3.5 evaluated at point $\mathbf{x} = (0.5, 0.5)$ and point $\mathbf{x} = (0.74, 0.33)$ are listed in Table 3.10 to Table 3.13, from which the Kronecker delta function property and partitions of unity of RPIM shape functions can be confirmed.

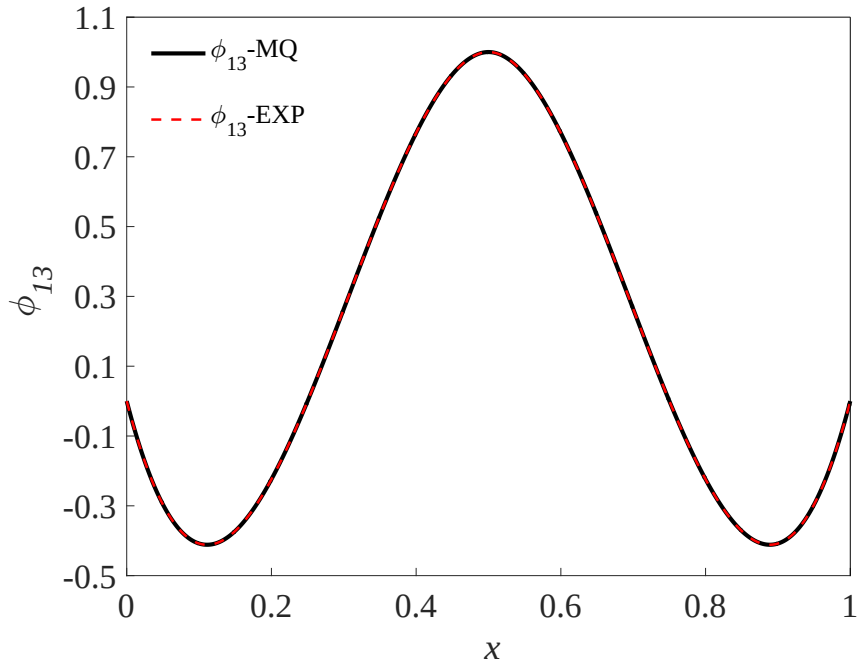

Figure 3.9: *RPIM shape functions for node 13 at* $\boldsymbol{x} = (0.5, 0.5)$ *along* $y = 0.5$.

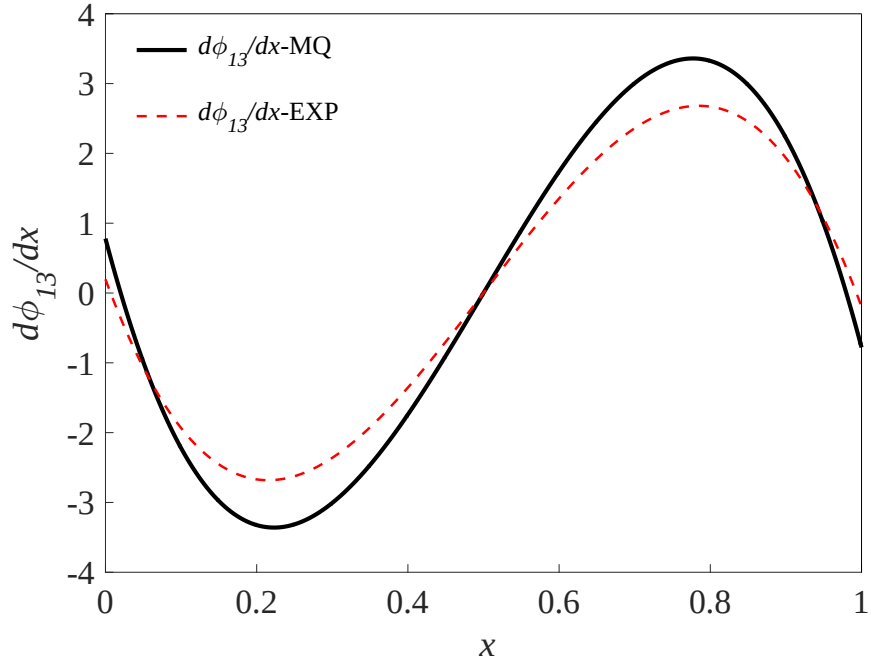

Figure 3.10: 1^{st} *derivative of RPIM shape functions for node 13 at* $\boldsymbol{x} = (0.5, 0.5)$ *along* $y = 0.5$.

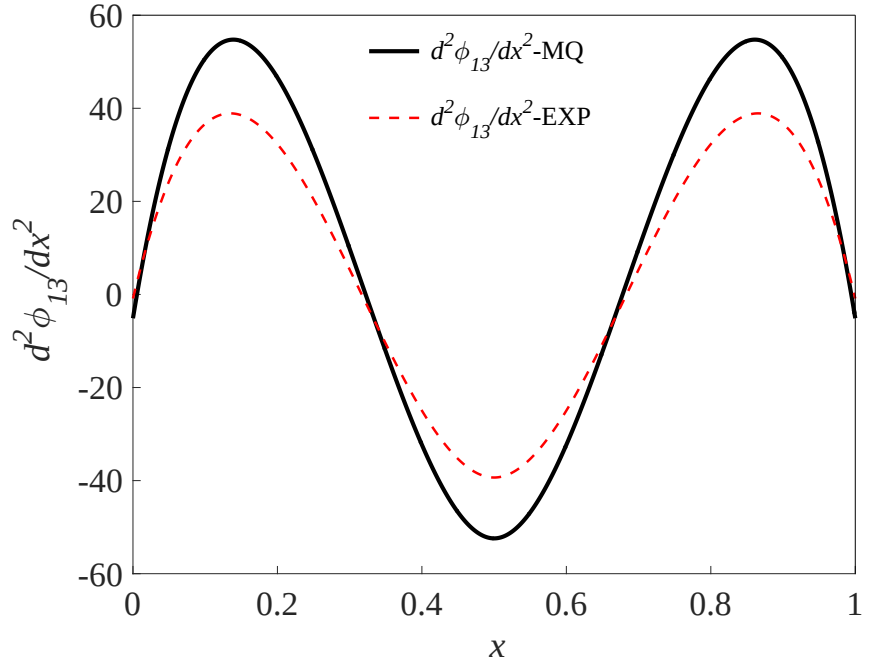

Figure 3.11: 2^{nd} *derivative of RPIM shape functions for node 13 at* $\boldsymbol{x} = (0.5, 0.5)$ *along* $y = 0.5$.

Table 3.10: *Numerical data of RPIM-MQ shape functions for node 13 calculated at* $\boldsymbol{x} = (0.5, 0.5)$ *by use of the global support domain (with quadratic polynomials)*

Node	x_k	y_k	ϕ_{13}	$\frac{d\phi_{13}}{dx}$	$\frac{d\phi_{13}}{dy}$	$\frac{d^2\phi_{13}}{dx^2}$	$\frac{d^2\phi_{13}}{dxdy}$	$\frac{d^2\phi_{13}}{dy^2}$
1	0	0	0.00000	-0.07252	-0.07252	0.34508	1.32799	0.34508
2	0.25	0	0.00000	0.06982	-0.04738	-0.70968	-3.21341	0.89142
3	0.5	0	0.00000	0.00000	0.77961	0.48095	0.00000	-5.12087
4	0.75	0	0.00000	-0.06982	-0.04738	-0.70968	3.21341	0.89142
5	1	0	0.00000	0.07252	-0.07252	0.34508	-1.32799	0.34508
6	0	0.25	0.00000	-0.04738	0.06982	0.89142	-3.21341	-0.70968
7	0.25	0.25	0.00000	0.04711	0.04711	-1.28558	11.54160	-1.28558
8	0.5	0.25	0.00000	0.00000	-3.31348	1.78132	0.00000	30.58200
9	0.75	0.25	0.00000	-0.04711	0.04711	-1.28558	-11.54160	-1.28558
10	1	0.25	0.00000	0.04738	0.06982	0.89142	3.21341	-0.70968
11	0	0.5	0.00000	0.77961	0.00000	-5.12087	0.00000	0.48095
12	0.25	0.5	0.00000	-3.31348	0.00000	30.58200	0.00000	1.78132
13	0.5	0.5	1.00000	0.00000	0.00000	-52.41180	0.00000	-52.41180
14	0.75	0.5	0.00000	3.31348	0.00000	30.58200	0.00000	1.78132
15	1	0.5	0.00000	-0.77961	0.00000	-5.12087	0.00000	0.48095
16	0	0.75	0.00000	-0.04738	-0.06982	0.89142	3.21341	-0.70968
17	0.25	0.75	0.00000	0.04711	-0.04711	-1.28558	-11.54160	-1.28558
18	0.5	0.75	0.00000	0.00000	3.31348	1.78132	0.00000	30.58200
19	0.75	0.75	0.00000	-0.04711	-0.04711	-1.28558	11.54160	-1.28558
20	1	0.75	0.00000	0.04738	-0.06982	0.89142	-3.21341	-0.70968
21	0	1	0.00000	-0.07252	0.07252	0.34508	-1.32799	0.34508
22	0.25	1	0.00000	0.06982	0.04738	-0.70968	3.21341	0.89142
23	0.5	1	0.00000	0.00000	-0.77961	0.48095	0.00000	-5.12087
24	0.75	1	0.00000	-0.06982	0.04738	-0.70968	-3.21341	0.89142
25	1	1	0.00000	0.07252	0.07252	0.34508	1.32799	0.34508

Table 3.11: *Numerical data of RPIM-MQ shape functions for node 13 calculated at* $\boldsymbol{x} = (0.74, 0.33)$ *by use of the global support domain (with quadratic polynomials)*

Node	x_k	y_k	ϕ_{13}	$\frac{d\phi_{13}}{dx}$	$\frac{d\phi_{13}}{dy}$	$\frac{d^2\phi_{13}}{dx^2}$	$\frac{d^2\phi_{13}}{dxdy}$	$\frac{d^2\phi_{13}}{dy^2}$
1	0	0	0.00298	0.11039	0.01521	-0.51323	-0.06588	-0.76473
2	0.25	0	0.00192	-0.15463	0.01324	2.42391	-1.00553	-0.50002
3	0.5	0	0.01425	0.30580	0.04507	-5.78576	2.67699	-2.51401
4	0.75	0	-0.11124	0.17877	-0.38803	9.15180	-2.03716	21.12150
5	1	0	0.02679	-0.45674	0.09190	-5.47810	0.69957	-4.68814
6	0	0.25	-0.00233	-0.41343	-0.03735	0.36586	2.02946	1.30525
7	0.25	0.25	-0.01370	1.29410	0.04663	-3.76466	-5.81377	0.64431
8	0.5	0.25	0.01499	-3.56743	-0.22395	21.46770	16.92420	3.06978
9	0.75	0.25	0.78152	1.15683	-4.09470	-37.74210	-4.06632	-28.96940
10	1	0.25	-0.04096	1.53633	0.01660	19.73220	-9.95582	5.78480
11	0	0.5	0.00431	-0.12544	0.02764	0.17006	-2.47327	-0.73865
12	0.25	0.5	-0.00488	0.65093	-0.07689	-0.08028	7.89107	-0.48556
13	0.5	0.5	0.02857	-1.86101	0.23740	8.70453	-22.78730	-2.51827
14	0.75	0.5	0.39078	0.80741	5.41927	-15.36540	5.96496	1.31952
15	1	0.5	0.00566	0.60736	-0.11343	7.60246	12.44320	-3.00922
16	0	0.75	-0.00223	0.02017	0.00462	-0.60364	0.42933	0.69695
17	0.25	0.75	0.00306	-0.16118	0.02690	0.84408	-1.55740	-0.38949
18	0.5	0.75	-0.00746	0.41983	-0.01834	-4.49696	4.81814	1.90585
19	0.75	0.75	-0.12229	-0.05340	-1.32476	6.62580	-0.54532	11.71490
20	1	0.75	0.00268	-0.33748	0.09237	-3.80339	-3.64743	0.81328
21	0	1	-0.00029	0.00867	-0.01221	-0.16415	0.10408	-0.09218
22	0.25	1	-0.00037	0.08897	-0.00563	0.70223	0.41822	-0.12237
23	0.5	1	-0.00233	-0.21385	-0.04040	0.20534	-1.57222	0.17614
24	0.75	1	0.03731	0.18775	0.38426	-0.25512	0.67148	-4.49275
25	1	1	-0.00674	-0.02871	-0.08542	0.05687	0.45667	0.73247
			$\sum \phi =$ 1.00000					

Table 3.12: *Numerical data of RPIM-EXP shape functions for node 13 calculated at* $\boldsymbol{x} = (0.5, 0.5)$ *by use of the global support domain (with quadratic polynomials)*

Node	x_k	y_k	ϕ_{13}	$\frac{d\phi_{13}}{dx}$	$\frac{d\phi_{13}}{dy}$	$\frac{d^2\phi_{13}}{dx^2}$	$\frac{d^2\phi_{13}}{dxdy}$	$\frac{d^2\phi_{13}}{dy^2}$
1	0	0	0.00000	-0.11364	-0.11364	0.47449	0.54578	0.47449
2	0.25	0	0.00000	0.12451	0.24187	-1.30314	-1.84239	-0.91674
3	0.5	0	0.00000	0.00000	0.19605	1.62926	0.00000	-0.86333
4	0.75	0	0.00000	-0.12451	0.24187	-1.30314	1.84239	-0.91674
5	1	0	0.00000	0.11364	-0.11364	0.47449	-0.54578	0.47449
6	0	0.25	0.00000	0.24187	0.12451	-0.91674	-1.84239	-1.30314
7	0.25	0.25	0.00000	-0.26502	-0.26502	2.57533	9.18646	2.57533
8	0.5	0.25	0.00000	0.00000	-2.62401	-3.20502	0.00000	20.44700
9	0.75	0.25	0.00000	0.26502	-0.26502	2.57533	-9.18646	2.57533
10	1	0.25	0.00000	-0.24187	0.12451	-0.91674	1.84239	-1.30314
11	0	0.5	0.00000	0.19605	0.00000	-0.86333	0.00000	1.62926
12	0.25	0.5	0.00000	-2.62401	0.00000	20.44700	0.00000	-3.20502
13	0.5	0.5	1.00000	0.00000	0.00000	-39.33550	0.00000	-39.33550
14	0.75	0.5	0.00000	2.62401	0.00000	20.44700	0.00000	-3.20502
15	1	0.5	0.00000	-0.19605	0.00000	-0.86333	0.00000	1.62926
16	0	0.75	0.00000	0.24187	-0.12451	-0.91674	1.84239	-1.30314
17	0.25	0.75	0.00000	-0.26502	0.26502	2.57533	-9.18646	2.57533
18	0.5	0.75	0.00000	0.00000	2.62401	-3.20502	0.00000	20.44700
19	0.75	0.75	0.00000	0.26502	0.26502	2.57533	9.18646	2.57533
20	1	0.75	0.00000	-0.24187	-0.12451	-0.91674	-1.84239	-1.30314
21	0	1	0.00000	-0.11364	0.11364	0.47449	-0.54578	0.47449
22	0.25	1	0.00000	0.12451	-0.24187	-1.30314	1.84239	-0.91674
23	0.5	1	0.00000	0.00000	-0.19605	1.62926	0.00000	-0.86333
24	0.75	1	0.00000	-0.12451	-0.24187	-1.30314	-1.84239	-0.91674
25	1	1	0.00000	0.11364	0.11364	0.47449	0.54578	0.47449

Table 3.13: *Numerical data of RPIM-EXP shape functions for node 13 calculated at* $\boldsymbol{x} = (0.74, 0.33)$ *by use of the global support domain (with quadratic polynomials)*

Node	x_k	y_k	ϕ_{13}	$\frac{d\phi_{13}}{dx}$	$\frac{d\phi_{13}}{dy}$	$\frac{d^2\phi_{13}}{dx^2}$	$\frac{d^2\phi_{13}}{dxdy}$	$\frac{d^2\phi_{13}}{dy^2}$
1	0	0	0.00799	0.11930	0.03991	0.10683	-0.12476	-1.77030
2	0.25	0	-0.02124	-0.09805	-0.09774	1.69395	-0.20239	4.05051
3	0.5	0	0.03334	0.07655	0.14498	-4.89636	1.22627	-5.82755
4	0.75	0	-0.09166	0.22007	-0.32924	6.58964	-0.93082	16.65940
5	1	0	0.01854	-0.31703	0.07250	-3.48099	0.05441	-2.99822
6	0	0.25	-0.01004	-0.51018	-0.06560	-1.12946	2.14494	3.19009
7	0.25	0.25	0.02129	1.36695	0.19996	-1.08427	-8.68885	-7.02440
8	0.5	0.25	-0.01826	-3.43690	-0.41185	17.46540	23.86290	9.93793
9	0.75	0.25	0.74728	1.21958	-4.11569	-32.47100	-11.68730	-21.07770
10	1	0.25	-0.03665	1.35262	-0.02067	17.09540	-5.70020	4.65403
11	0	0.5	0.01038	0.02729	0.02730	-0.84715	-2.38816	-2.64240
12	0.25	0.5	-0.03163	0.94944	-0.11372	7.00141	10.66420	5.54137
13	0.5	0.5	0.06192	-3.13667	0.30742	-4.55313	-30.26320	-8.02775
14	0.75	0.5	0.40545	2.23564	5.38755	-3.21572	15.23410	-5.84126
15	1	0.5	0.01242	-0.05692	-0.06953	1.90808	6.82232	-2.75314
16	0	0.75	-0.00085	-0.09683	0.03671	0.45807	0.21658	0.97738
17	0.25	0.75	0.00358	-0.32491	-0.08270	-4.52739	-1.94982	-1.58733
18	0.5	0.75	-0.00933	1.21906	0.09858	5.83730	6.45872	2.13430
19	0.75	0.75	-0.12972	-1.07821	-1.29971	-3.80358	-3.54647	16.51370
20	1	0.75	0.00052	0.26378	0.08894	1.76824	-1.20277	-0.08710
21	0	1	-0.00348	0.04664	-0.03841	-0.33516	0.15151	0.30163
22	0.25	1	0.00842	0.10567	0.09443	2.25431	0.17624	-1.14114
23	0.5	1	-0.01206	-0.39669	-0.13934	-3.38596	-1.28329	1.92766
24	0.75	1	0.04022	0.41002	0.35713	2.93971	0.92931	-6.28598
25	1	1	-0.00641	-0.16022	-0.07123	-1.38813	0.02660	1.17623
			$\sum \phi =$ 1.00000					

3.5.5 2D RPIM Shape Functions with Local Support Domain

The locally supported 2D RPIM shape functions are investigated by the same example shown in Figure 3.5 in Section 3.5.4. The interpolation schemes are implemented based on the MQ-RBF and EXP-RBF along with quadratic polynomials. Output samples for node 13 in Figure 3.5 evaluated at point $\mathbf{x} = (0.5, 0.5)$ and point $\mathbf{x} = (0.26, 0.43)$ are reported in Table 3.14 to Table 3.17 .

Table 3.14 and Table 3.16 have shown that not all of the field nodes in the problem domain are involved in the interpolation. However, the Kronecker delta function property is found over the field nodes in the local support domain. Moreover, the property related to partitions of unity is found in Table 3.15 and Table 3.17.

3.6 Interpolation Errors

The interpolation errors for meshless shape functions based upon different RBFs are investigated by fitting a given function $f(x, y) = e^{x+y}$ in a domain $(x_k, y_k) \in [0, 1] \times [0, 1]$. 5×5 field nodes are evenly and regularly distributed in the problem domain.

The EXP, MQ and Cubic RBFs listed in Table 3.1 are employed respectively to construct RPIM shape functions with quadratic linear polynomials. And the interpolation errors of function values are defined as $e = |(\bar{f}_i - f_i)|/f_i$, where f_i is the exact value of the given function, and $\bar{f}_i$ is the approximated value of the given function. Therefore, interpolation errors corresponding to the first order and second order derivatives of the approximated function are $e^{(1)} = |(\bar{f}_i^{(1)} - f_i^{(1)})|/f_i^{(1)}$ and $e^{(2)} = |(\bar{f}_i^{(2)} - f_i^{(2)})|/f_i^{(2)}$, in which $f_i^{(1)}$ and $f_i^{(2)}$ are exact values of the first order and second order derivatives of the function, and $\bar{f}_i^{(1)}$ and $\bar{f}_i^{(2)}$ are values of the first order and second order derivatives of the approximated function.

Table 3.14: *Numerical data of RPIM-MQ shape functions for node 13 calculated at* $\boldsymbol{x} = (0.5, 0.5)$ *by use of local support domains (with quadratic polynomials)*

Node	x_k	y_k	ϕ_{13}	$\frac{d\phi_{13}}{dx}$	$\frac{d\phi_{13}}{dy}$	$\frac{d^2\phi_{13}}{dx^2}$	$\frac{d^2\phi_{13}}{dxdy}$	$\frac{d^2\phi_{13}}{dy^2}$
3	0.5	0	0.00000	0.00000	0.58382	0.05318	0.00000	-2.82434
7	0.25	0.25	0.00000	-0.05055	-0.05055	-0.00322	4.00000	-0.00322
8	0.5	0.25	0.00000	0.00000	-3.06653	-0.20629	0.00000	27.30380
9	0.75	0.25	0.00000	0.05055	-0.05055	-0.00322	-4.00000	-0.00322
11	0	0.5	0.00000	0.58382	0.00000	-2.82434	0.00000	0.05318
12	0.25	0.5	0.00000	-3.06653	0.00000	27.30380	0.00000	-0.20629
13	0.5	0.5	1.00000	0.00000	0.00000	-48.63980	0.00000	-48.63980
14	0.75	0.5	0.00000	3.06653	0.00000	27.30380	0.00000	-0.20629
15	1	0.5	0.00000	-0.58382	0.00000	-2.82434	0.00000	0.05318
17	0.25	0.75	0.00000	-0.05055	0.05055	-0.00322	-4.00000	-0.00322
18	0.5	0.75	0.00000	0.00000	3.06653	-0.20629	0.00000	27.30380
19	0.75	0.75	0.00000	0.05055	0.05055	-0.00322	4.00000	-0.00322
23	0.5	1	0.00000	0.00000	-0.58382	0.05318	0.00000	-2.82434

Table 3.15: *Numerical data of RPIM-MQ shape functions for node 13 calculated at* $\boldsymbol{x} = (0.26, 0.43)$ *by use of local support domains (with quadratic polynomials)*

Node	x_k	y_k	ϕ_{13}	$\frac{d\phi_{13}}{dx}$	$\frac{d\phi_{13}}{dy}$	$\frac{d^2\phi_{13}}{dx^2}$	$\frac{d^2\phi_{13}}{dxdy}$	$\frac{d^2\phi_{13}}{dy^2}$
1	0	0	0.02195	0.42912	-0.25764	-2.91252	-2.80608	-1.72509
2	0.25	0	-0.07982	-0.35655	1.00891	5.03996	-0.91071	5.98467
3	0.5	0	0.01777	-0.11518	-0.20501	-1.98660	3.72786	-1.67361
6	0	0.25	-0.01955	-0.55828	0.35732	5.57904	13.03060	0.18606
7	0.25	0.25	0.32093	-0.33060	-5.17040	-12.15550	2.25982	7.76990
8	0.5	0.25	-0.00188	1.01669	0.05431	6.15397	-15.32370	0.28612
11	0	0.5	-0.04011	-1.73233	0.02058	20.48840	-9.67990	6.02568
12	0.25	0.5	0.84168	-0.83370	3.60198	-38.74540	-2.22966	-35.00990
13	0.5	0.5	0.01116	3.00580	0.20371	20.79820	12.45870	3.81312
14	0.75	0.5	-0.01144	-0.56758	0.05251	-2.11870	-0.51592	0.92900
16	0	0.75	0.02995	0.58907	-0.17278	-5.03622	-0.02873	-5.41566
17	0.25	0.75	-0.11871	-0.50191	0.71706	7.50484	-0.66721	24.04230
18	0.5	0.75	0.02806	-0.04456	-0.21054	-2.60946	0.68487	-5.21263
			$\sum\phi =$ 1.00000					

Table 3.16: *Numerical data of RPIM-EXP shape functions for node 13 calculated at* $\boldsymbol{x} = (0.5, 0.5)$ *by use of local support domains (with quadratic polynomials)*

Node	x_k	y_k	ϕ_{13}	$\frac{d\phi_{13}}{dx}$	$\frac{d\phi_{13}}{dy}$	$\frac{d^2\phi_{13}}{dx^2}$	$\frac{d^2\phi_{13}}{dxdy}$	$\frac{d^2\phi_{13}}{dy^2}$
3	0.5	0	0.00000	0.00000	0.46322	-0.01362	0.00000	-1.78514
7	0.25	0.25	0.00000	-0.04121	-0.04121	0.21709	4.00000	0.21709
8	0.5	0.25	0.00000	0.00000	-2.84402	-0.37971	0.00000	22.70640
9	0.75	0.25	0.00000	0.04121	-0.04121	0.21709	-4.00000	0.21709
11	0	0.5	0.00000	0.46322	0.00000	-1.78514	0.00000	-0.01362
12	0.25	0.5	0.00000	-2.84402	0.00000	22.70640	0.00000	-0.37971
13	0.5	0.5	1.00000	0.00000	0.00000	-41.92420	0.00000	-41.92420
14	0.75	0.5	0.00000	2.84402	0.00000	22.70640	0.00000	-0.37971
15	1	0.5	0.00000	-0.46322	0.00000	-1.78514	0.00000	-0.01362
17	0.25	0.75	0.00000	-0.04121	0.04121	0.21709	-4.00000	0.21709
18	0.5	0.75	0.00000	0.00000	2.84402	-0.37971	0.00000	22.70640
19	0.75	0.75	0.00000	0.04121	0.04121	0.21709	4.00000	0.21709
23	0.5	1	0.00000	0.00000	-0.46322	-0.01362	0.00000	-1.78514

Table 3.17: *Numerical data of RPIM-EXP shape functions for node 13 calculated at* $\boldsymbol{x} = (0.26, 0.43)$ *by use of local support domains (with quadratic polynomials)*

Node	x_k	y_k	ϕ_{13}	$\frac{d\phi_{13}}{dx}$	$\frac{d\phi_{13}}{dy}$	$\frac{d^2\phi_{13}}{dx^2}$	$\frac{d^2\phi_{13}}{dxdy}$	$\frac{d^2\phi_{13}}{dy^2}$
1	0	0	0.02166	0.42581	-0.20937	-2.31772	-2.17951	-2.47772
2	0.25	0	-0.08164	-0.45748	0.89960	4.24723	-0.44967	8.56098
3	0.5	0	0.01811	0.01172	-0.16712	-1.88915	2.63052	-2.32386
6	0	0.25	-0.02394	-0.76507	0.31639	5.85789	11.71740	1.69692
7	0.25	0.25	0.33551	-0.01868	-5.05920	-11.86990	1.79987	1.36341
8	0.5	0.25	-0.00680	0.84359	0.05348	5.89092	-13.52130	1.66149
11	0	0.5	-0.03135	-1.31592	0.03021	15.88060	-9.28157	4.04666
12	0.25	0.5	0.82199	-1.20414	3.53536	-30.69880	-1.73590	-27.96910
13	0.5	0.5	0.01456	3.09142	0.21822	15.34980	11.27730	2.74531
14	0.75	0.5	-0.00917	-0.63120	0.02553	-0.41049	-0.25577	0.45532
16	0	0.75	0.02360	0.44638	-0.16277	-3.01024	-0.00055	-3.72118
17	0.25	0.75	-0.10499	-0.53330	0.70084	5.08995	-0.38162	19.41070
18	0.5	0.75	0.02244	0.10686	-0.18118	-2.12007	0.38083	-3.44889
			$\sum \phi =$ 1.00000					

3.6.1 Influence of Free Parameter

Firstly, the influence of the free parameter c_0 in the MQ and EXP RBFs is examined. Parameter c_0 is taken as $c_0 = \Delta, 2\Delta, \ldots, 10\Delta$ respectively, in which Δ is the nodal distance. RPIM shape functions are implemented with global support domains and local support domains, respectively. Interpolation errors with respect to the function values and their derivatives at point $\mathbf{x} = (1, 1)$ when c_0 varies are present in Figure 3.12 and Figure 3.13.

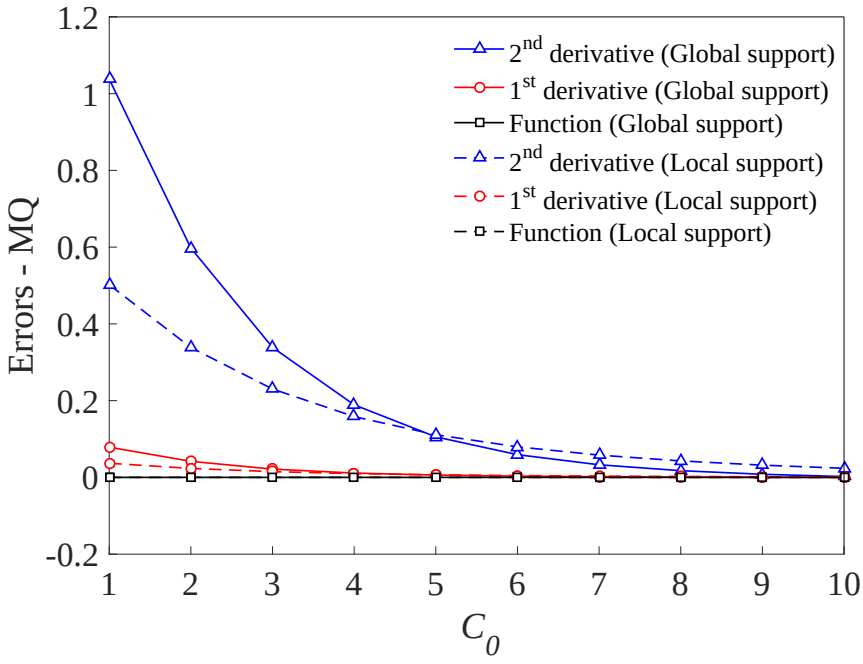

Figure 3.12: *Interpolation errors of RPIM-MQ at point* $\boldsymbol{x} = (1, 1)$ *for different* c_0.

It can be seen in Figure 3.12 that small c_0 values in MQ RBF result in large interpolation errors. Specifically, the effect of c_0 on approximated function values is insignificant. However, it greatly influences the accuracy of approximated derivatives. Interpolation errors go up when the derivative order rises. It also shows in Figure 3.12 that interpolation errors decrease obviously compared with errors resulting from globally supported RPIM-MQ when locally supported RPIM-MQ is

used.

While in Figure 3.13, one can see that a small or large c_0 value may lead to the increase of interpolation errors when the global support domain is employed. Therefore, the selection of c_0 is limited only in a certain range. However, by using the local support domain, the increase of c_0 values can guarantee smaller interpolation errors and hence, c_0 can be selected without too much limitation. Besides, interpolation errors decrease when locally supported RPIM-EXP is utilized.

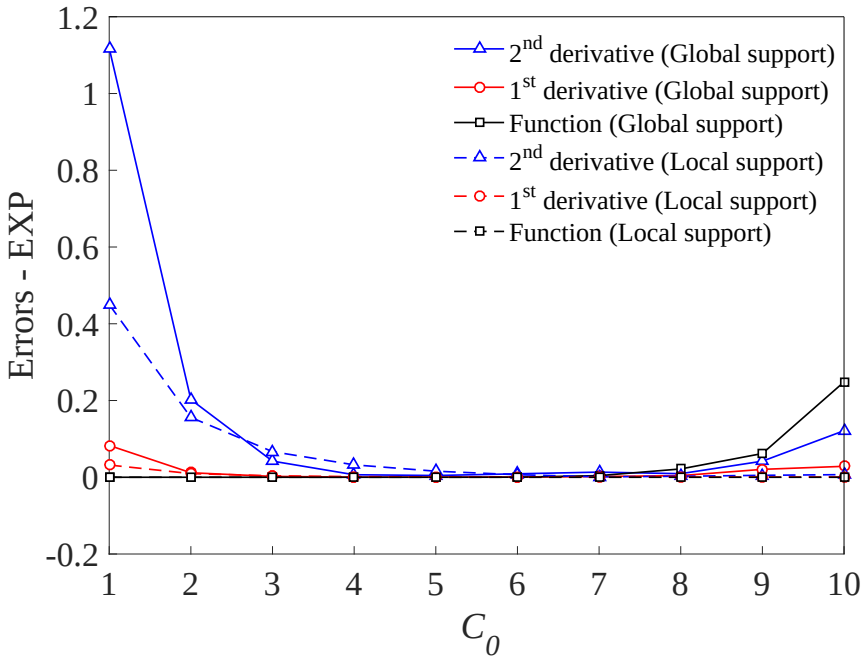

Figure 3.13: *Interpolation errors of RPIM-EXP at point* $\boldsymbol{x} = (1, 1)$ *for different* c_0.

3.6.2 Accuracy Study

In order to study the accuracy of different RBFs, interpolation results and errors of RPIM-MQ, RPIM-EXP and RPIM-Cubic for the given function at point $\mathbf{x} = (1, 1)$ with respect to the global and local support domain are listed in Table 3.18 and Table 3.19, respectively. In this case, the problem domain is represented by a set of

5×5 field nodes, and the free parameter c_0 is taken as 2Δ.

Table 3.18: *Interpolation results and errors of different RBFs at point* $\boldsymbol{x} = (1, 1)$ *using the global support domain*

RBFs	$\bar{f}(1,1)$ (Errors)	$\frac{d\bar{f}(1,1)}{dx}$ (Errors)	$\frac{d^2\bar{f}(1,1)}{dx^2}$ (Errors)
MQ (G)	7.38906 (1.53762E-13)	7.08022 (4.17971E-02)	2.97380 (5.97539E-01)
EXP (G)	7.38906 (1.07036E-11)	7.30219 (1.17565E-02)	5.89345 (2.02409E-01)
Cubic (G)	7.38906 (5.73121E-14)	5.39159 (2.70328E-01)	1.32659 (8.20466E-01)

G:Globally supported.

Table 3.19: *Interpolation results and errors of different RBFs at point* $\boldsymbol{x} = (1, 1)$ *using the local support domain*

RBFs	$\bar{f}(1,1)$ (Errors)	$\frac{d\bar{f}(1,1)}{dx}$ (Errors)	$\frac{d^2\bar{f}(1,1)}{dx^2}$ (Errors)
MQ (L)	7.38906 (4.28161E-14)	7.21681 (2.33105E-02)	4.88888 (3.38362E-01)
EXP (L)	7.38906 (2.17323E-14)	7.31881 (9.50653E-03)	6.23721 (1.55885E-01)
Cubic (L)	7.38906 (3.14949E-15)	6.87487 (6.95873E-02)	4.39986 (4.04543E-01)

L:Locally supported.

These two tables show that interpolation errors of function values are much smaller than that of derivatives, demonstrating that the accuracy of approximated function values is higher then that of derivatives. The accuracy of second order derivatives is lower than that of first order derivatives. Therefore, it can be con-

cluded that higher order derivatives have lower accuracies. Additionally, comparisons between these two tables also show that interpolation errors reduce by using local support domains, which means the locally supported RPIM shape functions can improve the accuracy of solutions. Furthermore, it can be found that the Cubic RBF has the highest accuracy in fitting function values in both tables, while it also has the highest error dealing with derivatives. And the EXP RBF is more accurate than other methods in interpolating derivatives in both tables.

3.6.3 Convergence Analysis

Then, the convergence of different methods is analyzed. Different densities of fields nodes, $5\times5, 11\times11, 21\times21, 31\times31, 41\times41$, are regularly and evenly distributed in the problem domain. And the free parameter $c_0 = 2\Delta$ is used. Interpolation errors at point $\mathbf{x} = (1, 1)$ of different methods for different node densities are plotted in Figure 3.14 to Figure 3.16.

When global support domains are used in RPIM shape function constructions, interpolation errors of the fitted function itself are very small as shown in Figure 3.14(a). However, errors become higher in RPIM-EXP when the number of field nodes increases. For interpolation errors of approximated first order derivatives in Figure 3.15(a), the convergence progress of RPIM-EXP is not stable even though its accuracy is higher than the other two methods when lower densities of nodes are used. And the convergences of RPIM-MQ and RPIM-Cubic are stable, but RPIM-MQ results in a lower error. Moreover, errors resulting from PRIM-EXP with respect to the second order derivatives rise shapely in Figure 3.16(a) and lead to wrong numerical solutions. This is duo to the singularity arises in the EXP RBF when the number of field nodes is large.

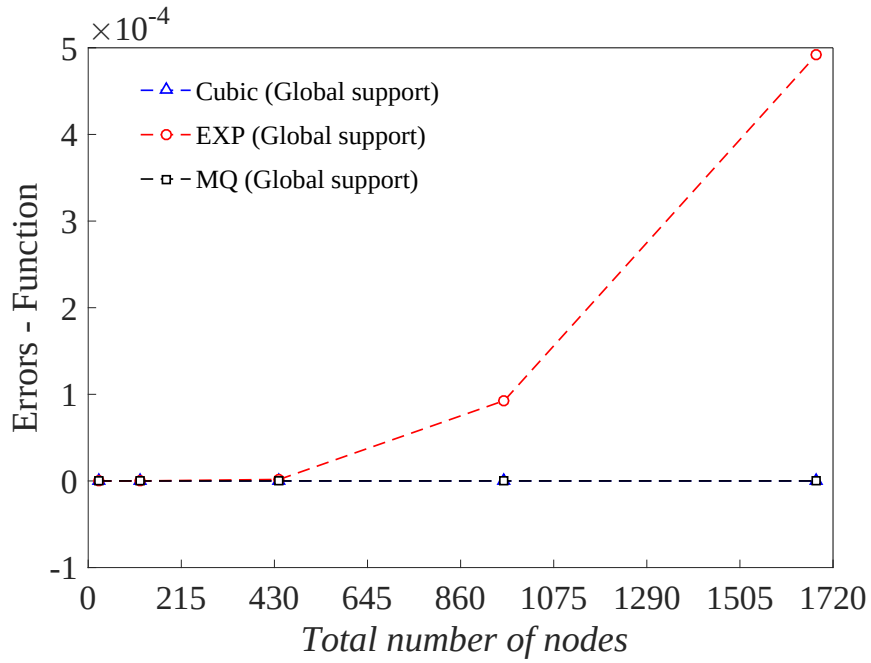

(a)

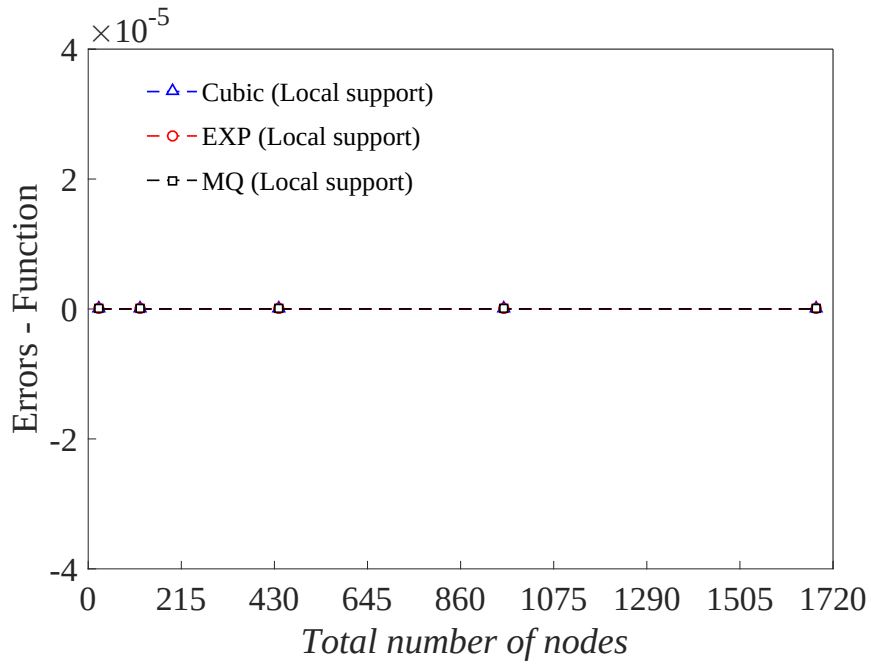

(b)

Figure 3.14: *Interpolation errors of function values for different node densities at* $\boldsymbol{x} = (1, 1)$*: (a) globally supported; (b) locally supported.*

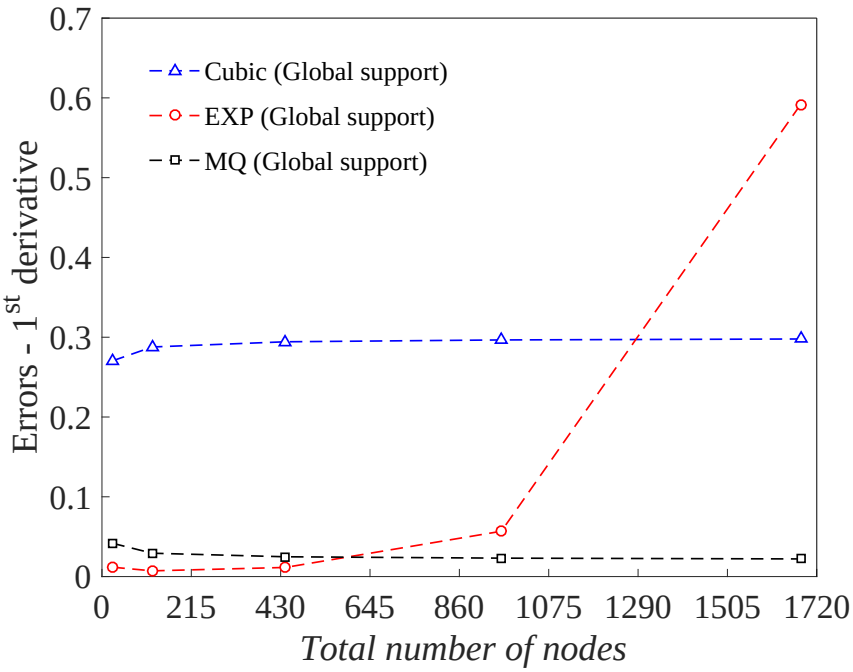

(a)

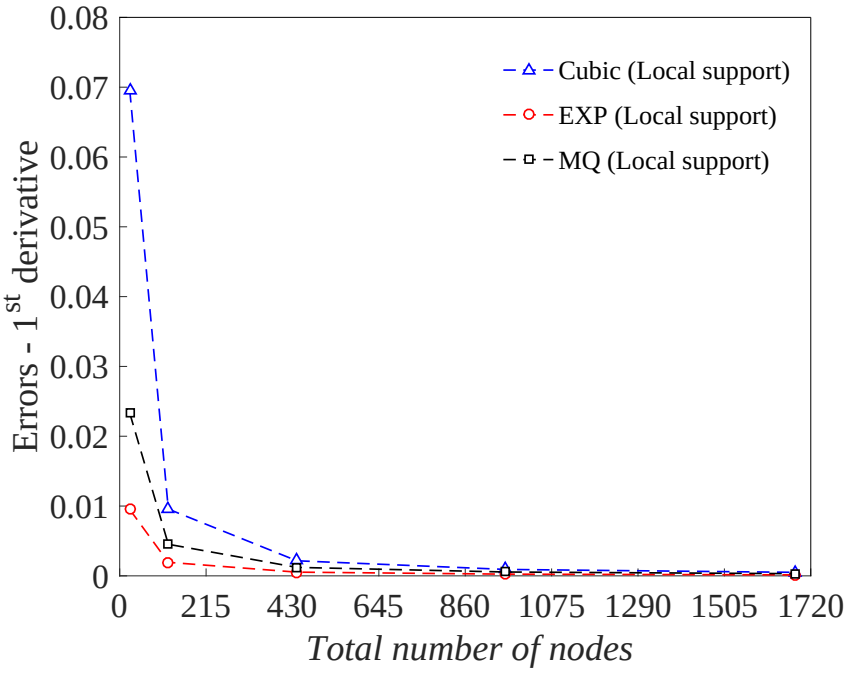

(b)

Figure 3.15: *Interpolation errors of* 1^{st} *derivatives for different node densities at* $\boldsymbol{x} = (1, 1)$*: (a) globally supported; (b) locally supported.*

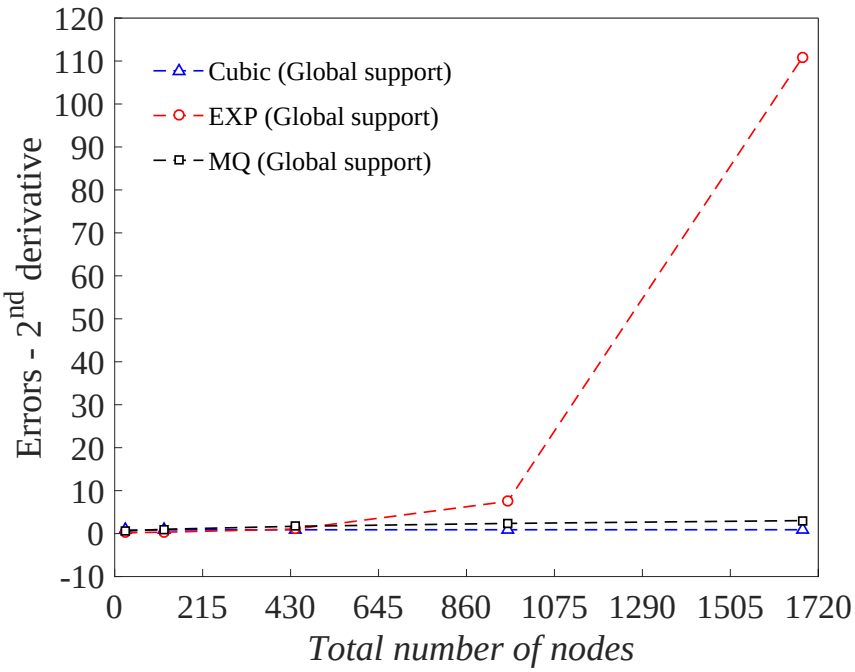

(a)

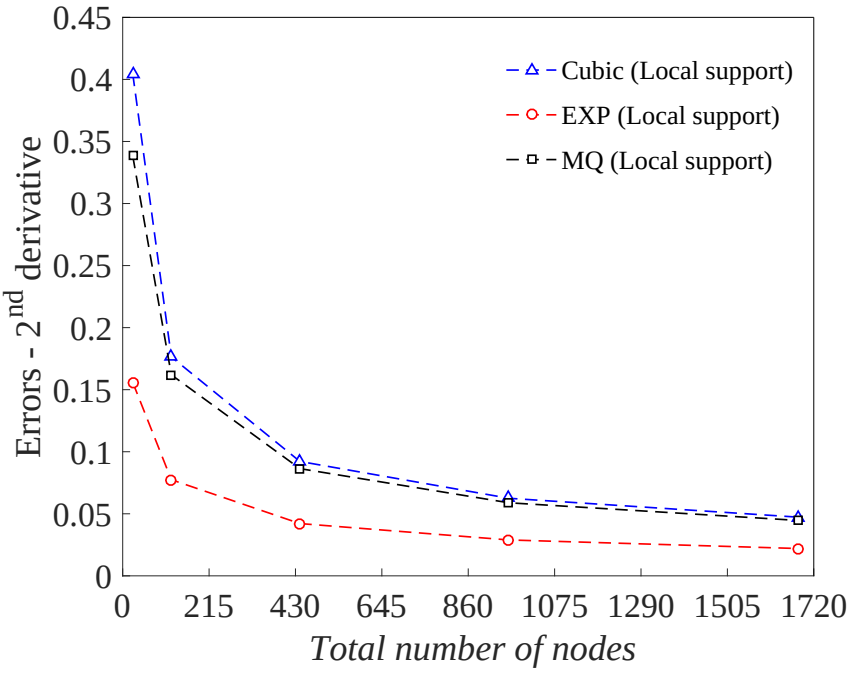

(b)

Figure 3.16: *Interpolation errors of* 2^{nd} *derivatives for different node densities at* $\boldsymbol{x} = (1, 1)$*: (a) globally supported; (b) locally supported.*

When RPIM shape functions are locally supported, convergence progresses of all methods become stable in Figure 3.14(b). Interpolation errors related to the first order and the second order derivatives shown in Figure 3.15(b) and Figure 3.16(a) are convergent, respectively. In this circumstance, the convergence of RPIM-EXP improves and its accuracy is higher than the other two methods. Besides, RPIM-MQ and RPIM-Cubic have steady convergence and RPIM-MQ is more accurate.

3.6.4 Number of Nodes in the Local Support Domain

Finally, the effect of the number of field nodes within the local support domain is investigated. A set of field nodes, 11×11, are evenly and regularly distributed in the domain. The free parameter c_0 in MQ and EXP RBFs is selected as 2Δ. Different number of nodes, $K = 5, 8, 12, 16, 20, 25, 36, 51, 101,$ are employed in the local support domain to construct RPIM shape functions. Interpolation errors at point $\mathbf{x} = (1, 1)$ related to RPIM-MQ, RPIM-EXP and RPIM-Cubic are plotted in Figure 3.17 to Figure 3.19.

Figure 3.17 shows that interpolation errors related to function values are very small when the number of nodes in the local support domain varies. While errors resulting from RPIM-EXP increase when K is over 40. In Figure 3.18, interpolation errors regarding to the approximated first order derivatives in RPIM-Cubic rise shapely with the number of nodes increases. Errors of RPIM-MQ and RPIM-EXP are both less than 2% regardless of the number of K, but RPIM-EXP is more accurate. Interpolation errors are obviously large in approximated second order derivatives plotted in Figure 3.19, in which RPIM-EXP produces fewer errors compared with the other two methods and it stays lower then 20% even the number of nodes go up. However, RPIM-MQ and RPIM-Cubic can only lead to numerical solutions with errors under 20% when K is selected between $5 - 12$.

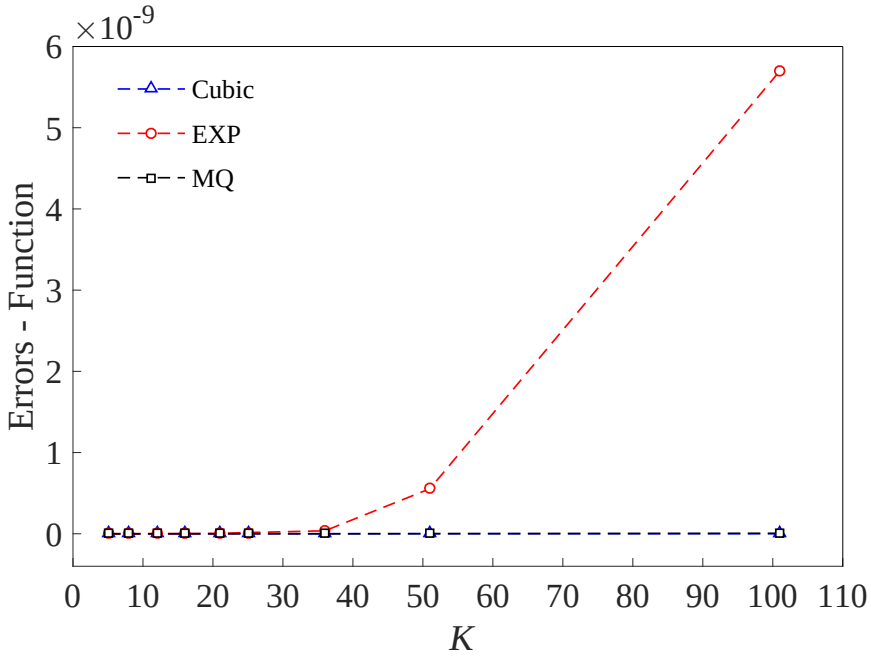

Figure 3.17: *Interpolation errors of different RPIM shape functions at* $\boldsymbol{x} = (1, 1)$ *for different number of nodes in the local support domain.*

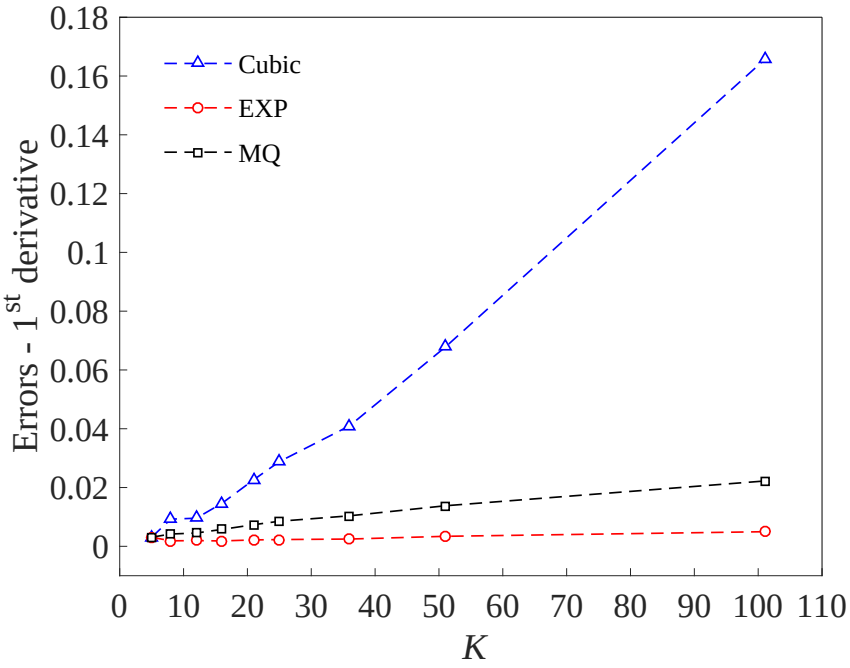

Figure 3.18: *Interpolation errors of* 1^{st} *derivatives at* $\boldsymbol{x} = (1, 1)$ *for different number of nodes in the local support domain.*

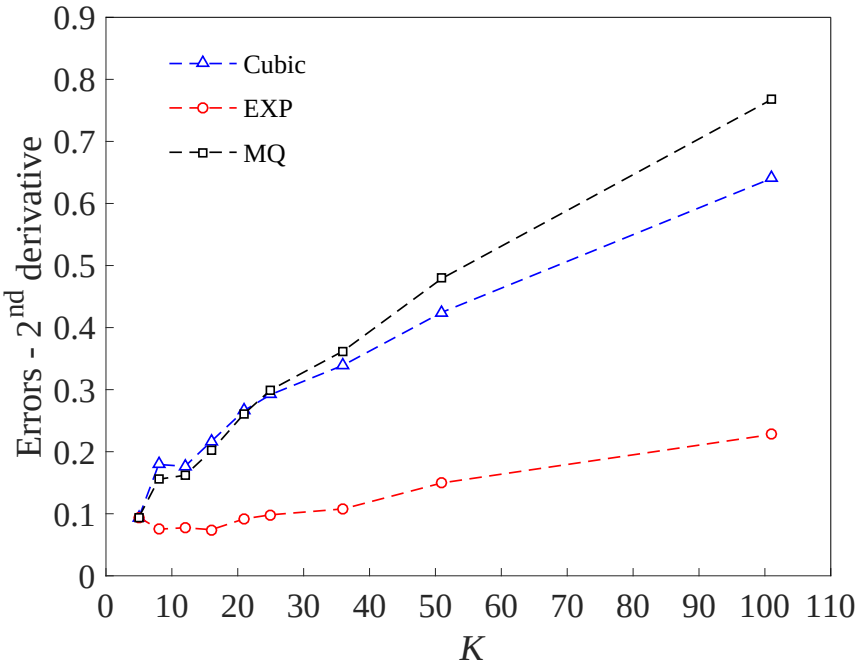

Figure 3.19: *Interpolation errors of* 2^{nd} *derivatives at* $\boldsymbol{x} = (1, 1)$ *for different number of nodes in the local support domain.*

3.7 Conclusions

In this chapter, shape function constructions especially by means of Point Interpolation Method (PIM), Radial Basis Functions (RBFs) and Radial Point Interpolation Method (RPIM) are systemically introduced, and some of their properties such as consistency and continuity are discussed. Implementations of RPIM shape functions in both 1D and 2D problem domains are carried out, and interpolation errors of meshless shape functions based on different RBFs are investigated by fitting of a given function. Following conclusions can be obtained:

(1) The influence of polynomials on RPIM shape functions is insignificant. However, polynomial terms improve the interpolation stability as well as the consistency of RPIM shape functions.

(2) RPIM shape functions possess the Kronecker delta function property with either global or local support domains.

(3) The partition of unity can be satisfied within the support domains of RPIM shape functions.

(4) The free parameter c_0 in MQ and EXP RBFs only has a slight effect on the approximated function values. For interpolation errors related to derivatives, a smaller c_0 results in a bigger error in globally supported RPIM-MQ. While in globally supported RPIM-EXP, both a small and a large c_0 may lead to the increase of errors. When the local support domain is employed, interpolation errors reduce obviously and the increase of c_0 can result in a smaller interpolation error.

(5) The accuracy of approximated function values is much higher than that of derivatives. The higher order derivatives, the lower accuracies. And the locally supported RPIM shape functions improve the accuracy of numerical solutions. RPIM-Cubic is more accurate in fitting function values, while RPIM-EXP has a higher accuracy in interpolating derivatives.

(6) The convergence study has found that when global support domain is used to construct RPIM shape functions, the EXP RBF is not convergent stably, and the singularity may arise when finer field nodes are employed. Convergence progress of MQ and Cubic RBFs are stable, and MQ-RBF has fewer interpolation errors. When the local support domain is utilized, convergences become stable for all methods and EXP RBF turns out to be the most accurate method. While in this circumstance Cubic RBF produces the largest interpolation errors.

(7) Approximated function values are not sensitive to the number of nodes in-

cluded in the local support domain, and RPIM-EXP produces the smallest errors dealing with derivatives when the number of nodes within the local support domain varies. Concerning about the second order derivatives, only K is selected between $5 - 12$, RPIM-MQ and RPIM-Cubic can lead to solutions with errors less than 20%.

CHAPTER 4

Meshless Point Collocation Methods

4.1 Introduction

In 1990, Kansa [117] presented an enhanced Multiquadrics (MQ) approximation scheme for scattering data and applied it to solve fluid dynamic problems, which is the initiate of meshless Point Collocation Method (PCM). Along this research line, meshless methods based on radial basis function approximations were springing up. Zhang [143] investigated meshless collocation methods on the basis of both globally supported and locally supported RBFs and proposed the Hermite type collocation method to improve boundary solutions. Chen [144] developed some novel RBF collocation methods to solve partial differential equations. And among others, Liu [145, 146] presented meshless collocation methods based upon RBFs and point interpolation, respectively.

All of the above-mentioned methods discretize the governing equations at field nodes by collocations, which means the discretized equations are acquired straightforward from the strong-forms of governing equations. Besides, the discretization is carried out with no use of weak-forms and thus, no numerical integrals and background grids are required. Consequently, PCM is simple and efficient compared

with other Galerkin-based approaches and it is a truly meshless method.

However, singularities may arise when applying meshless collocation methods and some remedies have been developed. The use of RBFs [117] and matrix triangularization algorithm [146] are all effective to prevent this problem.

Duo to its advantages, PCM has been applied to various aspects and just some recent developments are quoted, see [147, 148].

In this chapter, a meshless point collocation method based on the RPIM shape function, in which RBFs are employed to carry out approximations, is presented. Besides, several illustrated examples are reported, and the influence of support domains, different types of RBFs as well as free parameters is investigated. Comparisons between numerical solutions and Abaqus results validate the accuracy of PCM.

4.2 Point Collocation Method (PCM) for 1D Solids

The general meshless point collocation steps for establishing the discretized system equations and dealing with boundary conditions will be presented in this section by use of a simple one-dimensional (1D) problem.

4.2.1 Meshless Formulation for 1D Solids

Governing Equation

Consider a 1D plane stress problem in an arbitrary domain Ω. The governing equation is in the form, for isotropic medium, of

$$\frac{\partial \sigma_x}{\partial x} + f_x = 0 \tag{4.1}$$

where σ_x denotes the stress, f_x is the body force.

Recalling the Hook' law, we have

$$\sigma_x = E'\varepsilon_x \tag{4.2}$$

in which $E' = E/(1-\mu^2)$, E is the Young's modulus and μ is the Poisson's ratio. And $\varepsilon_x = \dfrac{\partial u}{\partial x}$ is the strain component, u represents the displacement. Therefore, the governing equation for 1D elastostatics can be expressed in terms of displacement components as,

$$E'\frac{\partial^2 u}{\partial x^2} + f_x = 0 \tag{4.3}$$

Meshless Approximation and System Equation Discretization

Assume that there are M nodes in the problem domain as shown in Figure 4.1, in which node 1 and node M are located on the boundary. The displacement component u in the governing partial differential equation can be approximated by using the RPIM shape functions introduced in Chapter 3 as

$$u(\mathbf{x}) = \sum_{k=1}^{K} \phi_k u_k \tag{4.4}$$

Therefore, (4.3) can be discretized at collocation points as (body force is ignored)

$$E' u^{(k)} \sum_{k=1}^{K} \phi_{k,xx} = 0 \tag{4.5}$$

where the comma denotes partial derivatives in terms of the variable that follows, K is the number of nodes in the support domain. In case $K = M$, all of the field nodes within the problem domain are used to construct the RPIM shape functions.

However, K usually less than M when employing the local support domain, see Figure 4.1.

Boundary Conditions

Displacement boundaries can be introduced immediately as

$$u(\mathbf{x}_k) = u^0 \tag{4.6}$$

where $k = 1, 2, \ldots, M_D$, M_D is the number of nodes located on the displacement boundaries, and u^0 is the prescribed displacement.

On traction boundaries, where the traction forces t_x^0 are prescribed, boundary conditions are

$$E' u^{(k)} \sum_{k=1}^{K} \phi_{k,x} = t_x^0 \tag{4.7}$$

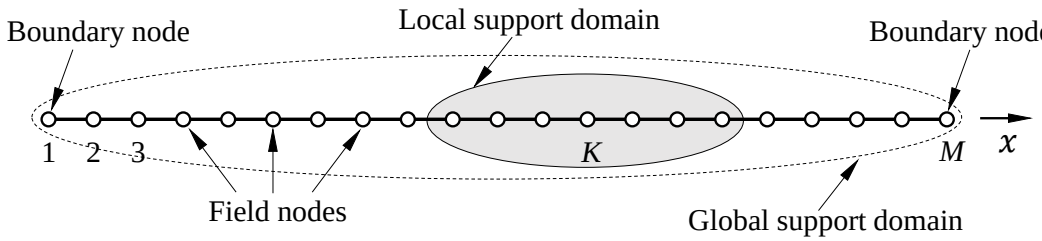

Figure 4.1: *A 1D problem domain and the distribution of field nodes.*

4.2.2 A Bar under Uniform Tension

To illustrate the application of meshless collocation methods to 1D solid, a bar problem set up in Figure 4.2 is considered. The bar is fixed at the edge $x = 0$, and it is subjected to a uniformly distributed tension $\sigma^0 = 1.0$ at the edge $x = L$. The total length L is 20 and the free parameter c_0 in RBFs is selected as 2Δ. 41

nodes are regularly and evenly distributed along the bar, and their coordinates are $x_k = 0.5(k-1)$. Material data are defined as: Young's modulus $E = 1.0$, Poisson's ratio $\mu = 0.0$. Gaussian (EXP) and Multiquadrics (MQ) RBFs listed in Table 3.1 are employed to build up the RPIM shape functions, respectively. And the average relative errors of approximated solutions over the entire domain can be calculated by

$$e = \frac{1}{M}\sum_{m=1}^{M}\left|\frac{\bar{f}_m - f_m}{f_m}\right| \tag{4.8}$$

where $\bar{f}_m$ represents the numerical solution, and f_m is the exact solution or the analytical solution.

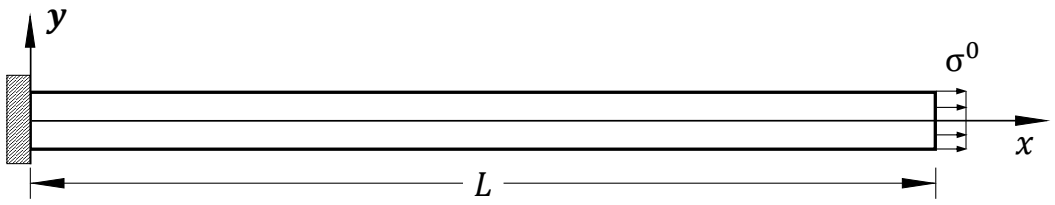

Figure 4.2: *A bar under uniform tension.*

Table 4.1 lists the average errors of numerical solutions related to displacements, strains and stresses along the bar. Approximations in PCM are carried out by using RPIM shape functions with the global support domain. The MQ and EXP RBFs employed present solutions with high accuracy in this case. However, RPIM-MQ lead to a smaller error. Both methods are time-consuming since all field nodes are involved in shape function constructions.

Numerical errors resulting from locally supported RPIM shape functions are reported in Table 4.2. The number of nodes in the local support domain is taken as 12 in this case. Accurate solutions are achieved since the average errors are very small. Specifically, the accuracy of RPIM-MQ only has a slight difference compared with that in Table 4.1. While the average errors of RPIM-EXP decrease when

local support domains are used. Besides, it is computationally efficient compared with globally supported RPIM.

Table 4.1: *Average errors of displacement, strain and stress solutions along the bar obtained by using the global support domain.*

x_k	u_x (MQ)	u_x (EXP)	ε_x (MQ)	ε_x (EXP)	σ_x (MQ)	σ_x (EXP)
Average errors	1.544E-10	5.688E-09	1.104E-12	4.170E-09	1.104E-12	4.170E-09

Table 4.2: *Avarage errors of displacement, strain and stress solutions along the bar obtained by using the local support domain.*

x_k	u_x (MQ)	u_x (EXP)	ε_x (MQ)	ε_x (EXP)	σ_x (MQ)	σ_x (EXP)
Average errors	4.290E-08	4.255E-07	1.206E-12	2.659E-10	1.206E-12	2.659E-10

In order to investigate the influence of free parameter c_0 in RBFs, PCM are implemented on the basis of different RBFs including MQ and EXP with $c_0 = \Delta$, $c_0 = 2\Delta$, $c_0 = 3\Delta$ and $c_0 = 4\Delta$, respectively. Average errors of displacements, strains and stresses along the bar with different c_0 values by using global support shape functions can be seen in Table 4.3, from which one can obviously see that RPIM-EXP shape functions lead to incorrect solutions when $c_0 = 3\Delta$ or $c_0 = 4\Delta$ since the errors are huge. This is duo to the singularity in EXP-RBF arises during the function approximation and hence RPIM-EXP shape functions become unstable. On the contrary, solutions obtained by MQ-based PCM have small average errors when c_0 differs, indicating that RPIM-MQ is more stable and not sensitive to the free parameter when the global support domain is used.

Additionally, when shape functions are locally supported, a total number of 12 nodes are included in the support domain to construct RPIM shape functions.

Average errors of their numerical solutions have been listed in Table 4.4, which shows that numerical errors are increasing when c_0 values arise. The accuracy of EXP-based PCM improve greatly and only a small error occurs when $c_0 = 4\Delta$, which reflects that the singularity issue can be solved by means of employing EXP-RBF together with local support domains. And the accuracy of RPIM-MQ is higher than that of RPIM-EXP in most cases.

Table 4.3: *Average errors of displacement, strain and stress solutions along the bar with different c_0 using the global support domain.*

c_0	u_x (MQ)	u_x (EXP)	ε_x (MQ)	ε_x (EXP)	σ_x (MQ)	σ_x (EXP)
1Δ	3.694E-11	9.219E-11	2.712E-13	4.467E-14	2.712E-13	4.467E-14
2Δ	1.544E-10	5.688E-09	1.104E-12	4.170E-09	1.104E-12	4.170E-09
3Δ	3.929E-11	9.678E-01	9.074E-12	9.718E-01	9.074E-12	9.718E-01
4Δ	5.685E-10	9.740E-01	1.752E-10	9.751E-01	1.752E-10	9.751E-01

Table 4.4: *Average errors of displacement, strain and stress solutions along the bar with different c_0 using the local support domain.*

c_0	u_x (MQ)	u_x (EXP)	ε_x (MQ)	ε_x (EXP)	σ_x (MQ)	σ_x (EXP)
1Δ	6.276E-10	2.847E-12	1.016E-12	2.753E-13	1.016E-12	2.753E-13
2Δ	4.290E-08	4.255E-07	1.206E-12	2.659E-10	1.206E-12	2.659E-10
3Δ	3.770E-07	1.662E-03	9.655E-12	2.506E-06	9.655E-12	2.506E-06
4Δ	1.105E-05	9.670E-01	2.380E-04	6.254E-03	2.380E-04	6.254E-03

Finally, the elapsed real time for calculating σ_x along the bar by using different kinds of support domains and RBFs are examined and listed in Table 4.5 and Table 4.6. Related parameters including the total number of field nodes, c_0 and K_0 can also be seen in the tables. It is shown that quite similar average errors have been

obtained, but PCMs using EXP approximations take more time in both tables. And When these two tables are compared, it is clearly shown that locally supported PCMs are computationally efficient as the elapsed real time is very small. A smaller amount of field nodes employed results in closed average errors with the globally supported PCMs, and only 5 nodes used in the local support domain can lead to high accurate solutions.

Table 4.5: *Elapsed real time for calculating σ_x along the bar by using the global support domain.*

RBF	Field nodes	c_0	Average errors	Elapsed real time (Second)
MQ	101	2.5Δ	2.511E-11	1.147
EXP	101	0.2Δ	2.593E-11	1.543

Table 4.6: *Elapsed real time for calculating σ_x along the bar by using the local support domain.*

RBF	Field nodes	K_0	c_0	Average errors	Elapsed real time (Second)
MQ	91	5	2.8Δ	2.581E-11	0.167
EXP	91	5	1.0Δ	2.543E-11	0.172

To sum up, MQ-based PCM presents a better performance compared with EXP-based PCM because of its insensitivity to the varying of the free parameter and its stability under different kinds of support domains . Besides, approximations carrying out in local support domains are superior to others since they are time saving and producing better solutions even different kinds of RBFs are selected. Therefore, in the following Sections and Chapters, RPIM-MQ shape functions that are locally supported will be used to carry out meshless approximations.

4.3 Point Collocation Method (PCM) for 2D Solids

In this section, PCM is applied to 2D solid mechanics problems. Meshless formulations are presented and three numerical examples are carried out to illustrate the convenience, accuracy and efficiency of strong-form meshless methods.

4.3.1 Meshless Formulation for 2D Solids

Consider a 2D problem domain of isotropic medium. The governing equations for the plane stress case defined in the $x-y$ plane are

$$\frac{\partial \sigma_x}{\partial x}+\frac{\partial \tau_{yx}}{\partial y}+f_x=0 \tag{4.9a}$$

$$\frac{\partial \sigma_y}{\partial y}+\frac{\partial \tau_{xy}}{\partial x}+f_y=0 \tag{4.9b}$$

in which σ_x , σ_y and $\tau_{xy}=\tau_{yx}$ are stress components. And f_x and f_y are two components of the external body forces applied at x and y directions, respectively.

Recalling Hook's Law and ignore the body forces, equilibrium equations in (4.9a) and (4.9b) can be written explicitly in terms of displacement components as

$$E'\frac{\partial^2 u}{\partial x^2}+G\frac{\partial^2 u}{\partial y^2}+\mu E'\frac{\partial^2 v}{\partial x \partial y}+G\frac{\partial^2 v}{\partial x \partial y}=0 \tag{4.10a}$$

$$E'\frac{\partial^2 v}{\partial y^2}+G\frac{\partial^2 v}{\partial x^2}+\mu E'\frac{\partial^2 u}{\partial x \partial y}+G\frac{\partial^2 u}{\partial x \partial y}=0 \tag{4.10b}$$

in which u and v are displacement components along axis x and y, respectively. And $G=\dfrac{E}{2(1+\mu)}$ is the shear modulus.

The above equations can be approximated by use of RPIM shape functions

presented in Chapter 3 and then discretized directly by collocating at field nodes. Therefore, the displacement at a point of interest **x** can be approximated as

$$\left\{ \begin{array}{c} u(\mathbf{x}) \\ v(\mathbf{x}) \end{array} \right\} = \sum_{k=1}^{K} \left[\begin{array}{cc} \phi_k & 0 \\ 0 & \phi_k \end{array} \right] \left\{ \begin{array}{c} u_k \\ v_k \end{array} \right\} \tag{4.11}$$

Substituting (4.11) into (4.10), the discretized system equations can be derived as

$$u^{(k)} \sum_{k=1}^{K} (E' \phi_{k,xx} + G\phi_{k,yy}) + v^{(k)} \sum_{k=1}^{K} (\mu E' \phi_{k,xy} + G\phi_{k,xy}) = 0 \tag{4.12a}$$

$$u^{(k)} \sum_{k=1}^{K} (\mu E' \phi_{k,xy} + G\phi_{k,xy}) + v^{(k)} \sum_{k=1}^{K} (E' \phi_{k,yy} + G\phi_{k,xx}) = 0 \tag{4.12b}$$

For nodes on the displacement boundaries, boundary conditions can be introduced straightforward as

$$u(\mathbf{x}_k) = u^0 \tag{4.13a}$$

$$v(\mathbf{x}_k) = v^0 \tag{4.13b}$$

where u^0 and v^0 are specified displacements in x and y directions, respectively.

On the traction boundaries, where the traction forces along x and y directions are prescribed, the boundary conditions are

$$t_x^0 = l\sigma_x + m\tau_{yx} \tag{4.14a}$$

$$t_y^0 = m\sigma_y + l\tau_{xy} \tag{4.14b}$$

where $l = cos(\mathbf{n}, x), m = cos(\mathbf{n}, y)$, **n** is the outward normal vector on the bound-

ary. Rewrite (4.14) in terms of displacement components, we have

$$t_x^0 = lE'\frac{\partial u}{\partial x} + mG\frac{\partial u}{\partial y} + \mu lE'\frac{\partial v}{\partial y} + mG\frac{\partial v}{\partial x} \tag{4.15a}$$

$$t_y^0 = \mu mE'\frac{\partial u}{\partial x} + lG\frac{\partial u}{\partial y} + mE'\frac{\partial v}{\partial y} + lG\frac{\partial v}{\partial x} \tag{4.15b}$$

RPIM shape functions are employed and then the traction boundary conditions can be rewritten as

$$\sum_{k=1}^{K}\left(lE'\phi_{k,x} + mG\phi_{k,y}\right)u^{(k)} + \sum_{k=1}^{K}\left(\mu lE'\phi_{k,y} + mG\phi_{k,x}\right)v^{(k)} = t_x^0 \tag{4.16a}$$

$$\sum_{k=1}^{K}\left(\mu mE'\phi_{k,x} + lG\phi_{k,y}\right)u^{(k)} + \sum_{k=1}^{K}\left(mE'\phi_{k,y} + lG\phi_{k,x}\right)v^{(k)} = t_y^0 \tag{4.16b}$$

Based on the strong-forms of governing equations in (4.12) and traction boundary conditions in (4.16), formulations related to plane strain problems can be obtained easily by replacing the Young's modules E in E' with

$$\bar{E} = \frac{E}{1-\mu^2} \tag{4.17}$$

and the Poisson ratio μ with

$$\bar{\mu} = \frac{\mu}{1-\mu} \tag{4.18}$$

However, displacement boundary conditions can still be imposed as (4.13).

The application of PCM to 2D elastostatics is demonstrated by the following

three examples. Approximation procedures are carried out by using the locally supported RPIM-MQ shape functions. Free parameter c_0 in the MQ RBF is taken as $c_0 = 2\Delta$. And the local support domain is selected as a circle of radius r_0 centred at collocation points **x**, in which $K = 12$ is used in all examples.

4.3.2 A Square Panel under Uniform Displacement

Firstly, a square panel of side $a = 5cm$ is investigated. The plate is fixed at $x = 0$ and subjected to a uniformly distributed displacement $u^0 = 0.001cm$ along the edge $x = 5cm$ as shown in Figure 4.3. In this case, material parameters are taken as: Young's modulus $E = 2.1 \times 10^6 N/cm^2$, Poisson ratio $\mu = 0.2$. The contour plot of ε_{xx} obtained from Abaqus is presented in Figure 4.4, which can be regarded as the benchmark to evaluate other numerical results.

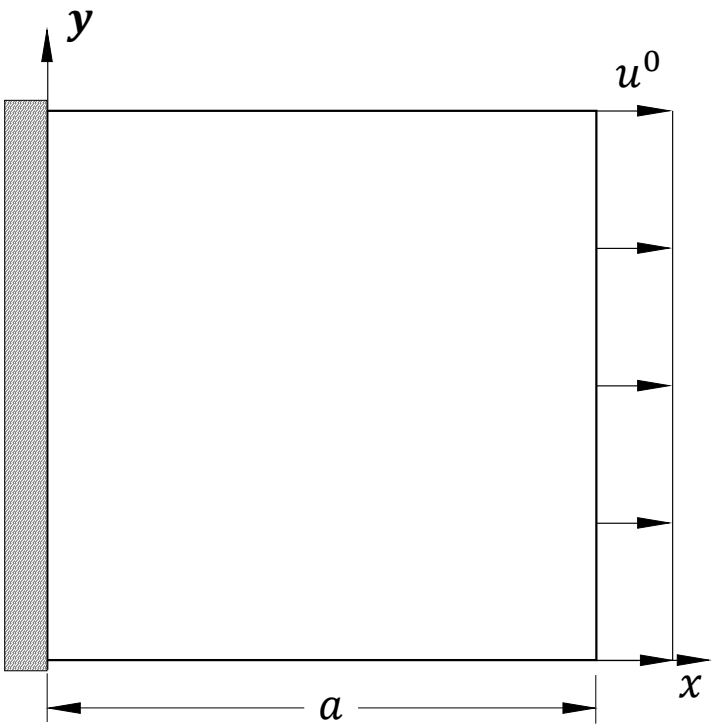

Figure 4.3: *A square panel under uniform displacement.*

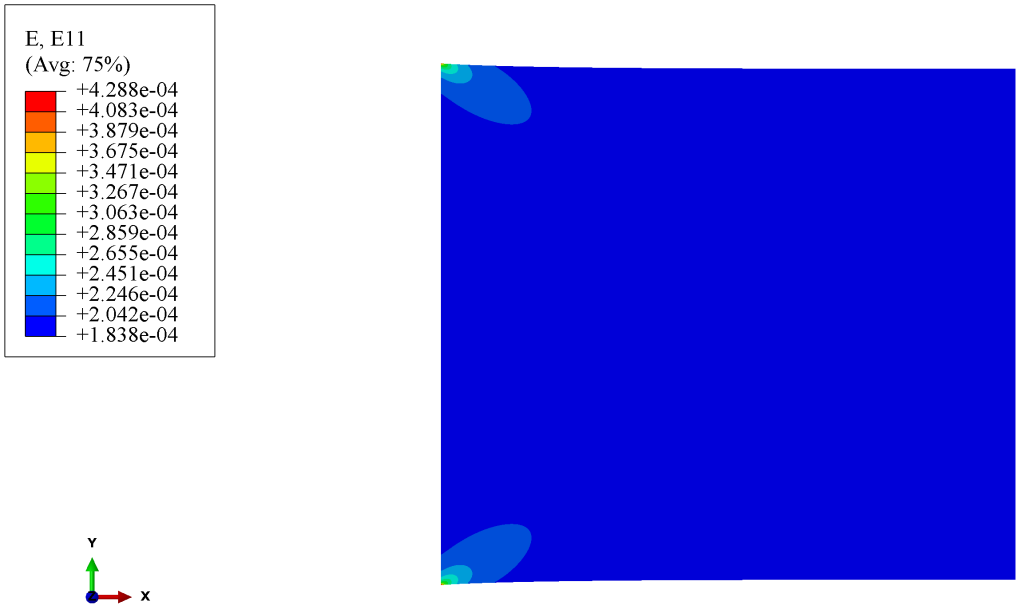

Figure 4.4: *Abaqus contour plot of ε_{xx} for a square panel under uniform displacement.*

Numerical errors for strains at point $(0.0, 2.5)$ with different values of c_0 are plotted in Figure 4.5. The problem domain is represented by a set of regularly and evenly distributed nodes and the node density is 31×31. The total number of nodes in the local support domain is selected as 12. Abaqus solution $\varepsilon_{xx}(0.0, 2.5) = 1.83823 \times 10^{-4}$ is regarded as the benchmark. It is shown that numerical errors are all less than 1% when c_0 changes, but it increases after c_0 is greater than 5Δ.

Figure 4.6 shows numerical errors for strains at point $(0.0, 2.5)$ with different number of nodes in the local support domain. In this case, a group of 31×31 field nodes are regularly and evenly distributed in the problem domain and the free parameter c_0 is selected as 2Δ. The total number of nodes involved in the local support domain to construct RPIM shape functions are taken as $K = 8, 12, 17, 25, 38, 53, 103$. It can be seen that numerical errors are increasing when K is greater than 17. And K values located within $12 - 25$ result in solutions with errors less than 0.1%. In addition, it requires more computing time to obtain the coefficient matrix with the increase of nodes in the local support domain.

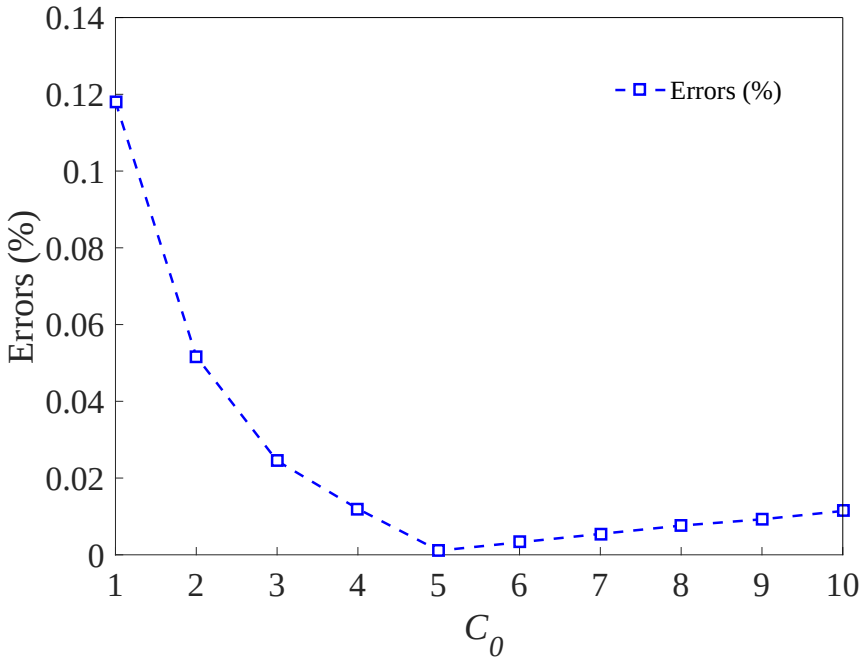

Figure 4.5: *Numerical errors of* $\varepsilon_{xx}(0.0, 0.25)$ *for different* c_0 *values.*

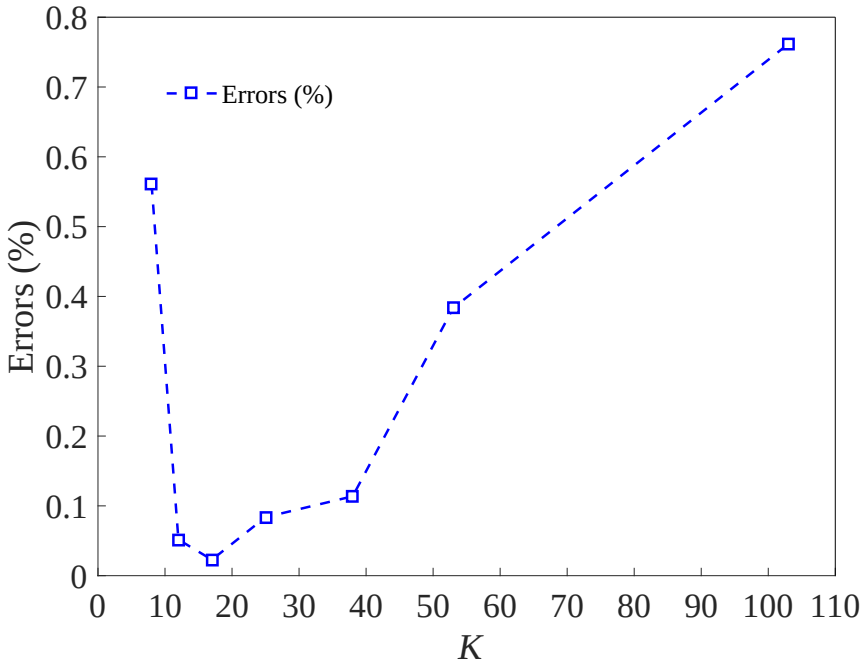

Figure 4.6: *Numerical errors of* $\varepsilon_{xx}(0.0, 0.25)$ *for different number of nodes in the local support domain.*

The convergence study is carried out by using different densities of field nodes in the problem domain. Related parameters are selected as $c_0 = 2\Delta$ and $K = 12$. Numerical solutions of $\varepsilon_{xx}(0.0, 0.25)$ and their errors compared with the Abaqus solution are listed in Table 4.7, showing that the accuracy of solutions increase when finer field nodes are employed, but the time needed for solving algebraic equations goes up when the total number of field nodes employed in the problem is large.

Table 4.7: *Numerical solutions and errors of $\varepsilon_{xx}(0.0, 0.25)$ for different densities of field nodes.*

M	ε_{xx}	Errors (%)
5×5	1.89065E-04	2.85166
11×11	1.83349E-04	0.25786
21×21	1.83748E-04	0.04080
31×31	1.83728E-04	0.05168
41×41	1.83734E-04	0.04842

In order to demonstrate the accuracy of PCM based on RPIM-MQ, strain distribution ε_{xx} versus x at $y = 0.019cm$ and $y = 2.519cm$ are plotted in Figure 4.7. While solutions for ε_{xx} versus y at $x = 0.019cm$ and $x = 2.519cm$ are shown in Figure 4.8. The field node density is 31×31 and other parameters are chosen to be $c_0 = 2\Delta$, $K = 12$. Abaqus solutions are also reported for comparison purpose. Good convergence have been achieved when $y = 2.519cm$ or $x = 2.519cm$. However, errors can be seen on geometrical boundaries when $y = 0.019cm$ or $x = 0.019cm$. This is duo to the singularity arises nearby geometrical boundaries.

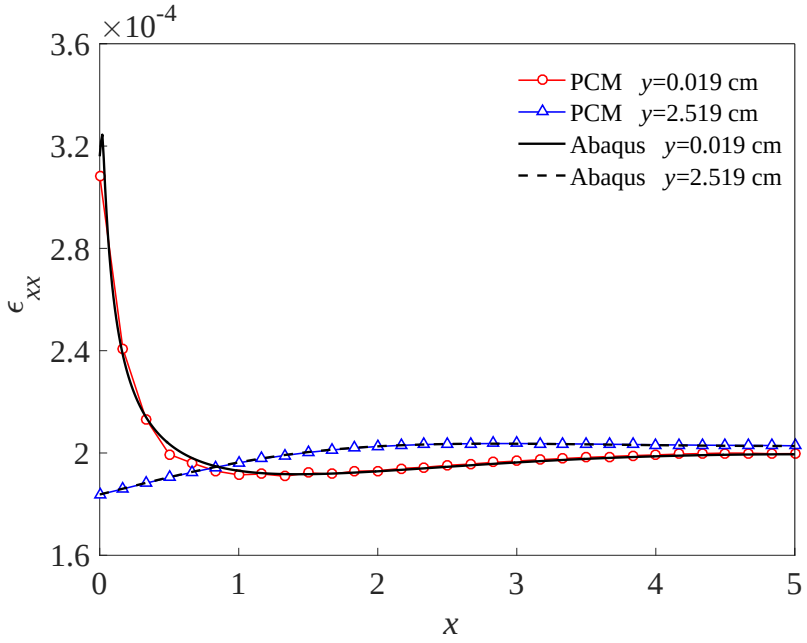

Figure 4.7: *Distribution of* ε_{xx} *versus* x *at* $y = 0.019cm$ *and* $y = 2.519cm$.

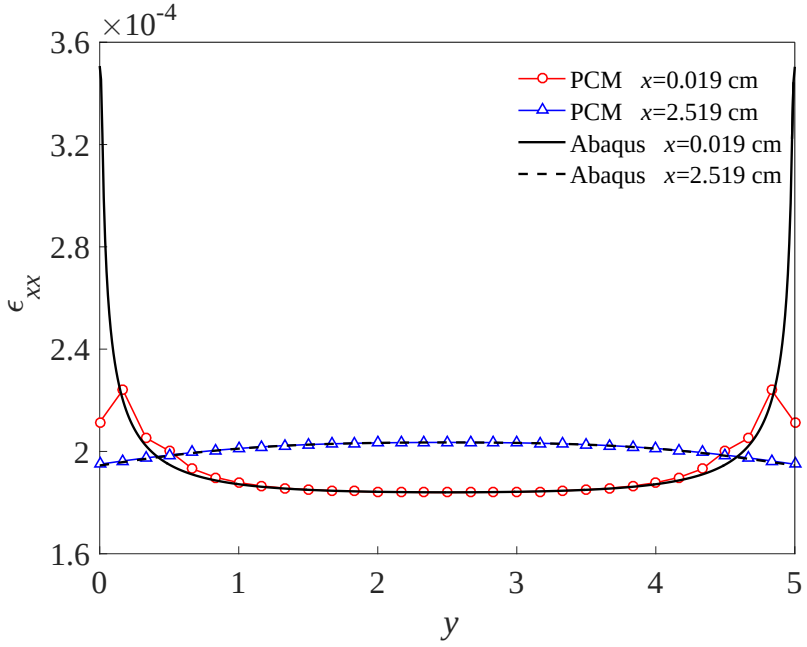

Figure 4.8: *Distribution of* ε_{xx} *versus* y *at* $x = 0.019cm$ *and* $x = 2.519cm$.

4.3.3 A Square Board with a Circle Hole under Tensile Load

Secondly, a square board of width $2b$ containing a circle hole of radius a subjected to a uniform tension load σ_0 on the top and the bottom is analyzed (where $b = 2a$) as shown in Figure 4.9(a). Due to the symmetry, only one-quarter of the plate is studied, see Figure 4.9(b). Young's modulus is one unit and Poisson ratio $\mu = 0.3$. The total number of field nodes is 1364. Other parameters are selected as $c_0 = 2\Delta$, $K = 12$.

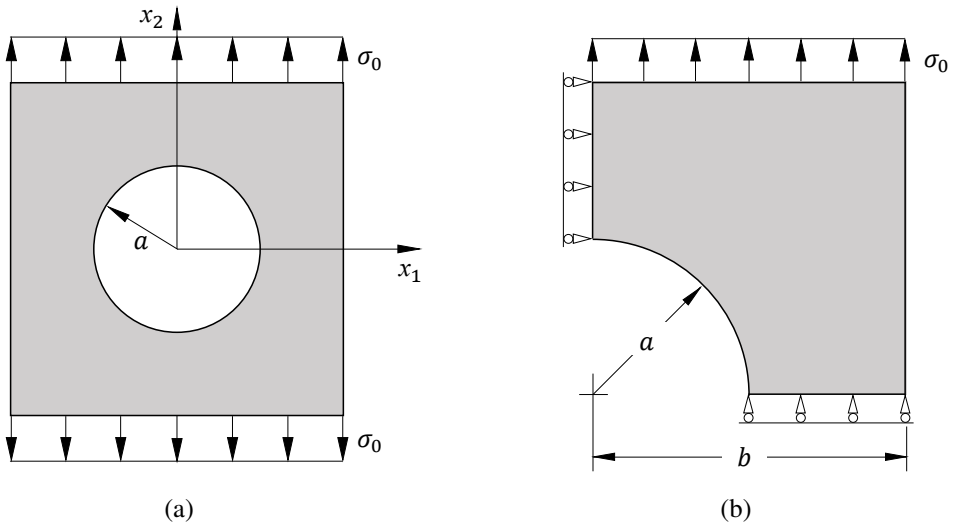

Figure 4.9: *A square board containing a circle hole under tensile load: (a) geometry; (b) a quarter of the plate.*

To demonstrate the accuracy of PCM, Abaqus contour plots related to the distribution of strains and stresses are presented in Figure 4.10 to Figure 4.11 for the sake of comparison. Variations of normalized strains and stresses along axis x_1 are plotted in Figure 4.12 and Figure 4.13. As expected, numerical solutions given by PCM are convergent with Abaqus results.

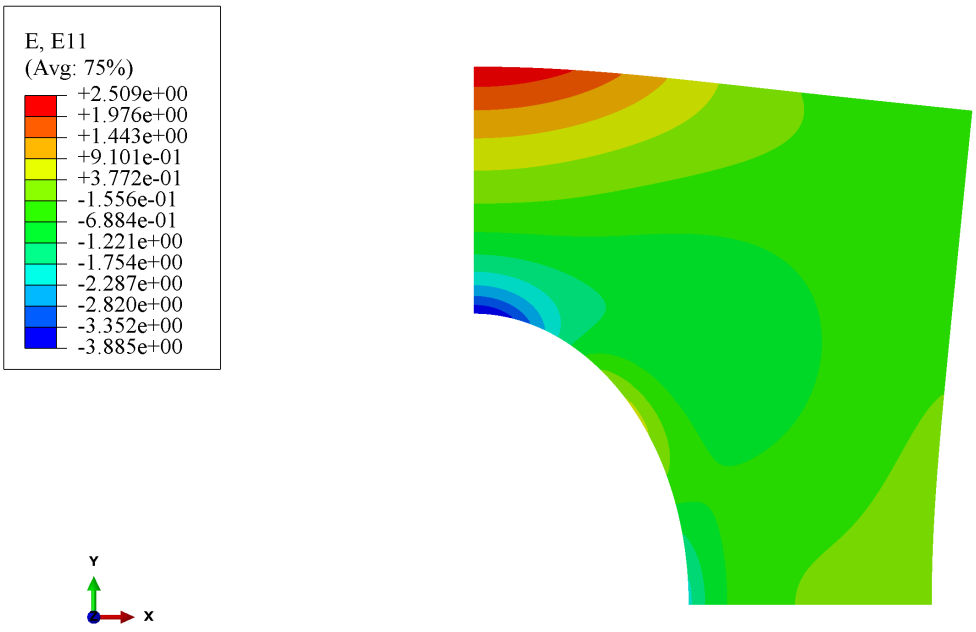

(a)

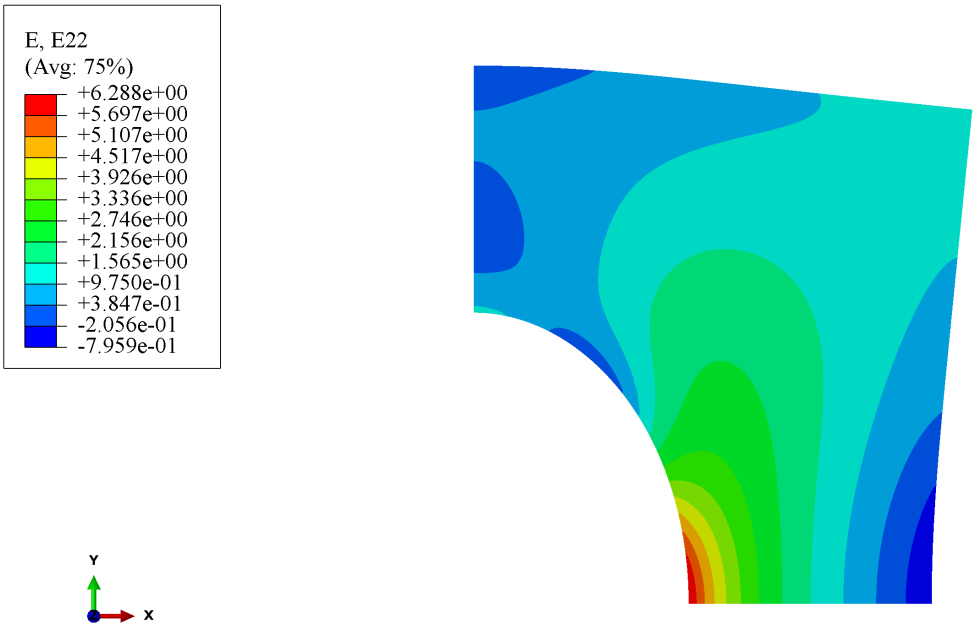

(b)

Figure 4.10: *Abaqus contour plot of strain distributions for a square board with a circle hole under tensile load: (a) ε_{11}; (b) ε_{22}.*

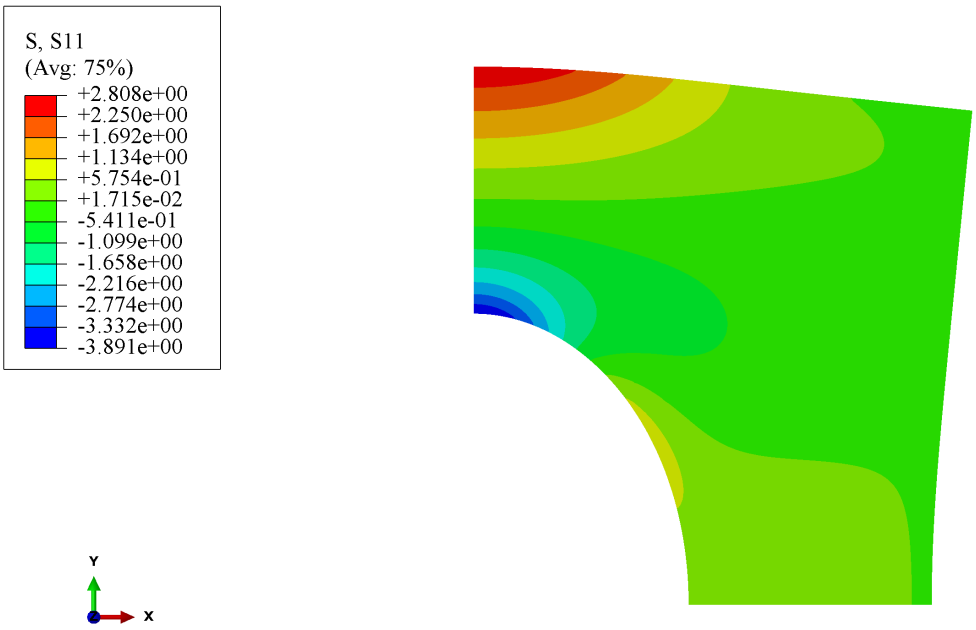

(a)

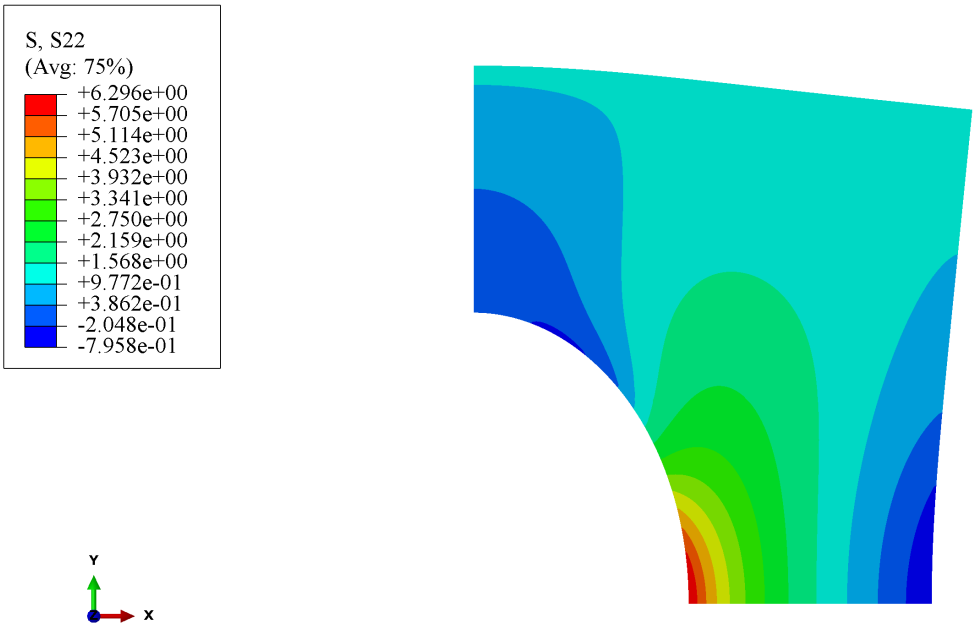

(b)

Figure 4.11: *Abaqus contour plot of stress distributions for a square board with a circle hole under tensile load: (a) σ_{11}; (b) σ_{22}.*

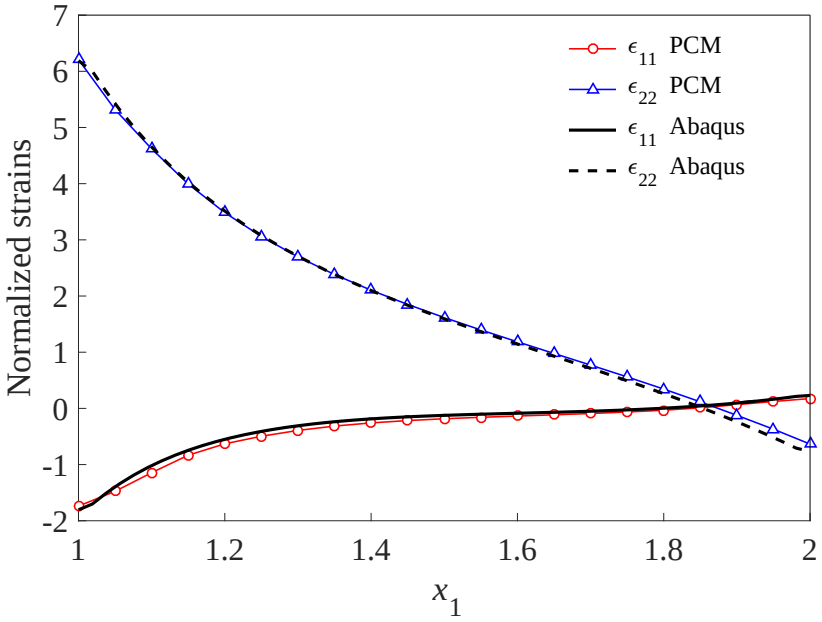

Figure 4.12: *Strain variations along axis x_1 for a square board with a circle hole under tensile load.*

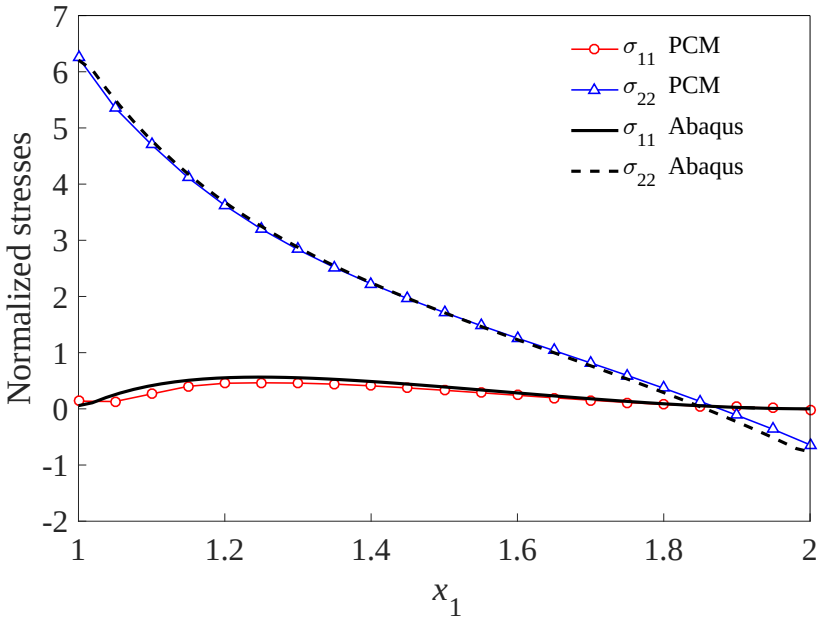

Figure 4.13: *Stress variations along axis x_1 for a square board with a circle hole under tensile load.*

4.3.4 A Disk under Internal Pressure

Finally, a disk under internal pressure is analyzed with dimensions $a = 1cm$, $b = 2cm$ as shown in Figure 4.14(a). Young's modulus is one unit and Poisson ratio $\mu = 0.3$. Again, only one-quarter of the disk is considered in this example because of the symmetry, see Figure 4.14(b). The total number of field nodes is 989. Parameter c_0 in RPIM-MQ is taken as 2Δ, and the number of nodes involved in the local support domain is 12.

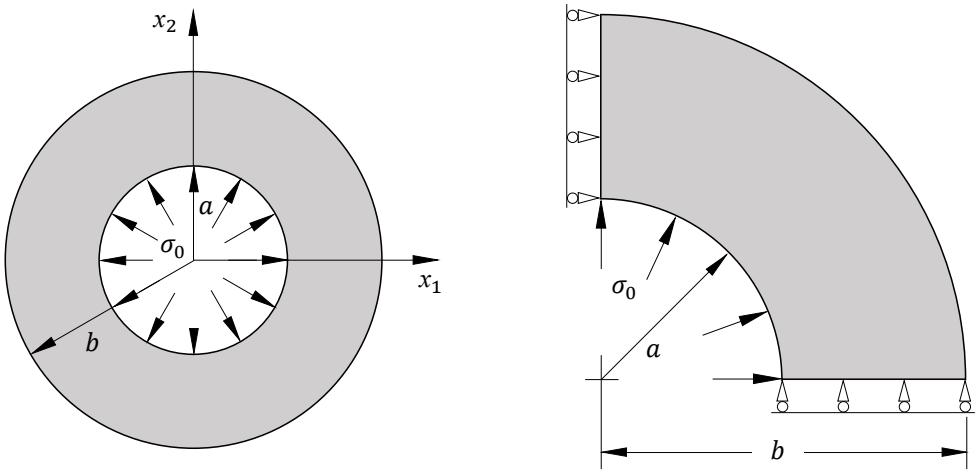

Figure 4.14: *A disk subjected to internal pressure: (a) geometry; (b) a quarter of the disk.*

ABAQUS contours with respect to the strain and stress distributions along x and y direction are reported respectively in Figure 4.15 and Figure 4.16 for comparison purpose. Besides, normalized strains and stresses along axis x_1 are plotted in Figure 4.17 and Figure 4.18, respectively. The maximum errors of numerical solutions are 5.56% for ε_{22} and 6.80% for σ_{22} appeared at point $(1.0, 0.0)$. Good agreement has been obtained for other field nodes, which again validates the accuracy of PCM to general problems.

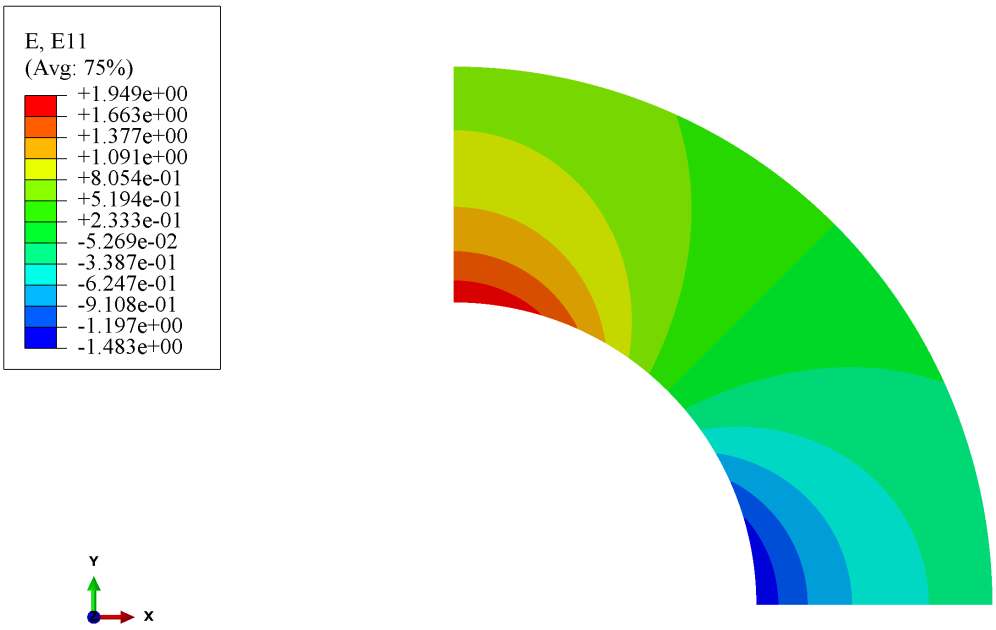

(a)

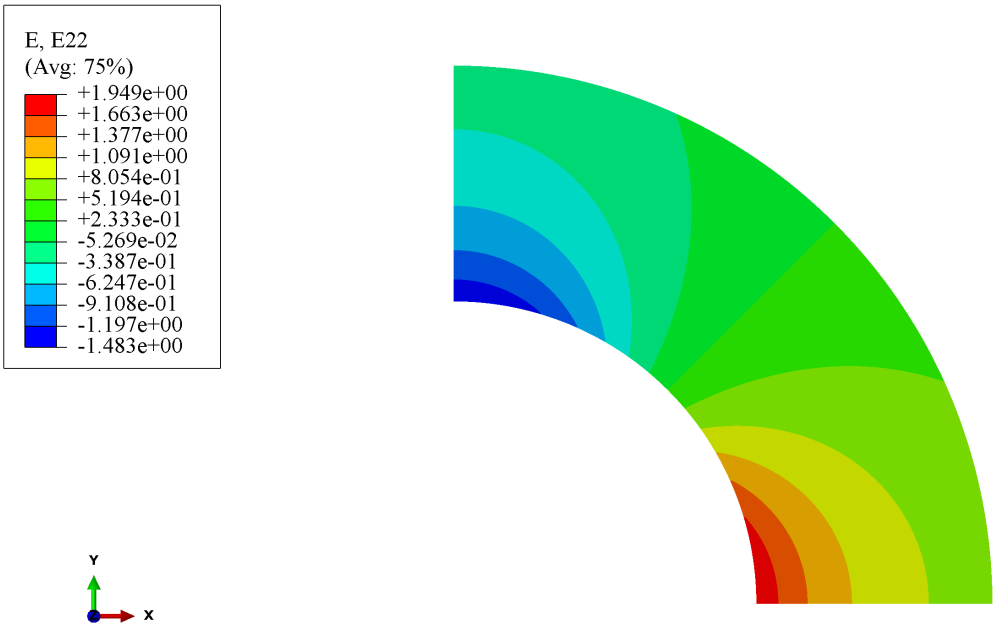

(b)

Figure 4.15: *Abaqus contour plot of strain distributions for a disk subjected to internal pressure: (a) ε_{11}; (b) ε_{22}.*

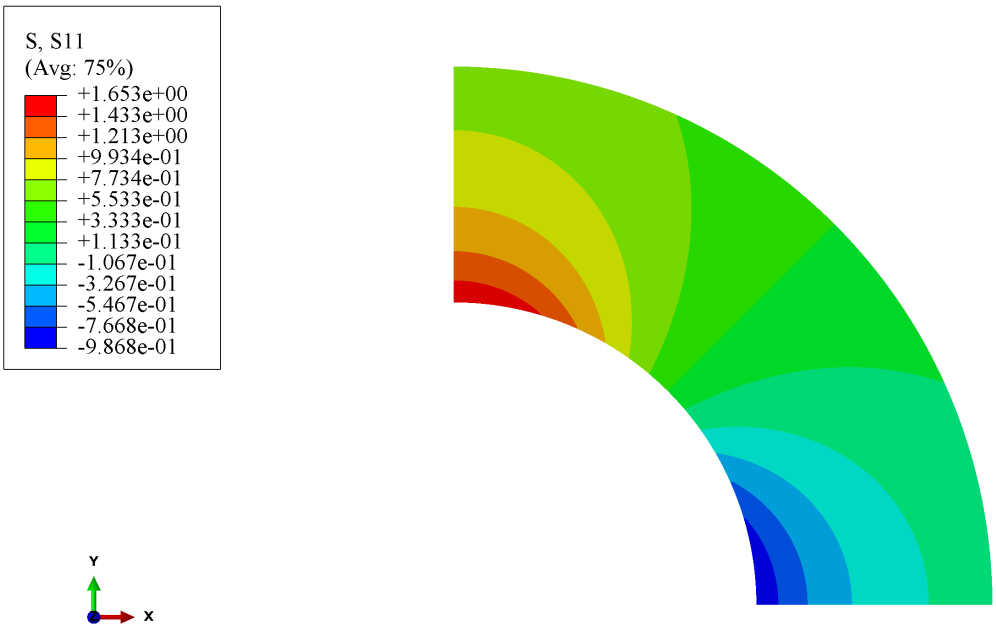

(a)

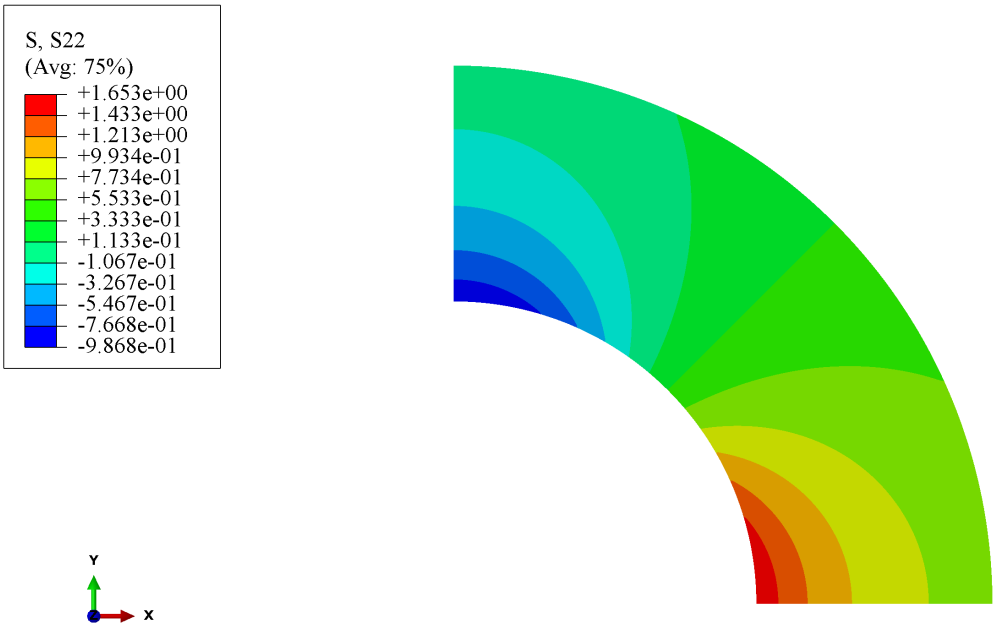

(b)

Figure 4.16: *Abaqus contour plot of stress distributions for a disk subjected to internal pressure: (a) σ_{11}; (b) σ_{22}.*

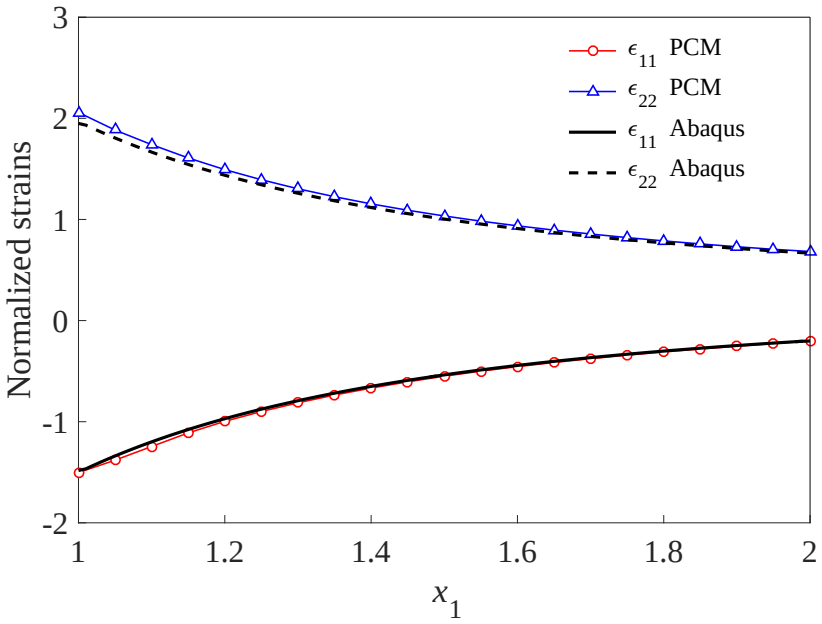

Figure 4.17: *Strain distributions along axis x_1 for a disk subjected to internal pressure.*

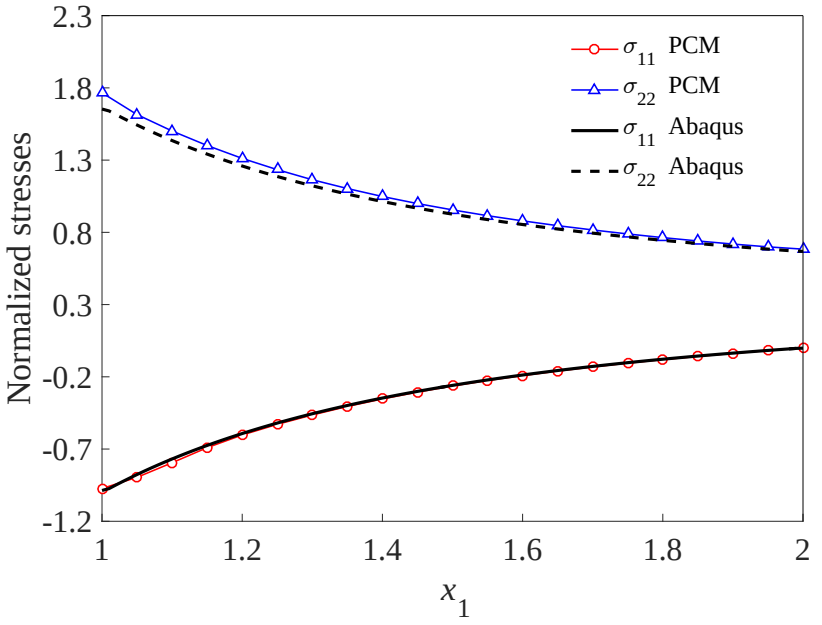

Figure 4.18: *Stress distributions along axis x_1 for a disk subjected to internal pressure.*

4.4 Conclusions

In this chapter, formulations of meshless Point Collocation Method (PCM) are presented for one- and two-dimensional solids. Meshless approximations are carried out by use of RBFs and governing equations are directly discretized at field nodes. A simple 1D problem is demonstrated to investigate the influence of support domains, types of RBFs as well as the free parameter c_0 on PCM solutions. In addition, three 2D examples are conducted in order to apply PCM based on the locally supported RPIM-MQ to general cases, in which the selection of c_0, the total number of nodes in the local support domain and the convergence of the presented method are discussed. Abaqus solutions are also reported and used for comparison. It can be concluded based on the study above that:

(1) Approximations based on the global support domain are time-consuming since all field nodes in the problem domain are involved to construct shape functions, and thus resulting in a set of fully populated system equations. On the contrary, approximations based on local support domains lead to a sparse system matrix, which significantly reduce the computational efforts.

(2) When the global support domain is employed, the EXP-RBF is sensitive to the varying of the free parameter, which indicates that inappropriate selections of free parameters in EXP-RBF give rise to singularities and consequently incorrect solutions are obtained. Nevertheless, approximations based on the MQ-RBF are numerically stable in the same circumstance and therefore provide accurate solutions.

(3) When the shape function is locally supported, the influence of c_0 drops evidently in PCM based on EXP RBF. Therefore, its singularity can be prevented by choosing suitable support domains and approximation schemes.

(4) The computing time spent on calculating the coefficient matrix increases when the total number of nodes in the local support domain is large. And numerical solutions with high accuracy can be obtained when the number of nodes in the local support domain locates in the range of 12 to 25.

(5) The accuracy of solutions increases when finer field nodes are used. But it requires more time to solve the discretized system equations.

(6) Applications of PCM based on the locally supported RPIM-MQ to 2D solid problems demonstrate its convenience, accuracy and computational efficiency.

CHAPTER 5

Meshless Local Integral Equation Methods

5.1 Introduction

Before the Meshless Local Petrov-Galerkin (MLPG) method was put forward, a class of mesh reduction methods, such as Element Free Galerkin (EFG) methods, are on the basis of global weak-forms, in which background grids have to be introduced in order to carry out numerical integrals and then deriving global integrals of governing equations over the entire problem domain. However, with the proposal of MLPG [104] based on the local weak-forms, numerical integrals can be carried out within the local domains with respect to every specific node. Therefore, global background cells are removed completely and achieve really and truly the 'meshfree' idea.

Inspired by the idea of MLPG, variety kinds of meshless methods based upon the local weak-forms were proposed by employing different approximation schemes and formulation procedures. Among others, Liu et al [149, 150] proposed the Local Point Interpolation Method (LPIM) and the Local Radial Point Interpolation

Method (LRPIM). The former one is based on polynomial basis functions and hence may lead to singularities. While in LRPIM, a more robust scheme, RBF approximations, are employed. Sladek et al [151] proposed the meshless Local Boundary Integral Equation method (LBIE), and a comparative study has been conducted between MLS and polynomial RBF approximations. Besides, analytical solutions of LBIE for 2D non-homogeneous elasticity were presented but quite complex [152]. Wen [153] applied LBIE to solid mechanics and derived closed forms for all domain integrals in local weak-forms based on RBF interpolations. The CPU time reduces greatly since the closed form of LBIE is obtained.

Applications of local weak-form meshless methods are far to be exhaustive in the literature. Recently, it was used to address functionally graded Reissner's plate problems [154], and poroelastic problems [155].

This chapter is structured as follows: formulations of meshless Local Integral Equation Method (LIEM) are presented for 2D isotropic medium. Then, a step function is selected as the test function, and the MQ RBF approximation is employed to derive analytical solutions for domain integrals. Finally, effects of parameters including the number of straight lines that enclose the local integral domain as well as the integral radius are observed, and the accuracy and convergence of LIEM are demonstrated by three examples. Comparisons are made with Abaqus solutions and PCM results.

5.2 Local Integral Equation Method (LIEM)

The governing equation for 2D isotropic medium is,

$$\sigma_{ij,j} + f_i = 0 \tag{5.1}$$

Consider a problem domain Ω with boundary Γ presented in Figure 5.1, the equilibrium equation in (5.1) can be satisfied over a local integral domain Ω_s bounded by Γ_s for any point of interest **x**, leading to the local weak-form of the governing equation as

$$\int_{\Omega_s} (\sigma_{ij,j} + f_i) u_i^* d\Omega = 0 \tag{5.2}$$

where u_i^* is the test function or weight function centred at **x**.

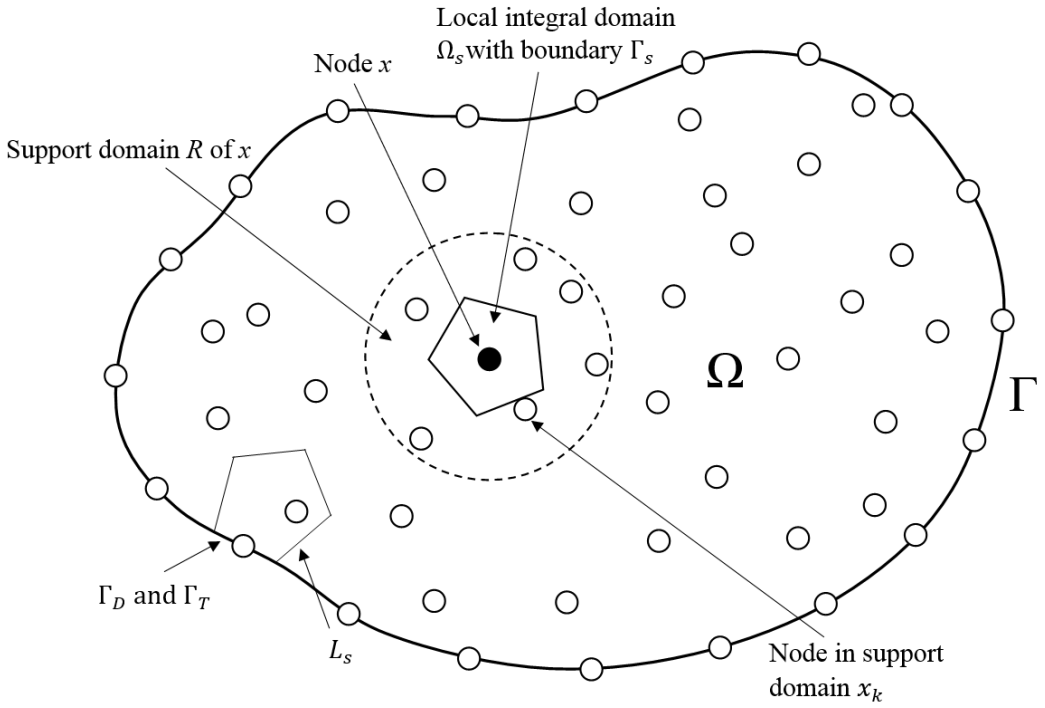

Figure 5.1: *A problem domain Ω with boundary Γ and the local integral domain Ω_s for a point **x** bounded by Γ_s.*

The use of the integration by parts yields

$$\int_{\Omega_s} \sigma_{ij,j} u_i^* d\Omega = \int_{\Gamma_s} \sigma_{ij} n_j u_i^* d\Gamma - \int_{\Omega_s} \sigma_{ij} u_{i,j}^* d\Omega \tag{5.3}$$

where n_j denotes the unit outward normal on the boundary. Substituting (5.3) into

(5.2) results in the following weak-form:

$$\int_{\Gamma_s} \sigma_{ij} n_j u_i^* d\Gamma - \int_{\Omega_s} (\sigma_{ij} u_{i,j}^* - f_i u_i^*) d\Omega = 0 \tag{5.4}$$

As shown in Figure 5.1, the local boundary Γ_s is formed by different components including Γ_D, Γ_T and L_s, namely, $\Gamma_s = \Gamma_D \cup \Gamma_T \cup L_s$, in which:

Γ_D is the displacement boundary that intersects with the global boundary Γ;

Γ_T is the traction boundary that has an intersection with the global boundary Γ;

L_s is the interior part of the local boundary that has no intersection with the global boundary.

Therefore, (5.4) can be written in the form of

$$\begin{aligned} \int_{\Gamma_D} \sigma_{ij} n_j u_i^* d\Gamma + \int_{\Gamma_T} \sigma_{ij} n_j u_i^* d\Gamma + \int_{L_s} \sigma_{ij} n_j u_i^* d\Gamma \\ - \int_{\Omega_s} (\sigma_{ij} u_{i,j}^* - f_i u_i^*) d\Omega = 0 \end{aligned} \tag{5.5}$$

Consider the relationship between the stress and the traction on the boundary, (5.5) can be expressed as

$$\int_{\Omega_s} \sigma_{ij} u_{i,j}^* d\Omega - \int_{L_s} t_i u_i^* d\Gamma - \int_{\Gamma_D} t_i u_i^* d\Gamma = \int_{\Gamma_T} t_i^0 u_i^* d\Gamma + \int_{\Omega_s} f_i u_i^* d\Omega \tag{5.6}$$

However, for the local boundary that has no intersection with the global boundary, which means the local integral domain is completely located within the problem domain, there is no need to consider the integration over Γ_D and Γ_T, but only L_s is left and in this instance $L_s = \Gamma_s$. Thus, (5.5) becomes

$$\int_{L_s} t_i n_j u_i^* d\Gamma - \int_{\Omega_s} (\sigma_{ij} u_{i,j}^* - f_i u_i^*) d\Omega = 0 \tag{5.7}$$

5.3 Analytical Solutions for Domain Integrals

With the purpose of simplifying the local weak-forms, the test function u_i^* in each integral domain can be purposely selected. When a step function is employed

$$u_i^*(\mathbf{x}) = \begin{cases} \phi_i(\mathbf{x}) & \text{at } \mathbf{x} \in (\Omega_s \cup \Gamma_s) \\ 0 & \text{at } \mathbf{x} \notin \Omega_s \end{cases} \tag{5.8}$$

where $\phi_i(\mathbf{x}) = 1$ and no body forces are taken into account, the local integral equations in (5.4) and (5.6) become

$$\int_{\Gamma_s} \sigma_{ij} n_j d\Gamma = 0 \tag{5.9}$$

and

$$\int_{L_s} t_i d\Gamma + \int_{\Gamma_D} t_i d\Gamma = -\int_{\Gamma_T} t_i^0 d\Gamma \tag{5.10}$$

Assume that the local integral domain Ω_s is enclosed by several straight lines, see Figure 5.2. Then (5.9) can be written as

$$\int_{\Gamma_s} \sigma_{ij} n_j d\Gamma = \sum_{l=1}^{L} n_j^l \int_{\Gamma_l} \sigma_{ij} d\Gamma \tag{5.11}$$

in which L denotes the number of straight lines that enclose the local integral domain.

Recalling the RPIM-MQ shape functions reported in Chapter 3, we have approximations of field variables in terms of nodal values as

$$u(\mathbf{x}) = \sum_{k=1}^{K} \phi_k u_k \tag{5.12a}$$

$$\phi(\mathbf{x}) = \sum_{m=1}^{M} R_m(r)a_m + \sum_{n=1}^{N} P_n(\mathbf{x})b_n \tag{5.12b}$$

Figure 5.2: *A local integral domain enclosed by straight lines.*

By using Hook's law and the meshless approximation scheme presented in (5.12a) and (5.12b), one has

$$\begin{aligned}\int_{\Gamma_l} \sigma_{xx} n_x^l d\Gamma &= \int_{\Gamma_l} n_x^l E' \left(\frac{\partial u}{\partial x} + \mu \frac{\partial v}{\partial y}\right) d\Gamma \\ &= n_x^l E' \sum_{k=1}^{K} \left[\left(\sum_{m=1}^{M} R_{mx} a_m + \sum_{n=1}^{N} P_{nx} b_n \right) u^{(k)} + \mu \left(\sum_{m=1}^{M} R_{my} a_m + \sum_{n=1}^{N} P_{ny} b_n \right) v^{(k)} \right]\end{aligned} \tag{5.13a}$$

$$\begin{aligned}\int_{\Gamma_l} \sigma_{yy} n_y^l d\Gamma &= \int_{\Gamma_l} n_y^l E' \left(\frac{\partial v}{\partial y} + \mu \frac{\partial u}{\partial x}\right) d\Gamma \\ &= n_y^l E' \sum_{k=1}^{K} \left[\left(\sum_{m=1}^{M} R_{my} a_m + \sum_{n=1}^{N} P_{ny} b_n \right) v^{(k)} + \mu \left(\sum_{m=1}^{M} R_{mx} a_m + \sum_{n=1}^{N} P_{nx} b_n \right) u^{(k)} \right]\end{aligned} \tag{5.13b}$$

$$\begin{aligned}\int_{\Gamma_l} \tau_{xy} n_y^l d\Gamma &= \int_{\Gamma_l} n_y^l G \left(\frac{\partial u}{\partial y} + \frac{\partial v}{\partial x}\right) d\Gamma \\ &= n_y^l G \sum_{k=1}^{K} \left[\left(\sum_{m=1}^{M} R_{my} a_m + \sum_{n=1}^{N} P_{ny} b_n \right) u^{(k)} + \left(\sum_{m=1}^{M} R_{mx} a_m + \sum_{n=1}^{N} P_{nx} b_n \right) v^{(k)} \right]\end{aligned} \tag{5.13c}$$

$$\int_{\Gamma_l} \tau_{yx} n_x^l d\Gamma = \int_{\Gamma_l} n_x^l G \left(\frac{\partial u}{\partial y} + \frac{\partial v}{\partial x} \right) d\Gamma$$
$$= n_x^l G \sum_{k=1}^{K} \left[\left(\sum_{m=1}^{M} R_{my} a_m + \sum_{n=1}^{N} P_{ny} b_n \right) u^{(k)} + \left(\sum_{m=1}^{M} R_{mx} a_m + \sum_{n=1}^{N} P_{nx} b_n \right) v^{(k)} \right] \tag{5.13d}$$

For an arbitrary boundary shape of the local integral domain shown in Figure 5.2, boundary integrals

$$R_{mx} = \int_0^{S_l} \frac{\partial R_m}{\partial x} ds \tag{5.14a}$$

$$R_{my} = \int_0^{S_l} \frac{\partial R_m}{\partial y} ds \tag{5.14b}$$

$$P_{nx} = \int_0^{S_l} \frac{\partial P_n}{\partial x} ds \tag{5.14c}$$

$$P_{ny} = \int_0^{S_l} \frac{\partial P_n}{\partial y} ds \tag{5.14d}$$

where $R_m = \sqrt{c_0^2 + (x - x_k)^2 + (y - y_k)^2}$ and $P_n = \{1, x, y, x^2, xy, y^2\}$.

Analytical solutions of boundary integrals in closed form can be found in [153], in which $n_x^l = \sin\beta_l$, $n_y^l = -\cos\beta_l$, and

$$\begin{aligned} R_{mx} =& (r_2 - r_1)\cos\beta_l \\ & - \left[\left(x_a^l - x_k \right) \sin\beta_l - \left(y_a^l - y_k \right) \cos\beta_l \right] \sin\beta_l \ln \frac{D_1}{D_2} \end{aligned} \tag{5.15a}$$

$$\begin{aligned} R_{my} =& (r_2 - r_1)\sin\beta_l \\ & - \left[\left(y_a^l - y_k \right) \cos\beta_l - \left(x_a^l - x_k \right) \sin\beta_l \right] \cos\beta_l \ln \frac{D_1}{D_2} \end{aligned} \tag{5.15b}$$

$$r_1 = \sqrt{c^2 + \left(x_a^l - x_k\right)^2 + \left(y_a^l - y_k\right)^2} \tag{5.15c}$$

$$r_2 = \sqrt{c^2 + \left(x_b^l - x_k\right)^2 + \left(y_b^l - y_k\right)^2} \tag{5.15d}$$

$$D_1 = \left(x_a^l - x_k\right)\cos\beta_l + \left(y_a^l - y_k\right)\sin\beta_l + r_1 \tag{5.15e}$$

$$D_2 = \left(x_b^l - x_k\right)\cos\beta_l + \left(y_b^l - y_k\right)\sin\beta_l + r_2 \tag{5.15f}$$

And the polynomial terms

$$P_{1x} = P_{3x} = P_{6x} = 0 \tag{5.16a}$$

$$P_{2x} = s, \tag{5.16b}$$

$$P_{4x} = 2x_a^l s + s^2\cos\beta_l \tag{5.16c}$$

$$P_{5x} = y_a^l s + \frac{s^2\sin\beta_l}{2} \tag{5.16d}$$

$$P_{1y} = P_{2y} = P_{4y} = 0 \tag{5.16e}$$

$$P_{3y} = s, \tag{5.16f}$$

$$P_{6y} = 2y_a^l s + s^2\sin\beta_l \tag{5.16g}$$

$$P_{5y} = x_a^l s + \frac{s^2\cos\beta_l}{2} \tag{5.16h}$$

$$s = \sqrt{\left(x_b^l - x_a^l\right)^2 + \left(y_b^l - y_a^l\right)^2} \tag{5.16i}$$

Substitute (5.13) into (5.11), we can obtain a set of discretized eqtions as

$$\begin{aligned}
&\sum_{l=1}^{L}\sum_{k=1}^{K}\left[n_x^l E'\left(\sum_{m=1}^{M} R_{mx}a_m + \sum_{n=1}^{N} P_{nx}b_n\right)u^{(k)}\right.\\
&\qquad\left. + \mu n_x^l E'\left(\sum_{m=1}^{M} R_{my}a_m + \sum_{n=1}^{N} P_{ny}b_n\right)v^{(k)}\right] +\\
&\sum_{l=1}^{L}\sum_{k=1}^{K}\left[n_y^l G\left(\sum_{m=1}^{M} R_{my}a_m + \sum_{n=1}^{N} P_{ny}b_n\right)u^{(k)}\right.\\
&\qquad\left. + n_y^l G\left(\sum_{m=1}^{M} R_{mx}a_m + \sum_{n=1}^{N} P_{nx}b_n\right)v^{(k)}\right] = 0
\end{aligned} \tag{5.17a}$$

$$\begin{aligned}
&\sum_{l=1}^{L}\sum_{k=1}^{K}\left[n_y^l E'\left(\sum_{m=1}^{M} R_{my}a_m + \sum_{n=1}^{N} P_{ny}b_n\right)v^{(k)}\right.\\
&\qquad\left. + \mu n_y^l E'\left(\sum_{m=1}^{M} R_{mx}a_m + \sum_{n=1}^{N} P_{nx}b_n\right)u^{(k)}\right] +\\
&\sum_{l=1}^{L}\sum_{k=1}^{K}\left[n_x^l G\left(\sum_{m=1}^{M} R_{my}a_m + \sum_{n=1}^{N} P_{ny}b_n\right)u^{(k)}\right.\\
&\qquad\left. + n_x^l G\left(\sum_{m=1}^{M} R_{mx}a_m + \sum_{n=1}^{N} P_{nx}b_n\right)v^{(k)}\right] = 0
\end{aligned} \tag{5.17b}$$

which can be rearrange as

$$\begin{aligned}
&\sum_{k=1}^{K} u^{(k)} \sum_{l=1}^{L}\left[\sum_{m=1}^{M}\left(n_x^l E' R_{mx} + n_y^l G R_{my}\right)a_m\right.\\
&\qquad\left. + \sum_{n=1}^{N}\left(n_x^l E' P_{nx} + n_y^l G P_{ny}\right)b_n\right] +\\
&\sum_{k=1}^{K} v^{(k)} \sum_{l=1}^{L}\left[\sum_{m=1}^{M}\left(\mu n_x^l E' R_{my} + n_y^l G R_{mx}\right)a_m\right.\\
&\qquad\left. + \sum_{n=1}^{N}\left(\mu n_x^l E' P_{ny} + n_y^l G P_{nx}\right)b_n\right] = 0
\end{aligned} \tag{5.18a}$$

$$\begin{aligned}
&\sum_{k=1}^{K} u^{(k)} \sum_{l=1}^{L} \left[\sum_{m=1}^{M} \left(\mu n_y^l E' R_{mx} + n_x^l G R_{mx} \right) a_m \right. \\
&\qquad \left. + \sum_{n=1}^{N} \left(\mu n_y^l E' P_{nx} + n_x^l G P_{ny} \right) b_n \right] + \\
&\sum_{k=1}^{K} v^{(k)} \sum_{l=1}^{L} \left[\sum_{m=1}^{M} \left(n_y^l E' R_{my} + n_x^l G R_{mx} \right) a_m \right. \\
&\qquad \left. + \sum_{n=1}^{N} \left(n_y^l E' P_{ny} + n_x^l G P_{nx} \right) b_n \right] = 0
\end{aligned} \tag{5.18b}$$

Traction boundary conditions can be introduced based upon (5.10) as

$$\int_{\Gamma - \Gamma_T} t_i d\Gamma = - \int_{\Gamma_T} t_i^0 d\Gamma \quad \text{for } \mathbf{x}_k \quad k = 1, 2, \ldots, M_T \tag{5.19}$$

And the displacement boundary conditions can be imposed straightway as

$$u_i(\mathbf{x}_k) = u_i^0 \quad \text{for } \mathbf{x}_k \quad k = 1, 2, \ldots, M_D \tag{5.20}$$

where M_D is the number of nodes located on the displacement boundary, and M_T is number of nodes located on the traction boundary.

5.4 Numerical Examples

In this section, LIEM is employed to solve 2D elastostatic problems. The local support domain is selected as a circle of radius r_0 centred at field points **x**, in which the minimum number of nodes $K \geq K_0$. It has been reported that the reasonable value of K_0 should be $8 \leq K_0 \leq 25$ [153]. Therefore, $K_0 = 12$ is taken for all examples followed. LIEM solutions are compared with Abaqus and PCM results.

5.4.1 A Square Panel under Uniform Displacement

A square panel subjected to a uniformly distributed displacement as shown in Figure 5.3 is analysed. The side $a = 5cm$ and the plate is fixed at $x = 0$. A prescribed displacement $u^0 = 0.001cm$ is applied along the edge $x = 5cm$. Material constants are : Young's modulus $E = 2.1 \times 10^6 N/cm^2$, Poisson ratio $\mu = 0.2$.

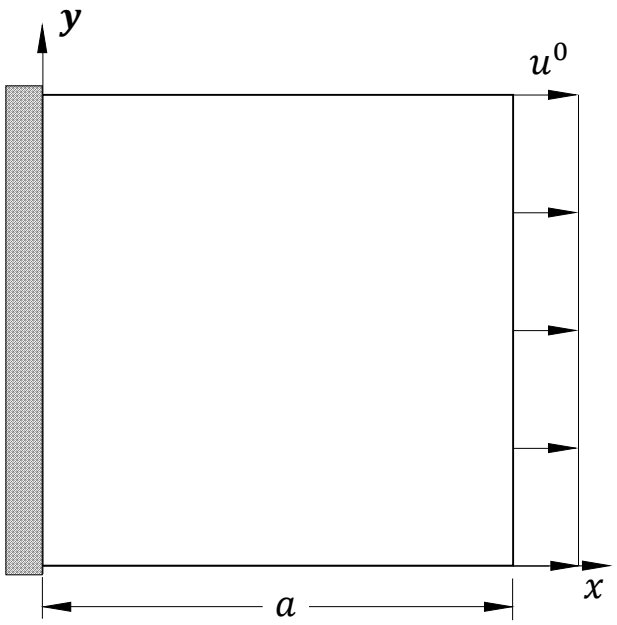

Figure 5.3: *A square panel subjected to a uniformly distributed displacement.*

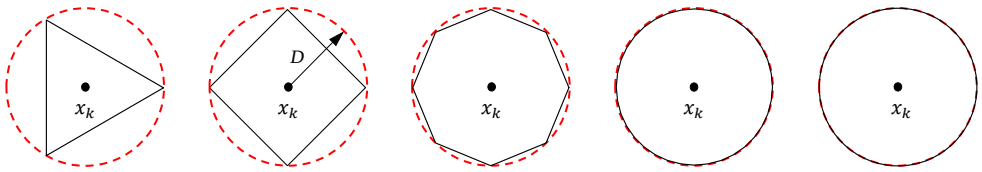

Figure 5.4: *Local integral domains enclosed by different number of straight lines.*

Table 5.1: *Strains ε_{xx} obtained by different L and D at point (0.0, 2.5)*

D/Δ	$L = 3(Errors)$	$L = 4(Errors)$	L=8 (Errors)	$L = 36(Errors)$	$L = 128(Errors)$
0.1	1.84188E-04 (0.19856%)	1.84016E-04 (0.10499%)	1.84167E-04 (0.18714%)	1.84164E-04 (0.18550%)	1.84164E-04 (0.18550%)
0.2	1.84111E-04 (0.15667%)	1.84098E-04 (0.14960%)	1.84084E-04 (0.14198%)	1.84079E-04 (0.13926%)	1.84079E-04 (0.13926%)
0.3	1.84067E-04 (0.13274%)	1.84051E-04 (0.12403%)	1.84033E-04 (0.11424%)	1.84026E-04 (0.11043%)	1.84026E-04 (0.11043%)
0.4	1.84036E-04 (0.11587%)	1.84178E-04 (0.19312%)	1.83993E-04 (0.09248%)	1.83985E-04 (0.08813%)	1.83985E-04 (0.08813%)
0.5	1.84011E-04 (0.10227%)	1.83986E-04 (0.08867%)	1.83958E-04 (0.07344%)	1.83948E-04 (0.06800%)	1.83948E-04 (0.06800%)
0.6	1.83988E-04 (0.08976%)	1.83958E-04 (0.07344%)	1.83924E-04 (0.05494%)	1.83913E-04 (0.04896%)	1.83912E-04 (0.04842%)
0.7	1.83967E-04 (0.07834%)	1.83929E-04 (0.05766%)	1.83891E-04 (0.03699%)	1.83878E-04 (0.02992%)	1.83877E-04 (0.02938%)
0.8	1.83945E-04 (0.06637%)	1.83899E-04 (0.04134%)	1.83858E-04 (0.01904%)	1.83844E-04 (0.01142%)	1.83843E-04 (0.01088%)
0.9	1.83924E-04 (0.05494%)	1.83869E-04 (0.02502%)	1.83825E-04 (0.00109%)	1.83817E-04 (0.00326%)	1.83817E-04 (0.00326%)
1.0	1.83904E-04 (0.04406%)	1.83841E-04 (0.00979%)	1.83601E-04 (0.12077%)	2.18725E-04 (18.98674%)	-3.96764E-05 (121.58402%)

The local integral domain enclosed by different number of straight lines are presented in Figure 5.4, in which D is the radius of the local integral domain. The strain ε_{xx} at point $(0.0, 2.5)$ obtained by using different number of L and D are listed in Table 5.1 . In this case, Abaqus solution $\varepsilon_{xx}(0.0, 2.5) = 1.83823 \times 10^{-4}$ is regarded as the benchmark and the problem domain is represented by 21×21 nodes that regularly and evenly distribute. Overall, the influence of L and D is insignificant except the situation when $D = \Delta$ and large number of L is used.

The convergence of LIEM is also observed with parameters $L = 36$ and $D/\Delta = 0.5$. Solutions obtained by different densities of field nodes are presented in Table 5.2. It can be seen clearly that strain values converge rapidly when the number of nodes increases. However, the CPU time goes up as well with the rise of node densities and a large amount of time have spent on solving the discretized system equations.

Table 5.2: *Strains ε_{xx} obtained with $L = 36$ and $D/\Delta = 0.5$ for different densities of field nodes at point (0.0, 2.5)*

M	11×11	21×21	31×31	41×41
ε_{xx}	1.85152E-04	1.83948E-04	1.83818E-04	1.83791E-04
Errors (%)	0.72298	0.06800	0.00272	0.01741

Then, the computing time for PCM and LIEM to obtain $\varepsilon_{xx}(0.0, 2.5)$ are investigated. Free parameters used in both methods are listed in Table 5.3 , in which the numerical solutions as well as their errors, and the elapsed real time are presented as well. It is found that the application of closed form LIEM improves the computational efficiency significantly, and it achieves an accurate solution without a high density of field nodes. Conversely, PCM requires more field nodes to get the same precision and it is time demanding.

Table 5.3: *Elapsed real time for calculating* $\varepsilon_{xx}(0.0, 2.5)$ *by LIEM and PCM*

Method	Field nodes	K_0	c_0	L	D/Δ	ε_{xx}(Error)	Elapsed real time (Second)
LIEM	31×31	10	Δ	8	0.5	1.83820E-04	8.617
						(0.00163%)	
PCM	41×41	6	2Δ			1.83826E-04	49.962
						(0.00163%)	

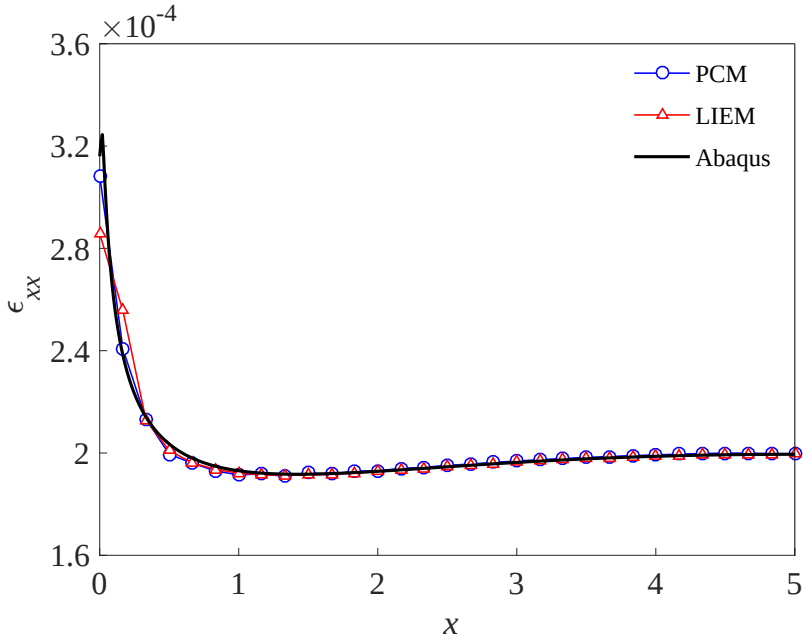

Figure 5.5: *Distribution of ε_{xx} versus x at $y = 0.019cm$.*

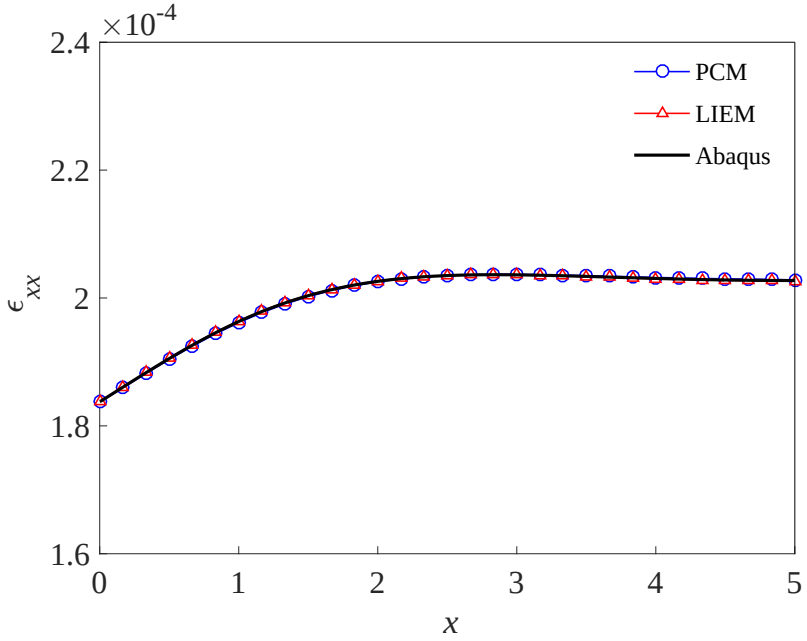

Figure 5.6: *Distribution of ε_{xx} versus x at $y = 2.519cm$.*

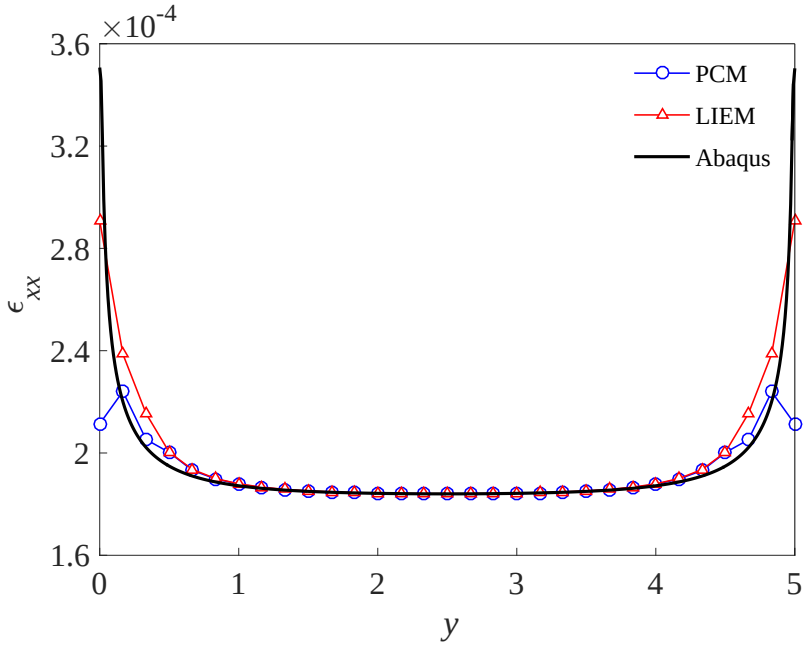

Figure 5.7: *Distribution of ε_{xx} versus y at $x = 0.019cm$.*

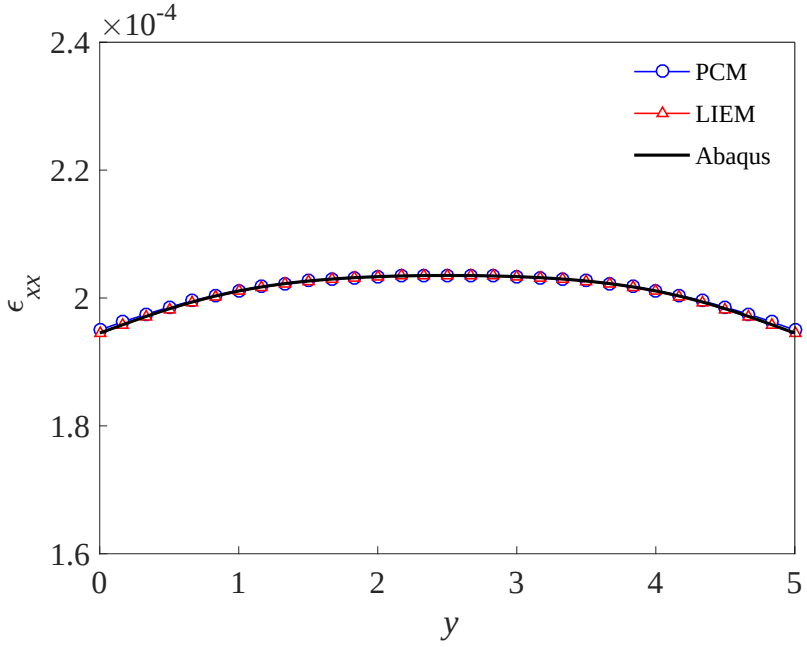

Figure 5.8: *Distribution of ε_{xx} versus y at $x = 2.519cm$.*

Finally, in order to demonstrate the accuracy of LIEM, strain distribution ε_{xx} along $y = 0.019cm$, $y = 2.519cm$ and $x = 0.019cm$, $x = 2.519cm$ are plotted in Figure 5.5 to Figure 5.8 with parameters $L = 36$, $D/\Delta = 0.5$ and 31×31 field nodes. Abaqus and PCM results obtained in the last Chapter are also reported for comparisons. It shows that solutions around geometrical boundaries improve greatly when LIEM is utilized, which validates the accuracy of LIEM indirectly.

5.4.2 A Square Board with a Circle Hole under Tensile Stress

A square board of width $2b$ containing a circle hole of radius a (where $a = b/2$) subjected to a uniformly distributed tensile stress σ_0 on top and bottom shown in Figure 5.9 is observed. Only one-quarter of the plate is studied because of symmetry. Young's modulus $E = 1.0$ and Poisson ratio $\mu = 0.3$. The total number of field nodes is 1364, and free parameters are selected as $L = 8$, $D/\Delta = 0.5$.

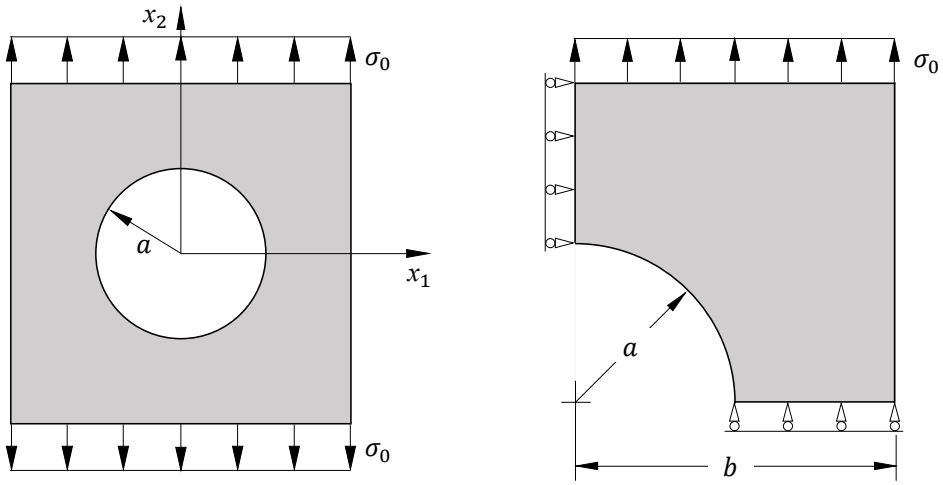

Figure 5.9: *A square board containing a circle hole subjected to tensile load: (a) geometry; (b) a quarter of the plate.*

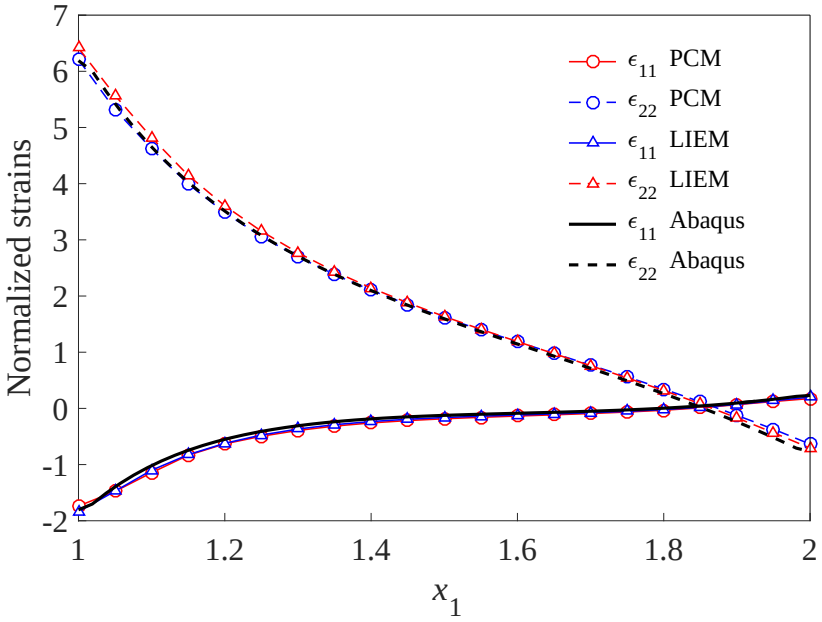

Figure 5.10: *Strain variations along axis x_1 for a square board with a circle hole under tensile load.*

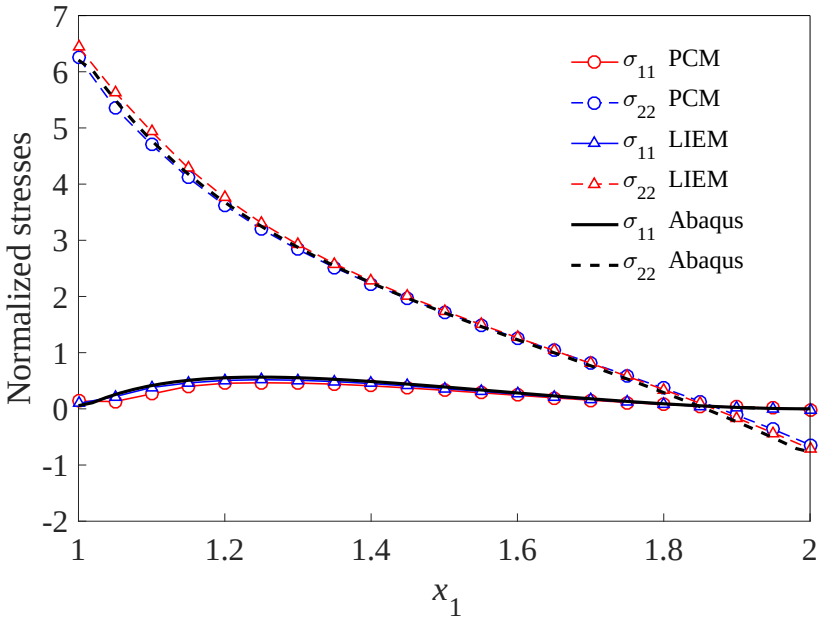

Figure 5.11: *Stress variations along axis x_1 for a square board with a circle hole under tensile load.*

LIEM results involve the distribution of strains and stresses along axis x_1 are plotted in Figure 5.10 and Figure 5.11, respectively. While Abaqus and PCM solutions are presented as well for the sake of comparisons. Good agreements have been achieved even though very small gaps can be found in the distribution of ε_{22} and σ_{22} nearby geometrical boundaries.

5.4.3 A Disk under Internal Pressure

A disk subjected to an internal pressure is investigated with dimensions $a = 1cm$, $b = 2cm$ as shown in Figure 5.12(a) and only a quarter of the disk is considered in this example, see Figure 5.12(b). Young's modulus $E = 1.0$ and Poisson ratio $\mu = 0.3$. The total number of field nodes is 989.

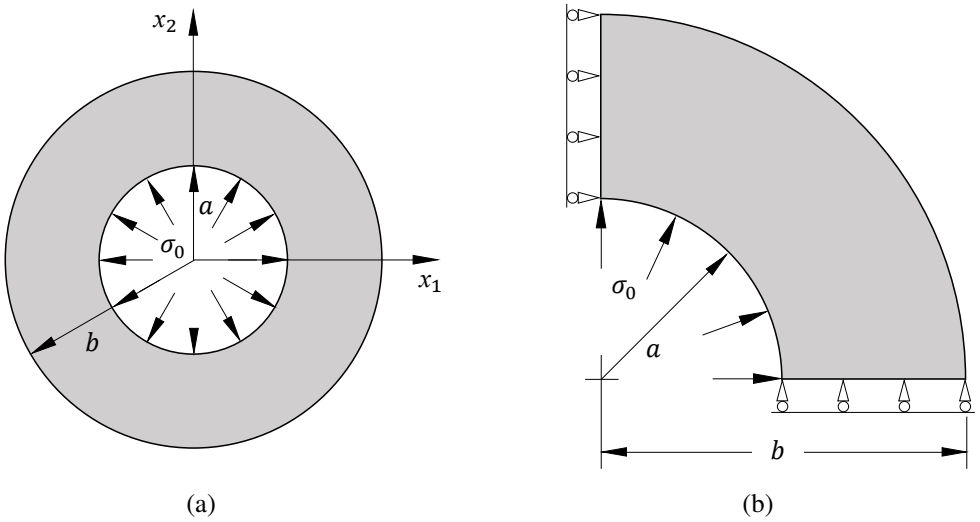

Figure 5.12: *A disk subjected to internal pressure: (a) geometry; (b) a quarter of the disk.*

The distribution of strains and stresses along axis x_1 are plotted in Figure 5.13 and Figure 5.14 respectively with free parameters $L = 8$, $D/\Delta = 0.5$. Comparisons have been made with Abaqus and PCM solutions, which show great convergence and again demonstrate the accuracy of LIEM.

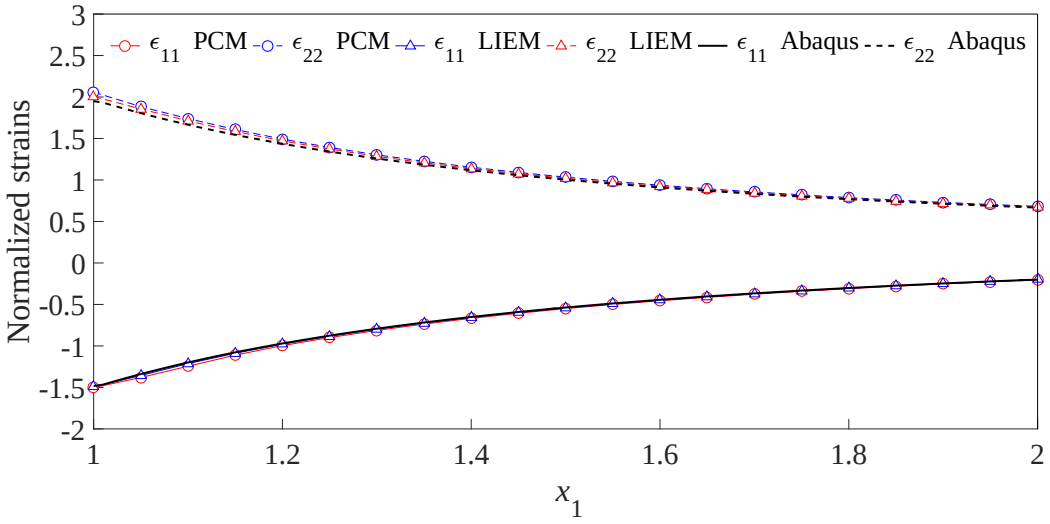

Figure 5.13: *Strain variations along axis x_1 for a ring under interior pressure.*

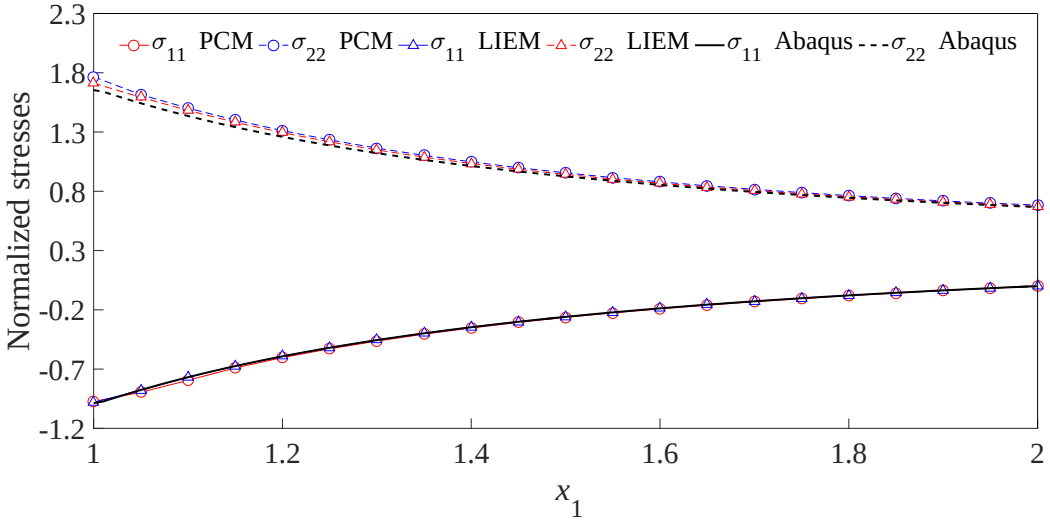

Figure 5.14: *Stress variations along axis x_1 for a ring under interior pressure.*

5.5 Conclusions

In this chapter, mathematical procedures of LIEM are presented for 2D solids. By use of the MQ RBF approximation, analytical solutions for domain integrals are derived. Three numerical examples are carried out and the following conclusions are obtained:

(1) Investigations with respect to the number of straight lines that enclose the local integral domain and the radius of the local integral domain indicate that they have slight effects on numerical solutions.

(2) When the densities of nodes located in the problem domain increases, numerical solutions of LIEM converge rapidly and only a little time is required to compute the coefficient matrix. However, it takes time for solving the discretized algebraic equations.

(3) The employment of analytical formulations of domain integrals improves the computational efficiency greatly, and PCM takes more time to achieve the same accuracy compared with LIEM.

(4) LIEM solutions for solid mechanics problems are accurate and convergent when appropriate parameters are chosen.

CHAPTER 6

Meshless Methods for Nonlocal Elastostatics

6.1 Introduction

Classical continuum mechanics is a local theory that involves a certain degree of inherent limitation because it ignores the long rang force in real materials. Therefore, nonlocal theories framed in the realm of continuum theories have been promising to model and simulate material properties exhibited at micro-, and even, at nano-scale levels. It should be a sufficient motivation for research work oriented to nonlocal theories.

The application of nonlocal theories has been extended to various aspects showing the ability to interpret and predict material physical properties at microscopic scales. Some recent examples include the gradient enhanced damage for quasi-brittle material [156], propagation of Rayleigh surface waves with small wavelengths in nonlocal solids[157], crack problems in piezoelectric materials and functionally graded materials [22, 158], and moreover, the bending, buckling and free vibration of nanobeams [32]. Above quoted references have successfully presented

the positive signs of nonlocal theories in explaining size effects.

However, nonlocal problems are complex to solve analytically even for a simple 1D issue. Therefore, numerical approaches are increasing used to resolve the dilemmas. A numerical method based on FEM has been proposed and employed to address 2D nonlocal elastic problems with a nonlocal stiffness matrix indicating the nonlocal characteristics [43]. The nonlocal Timoshenko nanobeams were investigated numerically by means of meshless collocation technique with RBF approximation schemes [49]. Additionally, Wen and Huang have applied PCM to the nonlocal elastic sphere and figured out solutions with high accuracy [52]. And, LIEM has been employed to address 2D nonlocal elastostatic mechanical cases and fracture problems [51, 53].

In this chapter, meshless methods including PCM and LIEM are employed to address nonlocal elastostatic problems respectively based on the Eringen's model. Formulations related to 2D nonlocal problems are reported and then numerical examples are carried out. Comparisons between solutions obtained form different methods are made and the feasibility and effectiveness of meshless methods for solving nonlocal static problems are validated.

6.2 Eringen's Model

A leap has been provided in extending nonlocal theories to practical problems since the simplified nonlocal elastic theories were promising for linear homogeneous isotropic media by the work of Eringen and co-workers [17], in which only the stress and strain relationship is regarded as nonlocality and characterized by an attenuation function. Its constitutive relation is in the form of

$$\sigma(\mathbf{x}) = \int_V \alpha(\mathbf{x}, \mathbf{x}', l)\mathbf{D}\varepsilon(\mathbf{x}')dV(\mathbf{x}') = \int_V \alpha(\mathbf{x}, \mathbf{x}', l)\bar{\sigma}(\mathbf{x}')dV(\mathbf{x}') \tag{6.1}$$

where V denotes the domain volume; l is the characteristic length; $\mathbf{x}$ is the collocation point and $\mathbf{x}'$ is the domain integration point; $\bar{\sigma}$ and ε are vectors of classical (local) stress and strain, respectively; $\mathbf{D}$ represents the elastic moduli matrix; α is the nonlocal kernel defined as a function of the ratio $|\mathbf{x}\text{-}\ \mathbf{x}'|^2/l$; σ is referred to as nonlocal stress, which is expressed as a weighted value of the local strain ε.

A variant integral model considering the stress as a weighted summation of the classical and nonlocal stress is the most prevailing one [159]. Its constitutive relation is:

$$\sigma(\mathbf{x}) = \xi_1 \bar{\sigma}(\mathbf{x}) + \xi_2 \int_V \alpha(\mathbf{x}, \mathbf{x}', l) \bar{\sigma}(\mathbf{x}') dV(\mathbf{x}') \tag{6.2}$$

The above equation considers the nonlocal elastic material as a two-phase material that involves the local elasticity with portion factor ξ_1 and the nonlocal elasticity with portion factor ξ_2, where ξ_1 and ξ_2 are positive constants and $\xi_1 + \xi_2 = 1$.

The functional form of the nonlocal kernel $\alpha(\mathbf{x}, \mathbf{x}', l)$ is still a controversial problem. However, it is clear that the nonlocal kernel has to follow some general conditions[160], e.g., reaching its maximum at $\mathbf{x} = \mathbf{x}'$ but attenuating rapidly with the increase of distances $|\mathbf{x}\text{-}\ \mathbf{x}'|$, and must satisfy the normalization condition over the infinite integration domain so that its integral gives unity as

$$\int_{V_\infty} \alpha\left(|\mathbf{x} - \mathbf{x}'|^2/l\right) dV' = 1 \tag{6.3}$$

in which V_∞ indicates the infinite domain embedding V. In practice, for simplicity, the nonlocal kernel is usually of Gaussian form as ,

$$\alpha\left(\mathbf{x}, \mathbf{x}', l\right) = \frac{1}{2\pi l^2} \exp\left(-|\mathbf{x} - \mathbf{x}'|^2/l\right) \tag{6.4}$$

6.3 PCM for Nonlocal Elastostatics (NL-PCM)

Recalling Hook's law, the stress components in the context of nonlcoal elasticity can be derived easily based upon (6.2), for 2D plane-stress problems, as

$$\begin{aligned}\sigma_{xx}(\mathbf{x}) =&\xi_1\left[E'\left(\frac{\partial u(\mathbf{x})}{\partial x}+\mu\frac{\partial v(\mathbf{x})}{\partial y}\right)\right]+\\ &\xi_2\int_V\alpha(\mathbf{x},\mathbf{x}',l)\left[E'\left(\frac{\partial u(\mathbf{x}')}{\partial x'}+\mu\frac{\partial v(\mathbf{x}')}{\partial y'}\right)\right]dV(\mathbf{x}')\end{aligned} \tag{6.5a}$$

$$\begin{aligned}\sigma_{yy}(\mathbf{x}) =&\xi_1\left[E'\left(\frac{\partial v(\mathbf{x})}{\partial y}+\mu\frac{\partial u(\mathbf{x})}{\partial x}\right)\right]+\\ &\xi_2\int_V\alpha(\mathbf{x},\mathbf{x}',l)\left[E'\left(\frac{\partial v(\mathbf{x}')}{\partial y'}+\mu\frac{\partial u(\mathbf{x}')}{\partial x'}\right)\right]dV(\mathbf{x}')\end{aligned} \tag{6.5b}$$

$$\begin{aligned}\tau_{xy}(\mathbf{x}) =&\xi_1\left[G\left(\frac{\partial u(\mathbf{x})}{\partial y}+\frac{\partial v(\mathbf{x})}{\partial x}\right)\right]+\\ &\xi_2\int_V\alpha(\mathbf{x},\mathbf{x}',l)\left[G\left(\frac{\partial u(\mathbf{x}')}{\partial y'}+\frac{\partial v(\mathbf{x}')}{\partial x'}\right)\right]dV(\mathbf{x}')\end{aligned} \tag{6.5c}$$

The equilibrium equation for 2D isotropic solids is expressed as

$$\sigma_{ij,j}+f_i=0 \tag{6.6}$$

Substitute stress components in (6.5) into (6.6), we have

$$\begin{aligned}&\xi_1\left[E'\left(\frac{\partial^2 u(\mathbf{x})}{\partial x^2}+\mu\frac{\partial^2 v(\mathbf{x})}{\partial x\partial y}\right)\right]+\\ &\xi_2\frac{\partial\int_V\alpha(\mathbf{x},\mathbf{x}',l)}{\partial x}\left[E'\left(\frac{\partial u(\mathbf{x}')}{\partial x'}+\mu\frac{\partial v(\mathbf{x}')}{\partial y'}\right)\right]dV(\mathbf{x}')+\\ &\xi_1\left[G\left(\frac{\partial^2 u(\mathbf{x})}{\partial y^2}+\frac{\partial^2 v(\mathbf{x})}{\partial x\partial y}\right)\right]+\\ &\xi_2\frac{\partial\int_V\alpha(\mathbf{x},\mathbf{x}',l)}{\partial y}\left[G\left(\frac{\partial u(\mathbf{x}')}{\partial y'}+\frac{\partial v(\mathbf{x}')}{\partial x'}\right)\right]dV(\mathbf{x}')=0\end{aligned} \tag{6.7a}$$

$$
\begin{aligned}
&\xi_1 \left[E' \left(\frac{\partial^2 v(\mathbf{x})}{\partial y^2} + \mu \frac{\partial^2 u(\mathbf{x})}{\partial x \partial y} \right) \right] + \\
&\xi_2 \frac{\partial \int_V \alpha(\mathbf{x}, \mathbf{x}', l)}{\partial y} \left[E' \left(\frac{\partial v(\mathbf{x}')}{\partial y'} + \mu \frac{\partial u(\mathbf{x}')}{\partial x'} \right) \right] dV(\mathbf{x}') + \\
&\xi_1 \left[G \left(\frac{\partial^2 u(\mathbf{x})}{\partial x \partial y} + \frac{\partial^2 v(\mathbf{x})}{\partial x^2} \right) \right] + \\
&\xi_2 \frac{\partial \int_V \alpha(\mathbf{x}, \mathbf{x}', l)}{\partial x} \left[G \left(\frac{\partial u(\mathbf{x}')}{\partial y'} + \frac{\partial v(\mathbf{x}')}{\partial x'} \right) \right] dV(\mathbf{x}') = 0
\end{aligned}
\tag{6.7b}
$$

Equations above can be rearranged as following:

$$
\begin{aligned}
&\xi_1 \left(E' \frac{\partial^2 u(\mathbf{x})}{\partial x^2} + G \frac{\partial^2 u(\mathbf{x})}{\partial y^2} \right) + \\
&\xi_2 \left(\int_V \frac{\partial \alpha(\mathbf{x}, \mathbf{x}', l)}{\partial x} E' \frac{\partial u(\mathbf{x}')}{\partial x'} + \int_V \frac{\partial \alpha(\mathbf{x}, \mathbf{x}', l)}{\partial y} G \frac{\partial u(\mathbf{x}')}{\partial y'} \right) dV(\mathbf{x}') + \\
&\xi_1 \left(E' \mu \frac{\partial^2 v(\mathbf{x})}{\partial x \partial y} + G \frac{\partial^2 v(\mathbf{x})}{\partial x \partial y} \right) + \\
&\xi_2 \left(\int_V \frac{\partial \alpha(\mathbf{x}, \mathbf{x}', l)}{\partial x} E' \mu \frac{\partial v(\mathbf{x}')}{\partial y'} + \int_V \frac{\partial \alpha(\mathbf{x}, \mathbf{x}', l)}{\partial y} G \frac{\partial v(\mathbf{x}')}{\partial x'} \right) dV(\mathbf{x}') = 0
\end{aligned}
\tag{6.8a}
$$

$$
\begin{aligned}
&\xi_1 \left(E' \mu \frac{\partial^2 u(\mathbf{x})}{\partial x \partial y} + G \frac{\partial^2 u(\mathbf{x})}{\partial x \partial y} \right) + \\
&\xi_2 \left(\int_V \frac{\partial \alpha(\mathbf{x}, \mathbf{x}', l)}{\partial y} E' \mu \frac{\partial u(\mathbf{x}')}{\partial x'} + \int_V \frac{\partial \alpha(\mathbf{x}, \mathbf{x}', l)}{\partial x} G \frac{\partial u(\mathbf{x}')}{\partial y'} \right) dV(\mathbf{x}') + \\
&\xi_1 \left(E' \frac{\partial^2 v(\mathbf{x})}{\partial y^2} + G \frac{\partial^2 v(\mathbf{x})}{\partial x^2} \right) + \\
&\xi_2 \left(\int_V \frac{\partial \alpha(\mathbf{x}, \mathbf{x}', l)}{\partial y} E' \frac{\partial v(\mathbf{x}')}{\partial y'} + \int_V \frac{\partial \alpha(\mathbf{x}, \mathbf{x}', l)}{\partial x} G \frac{\partial v(\mathbf{x}')}{\partial x'} \right) dV(\mathbf{x}') = 0
\end{aligned}
\tag{6.8b}
$$

Assume that the 2D problem domain is represented by a set of randomly distributed nodes. The locally supported RPIM-MQ shape function presented in Chapter 3 is employed to carry out the meshfree approximations. Then equations in (6.8) are discretized directly by collocating at field nodes. Finally, system equations of PCM with respect to nonlocal elastostatics, which can be referred to as NL-PCM,

are obtained as

$$\begin{aligned}
&\xi_1 \sum_{k=1}^{K} u^{(k)} \left(E' \phi_{k,xx} + G \phi_{k,yy}\right) + \\
&\xi_2 \sum_{k'=1}^{K'} u^{(k')} \left(\int_V \alpha(\mathbf{x}, \mathbf{x}', l)_{,x} E' \phi_{k',x'} + \int_V \alpha(\mathbf{x}, \mathbf{x}', l)_{,y} G \phi_{k',y'} \right) dV(\mathbf{x}') + \\
&\xi_1 \sum_{k=1}^{K} v^{(k)} \left(E' \mu \phi_{k,xy} + G \phi_{k,xy}\right) + \\
&\xi_2 \sum_{k'=1}^{K'} v^{(k')} \left(\int_V \alpha(\mathbf{x}, \mathbf{x}', l)_{,x} E' \mu \phi_{k',y'} + \int_V \alpha(\mathbf{x}, \mathbf{x}', l)_{,y} G \phi_{k',x'} \right) dV(\mathbf{x}') = 0
\end{aligned} \tag{6.9a}$$

$$\begin{aligned}
&\xi_1 \sum_{k=1}^{K} u^{(k)} \left(E' \mu \phi_{k,xy} + G \phi_{k,xy}\right) + \\
&\xi_2 \sum_{k'=1}^{K'} u^{(k')} \left(\int_V \alpha(\mathbf{x}, \mathbf{x}', l)_{,y} E' \mu \phi_{k',x'} + \int_V \alpha(\mathbf{x}, \mathbf{x}', l)_{,x} G \phi_{k',y'} \right) dV(\mathbf{x}') + \\
&\xi_1 \sum_{k=1}^{K} v^{(k)} \left(E' \phi_{k,yy} + G \phi_{k,xx}\right) + \\
&\xi_2 \sum_{k'=1}^{K'} v^{(k')} \left(\int_V \alpha(\mathbf{x}, \mathbf{x}', l)_{,y} E' \phi_{k',y'} + \int_V \alpha(\mathbf{x}, \mathbf{x}', l)_{,x} G \phi_{k',x'} \right) dV(\mathbf{x}') = 0
\end{aligned} \tag{6.9b}$$

in which $k = 1, 2, \ldots, K$ and $k' = 1, 2, \ldots, K'$ are the number of field nodes within the local support domain centred at point **x** and **x'**, respectively.

The domain integrals in (6.9) should be carried out by introducing a set of background grids as shown in Figure 6.1. The four-point standard scheme is employed and $\mathbf{x}'_p$ denotes the integral points in each sub integral volume ΔV_q, where

$$\Delta V_q = d_1 \times d_2 \tag{6.10}$$

and the coordinates of four sub integral points are

$$\mathbf{x}'_1 = \left(\frac{d_1}{2\sqrt{3}}, \quad \frac{d_2}{2\sqrt{3}}\right) \tag{6.11a}$$

$$\mathbf{x}'_2 = \left(-\frac{d_1}{2\sqrt{3}}, \quad \frac{d_2}{2\sqrt{3}}\right) \tag{6.11b}$$

$$\mathbf{x}'_3 = \left(-\frac{d_1}{2\sqrt{3}}, \quad -\frac{d_2}{2\sqrt{3}}\right) \tag{6.11c}$$

$$\mathbf{x}'_4 = \left(\frac{d_1}{2\sqrt{3}}, \quad -\frac{d_2}{2\sqrt{3}}\right) \tag{6.11d}$$

Therefore, the domain integral can be approximated as

$$\int_V \alpha(\mathbf{x}, \mathbf{x}', l) dV(\mathbf{x}') = \sum_{q=1}^{V} \sum_{p=1}^{4} \alpha(\mathbf{x}, \mathbf{x}'_p, l) \Delta V_q w_p \tag{6.12}$$

in which V is the number of sub integral domains and $w_p = 1/4$.

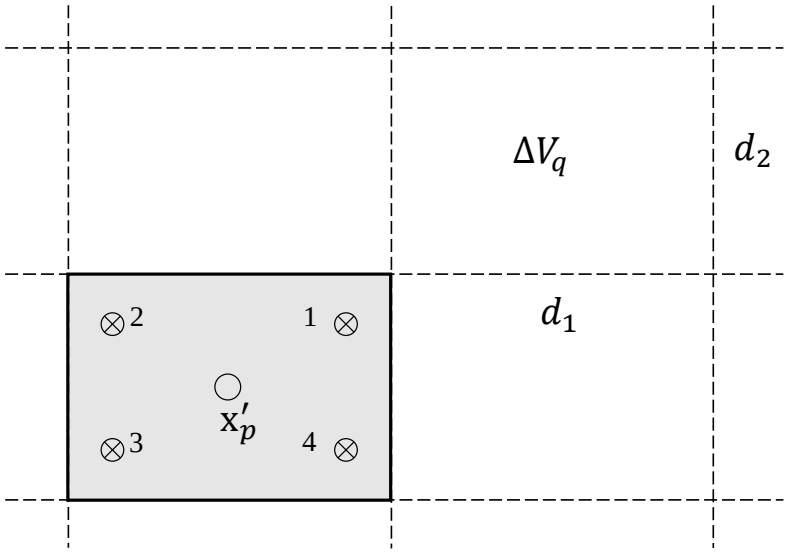

Figure 6.1: *Background grids and the four point standard scheme for domain integrals.*

Discretized equations of (6.9) can be derived by considering the domain integral approximation in (6.12) as

$$\begin{aligned}
&\xi_1 \sum_{k=1}^{K} u^{(k)} \left(E' \phi_{k,xx} + G \phi_{k,yy}\right) + \\
&\xi_2 \sum_{k'=1}^{K'} u^{(k')} \sum_{q=1}^{V} \sum_{p=1}^{4} \left(\alpha(\mathbf{x}, \mathbf{x'}_p, l)_{,x} E' \phi_{k',x'} + \alpha(\mathbf{x}, \mathbf{x'}_p, l)_{,y} G \phi_{k',y'}\right) \Delta V_q w_p + \\
&\xi_1 \sum_{k=1}^{K} v^{(k)} \left(E' \mu \phi_{k,xy} + G \phi_{k,xy}\right) + \\
&\xi_2 \sum_{k'=1}^{K'} v^{(k')} \sum_{q=1}^{V} \sum_{p=1}^{4} \left(\alpha(\mathbf{x}, \mathbf{x'}_p, l)_{,x} E' \mu \phi_{k',y'} + \alpha(\mathbf{x}, \mathbf{x'}_p, l)_{,y} G \phi_{k',x'}\right) \Delta V_q w_p = 0
\end{aligned} \tag{6.13a}$$

$$\begin{aligned}
&\xi_1 \sum_{k=1}^{K} u^{(k)} \left(E' \mu \phi_{k,xy} + G \phi_{k,xy}\right) + \\
&\xi_2 \sum_{k'=1}^{K'} u^{(k')} \sum_{q=1}^{V} \sum_{p=1}^{4} \left(\alpha(\mathbf{x}, \mathbf{x'}_p, l)_{,y} E' \mu \phi_{k',x'} + \alpha(\mathbf{x}, \mathbf{x'}_p, l)_{,x} G \phi_{k',y'}\right) \Delta V_q w_p + \\
&\xi_1 \sum_{k=1}^{K} v^{(k)} \left(E' \phi_{k,yy} + G \phi_{k,xx}\right) + \\
&\xi_2 \sum_{k'=1}^{K'} v^{(k')} \sum_{q=1}^{V} \sum_{p=1}^{4} \left(\alpha(\mathbf{x}, \mathbf{x'}_p, l)_{,y} E' \phi_{k',y'} + \alpha(\mathbf{x}, \mathbf{x'}_p, l)_{,x} G \phi_{k',x'}\right) \Delta V_q w_p = 0
\end{aligned} \tag{6.13b}$$

Displacement boundary conditions can be introduced directly as

$$u(\mathbf{x}_k) = u^0 \tag{6.14a}$$

$$v(\mathbf{x}_k) = v^0 \tag{6.14b}$$

where $k = 1, 2, \ldots, M_D$. u^0 and v^0 are specified displacements along x and y

directions.

While on traction boundaries, where tractions along x and y directions are prescribed, boundary conditions can be imposed as

$$\begin{aligned} t_x^0 &= l\left(\xi_1\bar{\sigma}_{xx}(\mathbf{x}) + \xi_2\int_V \alpha(\mathbf{x},\mathbf{x}',l)\bar{\sigma}_{xx}(\mathbf{x}')dV(\mathbf{x}')\right) \\ &+ m\left(\xi_1\bar{\tau}_{yx}(\mathbf{x}) + \xi_2\int_V \alpha(\mathbf{x},\mathbf{x}',l)\bar{\tau}_{yx}(\mathbf{x}')dV(\mathbf{x}')\right) \end{aligned} \tag{6.15a}$$

$$\begin{aligned} t_y^0 &= m\left(\xi_1\bar{\sigma}_{yy}(\mathbf{x}) + \xi_2\int_V \alpha(\mathbf{x},\mathbf{x}',l)\bar{\sigma}_{yy}(\mathbf{x}')dV(\mathbf{x}')\right) \\ &+ l\left(\xi_1\bar{\tau}_{xy}(\mathbf{x}) + \xi_2\int_V \alpha(\mathbf{x},\mathbf{x}',l)\bar{\tau}_{xy}(\mathbf{x}')dV(\mathbf{x}')\right) \end{aligned} \tag{6.15b}$$

which can be discretized as

$$\begin{aligned} &\xi_1\sum_{k=1}^{K} u^{(k)}\left(lE'\phi_{k,x} + mG\phi_{k,y}\right) + \\ &\xi_2\sum_{k'=1}^{K'} u^{(k')}\sum_{q=1}^{V}\sum_{p=1}^{4}\left(lE'\phi_{k',x'} + mG\phi_{k',y'}\right)\alpha(\mathbf{x},\mathbf{x'}_p,l)\Delta V_q w_p + \\ &\xi_1\sum_{k=1}^{K} v^{(k)}\left(\mu lE'\phi_{k,y} + mG\phi_{k,x}\right) + \\ &\xi_2\sum_{k'=1}^{K'} v^{(k')}\sum_{q=1}^{V}\sum_{p=1}^{4}\left(\mu lE'\phi_{k',y'} + mG\phi_{k',x'}\right)\alpha(\mathbf{x},\mathbf{x'}_p,l)\Delta V_q w_p = t_x^0 \end{aligned} \tag{6.16a}$$

$$\begin{aligned} &\xi_1\sum_{k=1}^{K} u^{(k)}\left(\mu mE'\phi_{k,x} + lG\phi_{k,y}\right) + \\ &\xi_2\sum_{k'=1}^{K'} u^{(k')}\sum_{q=1}^{V}\sum_{p=1}^{4}\left(\mu mE'\phi_{k',x'} + lG\phi_{k',y'}\right)\alpha(\mathbf{x},\mathbf{x'}_p,l)\Delta V_q w_p + \\ &\xi_1\sum_{k=1}^{K} v^{(k)}\left(mE'\phi_{k,y} + lG\phi_{k,x}\right) + \\ &\xi_2\sum_{k=1}^{K} v^{(k')}\sum_{q=1}^{V}\sum_{p=1}^{4}\left(mE'\phi_{k',y'} + lG\phi_{k',x'}\right)\alpha(\mathbf{x},\mathbf{x'}_p,l)\Delta V_q w_p = t_y^0 \end{aligned} \tag{6.16b}$$

6.4 LIEM for Nonlocal Elastostatics (NL-LIEM)

Consider a 2D problem domain shown in Figure 5.1 and the nonlocal constitutive relationship in (6.2), the local boundary integral equation in (5.11) becomes

$$\begin{aligned}
&\int_{\Gamma_s} \sigma_{ij}(\mathbf{x}) n_j(\mathbf{x}) d\Gamma(\mathbf{x}) \\
&= \sum_{l=1}^{L} n_j^l \int_{\Gamma_l} \left(\xi_1 \bar{\sigma}_{ij}(\mathbf{x}) + \xi_2 \int_V \alpha(\mathbf{x}, \mathbf{x}', l) \bar{\sigma}_{ij}(\mathbf{x}') dV(\mathbf{x}') \right) d\Gamma(\mathbf{x}) \\
&= \xi_1 \sum_{l=1}^{L} n_j^l \int_{\Gamma_l} \bar{\sigma}_{ij}(\mathbf{x}) d\Gamma(\mathbf{x}) + \xi_2 \sum_{l=1}^{L} n_j^l \Delta_l \int_V \alpha(\mathbf{x}, \mathbf{x}', l) \bar{\sigma}_{ij}(\mathbf{x}') dV(\mathbf{x}')
\end{aligned} \tag{6.17}$$

where Δ_l is the length of the l^{th} straight line that encloses the local integral domain.

Solutions of the local elasticity phase with portion factor ξ_1 can be easily obtained based on (5.18). Besides, by taking advantages of RPIM shape functions, in which

$$u(\mathbf{x}) = \sum_{k=1}^{K} \phi_k u_k \tag{6.18}$$

(6.17) can be overwritten in the form of

$$\begin{aligned}
&\xi_1 \sum_{k=1}^{K} u^{(k)} \sum_{l=1}^{L} \left[\sum_{m=1}^{M} \left(n_x^l E' R_{mx} + n_y^l G R_{my} \right) a_m + \sum_{n=1}^{N} \left(n_x^l E' P_{nx} + n_y^l G P_{ny} \right) b_n \right] + \\
&\xi_2 \sum_{l=1}^{L} \Delta_l \sum_{k'=1}^{K'} u^{(k')} \int_V \alpha(\mathbf{x}, \mathbf{x}', l) \left(n_x^l E' \phi_{k',x'} + n_y^l G \phi_{k',y'} \right) dV(\mathbf{x}') + \\
&\xi_1 \sum_{k=1}^{K} v^{(k)} \sum_{l=1}^{L} \left[\sum_{m=1}^{M} \left(\mu n_x^l E' R_{my} + n_y^l G R_{mx} \right) a_m + \sum_{n=1}^{N} \left(\mu n_x^l E' P_{ny} + n_y^l G P_{nx} \right) b_n \right] + \\
&\xi_2 \sum_{l=1}^{L} \Delta_l \sum_{k'=1}^{K'} v^{(k')} \int_V \alpha(\mathbf{x}, \mathbf{x}', l) \left(\mu n_x^l E' \phi_{k',y'} + n_y^l G \phi_{k',x'} \right) dV(\mathbf{x}') = 0
\end{aligned} \tag{6.19a}$$

$$\xi_1 \sum_{k=1}^{K} u^{(k)} \sum_{l=1}^{L} \left[\sum_{m=1}^{M} \left(\mu n_y^l E' R_{mx} + n_x^l G R_{my} \right) a_m + \sum_{n=1}^{N} \left(\mu n_y^l E' P_{nx} + n_x^l G P_{ny} \right) b_n \right] +$$
$$\xi_2 \sum_{l=1}^{L} \Delta_l \sum_{k'=1}^{K'} u^{(k')} \int_V \alpha(\mathbf{x}, \mathbf{x}', l) \left(\mu n_y^l E' \phi_{k',x'} + n_x^l G \phi_{k',y'} \right) dV(\mathbf{x}') +$$
$$\xi_1 \sum_{k=1}^{K} v^{(k)} \sum_{l=1}^{L} \left[\sum_{m=1}^{M} \left(n_y^l E' R_{my} + n_x^l G R_{mx} \right) a_m + \sum_{n=1}^{N} \left(n_y^l E' P_{ny} + n_x^l G P_{nx} \right) b_n \right] +$$
$$\xi_2 \sum_{l=1}^{L} \Delta_l \sum_{k'=1}^{K'} v^{(k')} \int_V \alpha(\mathbf{x}, \mathbf{x}', l) \left(n_y^l E' \phi_{k',y'} + n_x^l G \phi_{k',x'} \right) dV(\mathbf{x}') = 0 \tag{6.19b}$$

which can be rearranged as

$$\xi_1 \sum_{k=1}^{K} u^{(k)} \sum_{l=1}^{L} \left[\sum_{m=1}^{M} \left(n_x^l E' R_{mx} + n_y^l G R_{my} \right) a_m + \sum_{n=1}^{N} \left(n_x^l E' P_{nx} + n_y^l G P_{ny} \right) b_n \right] +$$
$$\xi_2 \sum_{k'=1}^{K'} u^{(k')} \int_V \left[\sum_{l=1}^{L} \Delta_l \left(n_x^l E' \phi_{k',x'} + n_y^l G \phi_{k',y'} \right) \alpha(\mathbf{x}, \mathbf{x}', l) \right] dV(\mathbf{x}') +$$
$$\xi_1 \sum_{k=1}^{K} v^{(k)} \sum_{l=1}^{L} \left[\sum_{m=1}^{M} \left(\mu n_x^l E' R_{my} + n_y^l G R_{mx} \right) a_m + \sum_{n=1}^{N} \left(\mu n_x^l E' P_{ny} + n_y^l G P_{nx} \right) b_n \right] +$$
$$\xi_2 \sum_{k'=1}^{K'} v^{(k')} \int_V \left[\sum_{l=1}^{L} \Delta_l \left(\mu n_x^l E' \phi_{k',y'} + n_y^l G \phi_{k',x'} \right) \alpha(\mathbf{x}, \mathbf{x}', l) \right] dV(\mathbf{x}') = 0 \tag{6.20a}$$

$$\xi_1 \sum_{k=1}^{K} u^{(k)} \sum_{l=1}^{L} \left[\sum_{m=1}^{M} \left(\mu n_y^l E' R_{mx} + n_x^l G R_{my} \right) a_m + \sum_{n=1}^{N} \left(\mu n_y^l E' P_{nx} + n_x^l G P_{ny} \right) b_n \right] +$$
$$\xi_2 \sum_{k'=1}^{K'} u^{(k')} \int_V \left[\sum_{l=1}^{L} \Delta_l \left(\mu n_y^l E' \phi_{k',x'} + n_x^l G \phi_{k',y'} \right) \alpha(\mathbf{x}, \mathbf{x}', l) \right] dV(\mathbf{x}') +$$
$$\xi_1 \sum_{k=1}^{K} v^{(k)} \sum_{l=1}^{L} \left[\sum_{m=1}^{M} \left(n_y^l E' R_{my} + n_x^l G R_{mx} \right) a_m + \sum_{n=1}^{N} \left(n_y^l E' P_{ny} + n_x^l G P_{nx} \right) b_n \right] +$$
$$\xi_2 \sum_{k'=1}^{K'} v^{(k')} \int_V \left[\sum_{l=1}^{L} \Delta_l \left(n_y^l E' \phi_{k',y'} + n_x^l G \phi_{k',x'} \right) \alpha(\mathbf{x}, \mathbf{x}', l) \right] dV(\mathbf{x}') = 0 \tag{6.20b}$$

The domain integrals in (6.20a) and (6.20b) can be treated by using the four-point standard integral scheme, then a set of discretized system equations can be derived for addressing nonlocal elastostatic problems based upon LIEM as

$$\xi_1 \sum_{k=1}^{K} u^{(k)} \sum_{l=1}^{L} \left[\sum_{m=1}^{M} \left(n_x^l E' R_{mx} + n_y^l G R_{my} \right) a_m + \sum_{n=1}^{N} \left(n_x^l E' P_{nx} + n_y^l G P_{ny} \right) b_n \right] +$$
$$\xi_2 \sum_{k'=1}^{K'} u^{(k')} \sum_{q=1}^{V} \sum_{p=1}^{4} \sum_{l=1}^{L} \Delta_l \left(n_x^l E' \phi_{k',x'} + n_y^l G \phi_{k',y'} \right) \alpha(\mathbf{x}, \mathbf{x}'_p, l) \Delta V_q w_p +$$
$$\xi_1 \sum_{k=1}^{K} v^{(k)} \sum_{l=1}^{L} \left[\sum_{m=1}^{M} \left(\mu n_x^l E' R_{my} + n_y^l G R_{mx} \right) a_m + \sum_{n=1}^{N} \left(\mu n_x^l E' P_{ny} + n_y^l G P_{nx} \right) b_n \right] +$$
$$\xi_2 \sum_{k'=1}^{K'} v^{(k')} \sum_{q=1}^{V} \sum_{p=1}^{4} \sum_{l=1}^{L} \Delta_l \left(\mu n_x^l E' \phi_{k',y'} + n_y^l G \phi_{k',x'} \right) \alpha(\mathbf{x}, \mathbf{x}'_p, l) \Delta V_q w_p = 0 \tag{6.21a}$$

$$\xi_1 \sum_{k=1}^{K} u^{(k)} \sum_{l=1}^{L} \left[\sum_{m=1}^{M} \left(\mu n_y^l E' R_{mx} + n_x^l G R_{my} \right) a_m + \sum_{n=1}^{N} \left(\mu n_y^l E' P_{nx} + n_x^l G P_{ny} \right) b_n \right] +$$
$$\xi_2 \sum_{k'=1}^{K'} u^{(k')} \sum_{q=1}^{V} \sum_{p=1}^{4} \sum_{l=1}^{L} \Delta_l \left(\mu n_y^l E' \phi_{k',x'} + n_x^l G \phi_{k',y'} \right) \alpha(\mathbf{x}, \mathbf{x}'_p, l) \Delta V_q w_p +$$
$$\xi_1 \sum_{k=1}^{K} v^{(k)} \sum_{l=1}^{L} \left[\sum_{m=1}^{M} \left(n_y^l E' R_{my} + n_x^l G R_{mx} \right) a_m + \sum_{n=1}^{N} \left(n_y^l E' P_{ny} + n_x^l G P_{nx} \right) b_n \right] +$$
$$\xi_2 \sum_{k'=1}^{K'} v^{(k')} \sum_{q=1}^{V} \sum_{p=1}^{4} \sum_{l=1}^{L} \Delta_l \left(n_y^l E' \phi_{k',y'} + n_x^l G \phi_{k',x'} \right) \alpha(\mathbf{x}, \mathbf{x}'_p, l) \Delta V_q w_p = 0 \tag{6.21b}$$

Finally, boundary conditions of NL-LIEM can be introduced as (5.19) and (5.20).

6.5 Numerical Examples

In this section, both of the NL-PCM and NL-LIEM are utilized to resolve 2D nonlocal elastostatic problems. In NL-PCM, free parameter c_0 in the MQ RBF is se-

lected as $c_0 = 2\Delta_{min}$. While free parameters in NL-LIEM are taken as: $c_0 = \Delta_{min}$, $D/\Delta_{min} = 0.5$, $L = 8$. And the number of nodes located within the local support domain is taken as $K_0 = 12$ for all examples followed.

6.5.1 A Square Panel under Uniform Displacement

A square panel of side $a = 5cm$ is investigated. The edge is fixed at $x = 0$, and it is subjected to a uniformly distributed displacement $u^0 = 0.001cm$ along the edge $x = 5cm$ as shown in Figure 6.2. The investigation is carried out by assuming material constants: Young's modulus $E = 2.1 \times 10^6 N/cm^2$, Poisson ratio $\mu = 0.2$. A total number of 961 nodes are regularly and evenly distributed in the problem domain, which means there are 30 subdomains along both x and y directions.

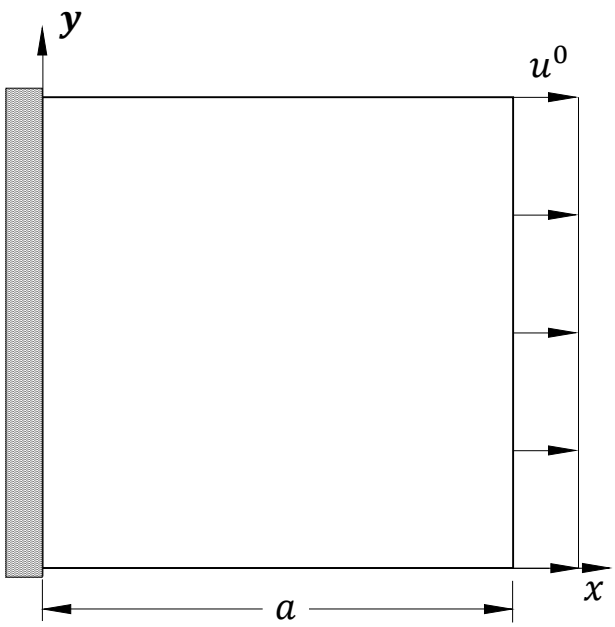

Figure 6.2: *A square panel subjected to a uniformly distributed displacement.*

Figure 6.3 and Figure 6.4 show the nonlocal solutions of strain distribution ε_{xx} along $y = 0.019cm$ and $y = 2.519cm$ respectively with characteristic length $l = 0.1cm$ and portion factor $\xi_1 = \xi_2 = 0.5$ by using NL-PCM and NL-LIEM.

Nonlocal results reported in [43], which is based upon FEM, are also presented for comparisons. Good agreements have been achieved, which validates the accuracy of NL-PCM and NL-LIEM.

Then, the elapsed real time for calculating ε_{xx} by means of NL-PCM and NL-LIEM are studied and presented in Table 6.1. Numerical solutions obtained in [43] (ε_{xx}(2.5, 0.019)=1.93E-04 and $\varepsilon_{xx}(2.5, 2.519)$=2.00E-04) are regarded as benchmarks. Parameters employed in both methods and the numerical errors are listed as well. Evidently, PCM saves more CPU time than LIEM in addressing nonlocal problems since there are no numerical integrals needed to be concerned.

Besides, NL-PCM and NL-LIEM solutions of strain distribution ε_{xx} along $x = 0.019cm$ and $x = 2.519cm$ with characteristic length $l = 0.1cm$ and portion factor $\xi_1 = \xi_2 = 0.5$ are presented in Figure 6.5 and Figure 6.6, respectively. Classical solutions obtained from Abaqus are plotted as well for comparisons. It can be seen that even though non-uniform nonlocal strain distributions appear at geometrical boundaries, there are only slight differences between nonlocal solutions and classical ones in the core domain.

Fourthly, the effect of portion factor ξ_1 is examined and therefore, NL-PCM and NL-LIEM are implemented with different values of ξ_1. Nonlocal strain distributions ε_{xx} along $y = 2.519cm$ and $x = 0.019cm$ are reported in Figure 6.7 and Figure 6.8 for $l = 0.25cm$ with different values of ξ_1 ($\xi_1 = 0.1$ and $\xi_1 = 0.5$). It clearly shows that the lower the value of ξ_1 is, the more obvious nonlocality can be seen, which can be described by the differences from classical solutions.

Finally, the influence of characteristic length l is studied and NL-PCM and NL-LIEM are also implemented with different values of l. The strain profiles with respect to ε_{xx} along $y = 2.519cm$ and $x = 4.750cm$ are obtained for $\xi_1 = 0.5$ with $l = 0.1cm$ and $l = 0.2cm$, respectively. As shown in Figure 6.9 and Figure 6.10, when the value of l goes up, the nonlocality extends towards the core domain.

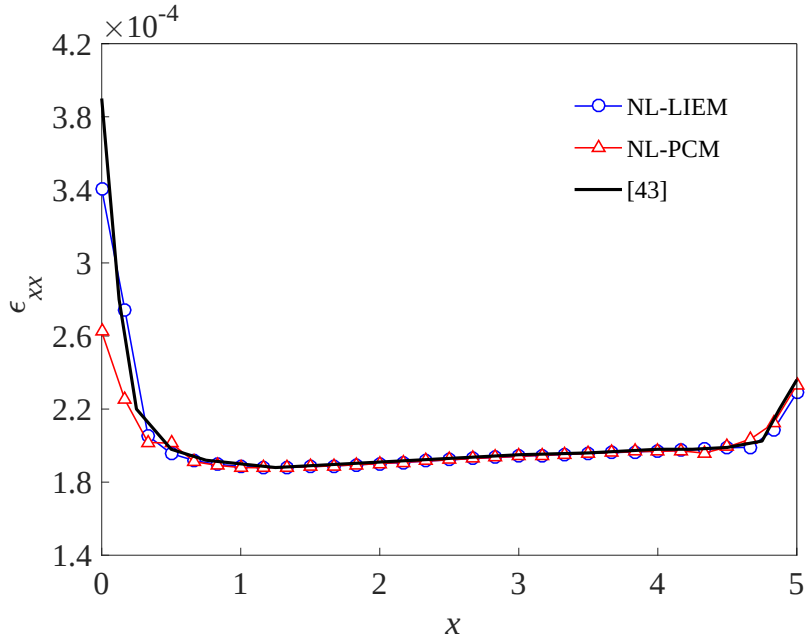

Figure 6.3: *Distribution of ε_{xx} along $y = 0.019cm$ of a panel under uniform displacement for $l = 0.1cm$ and $\xi_1 = 0.5$.*

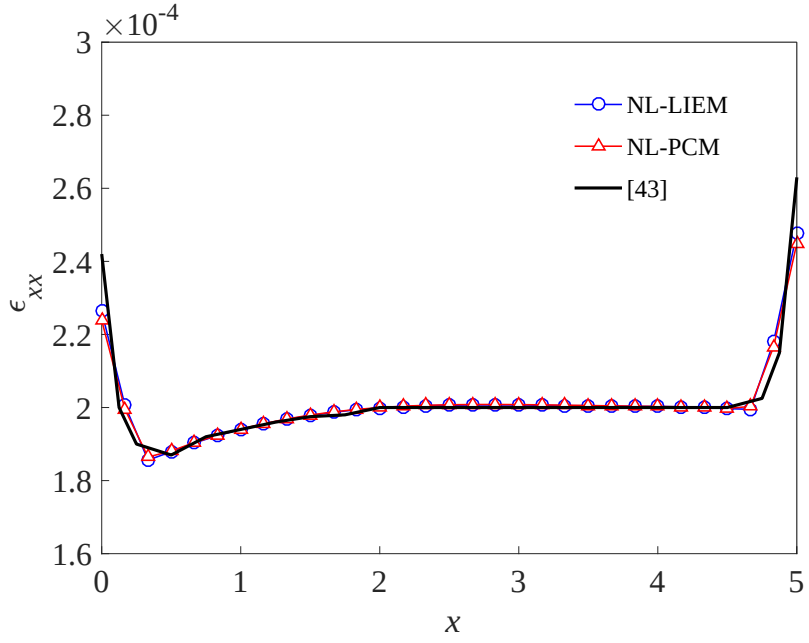

Figure 6.4: *Distribution of ε_{xx} along $y = 2.519cm$ of a panel under uniform displacement for $l = 0.1cm$ and $\xi_1 = 0.5$.*

Table 6.1: *Elapsed real time for calculating ε_{xx} by NL-PCM and NL-LIEM*

Method	Field nodes	K_0	c_0	L	D/Δ	$\varepsilon_{xx}(2.5, 0.019)$ (Error)	$\varepsilon_{xx}(2.5, 2.519)$ (Error)	Elapsed real time (Second)
NL-PCM	31×31	12	2Δ	36	0.5	1.92235E-04 (0.39662%)	2.00755E-04 (0.37740%)	3568.719
NL-LIEM	31×31	12	Δ			1.92200E-04 (0.41850%)	2.00600E-04 (0.30740%)	11667.700

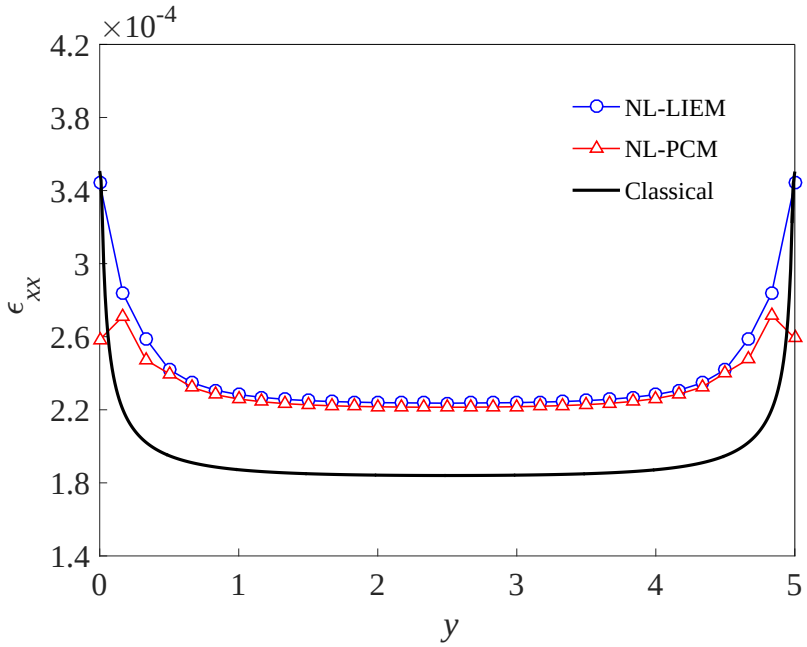

Figure 6.5: *Distribution of ε_{xx} along $x = 0.019cm$ of a panel under uniform displacement for $l = 0.1cm$ and $\xi_1 = 0.5$.*

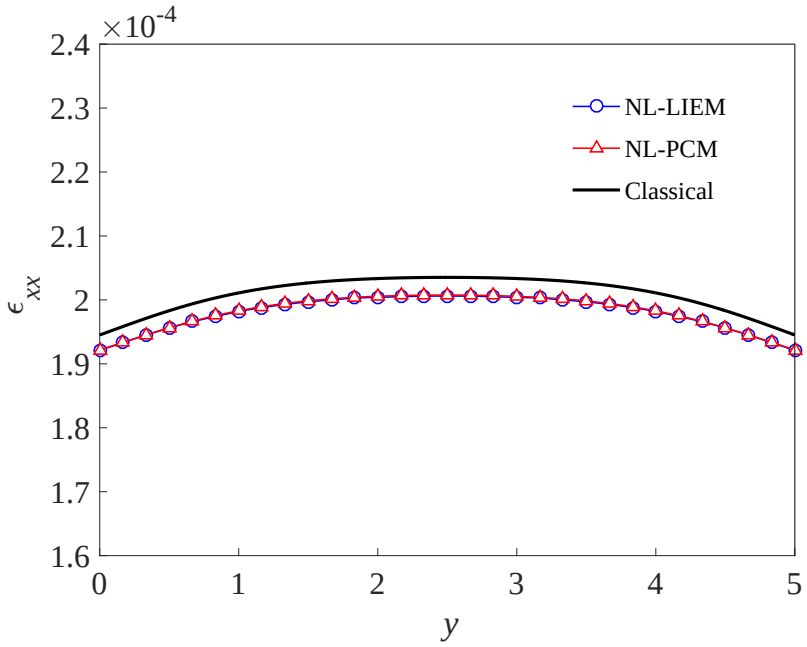

Figure 6.6: *Distribution of ε_{xx} along $x = 2.519cm$ of a panel under uniform displacement for $l = 0.1cm$ and $\xi_1 = 0.5$.*

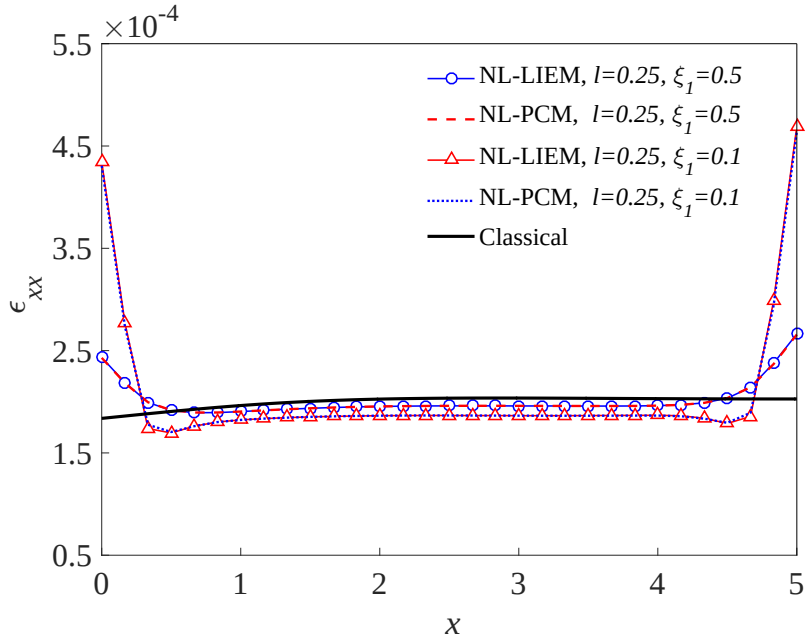

Figure 6.7: *Distribution of ε_{xx} along $y = 2.519cm$ of a plate under uniform displacement for $l = 0.25cm$ with $\xi_1 = 0.1$ and $\xi_1 = 0.5$.*

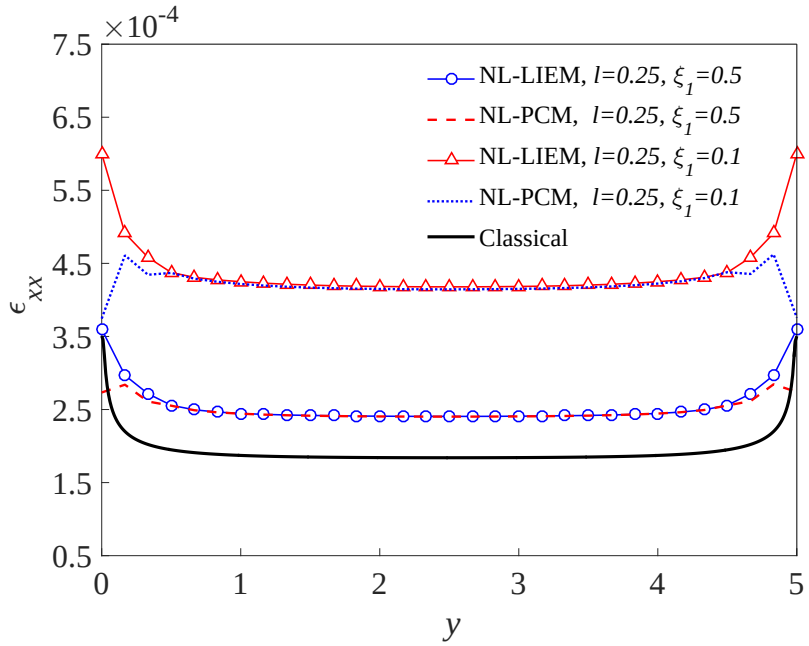

Figure 6.8: *Distribution of ε_{xx} along $x = 0.019cm$ of a panel under uniform displacement for $l = 0.25cm$ with $\xi_1 = 0.1$ and $\xi_1 = 0.5$.*

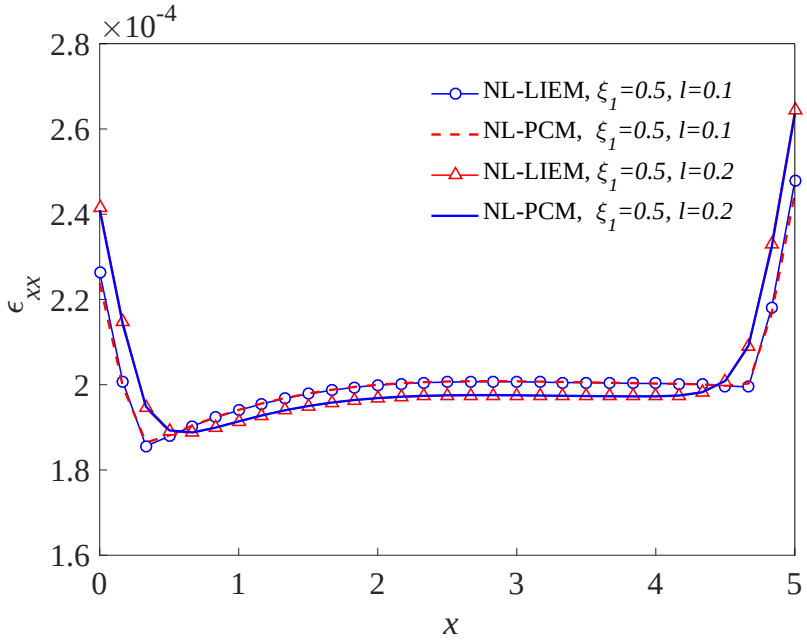

Figure 6.9: *Distribution of ε_{xx} along $y = 2.519cm$ of a panel under uniform displacement for $\xi_1 = 0.5$ with $l = 0.1cm$ and $l = 0.2cm$.*

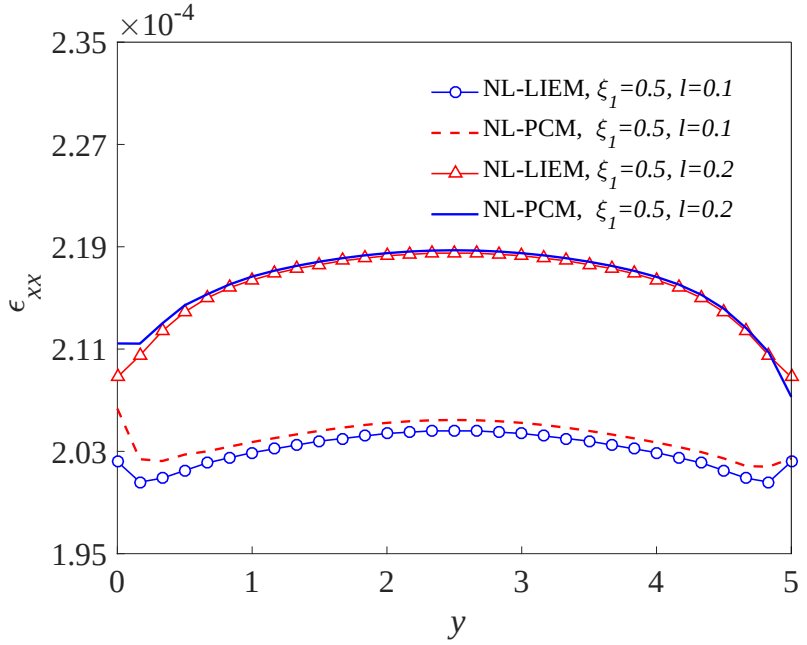

Figure 6.10: *Distribution of ε_{xx} along $x = 4.750cm$ of a panel under uniform displacement for $\xi_1 = 0.5$ with $l = 0.1cm$ and $l = 0.2cm$.*

6.5.2 A Square Board with a Circle Hole under Tensile Stress

A square board of width $2b$ containing a circle hole of radius a subjected to a uniformly distributed tensile load σ_0 on top and bottom is analysed (where $b = 2a$) as shown in Figure 6.11(a). Due to symmetry, only a quarter of the board is studied in this example with different portion factor ($\xi_1 = 0.1$ and $\xi_1 = 0.5$) for the characteristic length $l = 0.2$ and $l = 0.4$. However, in the domain integral of the governing equation, contributions of strains from the whole plate must be taken into account. The node distribution is shown in Figure 6.11(b). The number of background grids is selected as 40×40. Young's modulus $E = 1.0$ and Poisson ratio $\mu = 0.3$.

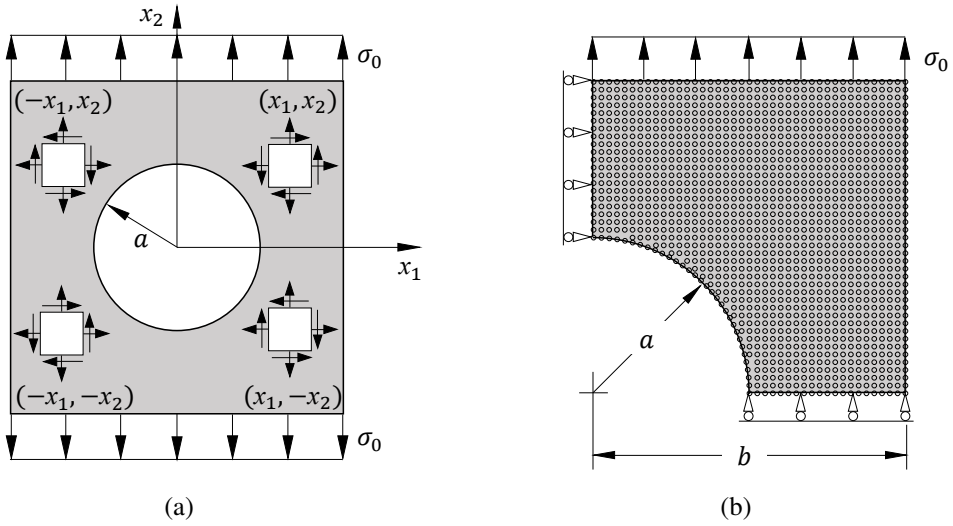

Figure 6.11: *A square board containing a circle hole subjected to tensile load: (a) geometry; (b) a quarter of the plate and the node distribution.*

Nonlocal solutions obtained from NL-PCM and NL-LIEM in terms of normalized strain distributions $E\varepsilon_{11}/\sigma_0$ and $E\varepsilon_{22}/\sigma_0$ along $x_2 = 0$ for different values of ξ_1 and l are plotted in Figure 6.12 to Figure 6.15, showing great agreements. Additionally, it illustrates that absolute values of nonlocal strains rise as the growth of l. And nonlocal strain distributions tend to the classical results when ξ_1 increases, which accords with the physical interpretation of the Eringen's model.

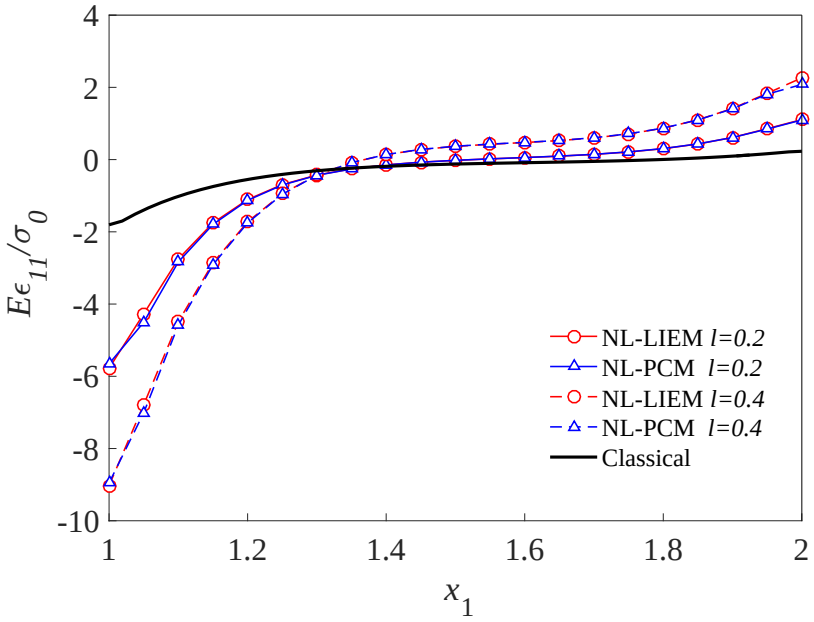

Figure 6.12: *Distribution of normalized strain* $E\varepsilon_{11}/\sigma_0$ *along* $x_2 = 0$ *for a square board containing a circle hole with* $\xi_1 = 0.1$, $l = 0.2$ *and* $l = 0.4$.

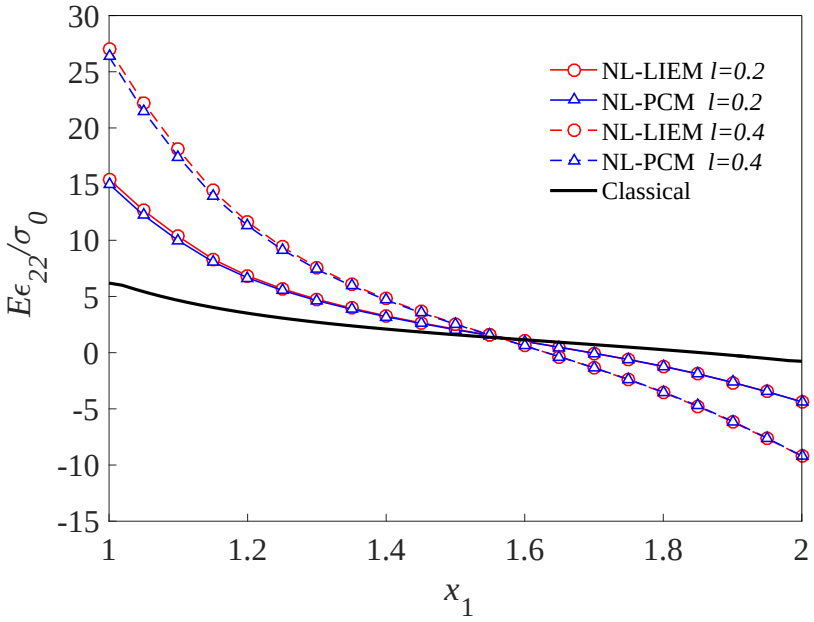

Figure 6.13: *Distribution of normalized strain* $E\varepsilon_{22}/\sigma_0$ *along* $x_2 = 0$ *for a square board containing a circle hole with* $\xi_1 = 0.1$, $l = 0.2$ *and* $l = 0.4$.

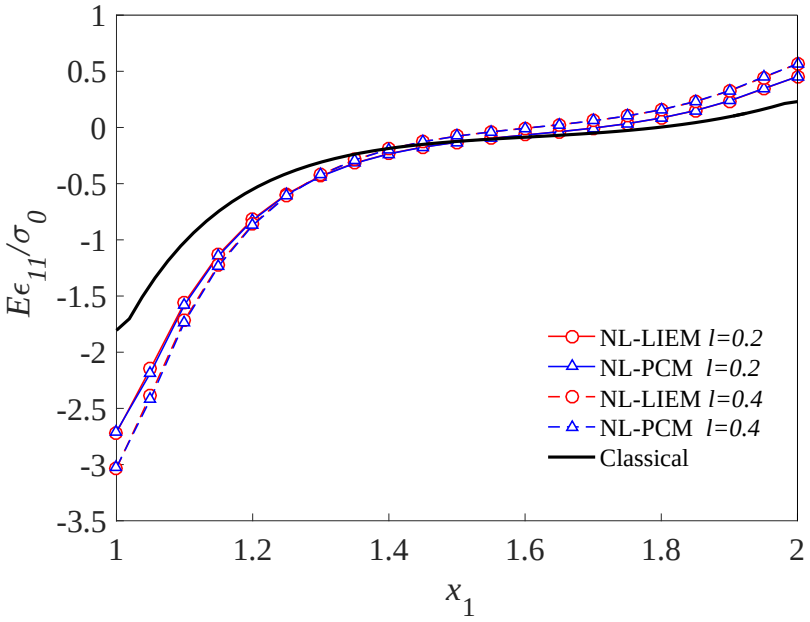

Figure 6.14: *Distribution of normalized strain* $E\varepsilon_{11}/\sigma_0$ *along* $x_2 = 0$ *for a square board containing a circle hole with* $\xi_1 = 0.5$, $l = 0.2$ *and* $l = 0.4$.

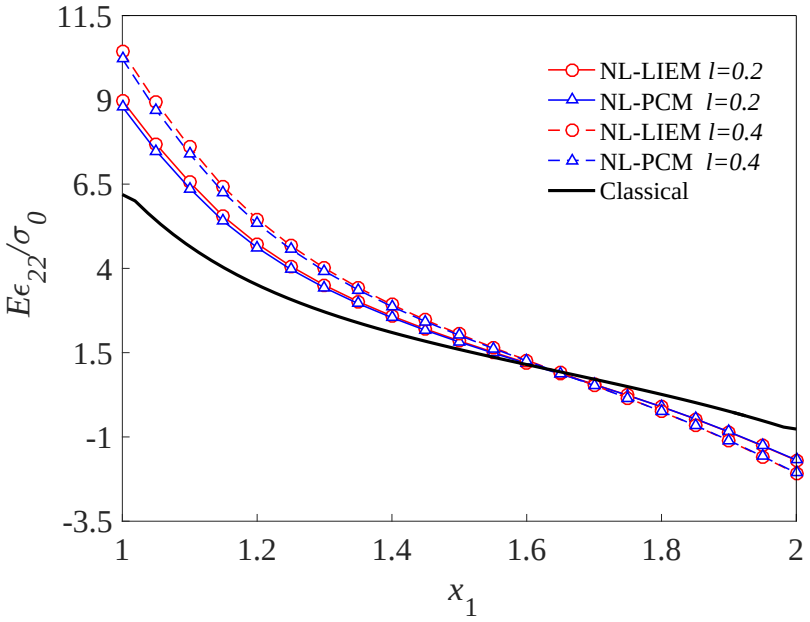

Figure 6.15: *Distribution of normalized strain* $E\varepsilon_{22}/\sigma_0$ *along* $x_2 = 0$ *for a square board containing a circle hole with* $\xi_1 = 0.5$, $l = 0.2$ *and* $l = 0.4$.

6.5.3 A Disk under Internal Pressure

A disk with dimensions $a = 1cm$ and $b = 2cm$ is examined in this example. It is subjected to an internal pressure σ_0 as shown in Figure 6.16(a) and only one quarter of the ring is considered, see Figure 6.16(b). The number of background grids is selected as 40×40 and material constants are taken as: Young's modulus $E = 1.0$, Poisson ratio $\mu = 0.3$.

Nonlocal distributions of normalized strains $E\varepsilon_{11}/\sigma_0$ and $E\varepsilon_{22}/\sigma_0$ derived from NL-PCM and NL-LIEM along axis x_1 for $\xi_1 = 0.1$ and $\xi_1 = 0.5$ with different values of l (in this case, $l = 0.2cm$ and $l = 0.4cm$ are selected) are presented in Figure 6.17 to Figure 6.20. As expected, strong-form solutions match with weak-form results. Besides, it is found that nonlocal solutions depart from the classical ones when the value of characteristic length goes up, and the same trend can be found when a small value of ξ_1 is used.

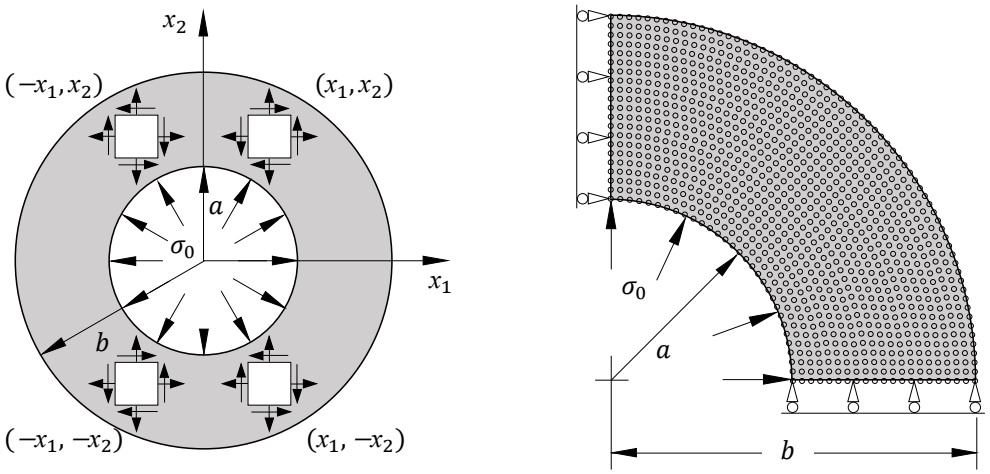

Figure 6.16: *A disk subjected to internal pressure: (a) geometry; (b) a quarter of the disk and the node distribution.*

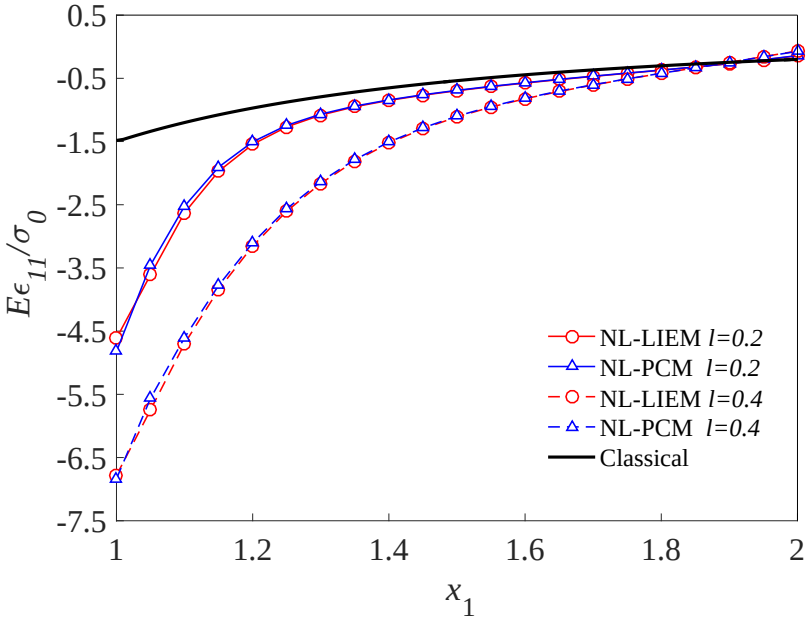

Figure 6.17: *Distribution of normalized strain* $E\varepsilon_{11}/\sigma_0$ *along* $x_2 = 0$ *for a disk with* $\xi_1 = 0.1$, $l = 0.2$ *and* $l = 0.4$.

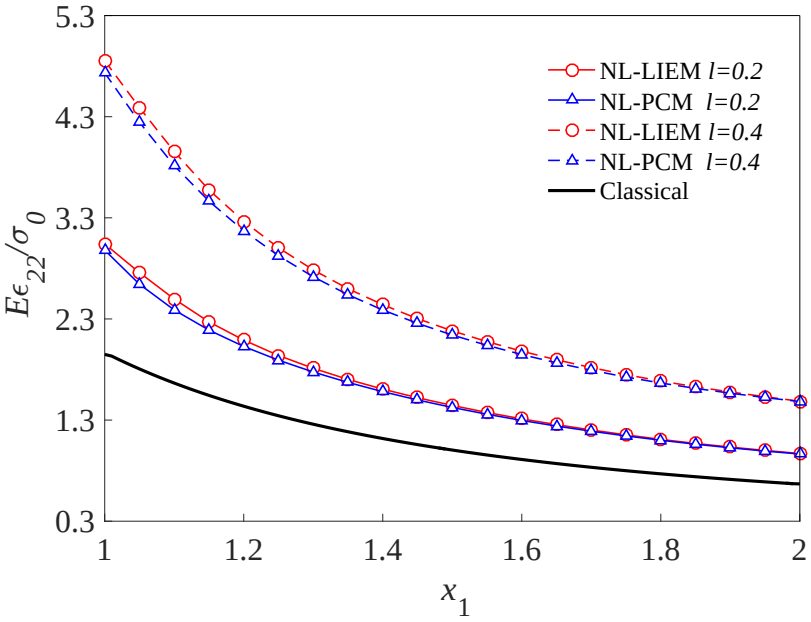

Figure 6.18: *Distribution of normalized strain* $E\varepsilon_{22}/\sigma_0$ *along* $x_2 = 0$ *for a disk with* $\xi_1 = 0.1$, $l = 0.2$ *and* $l = 0.4$.

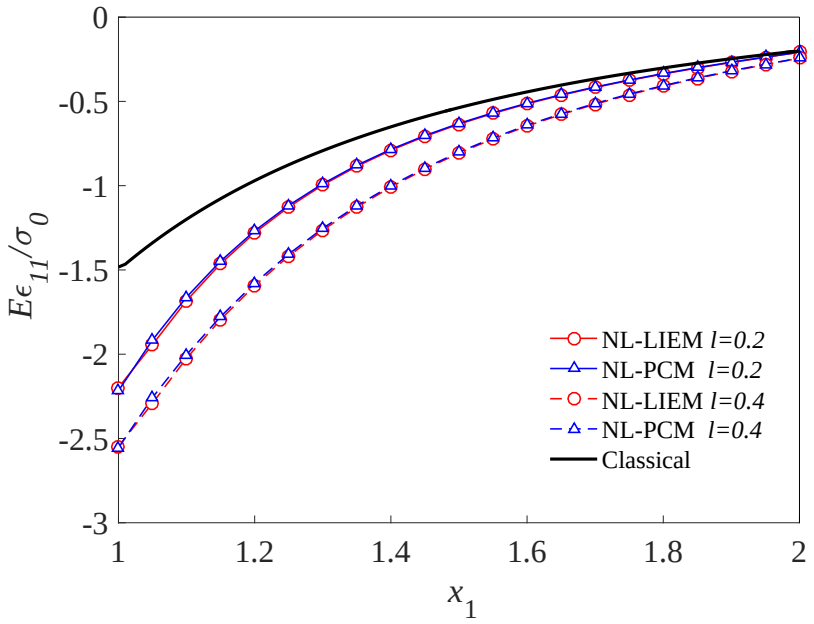

Figure 6.19: *Distribution of normalized strain* $E\varepsilon_{11}/\sigma_0$ *along* $x_2 = 0$ *for a disk with* $\xi_1 = 0.5$, $l = 0.2$ *and* $l = 0.4$.

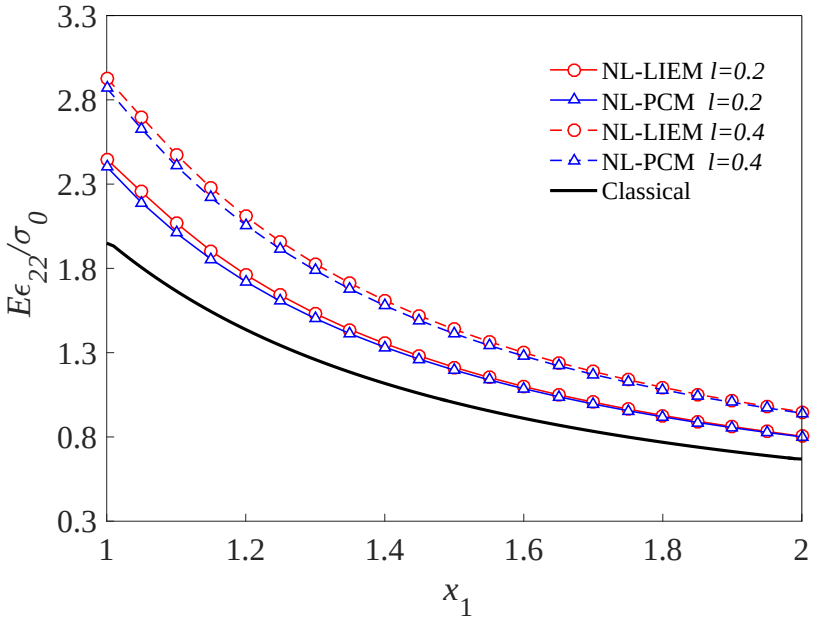

Figure 6.20: *Distribution of normalized strain* $E\varepsilon_{22}/\sigma_0$ *along* $x_2 = 0$ *for a disk with* $\xi_1 = 0.5$, $l = 0.2$ *and* $l = 0.4$.

6.6 Conclusions

In this chapter, meshless methods including PCM and LIEM are employed to deal with nonlocal elastostatic problems and their formulations are presented based upon the Eringen's model. Meshless approximations in both of the proposed methods are carried out by use of the MQ RBF. Three illustrated numerical examples demonstrate the accuracy and reliability of NL-PCM and NL-LIEM. In addition, it is concluded that:

(1) The lower the value of ξ_1 is, the more obvious nonlocality can be seen, which is corresponding to the physical significance of the Eringen's model as when ξ_1 decreases, the nonlocal solution is dominated by the nonlocal phase in the constitutive equation.

(2) When the value of characteristic length l increases, the nonlocal effect spreads towards the core domain, and nonlocal solutions at geometrical boundaries rise as well.

(3) Since no numerical integrals needed to be concerned in PCM, it saves more CPU time than LIEM in addressing nonlocal problems.

(4) Meshless methods can be extended to solve nonlocal elastodynamic cases easily.

CHAPTER 7

LIEM for Nonlocal Elastodynamics

7.1 Introduction

Time-dependent problems are appealing but challenging in the course of research. Two main kinds of methods are usually employed to solve elastodynamic cases including the frequency-domain approach as well as the time-domain approach. Frequency-domain formulations have been the subject of intense research work and are mainly related to the Laplace transformed domain method. Problems are usually solved in the Laplace domain initially with proper transform parameters, and then solutions in the real time-domain can be gained by taking advantage of the inverse transformation procedure, such as Durbin's [161], for Laplace transform. While in the time-domain formulation, discretizations are carried out spatially and temporally. Among others, the Houbolt method [162] has been widely used as the time marching scheme in time-domain approaches. Simultaneously, the Newmark method [163], which presents a good control of accuracy, has also been extensively employed in FEM formulations to deal with dynamic cases with no need for domain transformations.

Meshless methods were firstly applied by Liu and Belytschko [164] to address

dynamic problems in which the Element-Free Galerkin method was utilized. Besides, global and local integral equations with MLS approximations are used to solve dynamic problems in [165]. LIEM with the MLS approximation was applied to both transient as well as steady-state elastodynamics, which were solved by the Houbolt method and Laplace transformation approach, respectively [166]. More recently, a modified MLPG method was proposed and employed to deal with elastodynamic problems in the time-domain by the Houbolt method [167]. Analytical formulations of LIEM based on RBFs developed by Wen were applied to dynamic fracture mechanics problems by use of the Laplace transform technique [168]. In consideration of nonlocal dynamic problems, the finite integration method was applied to a nonlocal elastic bar subjected to dynamic loads in [169]. Even so, limited work has been found on the application of meshless methods to nonlocal elastodynamics.

In this chapter, analytical forms of LIEM based on RBF approximations are presented for nonlocal elastodynamic problems, which are treated both in the Laplace transformed-domain and in the time-domain, respectively. The Newmark scheme is implemented for the time marching in the time-domain technique, while the Durbin's inverse transformation is employed in the Laplace transform method. Two examples are demonstrated, and numerical solutions from both approaches are compared, showing reasonable agreement.

7.2 LIEM for Nonlocal Elastodynamics

Consider a linear elastic instance within a 2D domain Ω with boundary Γ as shown in Figure 5.1. The governing equation of motion is

$$\sigma_{ij,j} + f_i = \rho \ddot{u}_i \tag{7.1}$$

where ρ and $\ddot{u}_i$ are the mass density and the acceleration, respectively.

Two kinds of boundary conditions should be considered. For traction boundaries, we have

$$\sigma_{ij}n_j = t_i^0 \tag{7.2}$$

and for displacement boundaries, one has

$$u_i = u_i^0 \tag{7.3}$$

The weak-form of the governing equation in (7.1) over a local integral domain is in the form of

$$\int_{\Omega_s} (\sigma_{ij,j} + f_i - \rho\ddot{u}_i)u_i^* d\Omega = 0 \tag{7.4}$$

The above equation can be overwritten in the following symmetric weak-form by making use of the divergence theorem as

$$\int_{\Gamma_s} \sigma_{ij}n_j u_i^* d\Gamma - \int_{\Omega_s} (\sigma_{ij}u_{i,j}^* - f_i u_i^* + \rho\ddot{u}_i u_i^*)d\Omega = 0 \tag{7.5}$$

Recalling that $\Gamma_s = \Gamma_D \cup \Gamma_T \cup L_s$, (7.5) can be written in the form of

$$\begin{aligned}\int_{\Gamma_D} \sigma_{ij}n_j u_i^* d\Gamma + \int_{\Gamma_T} \sigma_{ij}n_j u_i^* d\Gamma + \int_{L_s} \sigma_{ij}n_j u_i^* d\Gamma \\ - \int_{\Omega_s} (\sigma_{ij}u_{i,j}^* - f_i u_i^* + \rho\ddot{u}_i u_i^*)d\Omega = 0\end{aligned} \tag{7.6}$$

For the local boundary that has no intersection with the global boundary, (7.6) becomes

$$\int_{\Omega_s} \sigma_{ij}u_{i,j}^* d\Omega - \int_{L_s} t_i u_i^* d\Gamma = \int_{\Omega_s} (f_i - \rho\ddot{u}_i)u_i^* d\Omega \tag{7.7}$$

However, if there is an intersection between the local boundary and the global boundary, (7.6) may be written as

$$\int_{\Omega_s} \sigma_{ij} u^*_{i,j} d\Omega - \int_{L_s} t_i u^*_i d\Gamma - \int_{\Gamma_D} t_i u^*_i d\Gamma = \int_{\Gamma_T} t^0_i u^*_i d\Gamma + \int_{\Omega_s} (f_i - \rho \ddot{u}_i) u^*_i d\Omega \tag{7.8}$$

A step function is employed as the test function u^*_i in each integral domain

$$u^*_i(x) = \begin{cases} \phi_i(\mathbf{x}) & \text{at } \mathbf{x} \in (\Omega_s \cup \Gamma_s) \\ 0 & \text{at } \mathbf{x} \notin \Omega_s \end{cases} \tag{7.9}$$

where $\phi_i(\mathbf{x}) = 1$.

Ignore body forces and the local integral equation in (7.5) and (7.8) can be rewritten as

$$\int_{\Gamma_s} \sigma_{ij} n_j d\Gamma = \int_{\Omega_s} \rho \ddot{u}_i d\Omega \tag{7.10}$$

and

$$\int_{L_s} t_i d\Gamma + \int_{\Gamma_D} t_i d\Gamma = \int_{\Omega_s} \rho \ddot{u}_i d\Omega - \int_{\Gamma_T} t^0_i d\Gamma \tag{7.11}$$

The integral of stress components in (7.10) can be approximated by integral of stresses over several straight lines that enclose the boundary as

$$\int_{\Gamma_s} \sigma_{ij} n_j d\Gamma = \sum_{l=1}^{L} n^l_j \int_{\Gamma_l} \sigma_{ij} d\Gamma \tag{7.12}$$

Therefore, recalling the nonlocal constitutive relationship in (6.2), (7.12) becomes

$$\begin{aligned}&\int_{\Gamma_s}\sigma_{ij}(\mathbf{x})n_j(\mathbf{x})d\Gamma(\mathbf{x})\\&=\xi_1\sum_{l=1}^{L}n_j^l\int_{\Gamma_l}\bar{\sigma}_{ij}(\mathbf{x})d\Gamma(\mathbf{x})+\xi_2\sum_{l=1}^{L}n_j^l\Delta_l\int_V\alpha(\mathbf{x},\mathbf{x}',l)\bar{\sigma}_{ij}(\mathbf{x}')dV(\mathbf{x}')\end{aligned}\tag{7.13}$$

Substitute (7.13) into (7.10), one derives

$$\xi_1\sum_{l=1}^{L}n_j^l\int_{\Gamma_l}\bar{\sigma}_{ij}(\mathbf{x})d\Gamma(\mathbf{x})+\xi_2\sum_{l=1}^{L}n_j^l\Delta_l\int_V\alpha(\mathbf{x},\mathbf{x}',l)\bar{\sigma}_{ij}(\mathbf{x}')dV(\mathbf{x}')=\int_{\Omega_s}\rho\ddot{u}_i d\Omega\tag{7.14}$$

7.3 Time Marching Schemes

7.3.1 LIEM in Laplace Transform Domain

The transformation of a function $f(t)$ in the real time-domain into the Laplace domain is defined as

$$\widehat{f}(p)=\int_0^\infty f(t)e^{-pt}dt\tag{7.15}$$

where p is the transformation parameter.

Transforming (7.14) into Laplace domain and one has

$$\begin{aligned}\xi_1\sum_{l=1}^{L}n_j^l\int_{\Gamma_l}\widehat{\bar{\sigma}}_{ij}(\mathbf{x})d\Gamma(\mathbf{x})+\xi_2\sum_{l=1}^{L}n_j^l\Delta_l\int_V\alpha(\mathbf{x},\mathbf{x}',l)\widehat{\bar{\sigma}}_{ij}(\mathbf{x}')dV(\mathbf{x}')\\=\int_{\Omega_s}p^2\rho\widehat{u}_i d\Omega\end{aligned}\tag{7.16}$$

Consider MQ RBF approximation schemes in Chapter 3, analytical forms of LIEM in Laplace domain can be obtained as

$$\xi_1 \sum_{k=1}^{K} \widehat{u}^{(k)} \sum_{l=1}^{L} \left[\sum_{m=1}^{M} \left(n_x^l E' R_{mx} + n_y^l G R_{my} \right) a_m + \sum_{n=1}^{N} \left(n_x^l E' P_{nx} + n_y^l G P_{ny} \right) b_n \right] +$$
$$\xi_2 \sum_{k'=1}^{K'} \widehat{u}^{(k')} \int_V \left[\sum_{l=1}^{L} \Delta_l \left(n_x^l E' \phi_{k',x'} + n_y^l G \phi_{k',y'} \right) \alpha(\mathbf{x}, \mathbf{x}', l) \right] dV(\mathbf{x}') +$$
$$\xi_1 \sum_{k=1}^{K} \widehat{v}^{(k)} \sum_{l=1}^{L} \left[\sum_{m=1}^{M} \left(\mu n_x^l E' R_{my} + n_y^l G R_{mx} \right) a_m + \sum_{n=1}^{N} \left(\mu n_x^l E' P_{ny} + n_y^l G P_{nx} \right) b_n \right] +$$
$$\xi_2 \sum_{k'=1}^{K'} \widehat{v}^{(k')} \int_V \left[\sum_{l=1}^{L} \Delta_l \left(\mu n_x^l E' \phi_{k',y'} + n_y^l G \phi_{k',x'} \right) \alpha(\mathbf{x}, \mathbf{x}', l) \right] dV(\mathbf{x}') = I_1 \tag{7.17a}$$

$$\xi_1 \sum_{k=1}^{K} \widehat{u}^{(k)} \sum_{l=1}^{L} \left[\sum_{m=1}^{M} \left(\mu n_y^l E' R_{mx} + n_x^l G R_{my} \right) a_m + \sum_{n=1}^{N} \left(\mu n_y^l E' P_{nx} + n_x^l G P_{ny} \right) b_n \right] +$$
$$\xi_2 \sum_{k'=1}^{K'} \widehat{u}^{(k')} \int_V \left[\sum_{l=1}^{L} \Delta_l \left(\mu n_y^l E' \phi_{k',x'} + n_x^l G \phi_{k',y'} \right) \alpha(\mathbf{x}, \mathbf{x}', l) \right] dV(\mathbf{x}') +$$
$$\xi_1 \sum_{k=1}^{K} \widehat{v}^{(k)} \sum_{l=1}^{L} \left[\sum_{m=1}^{M} \left(n_y^l E' R_{my} + n_x^l G R_{mx} \right) a_m + \sum_{n=1}^{N} \left(n_y^l E' P_{ny} + n_x^l G P_{nx} \right) b_n \right] +$$
$$\xi_2 \sum_{k'=1}^{K'} \widehat{v}^{(k')} \int_V \left[\sum_{l=1}^{L} \Delta_l \left(n_y^l E' \phi_{k',y'} + n_x^l G \phi_{k',x'} \right) \alpha(\mathbf{x}, \mathbf{x}', l) \right] dV(\mathbf{x}') = I_2 \tag{7.17b}$$

where the integral functions $I_i = \int_{\Omega_s} p^2 \rho \widehat{u}_i d\Omega$. When the area of the integral domain Ω is small, the integral functions can be approximated as

$$I_i = p^2 \rho \widehat{u}_i \Omega \tag{7.18}$$

the above approximation has been validated and reliable results have obtained in [168].

Thus, (7.17a) and (7.17b) can be modified into

$$\xi_1 \sum_{k=1}^{K} \widehat{u}^{(k)} \sum_{l=1}^{L} \left[\sum_{m=1}^{M} \left(n_x^l E' R_{mx} + n_y^l G R_{my} \right) a_m + \sum_{n=1}^{N} \left(n_x^l E' P_{nx} + n_y^l G P_{ny} \right) b_n \right] +$$
$$\xi_2 \sum_{k'=1}^{K'} \widehat{u}^{(k')} \int_V \left[\sum_{l=1}^{L} \Delta_l \left(n_x^l E' \phi_{k',x'} + n_y^l G \phi_{k',y'} \right) \alpha(\mathbf{x}, \mathbf{x}', l) \right] dV(\mathbf{x}') - p^2 \rho \widehat{u}^{(k)} \Omega +$$
$$\xi_1 \sum_{k=1}^{K} \widehat{v}^{(k)} \sum_{l=1}^{L} \left[\sum_{m=1}^{M} \left(\mu n_x^l E' R_{my} + n_y^l G R_{mx} \right) a_m + \sum_{n=1}^{N} \left(\mu n_x^l E' P_{ny} + n_y^l G P_{nx} \right) b_n \right] +$$
$$\xi_2 \sum_{k'=1}^{K'} \widehat{v}^{(k')} \int_V \left[\sum_{l=1}^{L} \Delta_l \left(\mu n_x^l E' \phi_{k',y'} + n_y^l G \phi_{k',x'} \right) \alpha(\mathbf{x}, \mathbf{x}', l) \right] dV(\mathbf{x}') = 0 \tag{7.19a}$$

$$\xi_1 \sum_{k=1}^{K} \widehat{u}^{(k)} \sum_{l=1}^{L} \left[\sum_{m=1}^{M} \left(\mu n_y^l E' R_{mx} + n_x^l G R_{my} \right) a_m + \sum_{n=1}^{N} \left(\mu n_y^l E' P_{nx} + n_x^l G P_{ny} \right) b_n \right] +$$
$$\xi_2 \sum_{k'=1}^{K'} \widehat{u}^{(k')} \int_V \left[\sum_{l=1}^{L} \Delta_l \left(\mu n_y^l E' \phi_{k',x'} + n_x^l G \phi_{k',y'} \right) \alpha(\mathbf{x}, \mathbf{x}', l) \right] dV(\mathbf{x}') +$$
$$\xi_1 \sum_{k=1}^{K} \widehat{v}^{(k)} \sum_{l=1}^{L} \left[\sum_{m=1}^{M} \left(n_y^l E' R_{my} + n_x^l G R_{mx} \right) a_m + \sum_{n=1}^{N} \left(n_y^l E' P_{ny} + n_x^l G P_{nx} \right) b_n \right] +$$
$$\xi_2 \sum_{k'=1}^{K'} \widehat{v}^{(k')} \int_V \left[\sum_{l=1}^{L} \Delta_l \left(n_y^l E' \phi_{k',y'} + n_x^l G \phi_{k',x'} \right) \alpha(\mathbf{x}, \mathbf{x}', l) \right] dV(\mathbf{x}') - p^2 \rho \widehat{v}^{(k)} \Omega = 0 \tag{7.19b}$$

The domain integral in (7.19a) and (7.19b) can be treated by using the four-point standard integral scheme. Then, the discretized system equations are derived in Laplace domain for nonlocal elastodynamics based upon LIEM as

$$\xi_1 \sum_{k=1}^{K} \widehat{u}^{(k)} \sum_{l=1}^{L} \left[\sum_{m=1}^{M} \left(n_x^l E' R_{mx} + n_y^l G R_{my} \right) a_m + \sum_{n=1}^{N} \left(n_x^l E' P_{nx} + n_y^l G P_{ny} \right) b_n \right] +$$
$$\xi_2 \sum_{k'=1}^{K'} \widehat{u}^{(k')} \sum_{q=1}^{V} \sum_{p=1}^{4} \sum_{l=1}^{L} \Delta_l \left(n_x^l E' \phi_{k',x'} + n_y^l G \phi_{k',y'} \right) \alpha(\mathbf{x}, \mathbf{x}'_p, l) \Delta V_q w_p - p^2 \rho \widehat{u}^{(k)} \Omega +$$
$$\xi_1 \sum_{k=1}^{K} \widehat{v}^{(k)} \sum_{l=1}^{L} \left[\sum_{m=1}^{M} \left(\mu n_x^l E' R_{my} + n_y^l G R_{mx} \right) a_m + \sum_{n=1}^{N} \left(\mu n_x^l E' P_{ny} + n_y^l G P_{nx} \right) b_n \right] +$$
$$\xi_2 \sum_{k'=1}^{K'} \widehat{v}^{(k')} \sum_{q=1}^{V} \sum_{p=1}^{4} \sum_{l=1}^{L} \Delta_l \left(\mu n_x^l E' \phi_{k',y'} + n_y^l G \phi_{k',x'} \right) \alpha(\mathbf{x}, \mathbf{x}'_p, l) \Delta V_q w_p = 0 \tag{7.20a}$$

$$\xi_1 \sum_{k=1}^{K} \widehat{u}^{(k)} \sum_{l=1}^{L} \left[\sum_{m=1}^{M} \left(\mu n_y^l E' R_{mx} + n_x^l G R_{my} \right) a_m + \sum_{n=1}^{N} \left(\mu n_y^l E' P_{nx} + n_x^l G P_{ny} \right) b_n \right] +$$
$$\xi_2 \sum_{k'=1}^{K'} \widehat{u}^{(k')} \sum_{q=1}^{V} \sum_{p=1}^{4} \sum_{l=1}^{L} \Delta_l \left(\mu n_y^l E' \phi_{k',x'} + n_x^l G \phi_{k',y'} \right) \alpha(\mathbf{x}, \mathbf{x}'_p, l) \Delta V_q w_p +$$
$$\xi_1 \sum_{k=1}^{K} \widehat{v}^{(k)} \sum_{l=1}^{L} \left[\sum_{m=1}^{M} \left(n_y^l E' R_{my} + n_x^l G R_{mx} \right) a_m + \sum_{n=1}^{N} \left(n_y^l E' P_{ny} + n_x^l G P_{nx} \right) b_n \right] +$$
$$\xi_2 \sum_{k'=1}^{K'} \widehat{v}^{(k')} \sum_{q=1}^{V} \sum_{p=1}^{4} \sum_{l=1}^{L} \Delta_l \left(n_y^l E' \phi_{k',y'} + n_x^l G \phi_{k',x'} \right) \alpha(\mathbf{x}, \mathbf{x}'_p, l) \Delta V_q w_p - p^2 \rho \widehat{v}^{(k)} \Omega = 0 \tag{7.20b}$$

Boundary conditions for nodes located on the traction boundary should be introduced as

$$\int_{\Gamma - \Gamma_T} \widehat{t}_i d\Gamma + \int_{\Gamma_T} \widehat{t}_i^0 d\Gamma = I_i \quad \text{for } \mathbf{x}_k \quad k = 1, 2, \ldots, M_T \tag{7.21}$$

While displacement boundary conditions can be imposed straightforward as

$$\widehat{u}_i(\mathbf{x}_k) = \widehat{u}_i^0 \quad \text{for } \mathbf{x}_k \quad k = 1, 2, \ldots, M_D \tag{7.22}$$

Time-dependent solutions in the real time-domain can be obtained by the inverse transformation procedure. The Durbin's [161] method is employed in the form of

$$f(t) = \frac{2e^{\eta t}}{T}\left[-\frac{1}{2}\widehat{f}(\eta) + \sum_{k=0}^{L} \text{Re}\left\{\widehat{f}\left(\eta + \frac{2k\pi}{T}i\right) \text{epx}\left(\frac{2k\pi t}{T}\right)\right\}\right] \tag{7.23}$$

in which $f(p_k)$ denotes the values in the Laplace domain for parameters $p_k = \eta + 2k\pi i/T$, $i = \sqrt{-1}$. Free parameters η and T have a slight influence on the accuracy of numerical results.

7.3.2 LIEM in Time-Domain

In order to solve nonlocal elastodynamic problems in the time-domain directly without transformation, the Newmark method [163], which is a general step-by-step approach of integration of the equations of motion in the time-domain technique, is employed. It's approximations are given as:

$$\dot{u}_{n+1} = \dot{u}_n + (1-\gamma)\Delta t\ddot{u}_n + \gamma\Delta t\ddot{u}_{n+1} \tag{7.24}$$

$$u_{n+1} = u_n + \Delta t\dot{u}_n + (\frac{1}{2} - \beta)\Delta t^2\ddot{u}_n + \beta\Delta t^2\ddot{u}_{n+1} \tag{7.25}$$

in which $\dot{u}$, $\ddot{u}$ and u represent the velocity, acceleration and displacement, respectively. The subscript n represents the time $t_n = n\Delta t$, and therefore, $t_{n+1} = (n+1)\Delta t$, where Δt is the selected time step. Parameters γ and β are closely related to the stability and accuracy of the Newmark approach and some observations have been found that if one takes $\gamma = \frac{1}{2}$ and $\beta = \frac{1}{6}$, (7.24) and (7.25) correspond to the linear acceleration method. However, for $\gamma = \frac{1}{2}$ and $\beta = \frac{1}{4}$, (7.24) and (7.25) correspond to the average acceleration method. Additionally, the method is

unconditionally stable when $2\beta \geq \gamma \geq \frac{1}{2}$.

$\dot{u}_{n+1}$ and $\ddot{u}_{n+1}$ can be expressed in terms of u_{n+1}, u_n, $\dot{u}_n$ and $\ddot{u}_n$ as

$$\dot{u}_{n+1} = \frac{\gamma}{\beta\Delta t}(u_{n+1} - u_n) + \frac{\beta - \gamma}{\beta}\dot{u}_n - \frac{\gamma - 2\beta}{2\beta}\Delta t\ddot{u}_n \tag{7.26}$$

$$\ddot{u}_{n+1} = \frac{1}{\beta\Delta t^2}(u_{n+1} - u_n) - \frac{1}{\beta\Delta t}\dot{u}_n - \frac{1 - 2\beta}{2\beta}\ddot{u}_n \tag{7.27}$$

The following equations can be derived based upon (7.14) by considering the MQ RBF approximations as

$$\begin{aligned}
&\xi_1 \sum_{k=1}^{K} u_{n+1}^{(k)} \sum_{l=1}^{L} \left[\sum_{m=1}^{M} \left(n_x^l E' R_{mx} + n_y^l G R_{my} \right) a_m + \sum_{n=1}^{N} \left(n_x^l E' P_{nx} + n_y^l G P_{ny} \right) b_n \right] + \\
&\xi_2 \sum_{k'=1}^{K'} u_{n+1}^{(k')} \int_V \left[\sum_{l=1}^{L} \Delta_l \left(n_x^l E' \phi_{k',x'} + n_y^l G \phi_{k',y'} \right) \alpha(\mathbf{x}, \mathbf{x}', l) \right] dV(\mathbf{x}') + \\
&\xi_1 \sum_{k=1}^{K} v_{n+1}^{(k)} \sum_{l=1}^{L} \left[\sum_{m=1}^{M} \left(\mu n_x^l E' R_{my} + n_y^l G R_{mx} \right) a_m + \sum_{n=1}^{N} \left(\mu n_x^l E' P_{ny} + n_y^l G P_{nx} \right) b_n \right] + \\
&\xi_2 \sum_{k'=1}^{K'} v_{n+1}^{(k')} \int_V \left[\sum_{l=1}^{L} \Delta_l \left(\mu n_x^l E' \phi_{k',y'} + n_y^l G \phi_{k',x'} \right) \alpha(\mathbf{x}, \mathbf{x}', l) \right] dV(\mathbf{x}') = I_1'
\end{aligned} \tag{7.28a}$$

$$\begin{aligned}
&\xi_1 \sum_{k=1}^{K} u_{n+1}^{(k)} \sum_{l=1}^{L} \left[\sum_{m=1}^{M} \left(\mu n_y^l E' R_{mx} + n_x^l G R_{my} \right) a_m + \sum_{n=1}^{N} \left(\mu n_y^l E' P_{nx} + n_x^l G P_{ny} \right) b_n \right] + \\
&\xi_2 \sum_{k'=1}^{K'} u_{n+1}^{(k')} \int_V \left[\sum_{l=1}^{L} \Delta_l \left(\mu n_y^l E' \phi_{k',x'} + n_x^l G \phi_{k',y'} \right) \alpha(\mathbf{x}, \mathbf{x}', l) \right] dV(\mathbf{x}') + \\
&\xi_1 \sum_{k=1}^{K} v_{n+1}^{(k)} \sum_{l=1}^{L} \left[\sum_{m=1}^{M} \left(n_y^l E' R_{my} + n_x^l G R_{mx} \right) a_m + \sum_{n=1}^{N} \left(n_y^l E' P_{ny} + n_x^l G P_{nx} \right) b_n \right] + \\
&\xi_2 \sum_{k'=1}^{K'} v_{n+1}^{(k')} \int_V \left[\sum_{l=1}^{L} \Delta_l \left(n_y^l E' \phi_{k',y'} + n_x^l G \phi_{k',x'} \right) \alpha(\mathbf{x}, \mathbf{x}', l) \right] dV(\mathbf{x}') = I_2'
\end{aligned} \tag{7.28b}$$

where the integral functions $I_i' = \int_{\Omega_s} \rho \ddot{u}_i d\Omega$.

The four-point standard integral scheme is used to carry out the domain integral in (7.28a) and (7.28b), then a set of discretized equations can be derived as

$$\begin{aligned}
&\xi_1 \sum_{k=1}^{K} u_{n+1}^{(k)} \sum_{l=1}^{L} \left[\sum_{m=1}^{M} \left(n_x^l E' R_{mx} + n_y^l G R_{my} \right) a_m + \sum_{n=1}^{N} \left(n_x^l E' P_{nx} + n_y^l G P_{ny} \right) b_n \right] + \\
&\xi_2 \sum_{k'=1}^{K'} u_{n+1}^{(k')} \sum_{q=1}^{V} \sum_{p=1}^{4} \sum_{l=1}^{L} \Delta_l \left(n_x^l E' \phi_{k',x'} + n_y^l G \phi_{k',y'} \right) \alpha(\mathbf{x}, \mathbf{x}_p', l) \Delta V_q w_p + \\
&\xi_1 \sum_{k=1}^{K} v_{n+1}^{(k)} \sum_{l=1}^{L} \left[\sum_{m=1}^{M} \left(\mu n_x^l E' R_{my} + n_y^l G R_{mx} \right) a_m + \sum_{n=1}^{N} \left(\mu n_x^l E' P_{ny} + n_y^l G P_{nx} \right) b_n \right] + \\
&\xi_2 \sum_{k'=1}^{K'} v_{n+1}^{(k')} \sum_{q=1}^{V} \sum_{p=1}^{4} \sum_{l=1}^{L} \Delta_l \left(\mu n_x^l E' \phi_{k',y'} + n_y^l G \phi_{k',x'} \right) \alpha(\mathbf{x}, \mathbf{x}_p', l) \Delta V_q w_p = I_1'
\end{aligned} \tag{7.29a}$$

$$\begin{aligned}
&\xi_1 \sum_{k=1}^{K} u_{n+1}^{(k)} \sum_{l=1}^{L} \left[\sum_{m=1}^{M} \left(\mu n_y^l E' R_{mx} + n_x^l G R_{my} \right) a_m + \sum_{n=1}^{N} \left(\mu n_y^l E' P_{nx} + n_x^l G P_{ny} \right) b_n \right] + \\
&\xi_2 \sum_{k'=1}^{K'} u_{n+1}^{(k')} \sum_{q=1}^{V} \sum_{p=1}^{4} \sum_{l=1}^{L} \Delta_l \left(\mu n_y^l E' \phi_{k',x'} + n_x^l G \phi_{k',y'} \right) \alpha(\mathbf{x}, \mathbf{x}_p', l) \Delta V_q w_p + \\
&\xi_1 \sum_{k=1}^{K} v_{n+1}^{(k)} \sum_{l=1}^{L} \left[\sum_{m=1}^{M} \left(n_y^l E' R_{my} + n_x^l G R_{mx} \right) a_m + \sum_{n=1}^{N} \left(n_y^l E' P_{ny} + n_x^l G P_{nx} \right) b_n \right] + \\
&\xi_2 \sum_{k'=1}^{K'} v_{n+1}^{(k')} \sum_{q=1}^{V} \sum_{p=1}^{4} \sum_{l=1}^{L} \Delta_l \left(n_y^l E' \phi_{k',y'} + n_x^l G \phi_{k',x'} \right) \alpha(\mathbf{x}, \mathbf{x}_p', l) \Delta V_q w_p = I_2'
\end{aligned} \tag{7.29b}$$

Consider the Newmark scheme presented above, the following discrete equations can be derived

$$\xi_1 C_{td} \sum_{k=1}^{K} u_{n+1}^{(k)} \sum_{l=1}^{L} \left[\sum_{m=1}^{M} \left(n_x^l E' R_{mx} + n_y^l G R_{my} \right) a_m + \sum_{n=1}^{N} \left(n_x^l E' P_{nx} + n_y^l G P_{ny} \right) b_n \right] +$$
$$\xi_2 C_{td} \sum_{k'=1}^{K'} u_{n+1}^{(k')} \sum_{q=1}^{V} \sum_{p=1}^{4} \sum_{l=1}^{L} \Delta_l \left(n_x^l E' \phi_{k',x'} + n_y^l G \phi_{k',y'} \right) \alpha(\mathbf{x}, \mathbf{x}'_p, l) \Delta V_q w_p + u_{n+1}^{(k)} +$$
$$\xi_1 C_{td} \sum_{k=1}^{K} v_{n+1}^{(k)} \sum_{l=1}^{L} \left[\sum_{m=1}^{M} \left(\mu n_x^l E' R_{my} + n_y^l G R_{mx} \right) a_m + \sum_{n=1}^{N} \left(\mu n_x^l E' P_{ny} + n_y^l G P_{nx} \right) b_n \right] +$$
$$\xi_2 C_{td} \sum_{k'=1}^{K'} v_{n+1}^{(k')} \sum_{q=1}^{V} \sum_{p=1}^{4} \sum_{l=1}^{L} \Delta_l \left(\mu n_x^l E' \phi_{k',y'} + n_y^l G \phi_{k',x'} \right) \alpha(\mathbf{x}, \mathbf{x}'_p, l) \Delta V_q w_p = \tilde{I}'_1 \tag{7.30a}$$

$$\xi_1 C_{td} \sum_{k=1}^{K} u_{n+1}^{(k)} \sum_{l=1}^{L} \left[\sum_{m=1}^{M} \left(\mu n_y^l E' R_{mx} + n_x^l G R_{my} \right) a_m + \sum_{n=1}^{N} \left(\mu n_y^l E' P_{nx} + n_x^l G P_{ny} \right) b_n \right] +$$
$$\xi_2 C_{td} \sum_{k'=1}^{K'} u_{n+1}^{(k')} \sum_{q=1}^{V} \sum_{p=1}^{4} \sum_{l=1}^{L} \Delta_l \left(\mu n_y^l E' \phi_{k',x'} + n_x^l G \phi_{k',y'} \right) \alpha(\mathbf{x}, \mathbf{x}'_p, l) \Delta V_q w_p +$$
$$\xi_1 C_{td} \sum_{k=1}^{K} v_{n+1}^{(k)} \sum_{l=1}^{L} \left[\sum_{m=1}^{M} \left(n_y^l E' R_{my} + n_x^l G R_{mx} \right) a_m + \sum_{n=1}^{N} \left(n_y^l E' P_{ny} + n_x^l G P_{nx} \right) b_n \right] +$$
$$\xi_2 C_{td} \sum_{k'=1}^{K'} v_{n+1}^{(k')} \sum_{q=1}^{V} \sum_{p=1}^{4} \sum_{l=1}^{L} \Delta_l \left(n_y^l E' \phi_{k',y'} + n_x^l G \phi_{k',x'} \right) \alpha(\mathbf{x}, \mathbf{x}'_p, l) \Delta V_q w_p + v_{n+1}^{(k)} = \tilde{I}'_2 \tag{7.30b}$$

where $C_{td} = -\dfrac{\beta \Delta t^2}{\rho \Omega_s}$, and $\tilde{I}'_i = u_i + \Delta t \dot{u}_i + \dfrac{1 - 2\beta}{2} \Delta t^2 \ddot{u}_i$.

Boundary conditions can be imposed as

$$\int_{\Gamma - \Gamma_T} t_i d\Gamma + \int_{\Gamma_T} t_i^0 d\Gamma = I'_i \quad \text{for } \mathbf{x}_k \quad k = 1, 2, \ldots, M_T \tag{7.31}$$

and

$$u_i(\mathbf{x}_k) = u_i^0 \quad \text{for } \mathbf{x}_k \quad k = 1, 2, \ldots, M_D \tag{7.32}$$

7.4 Numerical Examples

In this section, LIEM is employed to address 2D nonlocal elastodynamic problems in Laplace transform domain and in time domain, respectively. Free parameters in LIEM are taken as: $c_0 = \Delta_{min}$, $D/\Delta_{min} = 0.5$, $L = 8$. And the total number of nodes involved in the local support domain is taken as $K_0 = 12$ for all examples followed.

7.4.1 A Square Panel Subjected to Dynamic Load

Consider a square panel of side $a = 1.0$ subjected to a Heaviside load $\sigma_0 H(t)$ on top, and the plate is fixed along the edge at $x_2 = 0$ as shown in Figure 7.1(a) , where $H(t)$ is the Heaviside step function. And the regularly distributed collocation points (11×11) are presented in Figure 7.1(b). Young's modulus is one unit and Poisson's ration is taken as zero in order to compare with the analytical solutions when portion factor $\xi_1 = 1.0$.

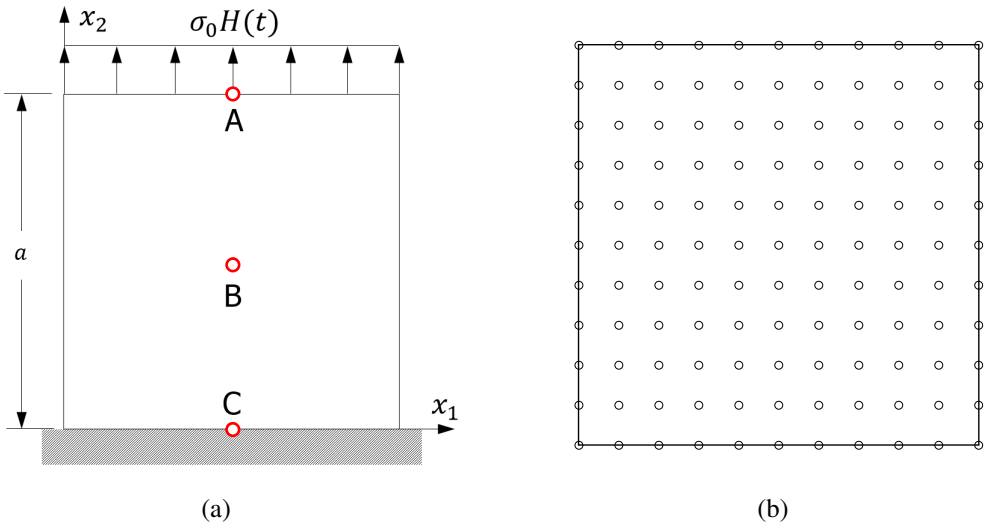

Figure 7.1: *A square panel subjected to a Heaviside load: (a) geometry; (b) node distributions.*

The sample number in Laplace domain is selected as 51, free parameters $\eta T = 5$ and $T/t_0 = 20$, in which $t_0 = b/c_1$ represents the unit time, b is the specified length and c_1 denotes the longitudinal wave speed. While in the Newmark approximations, time step $\Delta t = 0.1$ and free parameters $\gamma = 0.5$, $\beta = 0.25$.

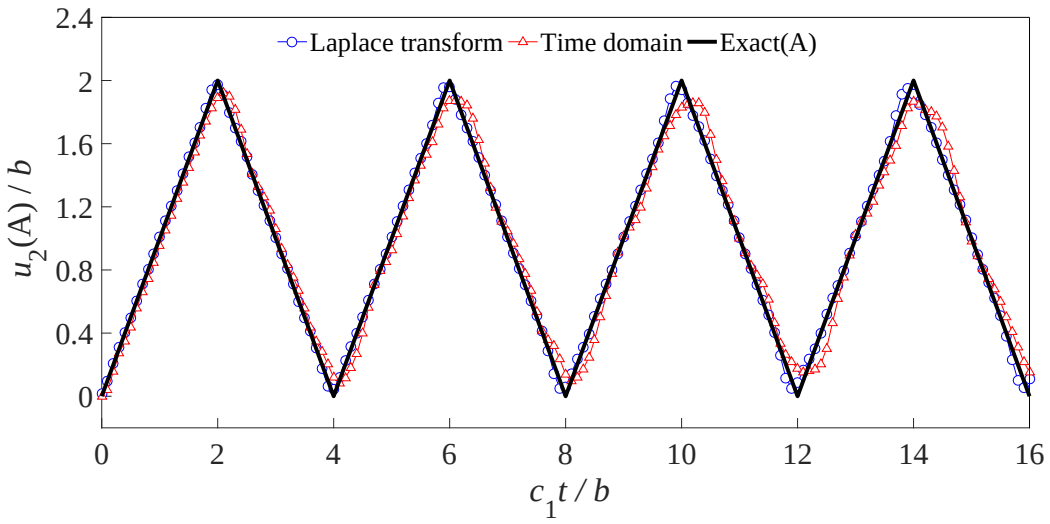

Figure 7.2: *Normalized displacement u_2/b for point A against normalized time $c_1 t/b$ when $\xi_1 = 1.0$.*

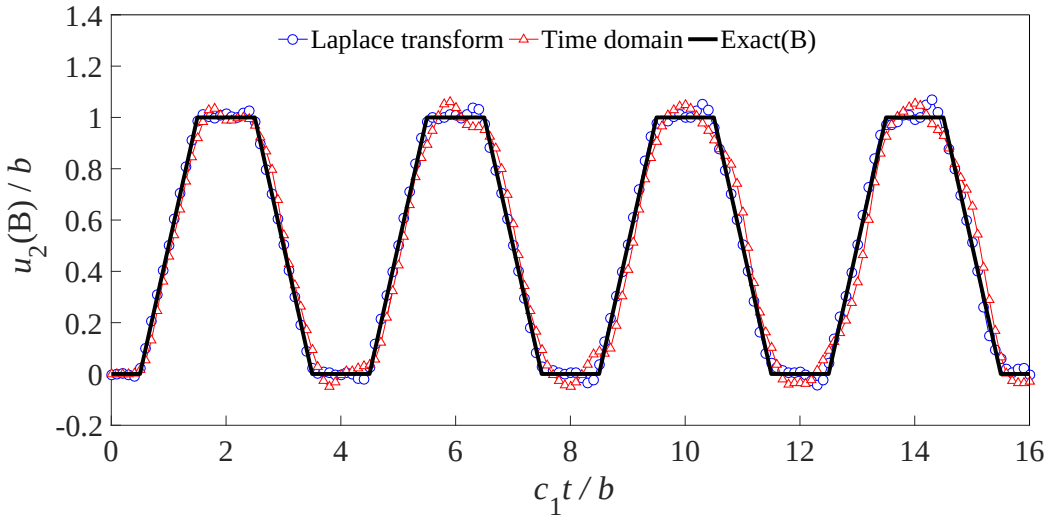

Figure 7.3: *Normalized displacement u_2/b for point B against normalized time $c_1 t/b$ when $\xi_1 = 1.0$.*

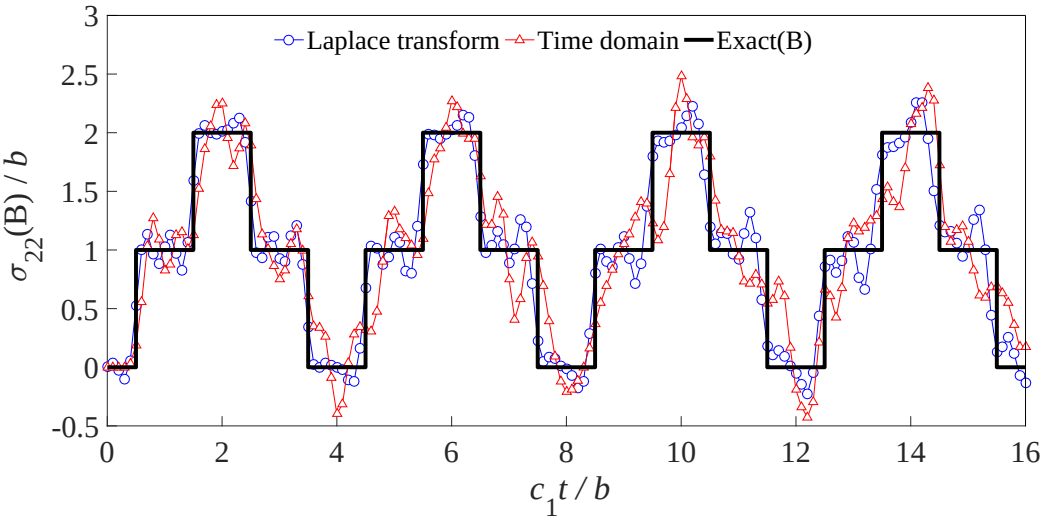

Figure 7.4: *Normalized stress σ_{22}/b for point B against normalized time $c_1 t/b$ when $\xi_1 =$ 1.0.*

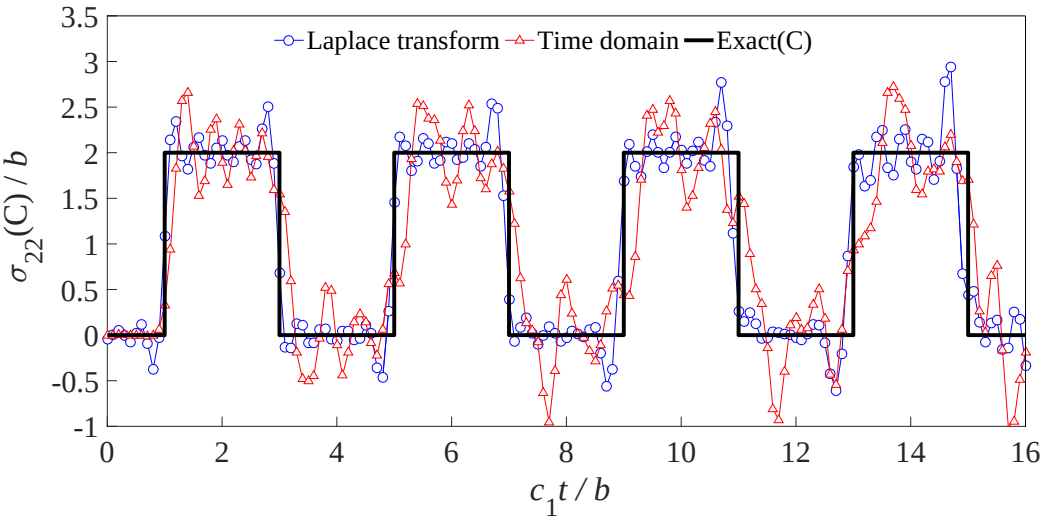

Figure 7.5: *Normalized stress σ_{22}/b for point C against normalized time $c_1 t/b$ when $\xi_1 =$ 1.0.*

Figure 7.2 and Figure 7.3 show the time-dependent displacements of point A and B when $\xi_1 = 1.0$. While the dynamic stresses with respect to $\xi_1 = 1.0$ of point B and C are plotted in Figure 7.4 and Figure 7.5. Analytical solutions are plotted as well for comparison purpose. As expected, dynamic numerical solutions obtained from LIEM implemented in the time domain and in the Laplace transform domain have achieved reasonable agreement with analytical solutions. However, fluctuations can be seen in stress solutions.

In addition, the normalized nonlocal dynamic displacements on point A and B with the characteristic length $l = 0.1$ and $l = 0.2$ for different portion factors ($\xi_1 = 0.5$ / $\xi_1 = 0.8$) are plotted in Figure 7.6 to Figure 7.11, which show that the period of oscillation increases when the portion factor ξ_1 decreases or the characteristic length l increases, and nonlocal dynamic solutions derive from both methods coincide with each other. Figure 7.12 to Figure 7.17 present the normalized nonlocal time dependent stress distributions of point B and C, similar conclusions can be drawn when the value of the characteristic length or portion factor varies.

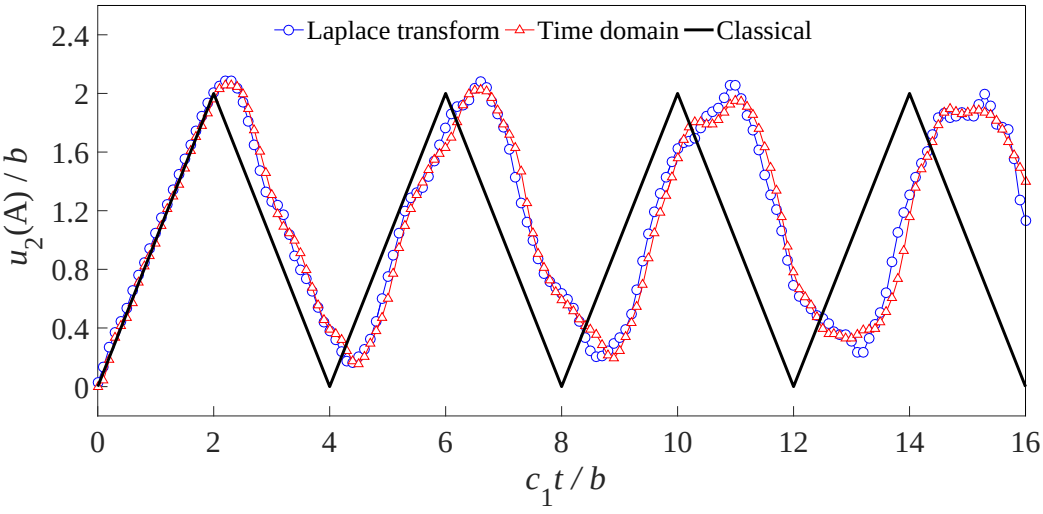

Figure 7.6: *Normalized displacement u_2/b for point A against normalized time $c_1 t/b$ when $\xi_1 = 0.5$, $l = 0.1$.*

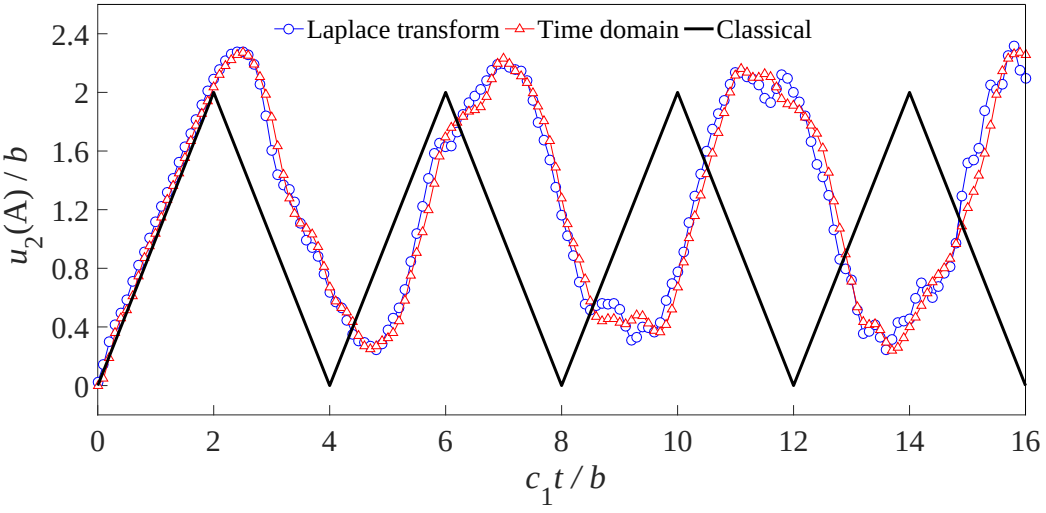

Figure 7.7: *Normalized displacement u_2/b for point A against normalized time $c_1 t/b$ when $\xi_1 = 0.5$, $l = 0.2$.*

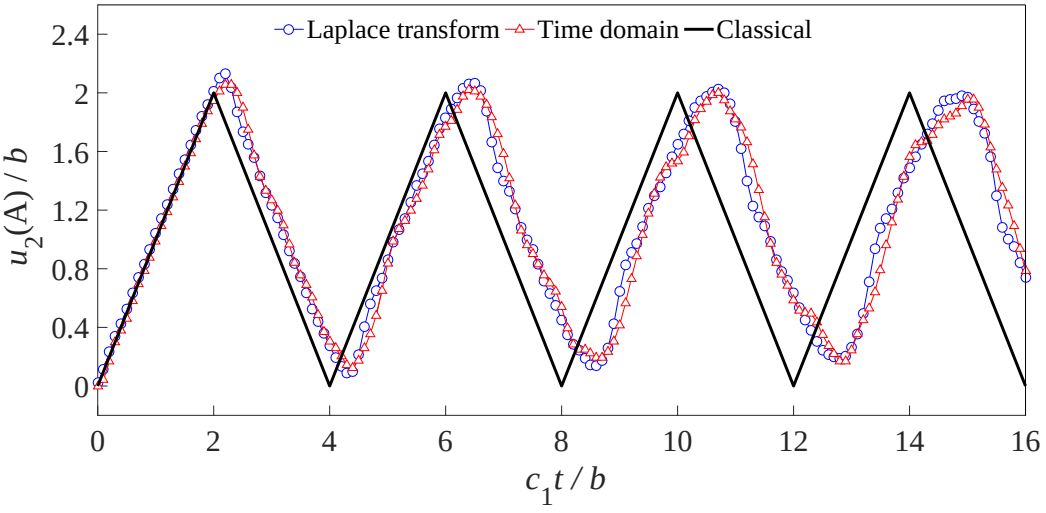

Figure 7.8: *Normalized displacement u_2/b for point A against normalized time $c_1 t/b$ when $\xi_1 = 0.8$, $l = 0.2$.*

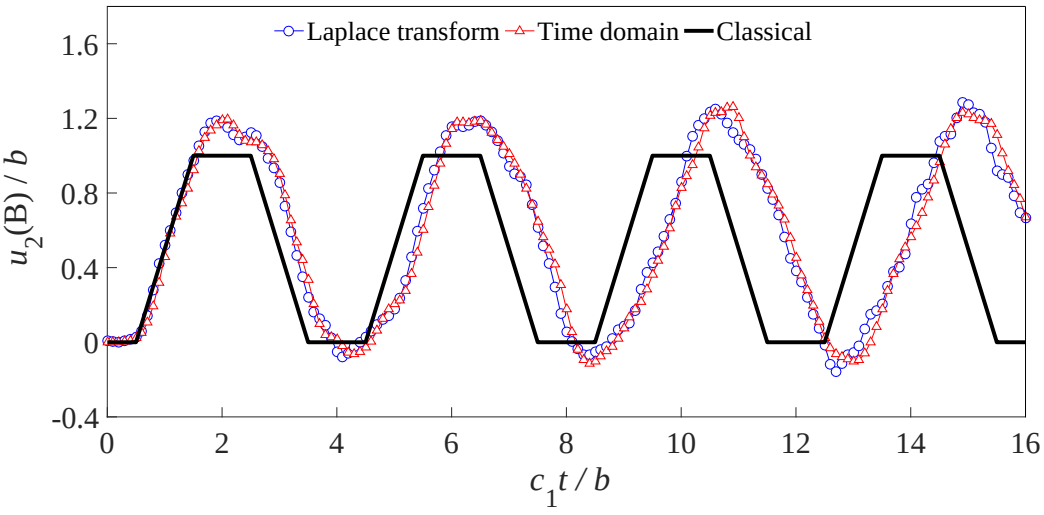

Figure 7.9: *Normalized displacement* u_2/b *for point B against normalized time* $c_1 t/b$ *when* $\xi_1 = 0.5$, $l = 0.1$.

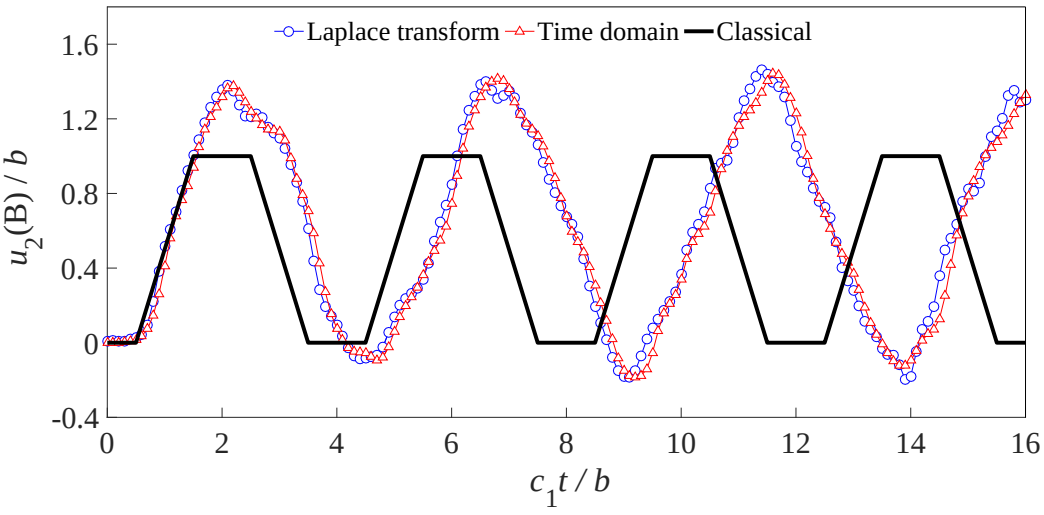

Figure 7.10: *Normalized displacement* u_2/b *for point B against normalized time* $c_1 t/b$ *when* $\xi_1 = 0.5$, $l = 0.2$.

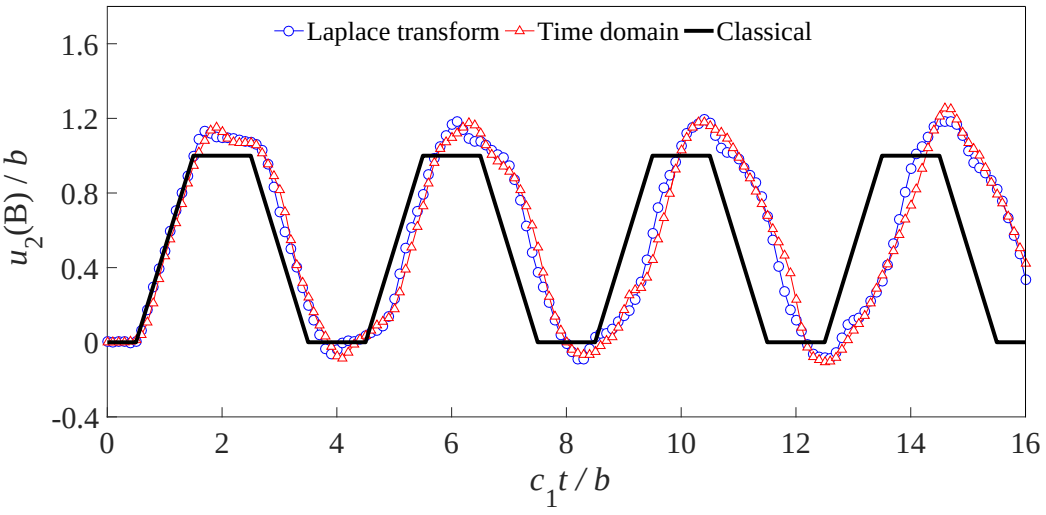

Figure 7.11: *Normalized displacement* u_2/b *for point B against normalized time* $c_1 t/b$ *when* $\xi_1 = 0.8$, $l = 0.2$.

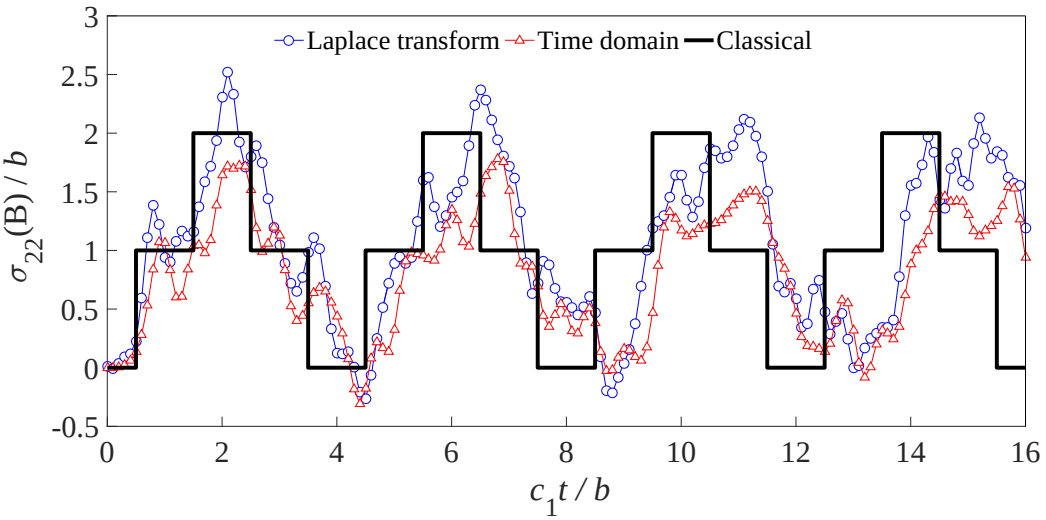

Figure 7.12: *Normalized stress* σ_{22}/b *for point B against normalized time* $c_1 t/b$ *when* $\xi_1 = 0.5$, $l = 0.1$.

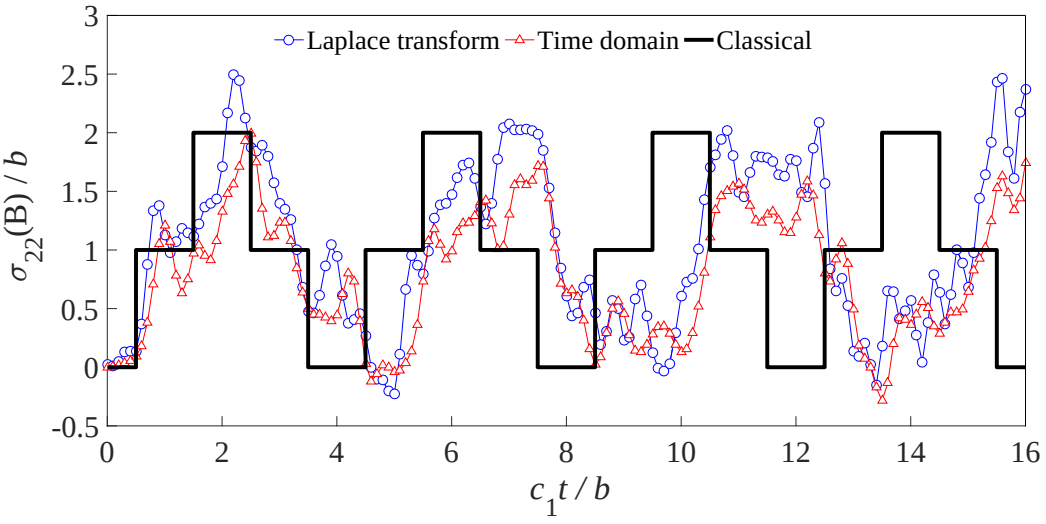

Figure 7.13: *Normalized stress σ_{22}/b for point B against normalized time $c_1 t/b$ when $\xi_1 = 0.5$, $l = 0.2$.*

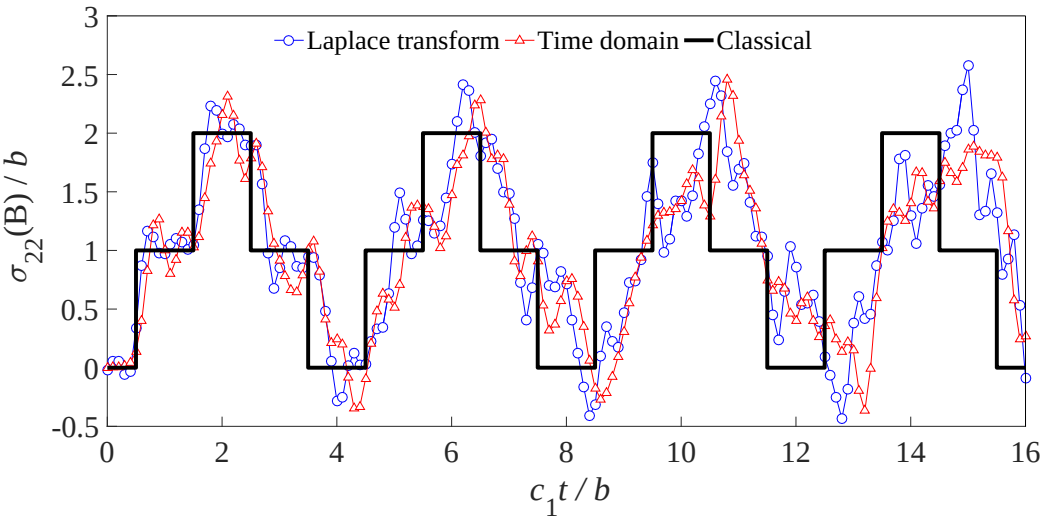

Figure 7.14: *Normalized stress σ_{22}/b for point B against normalized time $c_1 t/b$ when $\xi_1 = 0.8$, $l = 0.2$.*

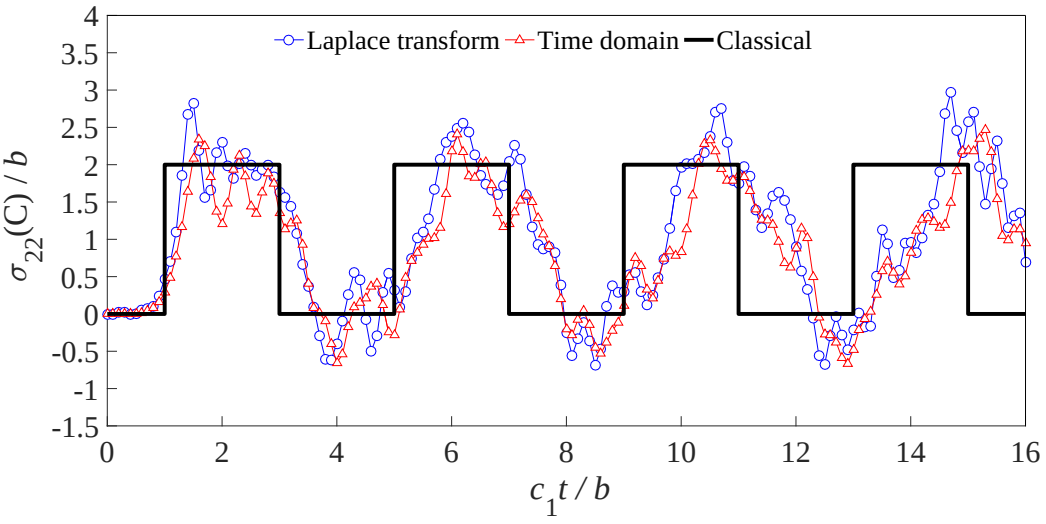

Figure 7.15: *Normalized stress σ_{22}/b for point C against normalized time $c_1 t/b$ when $\xi_1 = 0.5$, $l = 0.1$.*

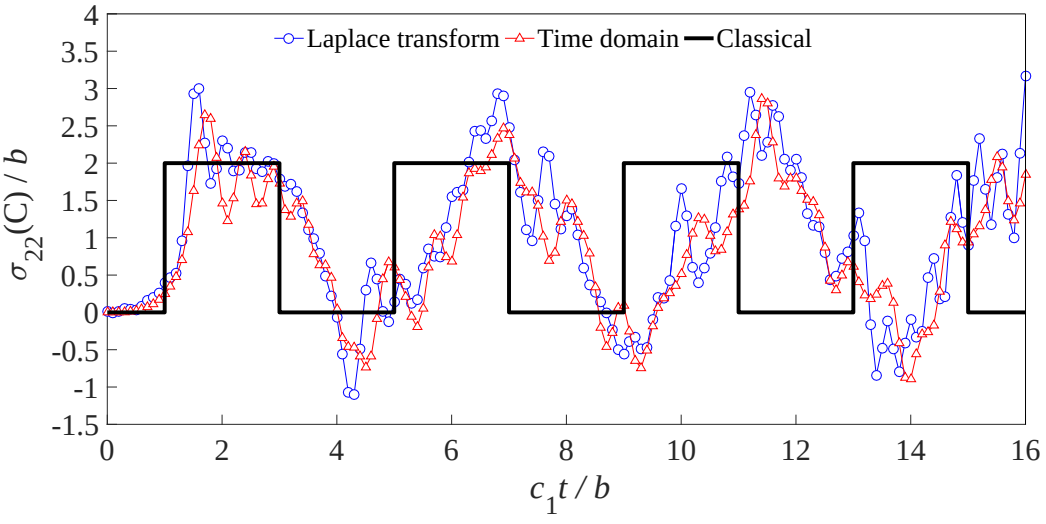

Figure 7.16: *Normalized stress σ_{22}/b for point C against normalized time $c_1 t/b$ when $\xi_1 = 0.5$, $l = 0.2$.*

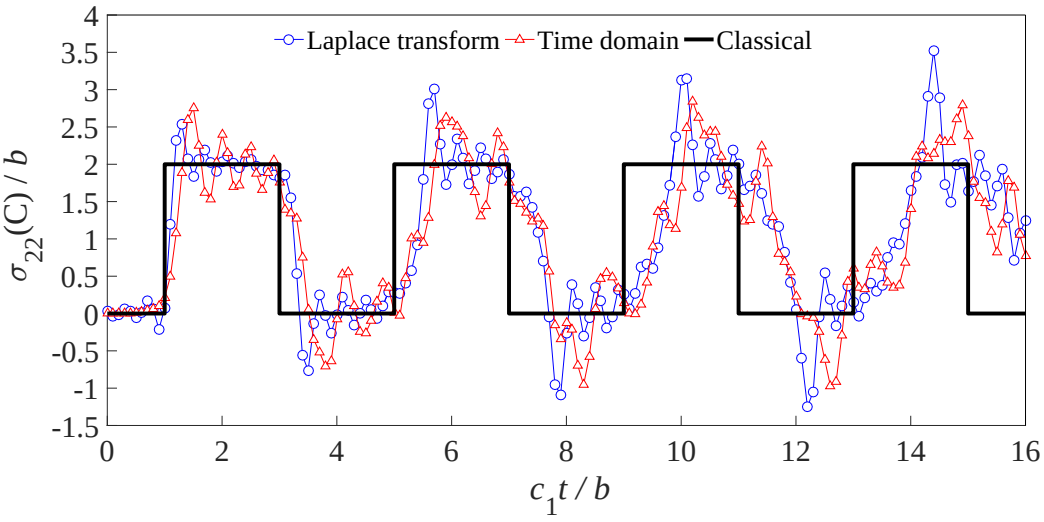

Figure 7.17: *Normalized stress σ_{22}/b for point C against normalized time $c_1 t/b$ when $\xi_1 = 0.8$, $l = 0.2$.*

7.4.2 A Ring under Internal Dynamic Pressure

In order to illustrate the application of LIEM embedded with Laplace transform method or time-domain technique to general nonlocal dynamic problems, a ring under an internal dynamic pressure is analysed as shown in Figure 7.18(a). Young's modulus $E = 1.0$, Poisson's ratio $\mu = 0.3$ and dimensions $a = 1cm$, $b = 2cm$. Due to the symmetry, only one-quarter of the ring is considered in this example. However, in the domain integrals in the governing equation, contributions of strains from the whole ring must be taken into account as presented in Figure 7.18(b). The total number of nodes and background grids are selected as 989 and 40×40, respectively. The sample number in Laplace domain is selected as 51, free parameters $\eta T = 5$ and $T/t_0 = 25$, while in the Newmark approximations, time step $\Delta t = 0.2$, and free parameters are taken as: $\gamma = 0.5$, $\beta = 0.25$.

The normalized dynamic tangential stresses at point A and B are plotted in Figure 7.19 and Figure 7.20 with the portion factor $\xi_1 = 1.0$. ABAQUS results are used for comparisons and good agreement have been achieved, which validate the

accuracy of both technique to general elastodynamic problems.

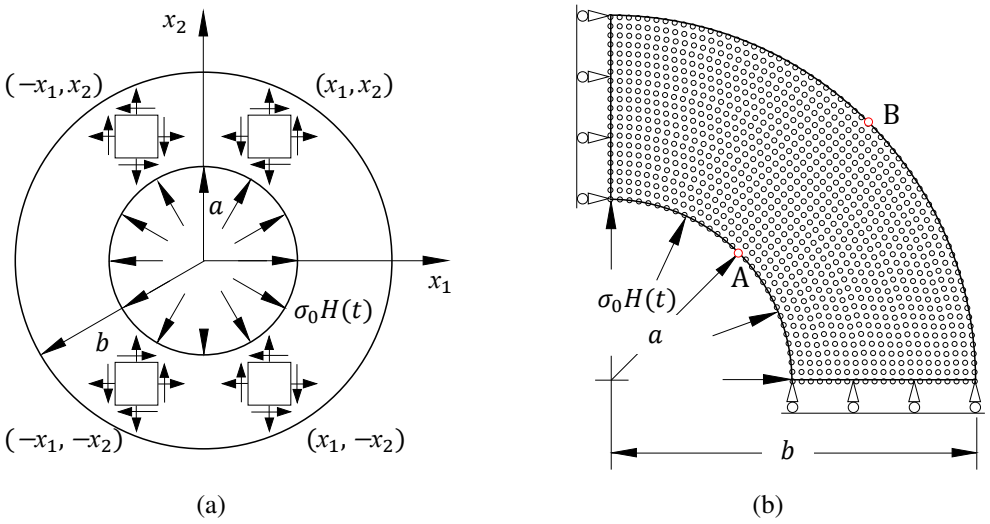

(a) (b)

Figure 7.18: *A ring under an internal dynamic pressure: (a) geometry; (b) node distributions.*

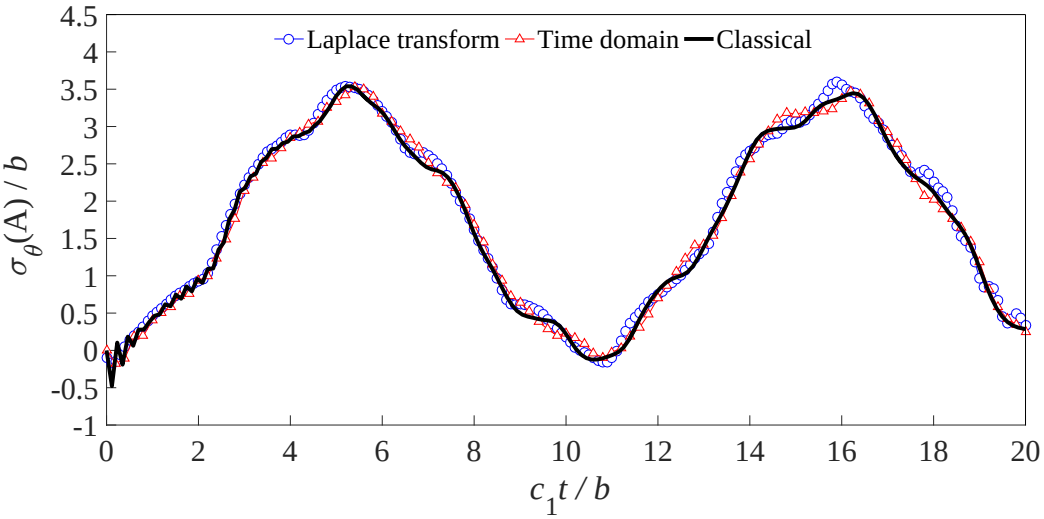

Figure 7.19: *Normalized tangential stress σ_θ/b for point A against normalized time $c_1 t/b$ when $\xi_1 = 1.0$.*

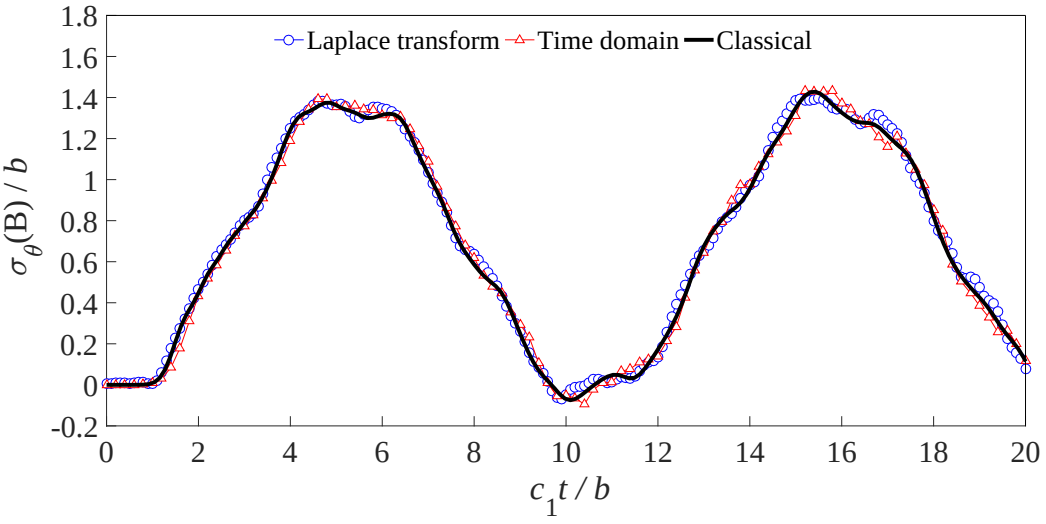

Figure 7.20: *Normalized tangential stress σ_θ/b for point B against normalized time $c_1 t/b$ when $\xi_1 = 1.0$.*

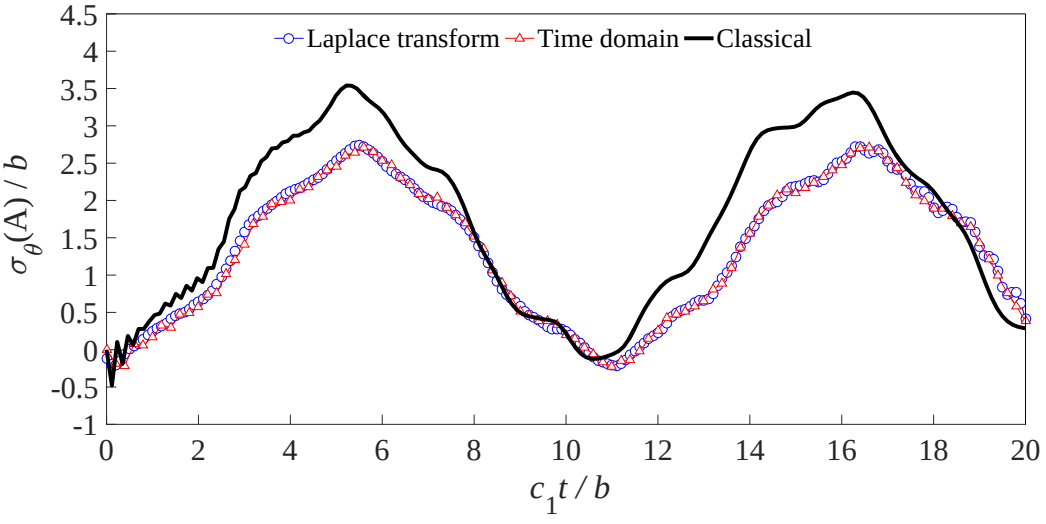

Figure 7.21: *Normalized tangential stress σ_θ/b for point A against normalized time $c_1 t/b$ when $\xi_1 = 0.5$, $l = 0.1$.*

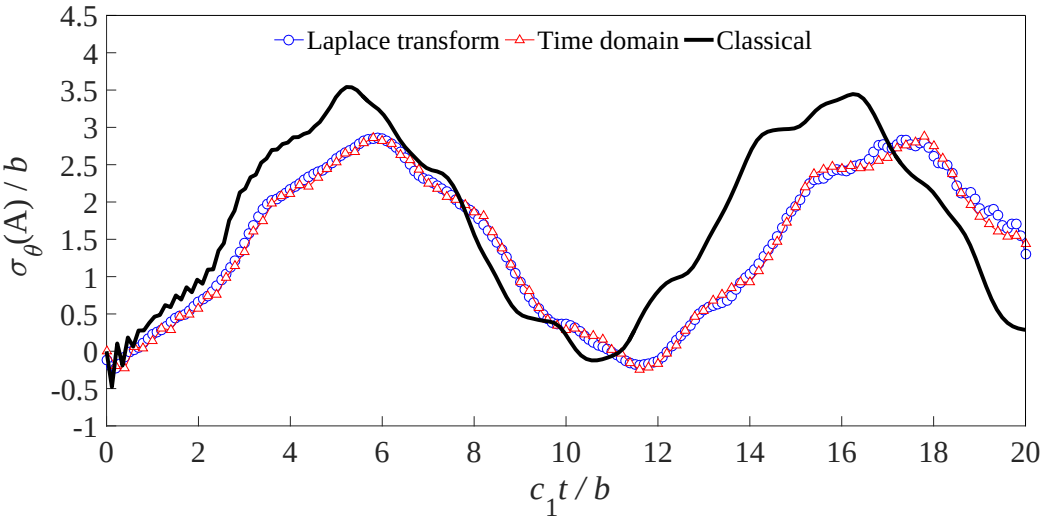

Figure 7.22: *Normalized tangential stress σ_θ/b for point A against normalized time $c_1 t/b$ when $\xi_1 = 0.5$, $l = 0.2$.*

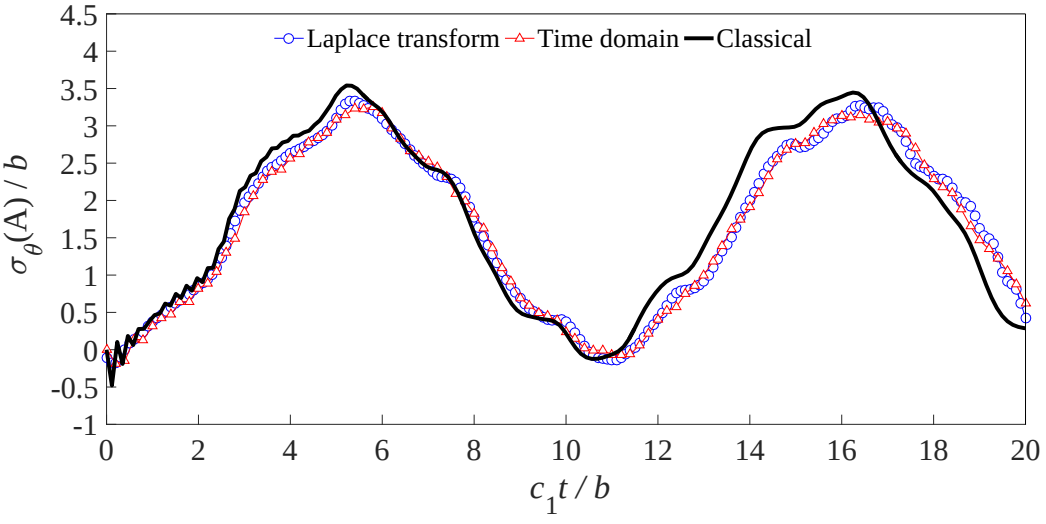

Figure 7.23: *Normalized tangential stress σ_θ/b for point A against normalized time $c_1 t/b$ when $\xi_1 = 0.8$, $l = 0.2$.*

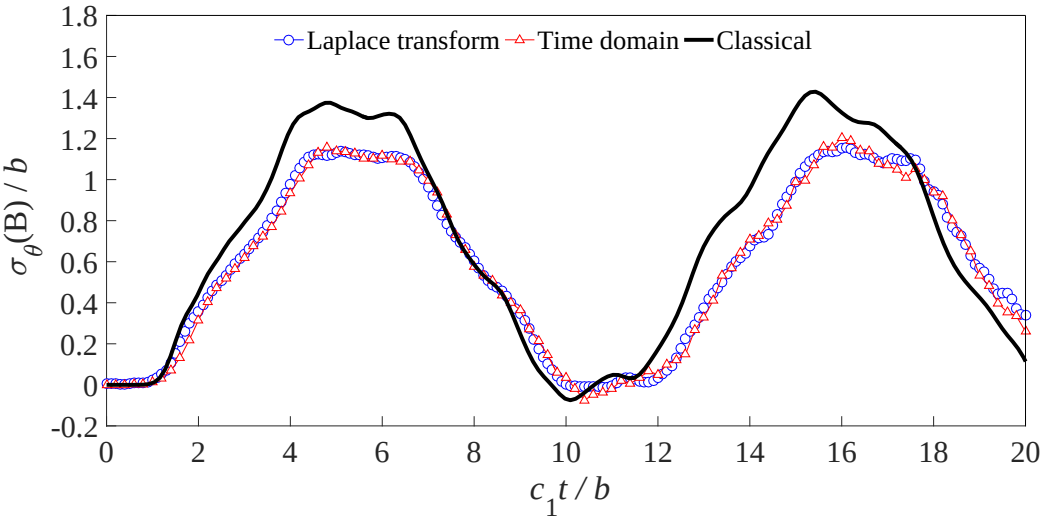

Figure 7.24: *Normalized tangential stress σ_θ/b for point B against normalized time $c_1 t/b$ when $\xi_1 = 0.5$, $l = 0.1$.*

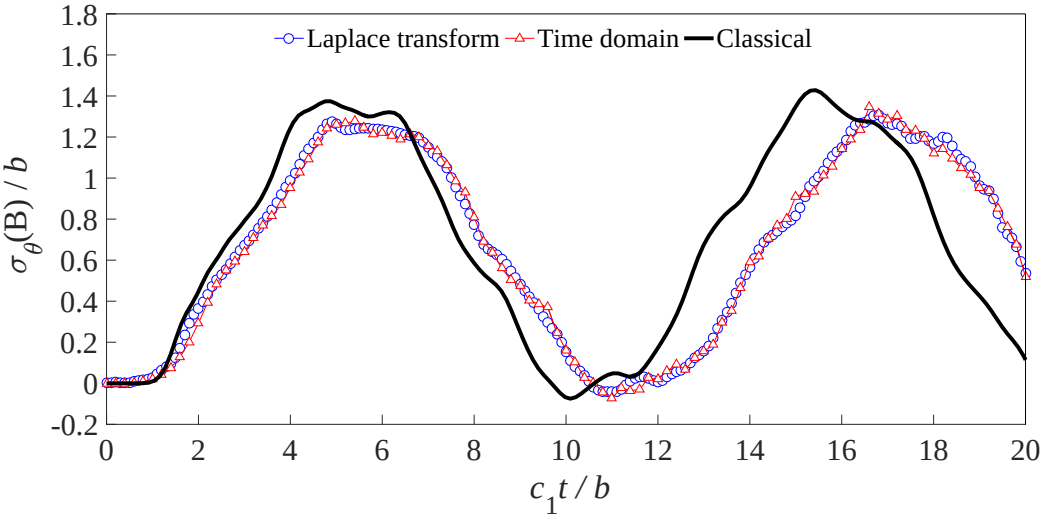

Figure 7.25: *Normalized tangential stress σ_θ/b for point B against normalized time $c_1 t/b$ when $\xi_1 = 0.5$, $l = 0.2$.*

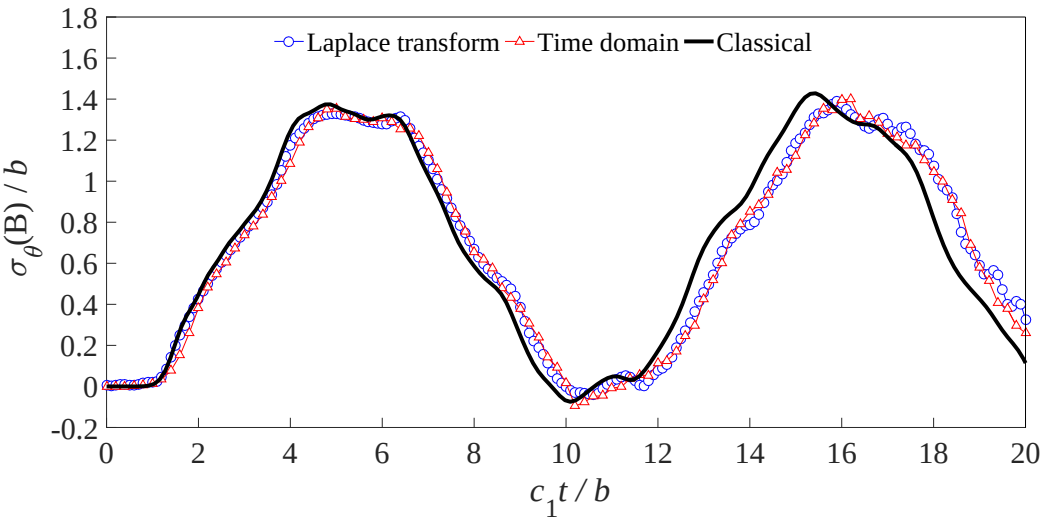

Figure 7.26: *Normalized tangential stress σ_θ/b for point B against normalized time $c_1 t/b$ when $\xi_1 = 0.8$, $l = 0.2$.*

Besides, the normalized nonlocal dynamic tangential stresses on point A and B with the characteristic length $l = 0.1$ and $l = 0.2$ for different portion factors ($\xi_1 = 0.5$ / $\xi_1 = 0.8$) are plotted in Figure 7.21 to Figure 7.26. It can be seen that the oscillation period go up when the value of l increases. And the nonlocal solutions become closed to the classical results when ξ_1 rises.

7.5 Conclusions

In this chapter, LIEM is employed to deal with 2D nonlocal elastodynamic problems both in the time domain and in the Laplace transformed domain. Consider a local integral domain and the radial basis function approximation, analytical forms of LIEM with respect to nonlocal elastodynamics are obtained. The Newmark method is selected as the approximation scheme in the time-domain method while in the Laplace transform technique, the Durbin's inversion method is adopted. Two numerical examples are carried out, and it is found that the period of oscillation increases when the portion factor ξ_1 decreases or the characteristic length l increases.

Besides, nonlocal solutions are closer to classical results when the value of ξ_1 rises, indicating that the nonlocality is less evident when the local phase becomes prominent. Numerical solutions demonstrated that both methods are stable, convergent and accurate when appropriate parameters are taken. Therefore, the aforementioned methods are efficient to solve nonlocal elasticity subjected to dynamic loads, and can be used to validate other numerical algorithms for nonlocal elastic analysis.

CHAPTER 8

Conclusions

8.1 Introduction

This last chapter concludes the thesis and suggests the possible direction for future work. The author's publications during the doctoral study are also listed.

8.2 Summary of Thesis

The research work reported in this thesis mainly focuses on the investigation of meshfree numerical methods to nonlocal elasticity. Specifically, nonlocal elastostatic problems are addressed by the meshfree strong-form method and the meshfree weak-form method, and the nonlocal elastodynamic problems are solved by the meshfree weak-form method.

In Chapter 3, the construction of meshless shape function by means of using PIM and RBF are introduced, and then RBFs are augmented by polynomials to form the RPIM shape functions. Some of the properties with respect to different types of meshless shape functions including continuity and consistency are discussed. RPIM shape functions are implemented in both 1D and 2D problem domains, and

it is found that polynomial terms only slightly affect the accuracy of the approximation. Besides, RPIM shape functions satisfy the partition of unity and possess the Kronecker delta function property within their support domains. Interpolation errors of different RPIM shape functions are examined, and it can be concluded that the free parameter c_0 in RBFs has an insignificant effect on numerical solutions. And the accuracy of the approximated function itself is higher than that of derivatives. Different RPIM shape functions are convergent if suitable parameters and field node densities are chosen. Moreover, when RPIM shape functions are locally supported, their sensitivity, accuracy and convergence improve evidently. However, the total number of field nodes located within the local support domain is supposed to purposefully selected.

In Chapter 4, formulations of Point Collocation Method (PCM), which is a strong-form meshless method, are presented for 1D and 2D solid mechanics problems. RBFs approximations are employed and governing equations are discretized directly at field nodes by certain forms of collocations. A 1D bar is set up and PCM is implemented to find out solutions numerically. It is found that duo to entire field nodes located in the problem domain are employed to construct shape functions, approximation schemes based upon the global support domain are time-consuming. Besides, it results in a set of fully populated system equations and therefore, it takes more time to solve the discretized algebraic equations. On the contrary, locally supported approximation schemes lead to a sparse system matrix, which significantly reduce the computational efforts. Different kinds of RBF approximations in PCM, i.e. EXP-RBF and MQ-RBF are examined as well. It shows that globally supported EXP-RBF in PCM gives rise to singularity and is sensitive to the varying of the free parameter. However, aforementioned issues can be solved easily by using local support domains when carrying out the approximations. What is more, MQ-RBF in PCM is always providing decent solutions in spite of local or global

support domains employed and changes of the free parameter, which indicates that MQ-RBF are numerically more stable and reliable. Finally, three 2D numerical examples are carried out to investigate the application of PCM to general problems. Abaqus contour plots and solutions are reported as well for comparison purposes. The convenience, accuracy and computational efficiency of PCM are demonstrated.

In Chapter 5, mathematical formulations of meshless Local Integral Equation Method (LIEM) based upon the local weak-form are presented for 2D isotropic solids. By taking advantage of the MQ RBF approximation scheme, analytical solutions for domain integrals in LIEM are derived. Three numerical examples are carried out to investigate the accuracy, convergence and the influence of related parameters of LIEM. It shows that duo to the employment of closed forms of local integrals, computational efficiency of LIEM improves obviously. Additionally, observations with respect to parameters including the number of straight lines that enclose the local integral domain as well as the integral radius indicate that they have slight effects on LIEM solutions. And the convergence study demonstrates that LIEM solutions converge rapidly when the densities of field nodes within the problem domain goes up and only a little time is needed for the coefficient matrix calculation. However, a large amount of time has been spent on solving the discretized system equations when the density of field nodes increases. Finally, comparisons have been made with Abaqus and PCM results, showing good agreements and validating the accuracy of LIEM solutions.

In Chapter 6, PCM and LIEM are applied to nonlocal elastostatics and referred to as NL-PCM and NL-LIEM, respectively. Firstly, the Eringen's model that characterized by an attenuation function is introduced. The equilibrium equation is approximated by means of using RPIM shape functions, and a set of discretized system equations are derived by directly collocating at field nodes in NL-PCM. In addition, background grids are introduced to carry out domain integrals in nonlo-

cal constitutive relations, and a four-point standard integral scheme is made use of. While in NL-LIEM, nonlocal constitutive relations are substituted into local boundary integral equations for each local domain and the final system equations are obtained by taking advantages of RBF approximations as well as the four-point standard integral scheme. Then, three illustrated examples are conducted to study the application of NL-PCM and NL-LIEM to 2D nonlocal elastostatic problems. The influence of characteristic length and portion factor are analyzed, and it can be concluded that the nonlocal effect spreads towards the core domain when the value of characteristic length goes up. In the meanwhile, nonlocal solutions at geometrical boundaries increase. Besides, the lower the value of portion factor ξ_1 is, the more nonlocality are shown, which accords with the physical interpretation of the Eringen's model. Comparisons among solutions from NL-PCM, NL-LIEM and references show good agreements, validating the accuracy and effectiveness of meshless methods for solving static nonlocal problems. But, NL-PCM is more computational efficient because of its collocation nature.

In Chapter 7, LIEM is employed to solve nonlocal elastodynamic problems. By use of the divergence theorem and the step function, the weak-form of the governing equation of motion with respect to nonlocal constitutive relations are obtained. Time marching is carried out both in the Laplace transform domain and the time domain. The Durbin's inverse transformation method is employed in the Laplace transform method to obtain numerical results in the real time domain. While in the time-domain technique, the Newmark scheme is adopted without domain transformations. Domain integrals in both approaches are treated by the four-point standard integral scheme. Then, two 2D nonlocal elastodynamic examples are presented, and the influence of characteristic length and portion factor on dynamic cases are studied as well. Numerical solutions indicate that the period of oscillation decreases when the portion factor ξ_1 increases or the characteristic length l drops.

Besides, nonlocal solutions tend to classical ones when the value of ξ_1 rises duo to the fact that nonlocal effects are less evident when the local phase in the constitutive relation becomes prominent. Comparisons with classical solutions show good agreement and nonlocal solutions of both methods coincide with each other, which demonstrate that both approaches are accurate, stable and reliable when appropriate parameters are chosen.

8.3 Future Work

The research exhibited in this thesis can be extended to the following aspects:

- The first is the follow-up work related to nonlocal problems.

    1. Only some basic numerical examples are presented in this thesis. Therefore, meshless methods can be extended to deal with more specific issues characterized by nonlocality.
    2. This thesis mainly focuses on 2D nonlocal problems. However, it can be extended to 3D nonlocal cases without much difficulties.
    3. Abaqus provides extensive user subroutines that allow users to adapt it to their particular analysis requirements. As a consequence, it can be used for comparisons if an Abaqus subroutine related to nonlocal constitutive is developed.
    4. Nonlocal numerical results at geometrical boundaries presented in this thesis show nonhomogeneous fields. It has been pointed out in the context of damage that nonlocal formulations of integral type are lack of symmetry since nonlocal interactions are changing nearby the boundaries. Some remedies related to the modification of the nonlocal kernel

have been developed with respect to damage model based on physical considerations, which can be used for reference and introduced to nonlocal elasticity.

5. The time-domain approach is a step-by-step solution technique, and can be easily applied to evaluate dynamic responses of nonlocal problems with physical and geometrical nonlinearities.

6. Extend nonlocal theories to size-dependent materials such as nanoplates and nanobeams, and then investigate their nonlocal properties.

- The second is to apply meshless methods to other new areas of research.

1. Meshless methods are effective ways to avoid mesh distortions. Thus, they can be applied to large deformation analysis and metal forming process simulations.

2. Meshless methods are able to effectively predict the crack extension due to the numerical difficulties resulting from mesh reconstructions are absent.

3. Applications of meshless approached to other research fields such as the heat transfer problems, fluid problems and even electromagnetic problems deserve beneficial attempts.

8.4 List of Publications

The author's publications during the doctoral study are listed below:

1. **XJ Huang** and PH Wen, *Meshless local integral equation method for two-dimensional nonlocal elastodynamic problems*. The 10th International Con-

ference and Workshop on Numerical Simulation of 3D Sheet Metal Forming Processes, Bristol, UK, 4-9 September 2016. (Oral presentation)

2. PH Wen, **XJ Huang** and MH Aliabadi, *Meshless approaches for fracture with nonlocal elasticity*. Key Engineering Materials, 627, 357-360 (2015).

3. PH Wen, **XJ Huang** and MH Aliabadi, *High accurate solutions of nonlocal elasticity for sphere*. Key Engineering Materials, 577-578, 509-512 (2014).

4. PH Wen, **XJ Huang** and MH Aliabadi, *Fracture with nonlocal elasticity: analytical and meshless approaches*. European Journal of Computational Mechanics, 23, 217-234 (2014).

5. PH Wen, **XJ Huang** and MH Aliabadi, *Two Dimensional Nonlocal Elasticity Analysis by Local Integral Equation Method*. Computer Modeling in Engineering and Science, 96(3), 199-225 (2013).

Bibliography

[1] E Kröner. Elasticity theory of materials with long range cohesive forces. *International Journal of Solids and Structures*, 3(5):731–742, 1967.

[2] IA Kunin. The theory of elastic media with microstructure and the theory of dislocations. In *Mechanics of generalized continua*, pages 321–329. Springer, 1968.

[3] JA Krumhansl. Some considerations of the relation between solid state physics and generalized continuum mechanics. In *Mechanics of generalized continua*, pages 298–311. Springer, 1968.

[4] DGB Edelen, AE Green, and N Laws. Nonlocal continuum mechanics. *Archive for Rational Mechanics and Analysis*, 43(1):36–44, 1971.

[5] A Cemal Eringen. Nonlocal polar elastic continua. *International journal of engineering science*, 10(1):1–16, 1972.

[6] Castrenze Polizzotto. Nonlocal elasticity and related variational principles. *International Journal of Solids and Structures*, 38(42):7359–7380, 2001.

[7] C Polizzotto, P Fuschi, and AA Pisano. A nonhomogeneous nonlocal elasticity model. *European Journal of Mechanics-A/Solids*, 25(2):308–333, 2006.

[8] Rodrigue Desmorat, Fabrice Gatuingt, and Frédéric Ragueneau. Nonlocal anisotropic damage model and related computational aspects for quasi-brittle materials. *Engineering Fracture Mechanics*, 74(10):1539–1560, 2007.

[9] Antonio Sellitto, Vito Antonio Cimmelli, and David Jou. Weakly nonlocal and nonlinear heat transport. In *Mesoscopic Theories of Heat Transport in Nanosystems*, pages 109–132. 2016.

[10] Castrenze Polizzotto. Thermodynamics-based gradient plasticity theories with an application to interface models. *International Journal of Solids and Structures*, 45(17):4820–4834, 2008.

[11] CW Lim, G Zhang, and JN Reddy. A higher-order nonlocal elasticity and strain gradient theory and its applications in wave propagation. *Journal of the Mechanics and Physics of Solids*, 78:298–313, 2015.

[12] L Vermare, P Hennequin, V Berionni, PH Diamond, G Dif-Pradalier, X Garbet, P Ghendrih, V Grandgirard, CJ McDevitt, P Morel, et al. Structure of nonlocality of plasma turbulence. *Nuclear Fusion*, 53(7):073029, 2013.

[13] H Stumpf, J Makowski, and K Hackl. Dynamical evolution of fracture process region in ductile materials. *International Journal of Plasticity*, 25(5):995–1010, 2009.

[14] Raffaele Barretta and Francesco Marotti de Sciarra. A nonlocal model for carbon nanotubes under axial loads. *Advances in Materials Science and Engineering*, 2013, 2013.

[15] Raffaele Barretta, Luciano Feo, Raimondo Luciano, and Francesco Marotti de Sciarra. Variational formulations for functionally graded nonlocal bernoulli–euler nanobeams. *Composite Structures*, 129:80–89, 2015.

[16] Ammar A Alsheghri and Rashid K Abu Al-Rub. Thermodynamic-based cohesive zone healing model for self-healing materials. *Mechanics Research Communications*, 70:102–113, 2015.

[17] A Cemal Eringen and Byoung Sung Kim. Stress concentration at the tip of crack. *Mechanics Research Communications*, 1(4):233–237, 1974.

[18] A Cemal Eringen, CG Speziale, and BS Kim. Crack-tip problem in non-local elasticity. *Journal of the Mechanics and Physics of Solids*, 25(5):339–355, 1977.

[19] R Abdollahi and B Boroomand. Benchmarks in nonlocal elasticity defined by eringen's integral model. *International Journal of Solids and Structures*, 50(18):2758–2771, 2013.

[20] AC Eringen. Theory of nonlocal elasticity and some applications. Technical report, DTIC Document, 1984.

[21] Zhen-Gong Zhou and Biao Wang. Nonlocal theory solution of two collinear cracks in the functionally graded materials. *International journal of solids and structures*, 43(5):887–898, 2006.

[22] Jun Liang. The nonlocal theory solution of a mode-i crack in functionally graded materials. *Science in China Series E: Technological Sciences*, 52(4):1101–1111, 2009.

[23] K Stamoulis and AE Giannakopoulos. Size effects on strength, toughness and fatigue crack growth of gradient elastic solids. *International Journal of Solids and Structures*, 45(18):4921–4935, 2008.

[24] Giuliano Allegri and Fabrizio L Scarpa. On the asymptotic crack-tip stress fields in nonlocal orthotropic elasticity. *International Journal of Solids and Structures*, 51(2):504–515, 2014.

[25] S Mahmoud Mousavi and Markus Lazar. Distributed dislocation technique for cracks based on non-singular dislocations in nonlocal elasticity of helmholtz type. *Engineering Fracture Mechanics*, 136:79–95, 2015.

[26] John Peddieson, George R Buchanan, and Richard P McNitt. Application of nonlocal continuum models to nanotechnology. *International Journal of Engineering Science*, 41(3):305–312, 2003.

[27] CM Wang, YY Zhang, Sai Sudha Ramesh, and S Kitipornchai. Buckling analysis of micro-and nano-rods/tubes based on nonlocal timoshenko beam theory. *Journal of Physics D: Applied Physics*, 39(17):3904, 2006.

[28] SC Pradhan and JK Phadikar. Nonlocal elasticity theory for vibration of nanoplates. *Journal of Sound and Vibration*, 325(1):206–223, 2009.

[29] T Murmu, J Sienz, S Adhikari, and C Arnold. Nonlocal buckling of double-nanoplate-systems under biaxial compression. *Composites Part B: Engineering*, 44(1):84–94, 2013.

[30] Liao-Liang Ke, Chen Liu, and Yue-Sheng Wang. Free vibration of nonlocal piezoelectric nanoplates under various boundary conditions. *Physica E: Low-dimensional Systems and Nanostructures*, 66:93–106, 2015.

[31] Chen Liu, Liao-Liang Ke, Yue-Sheng Wang, and Jie Yang. Nonlinear vibration of nonlocal piezoelectric nanoplates. *International Journal of Structural Stability and Dynamics*, 15(08):1540013, 2015.

[32] Metin Aydogdu. A general nonlocal beam theory: its application to nanobeam bending, buckling and vibration. *Physica E: Low-dimensional Systems and Nanostructures*, 41(9):1651–1655, 2009.

[33] Huu-Tai Thai. A nonlocal beam theory for bending, buckling, and vibration of nanobeams. *International Journal of Engineering Science*, 52:56–64, 2012.

[34] MA Eltaher, Samir A Emam, and FF Mahmoud. Static and stability analysis of nonlocal functionally graded nanobeams. *Composite Structures*, 96:82–88, 2013.

[35] Reza Nazemnezhad and Shahrokh Hosseini-Hashemi. Nonlocal nonlinear free vibration of functionally graded nanobeams. *Composite Structures*, 110:192–199, 2014.

[36] B Arash and Q Wang. A review on the application of nonlocal elastic models in modeling of carbon nanotubes and graphenes. *Computational Materials Science*, 51(1):303–313, 2012.

[37] Ali Alavinasab, Ratneshwar Jha, and G Ahmadi. Modeling of carbon nanotube composites based on nonlocal elasticity approach. *International Journal for Computational Methods in Engineering Science and Mechanics*, 15(1):17–25, 2014.

[38] Arya Fallahi, Tony Low, Michele Tamagnone, and Julien Perruisseau-Carrier. Nonlocal electromagnetic response of graphene nanostructures. *Physical Review B*, 91(12):121405, 2015.

[39] Dominik Rogula. Introduction to nonlocal theory of material media. In *Nonlocal theory of material media*, pages 123–222. 1982.

[40] S Burhanettin Altan. Uniqueness of initial-boundary value problems in nonlocal elasticity. *International journal of solids and structures*, 25(11):1271–1278, 1989.

[41] SB Altan. Existence in nonlocal elasticity. *Archives of Mechanics*, 41(1):25–36, 1989.

[42] Zdenek P Bazant and Milan Jirásek. Nonlocal integral formulations of plasticity and damage: survey of progress. *Journal of Engineering Mechanics*, 128(11):1119–1149, 2002.

[43] AA Pisano, A Sofi, and P Fuschi. Nonlocal integral elasticity: 2d finite element based solutions. *International Journal of Solids and Structures*, 46(21):3836–3849, 2009.

[44] Ted Belytschko and Tom Black. Elastic crack growth in finite elements with minimal remeshing. *International journal for numerical methods in engineering*, 45(5):601–620, 1999.

[45] SS Nanthakumar, T Lahmer, and T Rabczuk. Detection of multiple flaws in piezoelectric structures using xfem and level sets. *Computer Methods in Applied Mechanics and Engineering*, 275:98–112, 2014.

[46] Saleh Yazdani, Wilhelm JH Rust, and Peter Wriggers. An xfem approach for modelling delamination in composite laminates. *Composite Structures*, 135:353–364, 2016.

[47] YP Chen, JD Lee, and A Eskandarian. Dynamic meshless method applied to nonlocal crack problems. *Theoretical and applied fracture mechanics*, 38(3):293–300, 2002.

[48] Jan Sladek, Vladimir Sladek, and Zdeněk P Bažant. Non-local boundary integral formulation for softening damage. *International Journal for Numerical Methods in Engineering*, 57(1):103–116, 2003.

[49] CMC Roque, AJM Ferreira, and JN Reddy. Analysis of timoshenko nanobeams with a nonlocal formulation and meshless method. *International Journal of Engineering Science*, 49(9):976–984, 2011.

[50] S Kazem and JA Rad. Radial basis functions method for solving of a nonlocal boundary value problem with neumanns boundary conditions. *Applied Mathematical Modelling*, 36(6):2360–2369, 2012.

[51] PH Wen, XJ Huang, and MH Aliabadi. Two dimensional nonlocal elasticity analysis by local integral equation method. *Special Issue: Advances in Boundary Element Techniques Guest Editors: Antoine Sellier and Ferri Aliabadi*, page 199, 2013.

[52] PH Wen, XJ Huang, and MH Aliabadi. High accurate solutions of nonlocal elasticity for sphere. In *Key Engineering Materials*, volume 577, pages 509–512, 2014.

[53] PH Wen, XJ Huang, and MH Aliabadi. Fracture with nonlocal elasticity:

analytical and meshless approaches. *European Journal of Computational Mechanics*, 23(5-6):217–234, 2014.

[54] Tadeusz Liszka and Janusz Orkisz. The finite difference method at arbitrary irregular grids and its application in applied mechanics. *Computers & Structures*, 11(1-2):83–95, 1980.

[55] Leon B Lucy. A numerical approach to the testing of the fission hypothesis. *The astronomical journal*, 82:1013–1024, 1977.

[56] Robert A Gingold and Joseph J Monaghan. Smoothed particle hydrodynamics: theory and application to non-spherical stars. *Monthly notices of the royal astronomical society*, 181(3):375–389, 1977.

[57] Joseph J Monaghan. An introduction to sph. *Computer physics communications*, 48(1):89–96, 1988.

[58] Ted Belytschko, Yury Krongauz, Daniel Organ, Mark Fleming, and Petr Krysl. Meshless methods: an overview and recent developments. *Computer methods in applied mechanics and engineering*, 139(1):3–47, 1996.

[59] Gordon R Johnson and Stephen R Beissel. Normalized smoothing functions for sph impact computations. *International Journal for Numerical Methods in Engineering*, 39(16):2725–2741, 1996.

[60] CT Dyka and RP Ingel. Addressing tension instability in sph methods. Technical report, DTIC Document, 1994.

[61] R Vignjevic, J Campbell, and L Libersky. A treatment of zero-energy modes in the smoothed particle hydrodynamics method. *Computer methods in Applied mechanics and Engineering*, 184(1):67–85, 2000.

[62] Joe J Monaghan. Smoothed particle hydrodynamics. *Annual review of astronomy and astrophysics*, 30:543–574, 1992.

[63] MB Liu, GR Liu, Z Zong, and KY Lam. Numerical simulation of incompressible flows by sph. In *International Conference on Scientific & Engineering Computational, Beijing*, 2001.

[64] Joe J Monaghan. Simulating gravity currents with sph lock gates. *Annual review of astronomy and astrophysics*.

[65] Paul W Cleary. Modelling confined multi-material heat and mass flows using sph. *Applied Mathematical Modelling*, 22(12):981–993, 1998.

[66] PW Randles and LD Libersky. Smoothed particle hydrodynamics: some recent improvements and applications. *Computer methods in applied mechanics and engineering*, 139(1):375–408, 1996.

[67] MB Liu, GR Liu, KY Lam, and Z Zong. Smoothed particle hydrodynamics for numerical simulation of underwater explosion. *Computational Mechanics*, 30(2):106–118, 2003.

[68] Peter Lancaster and Kes Salkauskas. Surfaces generated by moving least squares methods. *Mathematics of computation*, 37(155):141–158, 1981.

[69] B Nayroles, G Touzot, and P Villon. Generalizing the finite element method: diffuse approximation and diffuse elements. *Computational mechanics*, 10(5):307–318, 1992.

[70] P Breitkopf, A Rassineux, J-M Savignat, and P Villon. Integration constraint in diffuse element method. *Computer Methods in Applied Mechanics and Engineering*, 193(12):1203–1220, 2004.

[71] Ted Belytschko, Yun Yun Lu, and Lei Gu. Element-free galerkin methods. *International journal for numerical methods in engineering*, 37(2):229–256, 1994.

[72] H-J Chung and T Belytschko. An error estimate in the efg method. *Computational mechanics*, 21(2):91–100, 1998.

[73] Ted Belytschko, Yury Krongauz, Mark Fleming, Daniel Organ, and Wing Kam Snm Liu. Smoothing and accelerated computations in the element free galerkin method. *Journal of Computational and Applied Mathematics*, 74(1):111–126, 1996.

[74] John Dolbow and Ted Belytschko. Numerical integration of the galerkin weak form in meshfree methods. *Computational mechanics*, 23(3):219–230, 1999.

[75] T Belytschko, D Organ, and C Gerlach. Element-free galerkin methods for dynamic fracture in concrete. *Computer Methods in Applied Mechanics and Engineering*, 187(3):385–399, 2000.

[76] Petr Krysl and Ted Belytschko. Analysis of thin shells by the element-free galerkin method. *International Journal of Solids and Structures*, 33(20):3057–3080, 1996.

[77] D Hegen. Element-free galerkin methods in combination with finite element approaches. *Computer Methods in Applied Mechanics and Engineering*, 135(1):143–166, 1996.

[78] Chongjiang Du. An element-free galerkin method for simulation of stationary two-dimensional shallow water flows in rivers. *Computer methods in applied mechanics and engineering*, 182(1):89–107, 2000.

[79] LW Cordes and B Moran. Treatment of material discontinuity in the element-free galerkin method. *Computer Methods in Applied Mechanics and Engineering*, 139(1):75–89, 1996.

[80] Xiong Zhang, Mingwan Lu, and JL Wegner. A 2-d meshless model for jointed rock structures. *International Journal for Numerical Methods in Engineering*, 47(10):1649–1661, 2000.

[81] Wing Kam Liu, Sukky Jun, and Yi Fei Zhang. Reproducing kernel parti-

cle methods. *International journal for numerical methods in fluids*, 20(8-9):1081–1106, 1995.

[82] Wing Kam Liu, Yijung Chen, R Aziz Uras, and Chin Tang Chang. Generalized multiple scale reproducing kernel particle methods. *Computer Methods in Applied Mechanics and Engineering*, 139(1):91–157, 1996.

[83] RA Uras, C-T Chang, Y Chen, and WK Liu. Multiresolution reproducing kernel particle methods in acoustics. *Journal of Computational Acoustics*, 5(01):71–94, 1997.

[84] Gregory J Wagner and Wing Kam Liu. Turbulence simulation and multiple scale subgrid models. *Computational Mechanics*, 25(2-3):117–136, 2000.

[85] Sang-Ho Lee, Hyo-Jin Kim, and Sukky Jun. Two scale meshfree method for the adaptivity of 3-d stress concentration problems. *Computational mechanics*, 26(4):376–387, 2000.

[86] J-S Chen, H-P Wang, S Yoon, and Y You. Some recent improvements in meshfree methods for incompressible finite elasticity boundary value problems with contact. *Computational Mechanics*, 25(2-3):137–156, 2000.

[87] Jiun-Shyan Chen, Cristina Maria Oliveira Lima Roque, Chunhui Pan, and Sérgio Tonini Button. Analysis of metal forming process based on meshless method. *Journal of Materials Processing Technology*, 80:642–646, 1998.

[88] Brian M Donning and Wing Kam Liu. Meshless methods for shear-deformable beams and plates. *Computer Methods in Applied Mechanics and Engineering*, 152(1):47–71, 1998.

[89] NR Aluru. A reproducing kernel particle method for meshless analysis of microelectromechanical systems. *Computational Mechanics*, 23(4):324–338, 1999.

[90] C Armando Duarte and J Tinsley Oden. Hp clouds-an hp meshless method.

Numerical methods for partial differential equations, 12(6):673–706, 1996.

[91] Wing-Kam Liu, Shaofan Li, and Ted Belytschko. Moving least-square reproducing kernel methods (i) methodology and convergence. *Computer methods in applied mechanics and engineering*, 143(1):113–154, 1997.

[92] P de TR Mendonça, CS de Barcellos, and A Duarte. Investigations on the hp-cloud method by solving timoshenko beam problems. *Computational Mechanics*, 25(2-3):286–295, 2000.

[93] Oscar Garcia, Eduardo A Fancello, Clovis S de Barcellos, and C Armando Duarte. hp-clouds in mindlin's thick plate model. *International Journal for Numerical Methods in Engineering*, 47(8):1381–1400, 2000.

[94] John Dolbow, Nicolas Moës, and Ted Belytschko. Discontinuous enrichment in finite elements with a partition of unity method. *Finite elements in analysis and design*, 36(3):235–260, 2000.

[95] CA Duarte, ON Hamzeh, TJ Liszka, and WW Tworzydlo. A generalized finite element method for the simulation of three-dimensional dynamic crack propagation. *Computer Methods in Applied Mechanics and Engineering*, 190(15):2227–2262, 2001.

[96] Jens M Melenk and Ivo Babuška. The partition of unity finite element method: basic theory and applications. *Computer methods in applied mechanics and engineering*, 139(1):289–314, 1996.

[97] E Onate, S Idelsohn, OC Zienkiewicz, and RL Taylor. A finite point method in computational mechanics. applications to convective transport and fluid flow. *International journal for numerical methods in engineering*, 39(22):3839–3866, 1996.

[98] E Onate, S Idelsohn, OC Zienkiewicz, RL Taylor, and C Sacco. A stabilized finite point method for analysis of fluid mechanics problems. *Computer*

Methods in Applied Mechanics and Engineering, 139(1):315–346, 1996.

[99] Eugenio Oñate, F Perazzo, and J Miquel. A finite point method for elasticity problems. *Computers & Structures*, 79(22):2151–2163, 2001.

[100] Enrique Ortega, Eugenio Oñate, Sergio Idelsohn, and Chinapat Buachart. An adaptive finite point method for the shallow water equations. *International journal for numerical methods in engineering*, 88(2):180–204, 2011.

[101] NR Aluru. A point collocation method based on reproducing kernel approximations. *International Journal for Numerical Methods in Engineering*, 47(6):1083–1121, 2000.

[102] RR Ohs and NR Aluru. Meshless analysis of piezoelectric devices. *Computational Mechanics*, 27(1):23–36, 2001.

[103] Xiaozhong Jin, Gang Li, and NR Aluru. Positivity conditions in meshless collocation methods. *Computer methods in applied mechanics and engineering*, 193(12):1171–1202, 2004.

[104] Satya N Atluri and Tulong Zhu. A new meshless local petrov-galerkin (mlpg) approach in computational mechanics. *Computational mechanics*, 22(2):117–127, 1998.

[105] Satya N Atluri1& Shengping Shen. The meshless local petrov-galerkin (mlpg) method: A simple & less-costly alternative to the finite element and boundary element methods. *Computer Modeling in Engineering & Sciences*, 3:11–51, 2002.

[106] SN Atluri and T-L Zhu. The meshless local petrov-galerkin (mlpg) approach for solving problems in elasto-statics. *Computational Mechanics*, 25(2-3):169–179, 2000.

[107] SN Atluri and Tulong Zhu. New concepts in meshless methods. *International Journal for Numerical Methods in Engineering*, 47(1-3):537–556, 2000.

[108] SN Atluri, JY Cho, and H-G Kim. Analysis of thin beams, using the meshless local petrov–galerkin method, with generalized moving least squares interpolations. *Computational Mechanics*, 24(5):334–347, 1999.

[109] JY Cho and SN Atluri. Analysis of shear flexible beams, using the meshless local petrov-galerkin method, based on a locking-free formulation. *Engineering Computations*, 18(1/2):215–240, 2001.

[110] Shuyao Long and SN Atluri. A meshless local petrov-galerkin method for solving the bending problem of a thin plate. *Computer Modeling in Engineering and Sciences*, 3(1):53–64, 2002.

[111] YT Gu and GR Liu. A meshless local petrov-galerkin (mlpg) formulation for static and free vibration analyses of thin plates. *Computer Modeling in Engineering and Sciences*, 2(4):463–476, 2001.

[112] HK Ching and RC Batra. Determination of crack tip fields in linear elastostatics by the meshless local petrov-galerkin (mlpg) method. *CMES- Computer Modeling in Engineering and Sciences*, 2(2):273–289, 2001.

[113] YL Wu, GR Liu, and YuanTong Gu. Application of meshless local petrov-galerkin (mlpg) approach to simulation of incompressible flow. *Numerical Heat Transfer, Part B: Fundamentals*, 48(5):459–475, 2005.

[114] Ying Liu and Ling Tian Gao. Numerical simulation for dynamic crack propagation by mlpg. In *Key Engineering Materials*, volume 324, pages 495–498, 2006.

[115] ZD Han, HT Liu, AM Rajendran, and SN Atluri. The applications of meshless local petrov-galerkin (mlpg) approaches in high-speed impact, penetration and perforation problems. *CMC-TECH SCIENCE PRESS-*, 4(2):119, 2006.

[116] Tulong Zhu, Jindong Zhang, and SN Atluri. A meshless numerical method

based on the local boundary integral equation (lbie) to solve linear and non-linear boundary value problems. *Engineering Analysis with Boundary Elements*, 23(5):375–389, 1999.

[117] Edward J Kansa. Multiquadricsa scattered data approximation scheme with applications to computational fluid-dynamicsi surface approximations and partial derivative estimates. *Computers & Mathematics with applications*, 19(8):127–145, 1990.

[118] Bartur Jumarhon, Sia Amini, and Ke Chen. The hermite collocation method using radial basis functions. *Engineering analysis with boundary elements*, 24(7):607–611, 2000.

[119] Manuel Kindelan, Francisco Bernal, Pedro González-Rodríguez, and Miguel Moscoso. Application of the rbf meshless method to the solution of the radiative transport equation. *Journal of Computational Physics*, 229(5):1897–1908, 2010.

[120] Soheil Soleimani, M Jalaal, H Bararnia, E Ghasemi, DD Ganji, and F Mohammadi. Local rbf-dq method for two-dimensional transient heat conduction problems. *International Communications in Heat and Mass Transfer*, 37(9):1411–1418, 2010.

[121] Gui-Rong Liu and YuanTong Gu. A point interpolation method for two-dimensional solids. *International Journal for Numerical Methods in Engineering*, 50(4):937–951, 2001.

[122] GR Liu and YT Gu. A local radial point interpolation method (lrpim) for free vibration analyses of 2-d solids. *Journal of Sound and vibration*, 246(1):29–46, 2001.

[123] JG Wang and GR Liu. A point interpolation meshless method based on radial basis functions. *International Journal for Numerical Methods in Engineer-*

ing, 54(11):1623–1648, 2002.

[124] GR Liu, KY Dai, KM Lim, and YT Gu. A radial point interpolation method for simulation of two-dimensional piezoelectric structures. *Smart Materials and Structures*, 12(2):171, 2003.

[125] JG Wang, GR Liu, and P Lin. Numerical analysis of biot's consolidation process by radial point interpolation method. *International Journal of Solids and Structures*, 39(6):1557–1573, 2002.

[126] Gui-Rong Liu. *Meshfree methods: moving beyond the finite element method*. Taylor & Francis, 2009.

[127] GR Liu and YT Gu. Boundary meshfree methods based on the boundary point interpolation methods. *Engineering Analysis with Boundary Elements*, 28(5):475–487, 2004.

[128] Xiong Zhang, Xiao-Hu Liu, Kang-Zu Song, and Ming-Wan Lu. Least-squares collocation meshless method. *International Journal for Numerical Methods in Engineering*, 51(9):1089–1100, 2001.

[129] Zhang Xiong Hu Wei Pan Xiaofei and Lu Mingwan. Meshless weighted least-squares method. *Acta Mechanica Sinica*, 4:005, 2003.

[130] GR Liu and YT Gu. A meshfree method: meshfree weak–strong (mws) form method, for 2-d solids. *Computational Mechanics*, 33(1):2–14, 2003.

[131] Yu Xie Mukherjee and Subrata Mukherjee. The boundary node method for potential problems. *International Journal for Numerical Methods in Engineering*, 40(5):797–815, 1997.

[132] Mandar K Chati and Subrata Mukherjee. The boundary node method for three-dimensional problems in potential theory. *International Journal for Numerical Methods in Engineering*, 47(9):1523–1547, 2000.

[133] S De and KJ Bathe. The method of finite spheres. *Computational Mechanics*, 25(4):329–345, 2000.

[134] Tania GB DeFigueiredo. *A new boundary element formulation in engineering*, volume 68. Springer Science & Business Media, 2013.

[135] YT Gu and GR Liu. Hybrid boundary point interpolation methods and their coupling with the element free galerkin method. *Engineering Analysis with Boundary Elements*, 27(9):905–917, 2003.

[136] Vinh Phu Nguyen, Timon Rabczuk, Stéphane Bordas, and Marc Duflot. Meshless methods: a review and computer implementation aspects. *Mathematics and computers in simulation*, 79(3):763–813, 2008.

[137] SL Ho, Shiyou Yang, José Márcio Machado, and Ho-ching Chris Wong. Application of a meshless method in electromagnetics. *Magnetics, IEEE Transactions on*, 37(5):3198–3202, 2001.

[138] Aaron Jon Katz. *Meshless methods for computational fluid dynamics*. ProQuest, 2009.

[139] Kim Meow Liew, Xin Zhao, and Antonio JM Ferreira. A review of meshless methods for laminated and functionally graded plates and shells. *Composite Structures*, 93(8):2031–2041, 2011.

[140] SD Daxini and JM Prajapati. A review on recent contribution of meshfree methods to structure and fracture mechanics applications. *The Scientific World Journal*, 2014, 2014.

[141] Rajul Garg, Harish Chandra Thakur, and Brajesh Tripathi. A review of applications of meshfree methods in the area of heat transfer and fluid flow: Mlpg method in particular. 2015.

[142] Elías Cueto and Francisco Chinesta. Meshless methods for the simulation of material forming. *International Journal of Material Forming*, 8(1):25–43,

2015.

[143] Xiong Zhang, Kang Zhu Song, Ming Wan Lu, and X Liu. Meshless methods based on collocation with radial basis functions. *Computational mechanics*, 26(4):333–343, 2000.

[144] Wen Chen. New rbf collocation methods and kernel rbf with applications. In *Meshfree methods for partial differential equations*, pages 75–86. 2003.

[145] Xin Liu, GR Liu, K Tai, and KY Lam. Radial point interpolation collocation method (rpicm) for partial differential equations. *Computers & Mathematics with Applications*, 50(8):1425–1442, 2005.

[146] Xin Liu and K Tai. Point interpolation collocation method for the solution of partial differential equations. *Engineering analysis with boundary elements*, 30(7):598–609, 2006.

[147] Božidar Šarler and Robert Vertnik. Meshfree explicit local radial basis function collocation method for diffusion problems. *Computers & Mathematics with applications*, 51(8):1269–1282, 2006.

[148] MR Eslahchi, Mehdi Dehghan, and M Parvizi. Application of the collocation method for solving nonlinear fractional integro-differential equations. *Journal of Computational and Applied Mathematics*, 257:105–128, 2014.

[149] GR Liu and YT Gu. A local point interpolation method for stress analysis of two-dimensional solids. *Structural Engineering and Mechanics*, 11(2):221–236, 2001.

[150] GR Liu and YT Gu. A local radial point interpolation method (lrpim) for free vibration analyses of 2-d solids. *Journal of Sound and vibration*, 246(1):29–46, 2001.

[151] Vladimir Sladek, Jan Sladek, and Chuanzeng Zhang. A comparative study of meshless approximations in local integral equation method. *CMC-TECH*

SCIENCE PRESS-, 4(3):177, 2006.

[152] V Sladek and J Sladek. Local integral equations implemented by mls-approximation and analytical integrations. *Engineering Analysis with Boundary Elements*, 34(11):904–913, 2010.

[153] P.H. Wen and M.H. Aliabadi. Analytical formulation of meshless local integral equation method. *Applied Mathematical Modelling*, 37(4):2115 – 2126, 2013.

[154] P.H. Wen and M.H. Aliabadi. Analysis of functionally graded plates by meshless method: A purely analytical formulation. *Engineering Analysis with Boundary Elements*, 36(5):639 – 650, 2012.

[155] D Soares Jr, V Sladek, J Sladek, M Zmindak, and S Medvecky. Porous media analysis by modified mlpg formulations. *Computers Materials and Continua*, 27(2):101, 2012.

[156] RHJ PEERLINGS R DE and JHP DE VREE. Gradient enhanced damage for quasi-brittle materials. *International Journal for numerical methods in engineering*, 39:3391–3403, 1996.

[157] DP Acharya and Asit Mondal. Propagation of rayleigh surface waves with small wavelengths in nonlocal visco-elastic solids. *Sadhana*, 27(6):605–612, 2002.

[158] Zhen-Gong Zhou, Lin-Zhi Wu, and Shan-Yi Du. Non-local theory solution for a mode i crack in piezoelectric materials. *European Journal of Mechanics-A/Solids*, 25(5):793–807, 2006.

[159] A. C. Eringen. On differential equations of nonlocal elasticity and solutions of screw dislocation and surface waves. *Journal of Applied Physics*, 54(9):4703–4710, 1983.

[160] A. C. Eringen. *Nonlocal Continuum Field Theories*. Springer-Verlag New

York, 2002.

[161] F. Durbin. Numerical inversion of laplace transforms: An efficient improvement to dubner and abate's method. *The Computer Journal*, 17(4):371–376, 1974.

[162] John C Houbolt. A recurrence matrix solution for the dynamic response of elastic aircraft. *Journal of the Aeronautical Sciences*, 17:540–550, 1950.

[163] Nathan M Newmark. A method of computation for structural dynamics. *Journal of the engineering mechanics division*, 85(3):67–94, 1959.

[164] YY Lu, Ted Belytschko, and M Tabbara. Element-free galerkin method for wave propagation and dynamic fracture. *Computer Methods in Applied Mechanics and Engineering*, 126(1):131–153, 1995.

[165] V Sladek, J Sladek, et al. New integral equation approach to solution of diffusion equation. *Computer Assisted Mechanics and Engineering Sciences*, 9:556–572, 2002.

[166] J Sladek, V Sladek, and Roger Van Keer. Meshless local boundary integral equation method for 2d elastodynamic problems. *International Journal for Numerical Methods in Engineering*, 57(2):235–249, 2003.

[167] D Soares, V Sladek, and J Sladek. Modified meshless local petrov–galerkin formulations for elastodynamics. *International Journal for Numerical Methods in Engineering*, 90(12):1508–1828, 2012.

[168] PH Wen and MH Aliabadi. Elastodynamic problems by meshless local integral method: Analytical formulation. *Engineering Analysis with Boundary Elements*, 37(5):805–811, 2013.

[169] M Li, YC Hon, T Korakianitis, and PH Wen. Finite integration method for nonlocal elastic bar under static and dynamic loads. *Engineering Analysis with Boundary Elements*, 37(5):842–849, 2013.